

# **Experimental characterisation of the thermohydraulic performance of a micro-pin fin evaporator: Heat transfer, flow visualization and modelling**

THÈSE N° 8423 (2018)

PRÉSENTÉE LE 16 FÉVRIER 2018

À LA FACULTÉ DES SCIENCES ET TECHNIQUES DE L'INGÉNIEUR  
LABORATOIRE DE TRANSFERT DE CHALEUR ET DE MASSE  
PROGRAMME DOCTORAL EN ENERGIE

ÉCOLE POLYTECHNIQUE FÉDÉRALE DE LAUSANNE

POUR L'OBTENTION DU GRADE DE DOCTEUR ÈS SCIENCES

PAR

Chiara FALSETTI

acceptée sur proposition du jury:

Dr P. Ott, président du jury  
Prof. J. R. Thome, Dr M. Magnini, directeurs de thèse  
Prof. H.-M. Prasser, rapporteur  
Prof. R. Revellin, rapporteur  
Prof. J. A. Schiffmann, rapporteur



ÉCOLE POLYTECHNIQUE  
FÉDÉRALE DE LAUSANNE

Suisse  
2018



Audentes Fortuna iuvat.  
— Virgilio (Eneide, X, 284)





# Acknowledgements

This research study has been carried out at the Heat and Mass Transfer Laboratory, École Polytechnique Fédérale de Lausanne (LTCM, EPFL), under the supervision of Prof. John R. Thome and Dr. Mirco Magnini. Throughout these years many people contributed in different ways to the completion of my doctorate (even if now I have more doubts than when I started!) and it is difficult to express my gratitude in few lines.

First of all, I would like to thank Prof. John R. Thome for the chance he gave to me to pursue a Ph.D. and for his constant scientific support during these years. I am deeply grateful to Dr. Mirco Magnini for being a great co-supervisor and mentor to navigate in the doctorate (and real life) world. I have learnt dedication and enthusiasm for research thanks to both of you.

I wish to express my gratitude to Prof. Horst-Michael Prasser, Prof. Rémi Revellin and Prof. Jürg Alexander Schiffmann, for being present as members of the jury and for your valuable efforts evaluating my work. My thanks to Dr. Peter Ott for accepting to be the president of the jury.

I would like to thank all my colleagues of LTCM lab: without your professional helps and scientific discussions my Ph.D. would not have been so edifying. All the work you have done in our lab was a great source of motivation for me.

I also would like to thank Cécile Taverney and Nathalie Matthey-de-l'Endroit for their support and help since my first day in Lausanne and at EPFL. Thanks to Laurent Chevalley for his technical work on the facility.

Special thanks go to Edoardo, to my special neighbours and to my dearest friends in Brescia and in Lausanne, who supported me during hard times, but also shared a lot of fun time with me outside the lab: ski weekends, hiking trips, parties and voyages. You clearly contributed to make these years an unforgettable period.

Finally, my sincere gratitude goes to my parents Leopoldo and Giulia, and to my sister Francesca: you have always been an example for me and you constantly pushed me to do what I love.

This thesis is dedicated to you.

*Lausanne, 11 January 2018*

Chiara Falsetti

# Abstract

The global tendency towards miniaturization driven by the microelectronics industry is pushing system density and packaging towards unprecedented values of thermal design power, with a dramatic reduction of the surface area of the devices. Vertical integration, which consists of single dies stacked and connected by means of Through-Silicon-Vias (TSVs), is a promising architecture, but it is hampered by the requirement of finding innovative and more effective cooling technology for dissipating the greater amount of heat.

On-chip interlayer two-phase cooling represents a very attractive long-term solution for this problem. However, the design of a two-phase-based cooling system and the ability to predict its performance depend on both the availability of high-accuracy experimental data and appropriate models.

The focus of the present study is thus to provide a broad experimental database to describe the physical processes associated with two-phase flow and characterise the thermal and hydraulic performances of a new micro-pin fin evaporator, in order to assess its feasibility for the realization of a two-phase-based cooling technology.

The micro-evaporator tested here has a heated area of  $1\text{ cm}^2$ , consisting of 66 rows of cylindrical in-line micro-pin fins with a diameter, height and pitch of respectively  $50\text{ }\mu\text{m}$ ,  $100\text{ }\mu\text{m}$  and  $91.7\text{ }\mu\text{m}$ . Channel entrances with and without inlet restrictions are tested in order to demonstrate the beneficial stabilizing effect of placing an extra row of micro-pin fins with a larger diameter of  $100\text{ }\mu\text{m}$  at the beginning of the flow passage area.

Insights on the local trends and magnitudes of the heat transfer coefficient and pressure drops were gained over a wide range of test conditions with mass flux varying from  $500\text{ kg m}^{-2}\text{ s}^{-1}$  to  $2500\text{ kg m}^{-2}\text{ s}^{-1}$ , heat flux ranging from  $20\text{ W cm}^{-2}$  to  $48\text{ W cm}^{-2}$ , and constant outlet saturation temperatures of  $25^\circ\text{C}$ ,  $30.5^\circ\text{C}$  and  $35^\circ\text{C}$ . The tested four refrigerants were R236fa, R245fa, R1234ze(E) and R134a.

Based on the experimental observations, the heat transfer coefficient trend enhances significantly with the applied heat and the vapor quality, while mass flux exhibits a slightly minor influence. These results evidence the mutual influence between the thermal performance of the micro-evaporator and the flow pattern development during its operation, which has been further investigated by synchronizing the infrared temperature measurements and the high speed flow visualization. Moreover, new insights on the nucleation process and on the interface dynamics were gained by applying image processing and time-strip technique to the high-speed camera videos.

Finally, a new heat transfer prediction method that focused on the physical understanding

and predictive capability of flow boiling in between micro-pin fins was developed and compared with the obtained experimental database (7219 local measurements). The new model incorporates the complex flow geometry and the characteristics of the flow regimes occurring along the micro-evaporator, and it successfully predicted the experimental data.

**Key words:** Two-phase flow; Micro-pin fin evaporator; On-chip cooling; Flow visualization; Heat transfer mechanisms; Two-phase flow regimes; Bubble interaction and dynamics; Heat transfer predictive model.

## Sommario

Negli ultimi anni, il trend generale nell'industria microelettronica è quello di promuovere la miniaturizzazione dei circuiti integrati, per ridurre i consumi e i costi, e aumentare la rapidità di trasmissione dei segnali. Sono state proposte dunque nuove architetture, fra le quali strutture 3D in cui i chip vengono integrati verticalmente e posti uno sopra l'altro, generando un nuovo sistema estremamente compatto, garantendo maggiore efficienza e consumi ridotti. Il limite di questi dispositivi, che mostrano prestazioni irraggiungibili con le tecnologie tradizionali, è l'elevato calore da dover dissipare per mantenere la temperatura del dispositivo sotto il suo valore critico nominale ( $\sim 85^\circ\text{C}$  per le CPU).

Trovare un metodo di raffreddamento efficace è quindi uno dei principali focus per lo sviluppo di dispositivi innovativi e compatti. Un sistema di raffreddamento integrato fra i chip, basato su flussi evaporativi bifase, rappresenta ora la soluzione più attraente, anche se, per ottimizzare il design di questi nuovi sistemi e per poter predirne le performances, sono necessari test sperimentali ad hoc e modelli predittivi accurati.

Considerando quanto riassunto, l'obiettivo principale di questo studio è di fornire un ampio range di risultati sperimentali per comprendere la fisica dei flussi bifase liquido-vapore, e poter successivamente caratterizzare le performances termiche e idrauliche di un microevaporatore per raffreddamento bifase.

La superficie totale del microevaporatore è di  $1\text{ cm}^2$ , e comprende 66 file parallele di micro-alette cilindriche di diametro  $50\text{ }\mu\text{m}$ , altezza  $100\text{ }\mu\text{m}$  e passo  $91.7\text{ }\mu\text{m}$ . All'ingresso dell'area di passaggio è stata fabbricata una linea di alette di diametro  $100\text{ }\mu\text{m}$ , per poter stabilizzare il flusso ed evitare instabilità all'ingresso. Attraverso un'ampia campagna sperimentale sono stati calcolati valori locali del coefficiente di scambio termico e delle perdite di carico, variando le condizioni iniziali per ogni test, quali la portata di refrigerante ( $500\text{ kg m}^{-2}\text{ s}^{-1}$  -  $2500\text{ kg m}^{-2}\text{ s}^{-1}$ ), il flusso termico imposto ( $20\text{ W cm}^{-2}$  -  $48\text{ W cm}^{-2}$ ), e la temperatura di saturazione all'uscita ( $25^\circ\text{C}$ ,  $30.5^\circ\text{C}$  e  $35^\circ\text{C}$ ). I refrigeranti testati sono i seguenti: R236fa, R245fa, R1234ze(E) e R134a.

I risultati sperimentali mostrano una forte dipendenza del coefficiente di scambio termico dal titolo di vapore e dal flusso termico, ed una più mitigata dipendenza dalla portata, suggerendo che lo scambio termico sia fortemente influenzato dai regimi di flusso che si sviluppano all'interno del microevaporatore, e viceversa. Per approfondire questo aspetto, sono state sincronizzate le misure di temperatura ottenute con una videocamera a raggi infrarossi, e la visualizzazione ad alta velocità del flusso bifase. Inoltre, una nuova tecnica per processare le immagini del flusso, detta "time-strip technique", è stata applicata per poter studiare il

processo di nucleazione e la dinamica dell'interfaccia liquido-vapore e dedurre i fenomeni di scambio termico associati. Infine, utilizzando i dati sperimentali ottenuti, è stato sviluppato un modello predittivo per il coefficiente locale di scambio termico durante l'evaporazione, che comprende gli effetti della geometria e dei regimi di flusso che si sviluppano all'interno del micro-evaporatore.

**Parole chiave:** Flussi bifase; Microevaporatore; Metodi di raffreddamento; Meccanismi di scambio termico; Visualizzazione e analisi di flussi con camera ad alta velocità; Modello predittivo per coefficiente di scambio termico.



# Contents

<b>Acknowledgements</b>	<b>i</b>
<b>Abstract (English/Italiano)</b>	<b>ii</b>
<b>Contents</b>	<b>vii</b>
<b>List of figures</b>	<b>xi</b>
<b>List of tables</b>	<b>xvii</b>
<b>Nomenclature</b>	<b>xix</b>
<b>1 Introduction</b>	<b>1</b>
1.1 Current trends and issues . . . . .	1
1.2 Research objectives and thesis outline . . . . .	3
<b>2 Literature review</b>	<b>5</b>
2.1 Micro-evaporator geometries . . . . .	5
2.2 Single phase flow studies . . . . .	6
2.3 Advantages of two-phase flow . . . . .	8
2.4 Flow boiling studies . . . . .	9
2.4.1 Heat transfer, pressure drop and flow visualization . . . . .	9
2.4.2 Heat transfer predictive models . . . . .	13
2.5 Conclusions . . . . .	15
<b>3 Experimental set-up and procedure</b>	<b>17</b>
3.1 Experimental test facility . . . . .	17
3.2 Test section: micro-pin fin evaporator . . . . .	21
3.2.1 Microfabrication process . . . . .	21
3.2.2 Geometrical specifications and design . . . . .	22
3.3 Experimental procedure and uncertainty . . . . .	24
3.3.1 Experimental procedure . . . . .	24
3.3.2 Experimental uncertainties and calibration . . . . .	27

<b>4</b>	<b>Single and two-phase data reduction</b>	<b>33</b>
4.1	Single phase data reduction . . . . .	34
4.1.1	Adiabatic single phase tests . . . . .	34
4.1.2	Diabatic single phase tests . . . . .	36
4.2	Two-phase data reduction . . . . .	38
4.2.1	Heat losses calculation . . . . .	38
4.2.2	Onset of two-phase flow and fluid temperature evaluation . . . . .	39
4.2.3	Pressure drops . . . . .	43
4.3	Conclusions . . . . .	46
<b>5</b>	<b>Operational maps, pressure drop, and heat transfer of R236fa</b>	<b>47</b>
5.1	Introduction . . . . .	47
5.2	Single phase validation results . . . . .	47
5.3	Two phase results . . . . .	50
5.3.1	Operational maps . . . . .	51
5.3.2	Pressure drop . . . . .	56
5.3.3	Heat transfer coefficient . . . . .	57
5.4	Conclusions . . . . .	61
<b>6</b>	<b>Hydrodynamic and thermal analysis of a micro-pin fin evaporator</b>	<b>63</b>
6.1	Introduction . . . . .	63
6.2	Single phase validation results . . . . .	63
6.3	Two phase results . . . . .	67
6.3.1	Operational maps . . . . .	67
6.3.2	Analysis of time-dependent patterns . . . . .	70
6.3.3	Pressure drop . . . . .	75
6.3.4	Heat transfer coefficient . . . . .	77
6.3.5	Comparison between R134a and R1234ze(E) . . . . .	82
6.4	Conclusions . . . . .	84
<b>7</b>	<b>Flow pattern-based boiling heat transfer model</b>	<b>87</b>
7.1	Introduction . . . . .	87
7.2	Presentation of the model . . . . .	87
7.2.1	Slug-to-annular flow transition . . . . .	89
7.2.2	Slug flow model . . . . .	93
7.2.3	Annular flow model . . . . .	97
7.2.4	Smoothing function . . . . .	100
7.3	Results . . . . .	102
7.3.1	Heat transfer coefficient trend versus vapor quality . . . . .	102
7.3.2	Evaluation of existing boiling heat transfer prediction models . . . . .	102
7.3.3	New model results . . . . .	105
7.4	Conclusions . . . . .	107



<b>8</b>	<b>Conclusions and recommendations</b>	<b>109</b>
8.1	Summary and highlights . . . . .	109
8.2	Future recommendations . . . . .	112
<b>A</b>	<b>3D heat conduction scheme</b>	<b>115</b>
A.1	Discretization and Tri-DiagonalMatrix Algorithm . . . . .	116
<b>B</b>	<b>Uncertainty analysis</b>	<b>121</b>
B.1	Examples of uncertainty propagation . . . . .	123
B.1.1	Base heat flux uncertainty . . . . .	123
B.1.2	Mass flux uncertainty . . . . .	123
B.1.3	Heat transfer coefficient uncertainty . . . . .	123
<b>C</b>	<b>Image processing techniques</b>	<b>125</b>
	<b>Bibliography</b>	<b>131</b>
	<b>Curriculum Vitae</b>	<b>143</b>



# List of Figures

1.1	Chip stack package with silicon embedded heat transfer structures from the NanoTera project CMOSAIIC started in 2009. . . . .	2
2.1	A schematic of the proposed 3D system with embedded microfluidic cooling [1].	6
2.2	Different micro-pin fin geometries tested by Renfer et al. [2, 3, 4]. . . . .	7
2.3	Micro-pin fin geometries of previous existing studies from (a) Kosar and Peles [5], and (b) Krishnamurthy and Peles [6]. . . . .	10
2.4	Staggered micro-pin fins tested by Isaacs et al. [7]. . . . .	11
3.1	Flow boiling test facility scheme. Cloosed loop of refrigerant. . . . .	18
3.2	Copper manifold housing the test section during the installation. (a) Top side where the inlet and outlet manifold slits are visible, and (b) bottom side with the installed thermocouples. . . . .	19
3.3	(a) Test section installation with pressure taps and connections. (b)-(c) Bottom side of the test section with the film heaters utilized to heat up the area of interest of 1 cm <sup>2</sup> . . . . .	19
3.4	Installation of the high-speed camera coupled with a microscope and if the IR camera respectively at the top and the bottom of the test section. In the zoom: PCB card and pressure transducers connection to the test section. . . . .	20
3.5	Schematic of the photolithography process utilized to fabricate the test sections: (a) PR coating and exposure, (b) dry etching, (c) heaters development, (d) Pyrex cover bounding. . . . .	21
3.6	Stacks of fabricated test sections, top and bottom side of the wafer. . . . .	22
3.7	Optical and SEM measurements on Si wafers after etching the micro-pin fins. . . . .	22
3.8	Micro-pin fin evaporator: (a) top side bounded with a Pirex cover and (b) bottom side with aluminium film heaters. . . . .	23
3.9	(a) Micro-pin fin geometry and configuration, and (b) inlet restrictions before the micro-pin fin array. . . . .	24
3.10	Interface of the LabVIEW program used for the data acquisition. . . . .	26
3.11	Calibration curve of (a) one single thermocouple, and (b) temperature difference between the reference and measured temperatures by four thermocouples to be calibrated versus the reference temperature. . . . .	27
3.12	Calibration curve for one single pixel of the infrared camera. . . . .	28

## List of Figures

---

3.13 Thermal map obtained via IR measurements (a) pre- and (b) post-calibration. .	29
3.14 Calibration curve for the inlet pressure sensor with the fitted correlation to correct the raw signal. . . . .	30
3.15 Experimental repeatability of the obtained local heat transfer coefficient along the micro-evaporator for 2 flow boiling tests with refrigerant R134a: (a) $G = 1000 \text{ kgm}^{-2} \text{ s}^{-1}$ and $q = 40 \text{ Wcm}^{-2}$ and (b) $G = 1500 \text{ kgm}^{-2} \text{ s}^{-1}$ and $q = 40 \text{ Wcm}^{-2}$ . Vertical bar errors represent the uncertainty of 12%. . . . .	31
4.1 Schematic of the micro-evaporator with the infrared camera looking at the bottom.	33
4.2 Single phase R236fa data utilized to develop the correlation for the present two-phase data reduction. Heat losses as a function of (a) the applied heat flux, and (b) of the temperature difference between the evaporator base and the surrounding. . . . .	39
4.3 (a) Local and saturation pressure profiles in the single phase region. (b) Local vapor quality calculated in the single phase region. . . . .	40
4.4 (a) Screenshot from the high-speed camera, and (b) corresponding time-strip analysis of the centerline channel. The vertical lines indicate the onset of two-phase flow. Test conditions of $G = 1000 \text{ kgm}^{-2} \text{ s}^{-1}$ , $q = 28 \text{ Wcm}^{-2}$ , fluid R1234ze(E) and $T_{sat} = 35^\circ \text{C}$ . Flow is from the left to the right. . . . .	41
4.5 (a) Micro-evaporator base temperature measured with the IR camera, and (b) base and footprint temperature profiles along the streamwise direction $z$ . The vertical lines indicate the onset of two-phase flow. Test conditions of $G = 1000 \text{ kgm}^{-2} \text{ s}^{-1}$ , $q = 28 \text{ Wcm}^{-2}$ , fluid R1234ze(E) and $T_{sat} = 35^\circ \text{C}$ . Flow is from the left to the right. . . . .	42
4.6 Fluid temperature profile along the microevaporator length. The temperature increases in the single phase region and after the onset of two-phase flow starts to decrease due to the two-phase pressure drop. . . . .	43
5.1 Total single phase pressure drop as function of the mass flux for: (a) micro-evaporator with inlet restrictions, and (b) micro-evaporator without inlet restrictions. Fluid R236fa. . . . .	48
5.2 Pressure drop along the micro-pin fins array as function of the mass flux for test sections with and without inlet restrictions. . . . .	49
5.3 Single phase friction factor as a function of the Reynolds number for the test sections with and without inlet restrictions. . . . .	50
5.4 Average Nusselt number for both the geometries and comparison with existing correlations. . . . .	51
5.5 (a) Thermal map from the IR camera and (b) screenshot from the high-speed camera taken simultaneously for test conditions of $q = 44 \text{ Wcm}^{-2}$ and $G = 2000 \text{ kgm}^{-2} \text{ s}^{-1}$ , test section with inlet restrictions. The square drawn in the figures identifies the heated area. Flow is from left to right. . . . .	52

5.6	Temperature versus time measured by the IR camera for 5 selected pixels (see Fig. 5.5(a)) within the heated area, for two different test conditions both characterized by the presence of inlet restrictions. . . . .	53
5.7	Two-phase flow operational maps for the test section (a) with inlet restrictions and (b) without inlet restrictions. Five flow regimes are identified: ● single phase; ● jet-flow; ● stable single-phase flow followed by two-phase flow; ● unstable two-phase flow with back flow; ● fully stable two-phase flow. . . . .	54
5.8	Screenshots from the high-speed camera of the four two-phase flow regimes showed in the operational maps for the case with inlet restrictions. For every flow regime 2 different time instants are showed in order to emphasize the time-dependent nature of the flow. (a) jet-flow $q = 24 \text{ W cm}^{-2}$ and $G = 1750 \text{ kg m}^{-2} \text{ s}^{-1}$ , (b) single phase followed by two-phase flow $q = 36 \text{ W cm}^{-2}$ and $G = 1750 \text{ kg m}^{-2} \text{ s}^{-1}$ , (c) unstable two-phase flow $q = 24 \text{ W cm}^{-2}$ and $G = 750 \text{ kg m}^{-2} \text{ s}^{-1}$ , and (d) fully stable two-phase flow $q = 48 \text{ W cm}^{-2}$ and $G = 1750 \text{ kg m}^{-2} \text{ s}^{-1}$ . Flow is from left to right. . . . .	55
5.9	Total measured pressure drop as function of the outlet vapor quality. . . . .	56
5.10	Comparison of the total pressure drop between the geometries with and without inlet restrictions. . . . .	57
5.11	Local heat transfer coefficient as a function of vapor quality for test section with inlet restrictions. Mass flux is $1500 \text{ kg m}^{-2} \text{ s}^{-1}$ . . . . .	58
5.12	Local heat transfer coefficient as a function of vapor quality for test section with inlet restrictions. Heat flux is $q = 20 \text{ W cm}^{-2}$ . . . . .	58
5.13	Local heat transfer coefficient as a function of vapor quality for test section with inlet restrictions. Heat flux is $q = 44 \text{ W cm}^{-2}$ . . . . .	59
5.14	Comparison of local heat transfer coefficient as a function of the vapor quality for the geometry with inlet restrictions and the geometry without. The test conditions shown are for a fixed mass flux equal to $2000 \text{ kg m}^{-2} \text{ s}^{-1}$ . . . . .	60
6.1	Total single phase pressure drop as function of the mass flux for the tested refrigerants: (a) R123ze(E), (b) R134a, and (c) R245fa. Saturation temperature of $T_{\text{sat}} = 25^\circ\text{C}$ . . . . .	64
6.2	Single phase friction factor as a function of the Reynolds number for each of the tested refrigerants. . . . .	65
6.3	Average Nusselt number versus Reynolds number. Fluids: (a) R245fa, (b) R123ze(E), (c) R134a. Comparison with existing correlations. Saturation temperature of $T_{\text{sat}} = 25^\circ\text{C}$ . . . . .	66
6.4	Two-phase flow operational map, fluids (1) R1234ze(E), (2) R134a and (3) R245fa. Four flow regimes are identified: ● single phase; ● jet-flow; ● unstable two-phase flow with back flow; ● fully stable two-phase flow. . . . .	69

## List of Figures

---

6.5	Instabilities of R245fa in different time steps. Explosive vapor burst are created nearby the inlet of the test section and move towards the exit. Flow is moving from left to right, along the $z$ direction. Test conditions: $G = 1000 \text{ kg m}^{-2} \text{ s}^{-1}$ , $q = 28 \text{ W cm}^{-2}$ and outlet saturation temperature of $T_{sat} = 25^\circ \text{C}$ . . . . .	70
6.6	Temperature fluctuations for the fluids R134a and R245 at the same test conditions: $G = 1250 \text{ kg m}^{-2} \text{ s}^{-1}$ , $q = 28 \text{ W cm}^{-2}$ and outlet saturation temperature of $T_{sat} = 25^\circ \text{C}$ . . . . .	71
6.7	(a) Temperature signal over time at the location indicated in Fig. 6.8(a), for $q = 28 \text{ W cm}^{-2}$ and $G = 1000 \text{ kg m}^{-2} \text{ s}^{-1}$ and (b) its Fourier transform. (c) Values of the fundamental frequency detected at different test conditions as a function of mass and heat flux. Fluid is R134a. . . . .	72
6.8	(a) Video frame from the high-speed camera indicating the channel where the time-strip analysis is conducted. The yellow dot shows the location where the temperature signal of Fig. 6.7(a) is extracted. Flow is from left to right. (b) Time-strip analysis of the light intensity for the channel of interest. Location A indicates the most upstream nucleation site, location B identifies the successive nucleation site. (c) Fourier transform of the light intensity at the location of interest (yellow dot in (a)). Flow conditions are $q = 28 \text{ W cm}^{-2}$ and $G = 1000 \text{ kg m}^{-2} \text{ s}^{-1}$ . Fluid is R134a. . . . .	73
6.9	(a) Light intensity signal over time at the location indicated with yellow dashed circles in the (b), (c) and (d) video frames at different time instants, for $q = 28 \text{ W cm}^{-2}$ and $G = 1000 \text{ kg m}^{-2} \text{ s}^{-1}$ . . . . .	74
6.10	Total measured pressure drop versus exit vapor quality for fluid R134a and all the tested conditions. The outlet saturation temperature is $25^\circ \text{C}$ . . . . .	76
6.11	Frictional and accelerational two-phase pressure drop components across versus exit vapor quality for fluid R134a when varying heat flux and constant mass fluxes of (a) $G = 1000 \text{ kg m}^{-2} \text{ s}^{-1}$ and (b) $G = 1500 \text{ kg m}^{-2} \text{ s}^{-1}$ . The outlet saturation temperature is $25^\circ \text{C}$ . . . . .	76
6.12	(a) Map of local heat transfer coefficient (110x110 values) covering the micro-pin fin area and (b) streamwise heat transfer coefficient averaged along the width-wise direction, under the test conditions of $G = 1500 \text{ kg m}^{-2} \text{ s}^{-1}$ , $q = 28 \text{ W cm}^{-2}$ and refrigerant R1234ze(E). The outlet saturation temperature is $25^\circ \text{C}$ . . . . .	77
6.13	(a) 2D temperature map obtained via the infrared camera for the test conditions $G = 1750 \text{ kg m}^{-2} \text{ s}^{-1}$ and $q = 28 \text{ W cm}^{-2}$ . (b) Widthwise averaged values of the footprint and fluid temperatures for $G = 1750 \text{ kg m}^{-2} \text{ s}^{-1}$ and two selected heat flux values. Fluid is R134a. The outlet saturation temperature is $25^\circ \text{C}$ . . . . .	78
6.14	Widthwise averaged values of the (a) footprint heat flux, and (b) heat transfer coefficient along the test section for $G = 1750 \text{ kg m}^{-2} \text{ s}^{-1}$ and two selected heat flux values. Fluid is R134a. The outlet saturation temperature is $25^\circ \text{C}$ . The insets in (b) show two image frames from the high-speed videos. . . . .	79

6.15	Two-phase heat transfer coefficient versus local vapor quality for fluid R134a at different values of mass flux and heat flux. The outlet saturation temperature is 25°C. . . . .	81
6.16	Two-phase heat transfer coefficient versus local vapor quality when varying the mass flux with error bars of 12%. Fluid is R134a. The outlet saturation temperature is 25°C. . . . .	82
6.17	Two-phase pressure drop versus outlet vapor quality. Comparison of refrigerants R134a and R1234ze(E). The outlet saturation temperature is 25°C. . . . .	83
6.18	Two-phase heat transfer coefficient versus local vapor quality. The outlet saturation temperature is 25°C. Comparison of refrigerants R134a and R1234ze(E). . . . .	84
7.1	(a) Working principle of the new flow pattern-based boiling heat transfer prediction model. A heat transfer prediction for slug flow ( $h_{SF}$ ) is used when $0 < x < x_{SF-AF} - \Delta x$ , and another one for annular flow ( $h_{AF}$ ) is used when $x \geq x_{SF-AF} + \Delta x$ . In the flow transition region, a smoothing function is used to ensure a smooth transition between $h_{SF}$ and $h_{AF}$ . (b) Top view schematic of flow regimes development along a channel between two parallel lines of micro-pin fins. . . . .	89
7.2	(a) High-speed camera screenshot and (b) reconstructed 2D gray intensity plot for a boiling test with conditions: $q = 36 \text{ W cm}^{-2}$ , $G = 1500 \text{ kg m}^{-2} \text{ s}^{-1}$ , R1234ze(E) and $T_{sat} = 35^\circ \text{C}$ . Flow is from left to right. The length of the slug flow region $dz$ , is measured from the onset of two-phase flow to the slug-to-annular flow transition. . . . .	90
7.3	(a) Time strip analysis of the light intensity along one single channel at the center of the test section. The slug flow region length is $dz$ . (b) Grey intensity signal along the length of the test section of the time-strip image for the same channel, at different time instants. The peak in the intensity signal evidences the extent of the bubbly region, which starts from the onset of two-phase flow $z_{onset}$ until the slug-to-annular flow transition $z_{SF-AF}$ . Test conditions are: $q = 36 \text{ W cm}^{-2}$ , $G = 1500 \text{ kg m}^{-2} \text{ s}^{-1}$ , R1234ze(E) and $T_{sat} = 35^\circ \text{C}$ . . . . .	91
7.4	Slug-to-annular flow transition vapor quality value $x_{SF-AF}$ under different test conditions. The horizontal red line indicates the mean value obtained from averaging the points in the plot, $x_{SF-AF} = 0.025$ . . . . .	92
7.5	(a) Micro-pin fins configuration. The yellow region is the area considered to calculate an averaged value for the channel width $\overline{W}_{ch}$ . (b) Averaged cross-section area of the flow passage with a uniform distribution of the liquid-phase around the perimeter with a constant thickness $\delta$ . . . . .	95
7.6	(a) Bubble generation frequency $\Omega$ for the slug flow model versus the Boiling number. (b) Dimensionless frequency $\Omega^*$ correlation and data-points versus Boiling number. . . . .	96
7.7	Two-phase friction factor versus Weber core number for annular flow data. Experimental data and correlation. . . . .	99

## List of Figures

---

7.8	Hyperbolic and linear expressions of the smoothing function $\Sigma(x)$ in the transitional range of vapor qualities, defined as: $x_{SF-AF} \pm \Delta x$ . The grey solid lines identify the buffer zone limits. . . . .	100
7.9	Experimental and predicted heat transfer coefficients with hyperbolic and linear smoothing functions in two different buffer zones centered at $x_{SF-AF} = 0.025$ : (a) when $\Delta x = 0$ , and (b) $\Delta x = 0.02$ . Test conditions are: $q = 28 \text{ W cm}^{-2}$ , $G = 1500 \text{ kg m}^{-2} \text{ s}^{-1}$ , R1234ze(E) and $T_{sat} = 30^\circ \text{C}$ . . . . .	101
7.10	Comparison of existing micro-pin fin predictive models with the experimental database. . . . .	104
7.11	Comparison of existing microchannels predictive models with the experimental database. . . . .	105
7.12	Results of the current model on predicting the entire experimental database for every refrigerant and saturation temperature tested. . . . .	106
A.1	Scheme conduction. . . . .	117
A.2	3D TDMA and Newton-Raphson algorithm flowchart. . . . .	118
C.1	Original screenshot extracted from a high-speed camera video during a flow boiling test. Flow is moving from left to right. . . . .	126
C.2	Processed screenshot by using the software <i>ImageJ</i> . . . . .	127
C.3	Time-strip technique applied to two selected channels extracted from the screenshot depicted in Fig. C.2. . . . .	128
C.4	Intensity grey oscillation versus time along the interface between single and two-phase flow. Analysis type 1. . . . .	129
C.5	Intensity grey oscillation versus space for each time step. Analysis type 2. . . . .	129



## List of Tables

2.1	Previous heat transfer predictive models for flow boiling across a micro-pin fin array. $H$ , $W$ and $D$ indicate respectively the height, the width and diameter of a single pin fin. . . . .	14
3.1	Thermophysical properties of interest of each tested refrigerant at $T_{sat} = 30^\circ\text{C}$ .	25
3.2	Experimental test conditions for each tested refrigerant. Dimensionless numbers are calculated at $T_{sat} = 30^\circ\text{C}$ . . . . .	26
3.3	Experimental uncertainties. FS stands for full-scale. . . . .	29
4.1	Heat losses correlation coefficients for each refrigerant. . . . .	39
6.1	Details about the existing correlations whose predictions are included in Fig. 6.3. The Mean Absolute Error is evaluated as $\text{MAE} = \frac{1}{n} \sum_{i=1}^n \frac{ Nu_{exp,i} - Nu_{pred,i} }{Nu_{exp,i}}$ . . . . .	66
7.1	Statistical comparison between the experimental data and existing correlations.	103
7.2	Heat transfer prediction results of the experimental database for each tested refrigerant. . . . .	107
B.1	Experimental uncertainties of the measured parameters. FS stands for full-scale.	122
B.2	Uncertainty propagation results of the calculated parameters. . . . .	122



# Nomenclature

## Roman letters

$A$	area
$Bo$	Boiling number, $q/Gh_{lv}$
$Bo_a$	acceleration Bond number, $\rho A_v d_h^2 / \sigma$
$B$	heated area width
$c_p$	specific heat
$Ca$	Capillary number, $\mu U / \sigma$
$d_h$	flow passage hydraulic diameter
$f$	Fanning friction factor
$G$	mass flux
$H$	height
$h$	heat transfer coefficient
$h_{lv}$	vaporization latent heat
$i$	enthalpy
$I$	current
$k$	thermal conductivity
$L$	heated area length
$\dot{m}$	mass flow rate
$N_{ch}$	number of channels between the pin fin lines
$N_{fin}$	total number of micro-pin fin
$Nu$	Nusselt number, $hd_h/k$
$p$	pressure
$P$	perimeter of the cross section of the channel
$P_{red}$	reduced pressure
$Pr$	Prandtl number, $Pr = \mu c_p / k$
$q$	heat flux
$Q_{el}$	electrical power input
$Q_{losses}$	heat losses
$Re$	Reynolds number, $Gd_h/\mu$
$r_b$	bubble radius
$S$	micro-pin fin pitch
$T$	temperature

## Nomenclature

---

### *Roman letters*

$T_{sat}$	saturation temperature
$t$	time
$t_w$	waiting time
$U$	velocity
$V$	voltage drop across the heater
$W$	width
$w$	width of the hyperbolic smoothing function
$We$	Weber number, $\rho U^2 d_h / \sigma$
$x$	vapor quality
$y, z$	widthwise and streamwise coordinates

*Greek letters*

$\alpha$	thermal diffusivity
$\delta$	liquid film thickness
$\mu$	dynamic viscosity
$\Omega$	bubble frequency
$\rho$	density
$\sigma$	surface tension
$\Sigma$	smooth function

*Subscripts*

<i>AF</i>	annular flow
<i>a</i>	accelerational
<i>amb</i>	ambient
<i>base</i>	base
<i>ch</i>	channel
<i>cont</i>	contraction
<i>end</i>	end of the test section
<i>exp</i>	expansion
<i>f</i>	liquid film
<i>fin</i>	micro-pin fin
<i>fl</i>	fluid
<i>ftp</i>	footprint
<i>g</i>	gas
<i>in</i>	inlet
<i>l</i>	liquid
<i>loc</i>	local
<i>onset</i>	onset of two-phase flow
<i>out</i>	outlet
<i>sat</i>	saturation
<i>sil</i>	silicon
<i>SF</i>	slug flow
<i>SF – AF</i>	slug-to-annular flow transition
<i>sp</i>	single phase
<i>tp</i>	two-phase
<i>tot</i>	total
<i>v</i>	vapor
<i>w</i>	wall



# 1 Introduction

## 1.1 Current trends and issues

Current trends in the microelectronics industry continue to show that integrated circuits (ICs) will become ever more densely packed, in order to reduce the interconnects length and increase the total computing performance. The exponential integration of transistors per area described by Moore's law is going to be surpassed [8], as the demand of computational power is increasing dramatically.

In order to satisfy the product demand, the semiconductor industry is approaching a new era of scaling, moving towards 3D structures of integrated-circuit dies, where single dies are stacked and connected one layer to another by means of Through-Silicon-Vias (TSVs), i.e. high aspect ratio communication lines, which pass through the silicon wafers and connect multiple dies, yielding proximity and inter-connectivity between units. In contrast to the most common planar architecture, the vertical integration technology permits the scalability in the third dimension, thus leading to a reduction of the signal delay time and power dissipation [9, 10, 11]. This novel 3D architecture represents a smart alternative to follow the ongoing miniaturization trend, and a number of researchers provided deep insight into its technological development and advantages [12, 13, 14, 15, 16, 17]. However, the thermal management of such systems emerges as one of the major challenges, as the chip stacking causes an increase in heat dissipation per unit volume [9, 18, 19].

In 2011, the International Technology Roadmap of Semiconductors (ITRS) projected that the power dissipation of a single microprocessor chip would increase to 800W by 2026, with the average heat flux reaching values of  $200\text{Wcm}^{-2}$  in high performance computers and  $450\text{Wcm}^{-2}$  in desktop computers [20]. In 2015, the ITRS confirmed these previsions and outlined the importance of hot spot thermal management for the device reliability.

Besides, the insatiable demand for information has seen data centers to grow, where a gigantic number of servers and memory banks are clustered. Data centers power consumption is rapidly escalating into the hundred of Megawatt range, as reported by ITRS in 2015.

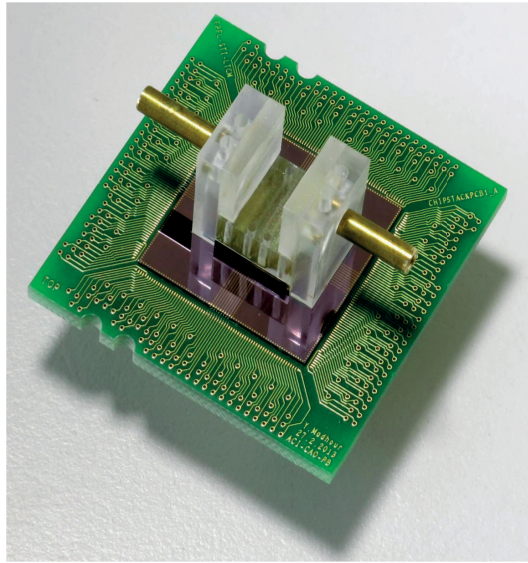


Figure 1.1 – Chip stack package with silicon embedded heat transfer structures from the NanoTera project CMOSAIC started in 2009.

In this framework, the traditional backside air cooling technology will rapidly become obsolete, due to three main reasons: (1) Air has a very low capacity for transporting heat (about  $1 \text{ kJ kg}^{-1} \text{ K}^{-1}$ ) and a low density, thus driving large power requirements to move it. It has been calculated that the power consumption dedicated to CRAC units and fans to cool, dry and circulate the air used as a coolant can represent up to 45% of the overall power consumption of a data centers [21, 22]. If one considers that, in 2011, the energy usage of data centers in the US was estimated to be more than 100 billion of kWh, with an annual cost of approximately \$7.4 billion [23], the dramatic impact of the cooling costs is indeed astonishing. (2) The thermal efficiency of air cooling is low. Saini and Webb [24] showed that air has a maximum heat removal capacity of about  $37 \text{ W cm}^{-2}$ , while later on Tullius et al. [25] reported a maximum limit of  $100 \text{ W cm}^{-2}$  using extended surfaces (fins) and fans, thus making air cooling not adequate as a long-term solution. (3) Conventional air-cooling systems are only capable of cooling single layer logical dies [26], while single and two-phase based interlayer cooling techniques have the capability of meeting the 3D-IC demands of thermal dissipation.

The idea of integrating a liquid-cooled heat sink for compact, high-performance ICs in order to maintain each layer below its critical operating temperature was first introduced by Tuckerman and Pease [27], who constructed a compact liquid water cold plate showing that the use of multi microchannels increased the surface area and thus reduced the heat sink thermal resistance. Starting from that pioneering work, several studies focused on the evaluation of the thermal and hydraulic performances of micro-evaporators for single and two-phase flow interlayer cooling of high-power microelectronics, as it will be outlined in the literature review (**Chapter 2**). Such an integrated cooling system, which comprises the chip stack and the TSV connections, is embedded in a fluid containment with electrical feed-throughs, as depicted



in Fig. 1.1 from the NanoTera project CMOSAIIC. The micro-evaporators can be etched into the backside of a chip, or attached directly to it by a thermal interface material (TIM). The coolant flows in-between each die and, in a system designed to operate in two-phase flow, it enters at quasi saturated conditions and evaporates along the heat sink, by absorbing the heat load generated by the device, thus forming a liquid-vapor mixture. The described microfluidic systems have the potential to achieve very low thermal resistance and to allow multiple tightly arranged CPUs or cores to be easily handled, leading to a very small form factor.

## 1.2 Research objectives and thesis outline

The present thesis aims to evaluate the thermal and hydraulic characteristics of a micro-pin fin evaporator for future use in interlayer on-chip cooling of next generation 3D integrated circuits (ICs), attempting to find a solution to the issues outlined above.

In order to assess the hydrothermal performance of the micro-evaporator and to define its optimal design guidelines, an extensive high-accuracy experimental work has been performed. A fine resolution infrared temperature measurement technique is synchronized and coupled with high-speed flow visualization to investigate the mutual dependency between the thermal characteristics of the present heat sink and the flow pattern development during operation.

Time-dependent features of the flow, operational maps, pressure drop and local heat transfer coefficient in stable flow conditions are evaluated and discussed in the present work, together with their dependency on test conditions, such as mass flux and heat flux. Lastly, the obtained experimental database is utilized to develop a flow pattern-based heat transfer prediction method that incorporates the complex flow geometry and flow pattern effects. The new model will consider the heat transfer mechanisms associated with slug and annular flow regimes.

The present thesis is organized as follows:

**Chapter 1:** Introduction.

**Chapter 2:** A review of existing experimental and numerical studies for the specific problem of interest is outlined. This will underline what are "open" issues in the existing literature and therefore what are the main objectives of the present study.

**Chapter 3:** In this chapter a detailed description of the experimental apparatus and of the micro-pin fin evaporator geometry is given. Additionally, the experimental procedures utilized and the uncertainty of the measured and calculated parameters are described.

**Chapter 4:** This chapter describes the single and two-phase methods utilized to reduce and process the data.

**Chapter 5:** The first experimental campaign performed with R236fa is presented, focusing on the influence of test conditions on the pressure drop and on the trends in the local heat transfer coefficient. Additionally, the beneficial effect of adding channel inlet restrictions is demonstrated by testing two different micro-evaporators under the same conditions, and an analysis of the surface temperature oscillations and of high-speed videos permits to define the stable operating conditions.

**Chapter 6:** This chapter presents the single phase and flow boiling results of three more refrigerants, R245fa, R1234ze(E) and R134a. A synchronized analysis of high-speed camera videos and time-dependent 2D temperature maps are performed to investigate the fluid dynamics (in particular the bubble dynamics) and heat transfer of flow boiling in the micro-evaporator.

**Chapter 7:** The collected database is utilized to develop a new flow pattern-based boiling heat transfer prediction method specific for a micro-pin fin geometry. The new model attempts to assess the heat transfer mechanisms associated with slug flow and annular flow regimes.

**Chapter 8:** This final chapter is dedicated to the conclusions and recommendations for future investigations.

## 2 Literature review

The present literature survey is divided into five main sections. The first part deals with the different geometries of the micro-structures characterizing a heat sink, in particular microchannels and micro-pin fins. The second part presents a number of representative experimental and modeling studies on single phase cooling systems. The third part evidences the advantages related to the use of two-phase flow cooling systems compared to other existing technologies, whilst the fourth part focuses on flow boiling studies, emphasizing the data reduction technique utilized, and the results obtained in terms of flow patterns, heat removal performances and prediction methods. Finally, the last section briefly outlines the conclusions that can be drawn from the literature review.

### 2.1 Micro-evaporator geometries

The most widely studied geometry for interlayer cooling to date consists of parallel multi-microchannels, which represent the state-of-the-art solution. For this, numerous fluids and channel dimensions have been tested and prediction methods proposed in the last decade [28, 29, 30, 31, 32, 33, 34, 20, 35, 36, 37].

Recently, advanced manufacturing techniques have been developed to fabricate new micro-structures or alter the evaporator's surface in order to promote the heat transfer performance, reduce pressure drop or avoid flow instabilities [38].

One potential enhancement solution is to implement micro-pin fins, which represent an alternative to conventional parallel microchannels. In fact, micro-pin fins are compatible with the Through Silicon Vias (TSV) connections, and their dimensions are in line with the dice thickness needed for embedded microfluidic cooling [39, 1]. Figure 2.1 shows a schematic of the proposed 3D system with embedded microfluidic cooling with micro-pin fin geometry. Indeed, in order to achieve higher cooling performances, the chip thickness and the TSV aspect ratio play a critical role in energy dissipation and latency. Besides, they enhance the fluid mixing by disrupting the boundary layer, leading to a more uniform flow distribution and an increase of the heat transfer, as already outlined by previous studies [40, 41, 3, 4, 42, 43].

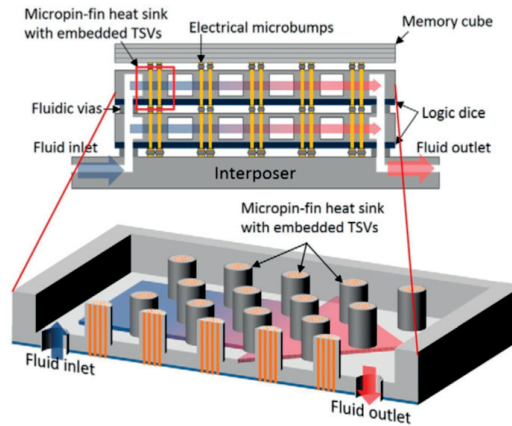


Figure 2.1 – A schematic of the proposed 3D system with embedded microfluidic cooling [1].

Compared to microchannels, the thermal and hydraulic characteristics of micro-pin fin evaporators have received much less attention and the available literature is still rather limited. In the following sections the literature on single and two-phase flow across micro-pin fin arrays will be reviewed in details.

## 2.2 Single phase flow studies

Brunschwiler et al. [10] studied water in single phase flow with a double-sided heated test section for different geometries of micro-pin fins etched in silicon, including in-line and staggered configurations, of round and drop-like shapes and pitches ranging from  $50\text{ }\mu\text{m}$  to  $200\text{ }\mu\text{m}$ , at Reynolds numbers smaller than 1000. The pin fin in-line structures experienced a flow regime transition, resulting in an abrupt pressure gradient change. The micro-evaporator dissipated up to above  $200\text{ Wcm}^{-2}$  for pitches larger than  $50\text{ }\mu\text{m}$  with a pressure drop of  $0.6 \cdot 10^5\text{ Pa}$ .

Renfer et al. [2, 3, 4] investigated the hydrodynamics of single phase water flow across a micro-pin fin array, testing both in-line and staggered configurations with a pin fin diameter of  $100\text{ }\mu\text{m}$ . The different tested geometries are depicted in Fig. 2.2. Here, the flow thermal map was visualized via a micron-resolution laser-induced fluorescence ( $\mu\text{LIF}$ ) technique, which was useful to see the start of vortex shedding downstream of each micro-pin fin. At low Reynolds numbers they found a laminar pre-transition regime in which there were recirculation zones behind the micro-pin fins and channel-like flow between the pin fins in the array. At a value of Reynolds number (based on the hydraulic diameter) of about 350, a hydrodynamic transition was visible in the form of an abrupt rise in the pressure drop slope for the in-line pin fins. At larger Reynolds numbers, transversal fluctuations helped to mix the flow between channels and the Nusselt number curve increased significantly. This flow transitions enhanced the heat transfer performance by up to 230% and reduced the chip temperature non-uniformity.

Prasher et al. [44] studied circular and square shape micro-pin fins with the dimensions ranging from  $50\ \mu\text{m}$  to  $150\ \mu\text{m}$ . The experiments were conducted using water over a Reynolds number range varying from 40 to 1000. They showed how micro-pin fins have a dramatic effect on both the hydrodynamic and thermal behaviour of their cold plates. This was underlined by a transition in the friction factor at a value of the Reynolds number of about 100. After this transition, the friction factor presented an almost zero-dependency on the Reynolds number, as typical for the turbulent flow regime.

A similar transition was observed in the adiabatic single phase results of Kosar et al. [45] for Reynolds number of about 60. In their study, the friction factor measurements were obtained for deionized water flowing across a variety of  $100\ \mu\text{m}$  long pin fins of  $50\ \mu\text{m}$  and  $100\ \mu\text{m}$  hydraulic diameter in both in-line and staggered configurations. They showed how the pin fin height to diameter ratio had a significant effect on the friction factor due to the wall-fin interactions, which reduces at higher Reynolds number.

In a subsequent work, Kosar and Peles [46] studied single phase R-123 and water flow in an array of staggered micro-pin fins of height  $243\ \mu\text{m}$ , diameter of  $99.5\ \mu\text{m}$  and a pitch size equal to  $150\ \mu\text{m}$ , within a range of heat fluxes from  $3.5\ \text{Wcm}^{-2}$  to  $65.5\ \text{Wcm}^{-2}$  and Reynolds numbers from 134 to 314. The Nusselt number was affected by the Prandtl number due to endwalls effects, in particular for water at Reynolds numbers smaller than 100.

Qu et al. [47] performed several experimental studies using deionized water as the working fluid in single phase flow, in an array of square staggered micro-pin fins. The micro-pin fins were made from copper, machined using a microend mill. They compared their measurements of Nusselt number and friction factor with selected correlations from the open literature of intermediate and large scale showing that they all overpredicted their data.

More recently, Mita and Qu [48] investigated the single phase pressure drop across a staggered array of circular micro-pin fins of  $18\ \mu\text{m}$  diameter,  $683\ \mu\text{m}$  height and  $399\ \mu\text{m}$  pitch in both

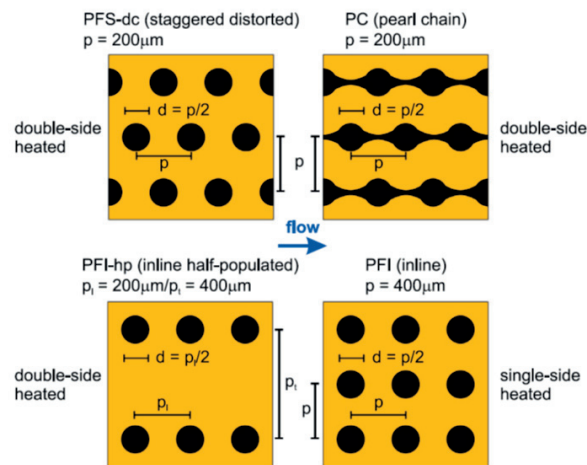


Figure 2.2 – Different micro-pin fin geometries tested by Renfer et al. [2, 3, 4].

directions, using water as the cooling fluid. The test section was fabricated as in a previous work of the same author [47]. They showed that the existing friction factor correlations for micro-pin fin arrays as well as those for tube banks were not able to predict their experimental data. They developed a correlation for friction factor as a function of the Reynolds number using the same power series form as that for tube bundles developed by Zukauskas and Ulinskas [49].

In addition to the experimental studies reported above, some numerical investigations have been carried out to evaluate the thermal and hydraulic performances of a micro-pin fin heat sink. These are noted below.

Yu et al. [50] performed an experimental and numerical study on single phase HFE-7000 flow through a piranha pin fin heat sink. They concluded that the pin fin structures enhanced the heat transfer thanks to the additional exchange area and to the boundary layer separation and mixing of the velocity flow field. The friction factor was comparable with the plain channels.

Wan and Joshi [51] built a numerical model to characterize the performances of a single phase water flow through a micro-pin fin evaporator, showing that circular pin fins present a better heat removal rate than square pin fins for the same pumping power.

A comparison of the different micro-pin fin configurations, such as in-line and staggered, under water single phase laminar flow, has been studied numerically by Rubio-Jimenez et al. [52]. In their study, the staggered configuration performed better than the in-line one, with a thermal resistance on the order of 0.1 K/W.

The effect of fin spacing on the flow development across a six-row inline pin fins under laminar conditions was studied numerically by Liang et al. [53]. The last three pins experienced a maximum value of drag and vortex shedding for a specific critical pitch-to-diameter ratio range between 3 and 3.6, but the frequency of the shedding phenomenon was constant along the pin fin line.

The majority of these research studies are based on single phase water cooled systems, which represent an emergent technology due to their low working pressure, and water's high thermal capacity. This cooling methods have been employed in several applications, but they present two main disadvantages: (i) non-uniform distribution of temperature in the heated area and thus the chip, and (ii) risk of damage to the electronics in case of water leakage [54].

The advantages of implementing two-phase flow cooling systems with dielectric refrigerants are outlined in the following section.

### 2.3 Advantages of two-phase flow

In the framework described above, one promising long-term solution to the thermal management of high power density micro-electronics is the application of interlayer on-chip

two-phase cooling. Indeed, two-phase interlayer cooling is nowadays recognized as one of the most efficient technologies, and some efforts in its development for high heat flux electronic components [55, 26, 10, 56, 20, 57, 58, 28, 59, 60], and data centers [61, 62, 63, 64, 65], are performed by a number of studies.

The use of evaporating flow presents substantial advantages compared to air cooling and single-phase technologies: (i) The use of latent heat yields very large heat transfer performance. As an example, Agostini et al. [60] showed that heat fluxes as high as  $300 \text{ W cm}^{-2}$  and above can be achieved using a two-phase refrigerant; (ii) smaller flow rates of refrigerant and lower pumping power to circulate the fluid at the same heat load are required, thus decreasing the overall cooling costs and making the system more compact; (iii) flow boiling can achieve a more uniform chip surface temperature. This significantly improves the durability of the electronic device due to the reduction of the thermo-mechanical stresses inside the chip [66]. Moreover, a non-uniform temperature also leads to resistance and capacitance variations of the communication lines, causing a latency of the signal propagation and affecting the ICs performance [67]. (iv) Besides, as outlined by Marcinichen et al. [68], the use of on-chip two-phase cooling in data centers also presents the advantage of reusing the heat gained from cooling the chips, for example into a District Heating Network, or for boiler feed water preheating in a power plant [69].

The ultimate cooling solution is to deploy efficient passive two-phase cooling systems, such as a closed-loop two-phase thermosyphon, which eliminates the need of a pump or a compressor, since it operates thanks to a height and density difference [70, 71]. These strategies can reduce data center energy costs and their carbon footprint, i.e. their environmental impact.

The goal of the present study is to experimentally evaluate the thermal and hydraulic performances of a micro-pin fin evaporator for future use in the interlayer on-chip cooling of next generation 3D integrated circuits. Therefore, the related literature will be presented in the following section.

## 2.4 Flow boiling studies

The literature of micro-pin fin flow boiling will be reviewed in two main sections. Firstly, the experimental and numerical studies on heat transfer, pressure drop and flow visualization analysis and, afterwards, the few existing heat transfer prediction methods within a micro-pin fin evaporator will be presented.

### 2.4.1 Heat transfer, pressure drop and flow visualization

A number of studies have focused on micro-pin fin flow boiling heat sinks, in order to evaluate the thermal and hydraulic performances, and optimize the design of such complex systems. Flow boiling offers several benefits, as outlined in the previous section, but it requires a comprehensive understanding of the various phenomena involved. In addition, in such a peculiar micro-scale geometry the fluid dynamics play a fundamental role in determining the



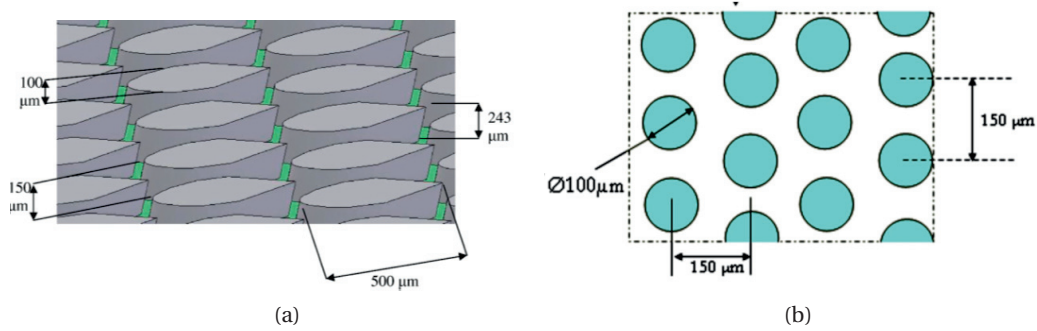


Figure 2.3 – Micro-pin fin geometries of previous existing studies from (a) Kosar and Peles [5], and (b) Krishnamurthy and Peles [6].

flow boiling heat transfer characteristics. Hence, flow visualization techniques emerge as a valuable tool to better investigate the performance of the heat sink, providing a precious insight on the mutual dependency between flow configuration and heat transfer characteristics.

Kosar and Peles [5] performed flow boiling experiments on arrays of hydrofoil shaped pin fins with R-123 (see Fig. 2.3(a)), for heat fluxes ranging from  $19 \text{ W cm}^{-2}$  to  $312 \text{ W cm}^{-2}$ , and mass fluxes from  $976 \text{ kg m}^{-2} \text{ s}^{-1}$  to  $2349 \text{ kg m}^{-2} \text{ s}^{-1}$ . The average surface temperature was estimated using 1-D steady state heat conduction starting from the heater temperature, which was found using an electrical resistance-temperature calibration curve, while the saturation temperature was calculated from a linear pressure profile assumed between the inlet and outlet measured pressure values. They showed that the obtained average heat transfer coefficients were strongly dependent on mass velocity and vapor quality, increasing with heat flux until the critical heat flux condition was reached. They observed three flow patterns that they classified as bubbly, wavy and spray-annular flows depending on the Boiling number.

Krishnamurthy and Peles [6] also conducted flow boiling experiments with an array of circular, staggered micro-pin fins using water as the coolant for heat fluxes from  $20 \text{ W cm}^{-2}$  to  $350 \text{ W cm}^{-2}$  and mass fluxes from  $346 \text{ kg m}^{-2} \text{ s}^{-1}$  to  $794 \text{ kg m}^{-2} \text{ s}^{-1}$ . The tested micro-pin fins are depicted in Fig. 2.3(b). The evaporator surface temperature was estimated starting from the base temperature by utilizing a 1D heat conduction model, while the saturation temperature was obtained using a pressure profile reconstructed by means of a modified version of the Chisholm model [72]. They showed that the average two-phase heat transfer coefficients were independent of heat flux, such that convective boiling was identified to be the dominant heat transfer mechanism. In a subsequent work [73], they examined flow boiling of HFE-7000 in  $222 \mu\text{m}$  hydraulic diameter parallel channels, each containing a single row of 24 in-line pin fins of  $100 \mu\text{m}$  of diameter. The mass fluxes ranged from  $350 \text{ kg m}^{-2} \text{ s}^{-1}$  to  $827 \text{ kg m}^{-2} \text{ s}^{-1}$  and wall heat fluxes ranged from  $10 \text{ W cm}^{-2}$  to  $110 \text{ W cm}^{-2}$ . The heat transfer coefficients were found to be higher with this geometry than with the plain microchannels and the flow visualization confirmed the presence of different patterns along the channel length, i.e. isolated bubbles, interacting bubbles and annular flow.



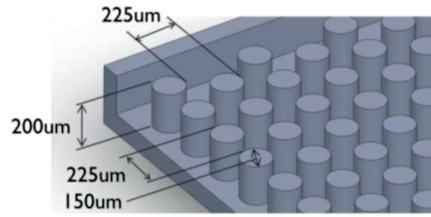


Figure 2.4 – Staggered micro-pin fins tested by Isaacs et al. [7].

Qu and Siu-Ho [74] performed experiments of flow across a staggered array of circular micro-pin fins of  $18\text{ }\mu\text{m}$  diameter,  $683\text{ }\mu\text{m}$  height and  $399\text{ }\mu\text{m}$  pitch in both directions, using water as the cooling fluid, over a range of mass fluxes of  $183\text{ kgm}^{-2}\text{s}^{-1}$ - $420\text{ kgm}^{-2}\text{s}^{-1}$  and heat fluxes of  $23,7\text{ Wcm}^{-2}$  -  $248\text{ Wcm}^{-2}$ . In their data reduction, they computed the micro-pin fin surface temperatures by means of a 1D heat conduction model from a single thermocouple measurement at the micro-evaporator base (similarly to what was done by Krishnamurthy and Peles [6, 73]), while the saturation temperature was obtained from the local pressure, assumed to decrease linearly in the boiling region. The calculated average heat transfer coefficients were dependent on the mass flux at lower vapor quality values, whilst at higher qualities they were almost insensitive to both mass flux and quality. Flow visualization results indicated that annular flow to be the dominant flow pattern.

Mita and Qu [75] evaluated the two-phase pressure drop of the micro-evaporator tested in their previous single phase work [47], showing that it was strongly dependent on vapor quality and that the Lockart and Martinelli prediction procedure could still be applied to evaluate the pressure drop [76].

Isaacs et al. [7] performed experiments with R245fa for an array of staggered micro-pin fins with a  $150\text{ }\mu\text{m}$  diameter,  $200\text{ }\mu\text{m}$  height and  $225\text{ }\mu\text{m}$  pitch, see Fig. 2.4. They evaluated average values of the heat transfer coefficient for multiple heat loads (from  $20\text{ Wcm}^{-2}$  to  $35\text{ Wcm}^{-2}$ ) and flow rates ( $20\text{ ml min}^{-1}$  -  $40\text{ ml min}^{-1}$ ) in two-phase flow. The fluid temperature was considered constant over the fin array, and estimated as the saturation temperature corresponding to an average pressure value between inlet and outlet measurements. In their tests, the average heat transfer coefficient decreased with increasing heat flux and vapor quality. Flow visualization suggested that the reduction of the heat transfer coefficient could be explained by the development of a larger partial and intermittent dry-out zone near the evaporator exit.

Reeser et al. [77] investigated staggered and inline micro-pin fins with  $153\text{ }\mu\text{m}$  width and  $305\text{ }\mu\text{m}$  height using water over a range of mass fluxes of  $400\text{ kgm}^{-2}\text{s}^{-1}$ - $1300\text{ kgm}^{-2}\text{s}^{-1}$ , heat fluxes of  $27\text{ Wcm}^{-2}$  -  $118\text{ Wcm}^{-2}$ , and for HFE-7200 with mass fluxes of  $200\text{ kgm}^{-2}\text{s}^{-1}$  -  $600\text{ kgm}^{-2}\text{s}^{-1}$  and heat fluxes of  $1\text{ Wcm}^{-2}$  -  $36\text{ Wcm}^{-2}$ . In their study, the average heat transfer coefficient was obtained by utilizing a similar data reduction of the studies listed above, and it was strongly dependent on the mass flux for both fluids, while almost no dependence on the heat flux was observed.

Lie et al. [78] performed flow visualization analysis and heat transfer coefficient calculations with refrigerant FC-72 for a range of mass fluxes of  $287 \text{ kg m}^{-2} \text{ s}^{-1}$ – $431 \text{ kg m}^{-2} \text{ s}^{-1}$  and heat fluxes of  $0,1 \text{ W cm}^{-2}$  –  $10 \text{ W cm}^{-2}$ . The micro-structures were in-line square pin fins with a height of  $70 \mu\text{m}$  and two different widths  $100 - 200 \mu\text{m}$ . The fluid temperature was estimated as the saturation temperature of the refrigerant, whilst the wall temperature was estimated from lower surface measured data by accounting for the 1D heat conduction across the chip. The average two-phase heat transfer coefficient increased with the applied heat flux, whilst the mass flux had an almost negligible effect. The bubble characteristics obtained from flow visualization evidenced that the active nucleation site density increased, thanks to the addition of micro-pin-fin structures to the base surface.

Comparative experimental and numerical studies have demonstrated the better thermal performances of micro-pin fins over conventional parallel microchannels. As an example, Ma et al. [79] achieved a substantial flow boiling heat transfer enhancement with the coolant FC-72 in an array of square micro-pin fins with heights and width of, respectively,  $60 - 120 \mu\text{m}$  and  $30 \mu\text{m}$ , compared to a smooth surface.

Chang et al. [80] performed FC-72 flow boiling experiments within micro-pin fins with the same size, and under the same test conditions presented by a previous work of Lie et al. [78]. The pin fins were mounted on the bottom of a horizontal rectangular channel, promoting an increase of the flow boiling heat transfer coefficients. Their experimental and flow visualization results were similar to those obtained by Lie et al. [78].

An augmentation in heat transfer and a delay of onset of critical heat flux when using micro-pin fins instead of microchannels has been observed also by Law and Lee [81] and Deng et al. [82]. The former study [81] showed how the presence of micro pin fins promotes a continuous development and disruption of the thin liquid film during the two-phase flow development, which is beneficial for heat transfer. To calculate the local heat transfer coefficient, the bulk fluid temperature within the saturated region, was equal to the local saturation temperature corresponding to the local pressure obtained as a linear interpolation between the inlet and outlet measurements. A 1D heat conduction assumption was used to extrapolate the temperature readings of the thermocouple and evaluate the wall temperature. The obtained heat transfer coefficients showed an augmentation of between 1.2 and 6.2 times by adding oblique-finned channels with respect to plane channels. In the latter [82], experiments on water and ethanol flow boiling were conducted varying mass fluxes from  $200 \text{ kg m}^{-2} \text{ s}^{-1}$  to  $300 \text{ kg m}^{-2} \text{ s}^{-1}$  and dissipating heat fluxes up to  $106 \text{ W cm}^{-2}$ . Micro cone pin fins were fabricated on the bottom surface of rectangular microchannels of height and width of  $100 \mu\text{m}$  and  $640 \mu\text{m}$ , with an in-line spacing of  $5 \mu\text{m}$ . Their results demonstrated that the addition of micro-pin fins promoted a significant heat transfer enhancement, i.e., of 10–104% for water, and 90–175% for ethanol cases.

David et al. [83] studied flow boiling of R134a across an array of staggered square pin fins with  $350 \mu\text{m}$  width and 1 mm height, under a range of heat fluxes from  $30 \text{ W cm}^{-2}$  to  $170 \text{ W cm}^{-2}$

and mass fluxes from  $230 \text{ kg m}^{-2} \text{ s}^{-1}$  to  $380 \text{ kg m}^{-2} \text{ s}^{-1}$ . The evaporator was installed in an open flow loop, which induced smaller pressure drop than a closed one. The saturation temperature of the refrigerant was calculated using the mean temperature between the inlet and the outlet of the heat sink, whilst the average wall temperature was obtained with a 1D conduction starting from the heater temperature. The heat transfer coefficient increased linearly with heat flux at constant mass flux, while it showed a decreasing trend with exit vapor quality.

Recently, Woodcock et al. [84] performed HFE-7000 flow boiling experiments across a 2.4 mm wide silicon microchannel with an array of entrenched piranha pin fins with diameter of  $150 \mu\text{m}$ . The data were obtained for two flow configurations within the micro-device, open and extraction flow, varying mass fluxes from  $1200 \text{ kg m}^{-2} \text{ s}^{-1}$  to  $7000 \text{ kg m}^{-2} \text{ s}^{-1}$  and heat fluxes up to  $700 \text{ W cm}^{-2}$ . The extraction flow configuration showed the best thermal performance, but also a larger pressure drop.

McNeil et al. [85] compared intermediate size square pin fins, having a width and height of  $1000 \mu\text{m}$ , with a plate surface, performing R113 flow boiling tests over a range of heat fluxes from  $0.5 \text{ W cm}^{-2}$  to  $14 \text{ W cm}^{-2}$  and mass fluxes from  $50 \text{ kg m}^{-2} \text{ s}^{-1}$  to  $250 \text{ kg m}^{-2} \text{ s}^{-1}$ . The obtained heat-transfer coefficients for the pin-fin surface were higher than those for the planar surface, but the pressure drops were about 7 times larger.

Two configurations of micro-structures, a bare and a inline micro-pin fin populated microgaps of width equal to  $10 \mu\text{m}$ , were tested by Nasr et al. [86] under extreme flow conditions, reaching a mass flux value higher than  $3000 \text{ kg m}^{-2} \text{ s}^{-1}$ , and heat flux up to  $1500 \text{ W cm}^{-2}$ . The presence of the pin fins enhanced the heat transfer by about 4 times. Two dominant two-phase regimes were observed by means of flow visualization, vapor plumes and liquid slugs. During the vapor plumes regime, the heat transfer coefficient increased with both heat flux and vapor quality, whilst the opposite was found during the liquid slug regime.

### 2.4.2 Heat transfer predictive models

The paucity and large discrepancy in the currently available two-phase data evidenced in the previous section, severely compromises the accuracy of heat transfer predictive relations. However, predicting the dependency of the two-phase heat transfer characteristics on the occurring flow regimes is of paramount importance to estimate the thermal and hydraulic performances of a micro-evaporator. Indeed, fundamental understanding and accurate heat transfer predictive models are required for the optimal design of a micro-pin fin heat sink intended for high heat flux dissipation.

The few flow boiling heat transfer predictive models for micro-pin fin heat sinks available to date are empirical correlations based on the fit of specific experimental data sets for one single coolant, water in the majority of cases. The few existing micro-pin fin prediction methods are listed in Table 2.1.

Table 2.1 – Previous heat transfer predictive models for flow boiling across a micro-pin fin array.  $H$ ,  $W$  and  $D$  indicate respectively the height, the width and diameter of a single pin fin.

Reference	Test conditions	Geometry	Correlation	Main observations
Kosar and Peles [5]	$q = 19 - 312 \text{ W/cm}^2$ $G = 976 - 2349 \text{ kg/(m}^2\text{s)}$ fluid: R-123	$H = 243 \mu\text{m}$ $W = 100 \mu\text{m}$ Hydrofoil shape	$h_{tp} = \frac{3.42 \cdot 10^7}{(G h_{tp})^{1.16}} q^{1.01} + 0.12 h_{sp}^{0.7}$ , low $G$ $h_{sp} = (0.24 Re_l^{0.75} - 8.88) \frac{k_l}{D_h}$ $h_{tp} = 819 Re_l^{0.6} (1 - x_e)^{0.22} \left( \frac{1 - x_e}{x_e} \right)^{0.01}$ high $G$	Nucleate boiling, $h_{tp}$ depends on $Bo$ . $h_{sp}$ derived from their experimental data. Convective boiling, $h_{tp}$ depends on $Re_l$ .
Krishnamurthy and Peles [6]	$q = 20 - 350 \text{ W/cm}^2$ $G = 346 - 794 \text{ kg/(m}^2\text{s)}$ fluid: water	$H = 250 \mu\text{m}$ $D = 100 \mu\text{m}$ Circular, staggered	$h_{tp} = F h_{sp} = \zeta (\Phi^2)^{0.247} P_r^{0.33} h_{sp}$ corr. 1: $\zeta = 1.4$ ; $\Phi^2$ from Kawahara et al. [88] corr. 2: $\zeta = 1$ ; $\Phi^2$ based on pin fin data [5]	Two correlations based on Chen-type equation [87]. Effects of nucleate boiling neglected. $h_{sp}$ evaluated from Short et al. [89].
Qu and Siu-Ho [74]	$q = 23.7 - 248 \text{ W/cm}^2$ $G = 183 - 420 \text{ kg/(m}^2\text{s)}$ fluid: water	$H = 670 \mu\text{m}$ $W = 200 \mu\text{m}$ Square, staggered	$h_{tp} = F h_{tp,eq}$ $F = 1 - 12.2 x_e^{-1} (101 x + 29.4) x$ $h_{tp,eq} = 50.44 \text{ kW/m}^2 \text{ K}$	$h_{tp}$ constant at higher $x$ . F accounts for subcooling effects. $h_{tp,eq}$ obtained by averaging data at high $x$ .

Considering the microchannel literature, physics-based mechanistic models are a preferred alternative as modelling strategies, as they attempt to capture the two-phase characteristics and transport processes.

Flow pattern specific methods model a single flow regime along the channel, see for instance the three-zone model developed by Thome et al. [90, 91] for the slug flow regime, and the annular flow models of Qu and Mudawar [92], and Cioncolini and Thome [93]. Magnini and Thome implemented transient and dynamic effects of elongated bubbles [94, 95] and updated the three-zone model model of Thome et al. [90, 91] by introducing a new liquid film thickness prediction method and a new bubble nose velocity calculation based on capillary flow theory [96]. Flow pattern based models consider the development of different flow regimes along the channels to better catch the two-phase hydrodynamics and its related heat transfer fundamental mechanisms. As an example, Costa-Patry and Thome [97] merged the three-zone model [90, 91] and the annular flow model [93] to create a new prediction method, and they implemented a heat-flux dependent transition criterion between slug and annular flow. Harirchian and Garimella [98] developed a flow regime-based model to predict the heat transfer coefficient accounting for the successive development of slug and annular flow regimes. Huang and Thome [99] modified the coefficients of the Costa-Patry and Thome correlations for the heat transfer coefficient and the transition criteria to fit their experimental data, also including heat transfer prediction for the subcooled region. In the field of microchannels, a number of previous studies [100, 101, 97, 102, 98] focused on the definition and modelling of flow pattern maps and flow transition criteria for evaporating flows, which are essential tools to develop a flow-pattern based model.

In the present study a new flow pattern based model to predict the local two-phase heat transfer coefficient across a micro-pin fin evaporator is developed, which is to date missing in the open literature, and it will be presented in a later section.

## **2.5 Conclusions**

The main conclusions that can be drawn from the literature review are summarized in this section.

The single phase flow studies reported above underline how the hydrodynamics through a micro-pin fin array has a strong impact on its hydraulic and thermal behaviour. In particular, the effects of the configuration and the geometrical features of a micro-pin fin array have been investigated. Moreover, it has been largely demonstrated that the correlations for macro-scale cylinder arrays (or tube bundles) cannot predict the single phase friction factor and Nusselt number trends in such micro-scale systems adequately. This can be mainly ascribed to the role of the flow confinement in low aspect ratio cavities, which enhance endwall effects.

Addressing now the two-phase flow literature review, it clearly indicates that the presence of micro-pin fins enhance the flow boiling heat transfer, by increasing the surface area and by

## Chapter 2. Literature review

---

influencing the associated two-phase flow development and bubble dynamics. However, the analysis of the literature emphasizes the contrasting heat transfer trends when varying the operating conditions observed by the few independent studies available.

In the majority of the cited studies, the wall temperature was evaluated by means of a 1D heat conduction model starting from a single point value of the temperature measured by a thermocouple or a thermistor, which does not account for lateral heat spreading and for possible hot spot locations. The saturation temperature was nearly always considered to vary linearly between the inlet and the outlet measured values, without taking into account the actual non-linear two-phase pressure drop profile. Szczukiewicz et al. [34] showed that errors in local heat transfer coefficients may approach 100% if the data reduction is done inappropriately, thus motivating the contrasting trends observed in different independent studies. A data reduction procedure better accounting for local temperature and pressure values, which merges together both temperature measurement and flow visualization, should potentially reduce the discrepancy among data from independent laboratories, and such tests are proposed here.

As a matter of fact, the experimental analysis and development of accurate predictive methods for heat transfer and pressure drop in micro-pin fin geometries are limited by the complex fluid mechanics involved, which is tightly correlated to the heat removal rate.

More work is needed to create a larger experimental database of local flow boiling heat transfer coefficients rather than mean data, necessary for modeling purposes, which is also one of the objectives of the current study.

## 3 Experimental set-up and procedure

In the present chapter the experimental flow boiling facility, the micro-pin fin evaporator and the data reduction procedure utilized will be described.

### 3.1 Experimental test facility

The test facility was built and modified by previous PhD students of LTCM to study flow boiling and evaporation in multi-microchannels [103, 104, 105, 106, 107]. The experimental set-up consists of a closed loop of refrigerant, schematically presented in Fig. 3.1. In the loop, an oil-free micro-pump of 21 W is utilized to drive the fluid, while a frequency controller and a Coriolis mass flow meter are adopted to set the refrigerant flow rate and to measure it with an accuracy of 0.35%. The refrigerant is contained in a reservoir which is used to control the saturation pressure in the circuit, by changing its temperature with an RK 20 KP LAUDA compact low-temperature thermostat. Direct DC current is applied to the electrical pre-heater and the voltage drop across it is measured via the National Instrument data acquisition system (NI DAQ) with a sampling rate of 1 kHz over 1 min and then averaged. Before the micro-pump, a 15  $\mu\text{m}$  filter is installed to prevent any contaminants from entering the test section.

In order to set and modify the inlet flow temperature, a sub-cooler and an electrical pre-heater are installed upstream of the test section. Before arriving into the manifold inlet slit, the flow passes through a needle valve, which can be utilized to vary the mass flow rate manually and to stabilize the flow. The refrigerant flows through the test section and it is afterwards condensed by a tube-in-tube heat exchanger. Four K-Type thermocouples are installed along the flow loop to evaluate the fluid temperature and keep the pre-heater wall temperature controlled. All the thermocouples have been calibrated, as it will be presented below, and they have an accuracy of about 0.1 °C.

The test section, which will be described in detail in the following section, is placed in a copper manifold, used to provide and remove the refrigerant via the inlet and outlet manifold slits, which are, respectively, 1 mm and 2 mm wide. The copper manifold has two openings in

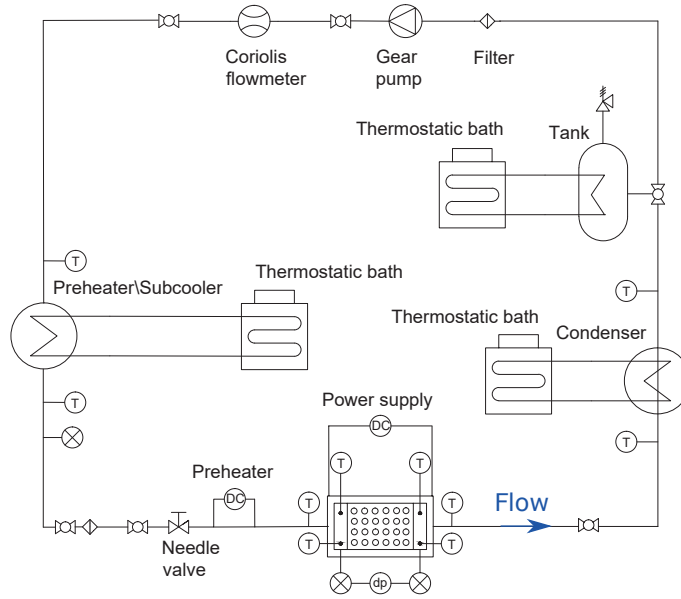


Figure 3.1 – Flow boiling test facility scheme. Closed loop of refrigerant.

order to allow optical access to both the top and the bottom side of the micro-evaporator, see Fig. 3.2(a)-(b). In the manifold inlet and outlet slits there are respectively two Thermocoax 0.25 mm K-Type thermocouples, see Fig. 3.2(b). Their measurements are averaged to get inlet and outlet fluid temperature values.

Moreover, two pressure taps have been placed in the slits, where absolute pressure measurements are performed by 10 bar absolute pressure transducers with a full-scale accuracy of 0.1%, while a differential pressure transducer with a 0.023% full-scale accuracy is used to evaluate the total pressure drop between the inlet and the outlet manifold's plenums. The pressure taps and the connections are depicted in Fig. 3.3(a). Two  $10.5 \times 0.5$  mm EPDM O-rings are positioned around the manifold plenums, and an EPDM gasket of 1 mm thickness is placed between the test section and the manifold cover to prevent leakage and reduce the mechanical stress on the test section.

In order to simulate the heat coming from a chip surface, two aluminium film heaters are printed on the bottom side of the test section, as depicted in Fig. 3.3(b)-(c), where the serpentine covers the heated area of  $1 \text{ cm}^2$ . The two heaters are connected with the electrical power supply via an edge connector installed on the Printed Circuit Board (PCB), see Fig. 3.3(a).

As illustrated in Fig. 3.4, a high speed Photron Fastcam SA3 digital camera is fixed on the top of the test section to record the single and two-phase flow dynamics along the pin fin array. The camera is capable of recording up to 120000 fps, it has a 12-bit  $1024 \times 1024$  pixels CMOS sensor with  $17 \mu\text{m}$  pixel size and adjustable shutter speed, and it is coupled with a Nikon AF Micro Nikkor lens with a focal length of 60 mm to observe the region of interest. It is worth noting that the first experimental session was performed by utilizing an older camera, Photron APX.



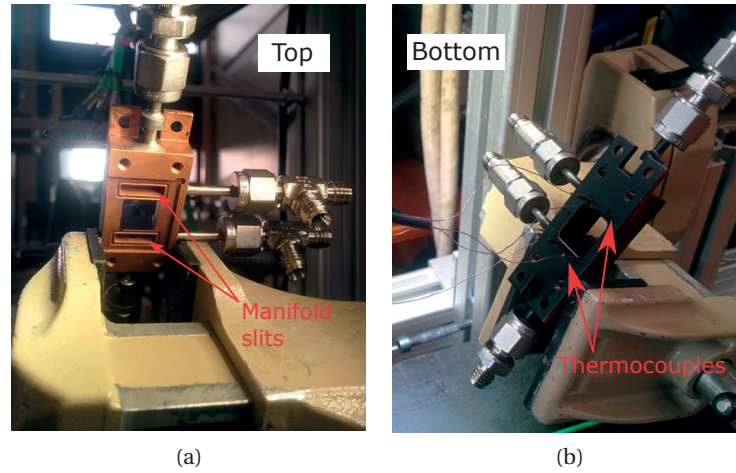


Figure 3.2 – Copper manifold housing the test section during the installation. (a) Top side where the inlet and outlet manifold slits are visible, and (b) bottom side with the installed thermocouples.

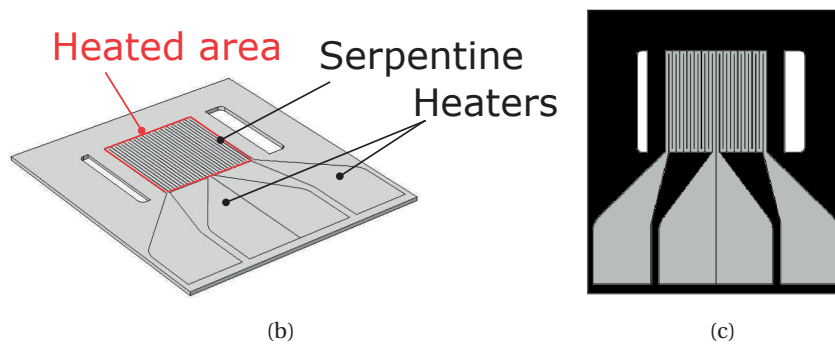
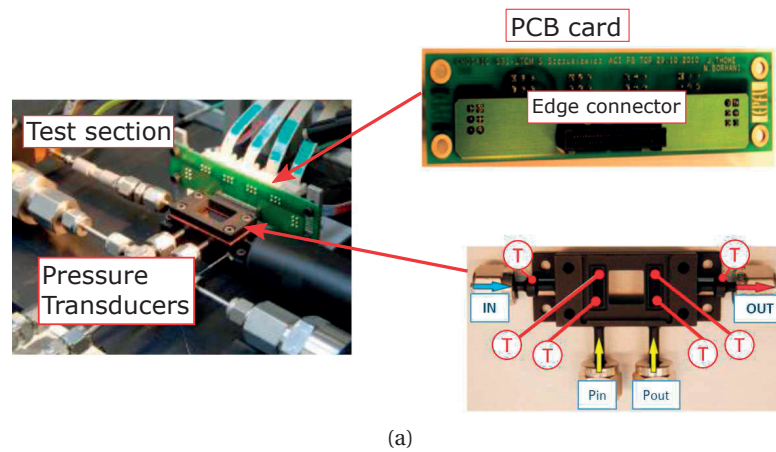


Figure 3.3 – (a) Test section installation with pressure taps and connections. (b)-(c) Bottom side of the test section with the film heaters utilized to heat up the area of interest of  $1 \text{ cm}^2$ .

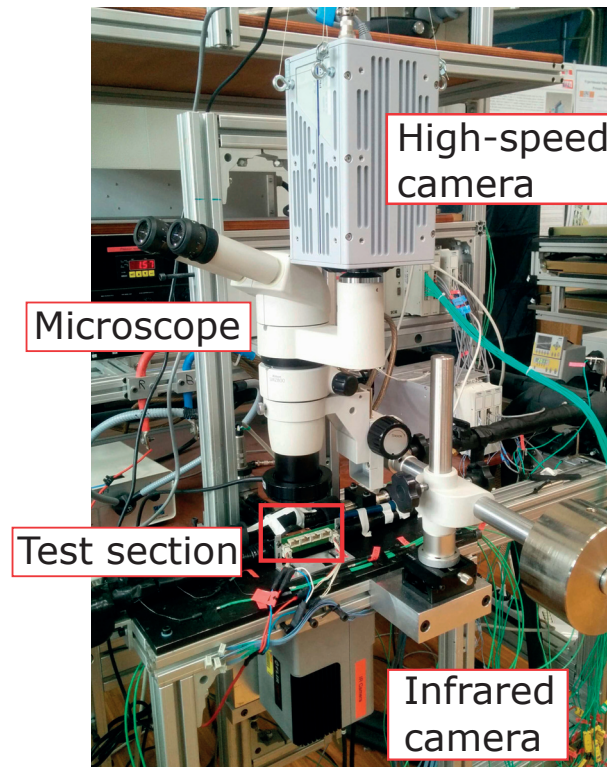


Figure 3.4 – Installation of the high-speed camera coupled with a microscope and if the IR camera respectively at the top and the bottom of the test section. In the zoom: PCB card and pressure transducers connection to the test section.

Below the test section, a ThermaCAM SC3000 high-speed IR camera, having a maximum frame rate of 900 fps, is installed in order to have a fully 2D temperature map of the micro-evaporator bottom surface. The IR camera has a close up lens LW 34/80 and the space between the lens and the chip surface was enclosed in a paper box in order to improve the accuracy of the measurement. Moreover, the bottom surface of the test section was painted with a mat black spray in order to have a surface emissivity as close as possible to 1,  $\epsilon \sim 1$ , to reduce errors from the surrounding ambient.

### 3.2 Test section: micro-pin fin evaporator

In the following subsections, the microfabrication process utilized to fabricate the test sections and its geometrical details are presented.

#### 3.2.1 Microfabrication process

The microfabrication process was based on photolithography and a Deep Reactive Ion Etching (DRIE) process to etch the micro-pin fins in a  $380\mu\text{m}$  thick double-side polished silicon wafer in the Center of Micro-Nano Technology (CMI) at EPFL. The microfabrication process was performed by a previous PhD student in the LTCM lab, H. Jafarpoorchekab, and it is schematically depicted in Fig. 3.5. Silicon has been chosen as the material for the micro-pin fins since it is the most common CMOS compatible material. The material for the electrical heaters is aluminium, which has a simpler deposition process and it is CMOS processing and post-processing compatible. Moreover, it presents a good resistance to delamination that might occur during experiments. The procedure was as follows. First, the wafer was cleaned to remove contaminants and particulates. In order to improve the photoresist adhesion to the wafer surface, a HDMS (Hexamethyldisilazane) vapor priming was performed.

The top side mask pattern, which consists of a  $2\mu\text{m}$  thick layer of the positive photoresist AZ1512, is transferred onto the silicon wafer through a photolithography step. The wafer is then etched via a DRIE Bosh process, and silicon was removed from the places not covered by the photoresist-mask forming vertical trenches of  $100\mu\text{m}$ , see Fig. 3.5(a)-(b). Once the top side was completed, the heaters were created on the wafer back side by means of a sputter deposition. A  $20\text{ nm}$  thick layer of titanium was deposited to enhance the adhesion with the wafer, and afterwards a  $1.5\mu\text{m}$  layer of aluminium was sputtered. Subsequently, the same photolithography process described above was utilized to create the heaters on the bottom side, schematically represented by Fig. 3.5(c). Finally, the silicon die was stripped of any remaining

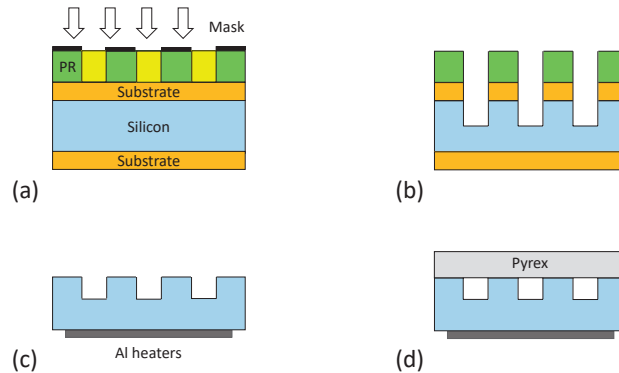


Figure 3.5 – Schematic of the photolithography process utilized to fabricate the test sections: (a) PR coating and exposure, (b) dry etching, (c) heaters development, (d) Pyrex cover bounding.

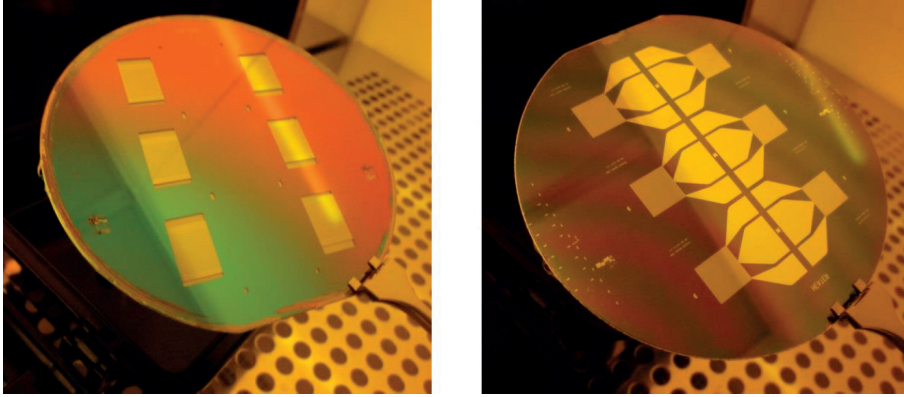


Figure 3.6 – Stacks of fabricated test sections, top and bottom side of the wafer.

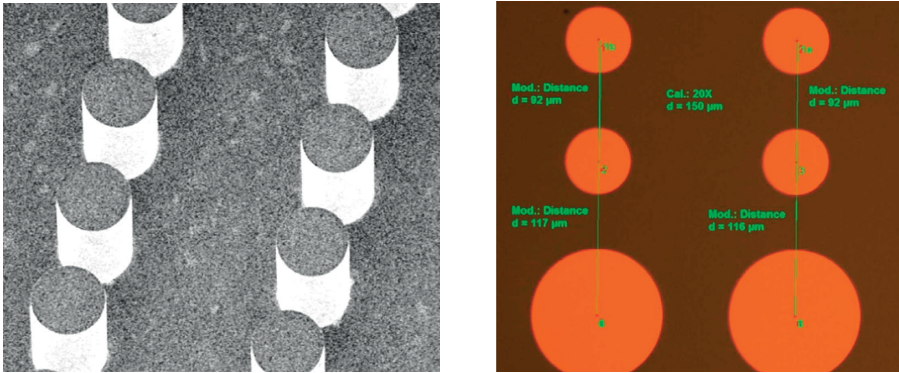


Figure 3.7 – Optical and SEM measurements on Si wafers after etching the micro-pin fins.

oxide and passivation layers and then anodically bonded to a  $525\mu\text{m}$  thick transparent Pyrex cover plate closing the channels from the top, thus allowing flow visualization through the top, see Fig. 3.5(d). After the bonding process, the stack, which comprises six samples as illustrated in Fig. 3.6, was die-sawed to separate the different six test sections.

The fabricated test sections were then characterized by optical microscopy and Scanning Electron Microscopy (SEM). Figure 3.7 shows some typical optical and SEM measurements underlying the precision of the microfabrication process. The optical profiler used was a Veeco Wyko NT1100, with a VSI (Vertical scanning interferometry) vertical resolution of 3 nm, PSI (Phase shifting interferometry) resolution of 0.3 nm and spatial resolution of  $1\mu\text{m}$  and a mechanical profiler Bruker Dektak XT. The measured average surface roughness was about 40 nm, and the electrical resistance of the microfabricated heaters, measured by an open probe station, was about  $15\Omega$ .

### 3.2.2 Geometrical specifications and design

The test section consists of a silicon micro-evaporator with the total perimeter dimensions of  $25.4 \times 28\text{mm}$  and a thickness of  $905\mu\text{m}$  (comprising the silicon of  $380\mu\text{m}$  and the Pyrex

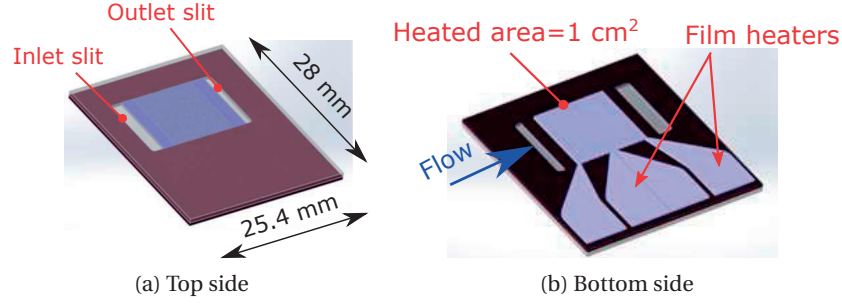


Figure 3.8 – Micro-pin fin evaporator: (a) top side bounded with a Pirex cover and (b) bottom side with aluminium film heaters.

cover of  $525\ \mu\text{m}$ , see Fig. 3.8. As presented previously, the fluid enters the test section via the manifold inlet slit, it flows through the pin fin array and it exits from the manifold outlet slit. The top side of the micro-evaporator is anodically bounded with a Pyrex glass cover, whilst on the bottom side two aluminum film heaters of  $1.5\ \mu\text{m}$  thickness are printed. The heaters are then connected to the electrical power supply via an edge spring connector installed on a Printed Circuit Board (PCB) card, as illustrated in the previous section in Fig. 3.3(a). They can be switched on together or separately to heat up the micro-pin fin area, which covers a total surface of  $L \times L = 1 \times 1\ \text{cm}^2$ , see Fig. 3.8(b) and Fig. 3.9(a). The applied heat flux may be varied between  $0\ \text{W cm}^{-2}$  and  $100\ \text{W cm}^{-2}$  (although the highest heat flux tested in the present study will be  $50\ \text{W cm}^{-2}$ ). The available power source associated with the micro-heater on the facility is a SORENSEN DLM32-95E: 0-32V, 0-95A.

The flow region, i.e. the heated area, is traversed by 66 in-line rows of circular micro-pin fins of diameter and height of respectively  $D_{fin} = 50\ \mu\text{m}$  and  $H_{fin} = 100\ \mu\text{m}$ , as shown in Fig. 3.9(a). The pitch in the streamwise direction is equal to  $91.7\ \mu\text{m}$  and in the widthwise direction is equal to  $150\ \mu\text{m}$ , thus having 67 channels of  $W_{ch} = 100\ \mu\text{m}$  width separated by 66 rows of in-line micro-pin fins. Two versions of test section were fabricated and tested, one with and one without inlet restrictions. The inlet restrictions consist of an extra row of pin fins with a diameter of  $100\ \mu\text{m}$  placed before the heated area, at the inlet of the test section, see Fig. 3.9(b). These dimensions were set equal to the dimensions of previous multi-microchannels test sections utilized in previous studies of the LTCM laboratory [106, 107]. This was done in order to allow a comparison between the performances of a multi-microchannel and a micro-pin fin evaporator.

The restrictions are characterized by their expansion ratio, which is defined as the ratio between the channels width  $W_{ch}$  and the restrictions width  $W_{restr}$ , as follows:

$$e_{restr} = \frac{W_{ch}}{W_{restr}} = 2 \quad (3.1)$$

Previous studies of flow boiling within microchannels demonstrated that inlet restrictions suppress flow instabilities, such as vapor back flow, which can block the flow passage and



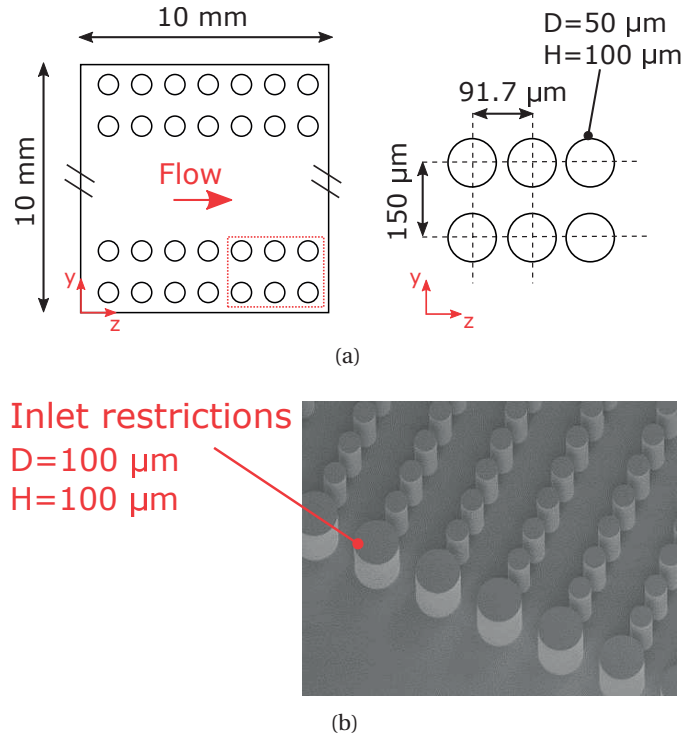


Figure 3.9 – (a) Micro-pin fin geometry and configuration, and (b) inlet restrictions before the micro-pin fin array.

cause local dry-out [36]. Vapor back flow leads to high-amplitude and high-frequency temperature and pressure oscillations [108], which can damage or even break the micro-evaporator. Another advantage of inlet restrictions is that they promote vapor flashing. As explained by Park and Thome [109], when flashing is present the boiling starts at a lower heat flux, thus increasing the uniformity of the surface temperature.

### 3.3 Experimental procedure and uncertainty

#### 3.3.1 Experimental procedure

In the present study four different refrigerants were tested: R236fa, R245fa, R1234ze(E) and R134a. REFPROP 8.0 (NIST 2013, Version 9.1) was utilized for the refrigerant thermophysical properties, which are listed in Table 3.1 at a corresponding saturation temperature of 30 °C. This value of temperature has been chosen here as all the tests were performed in a range of saturation temperature of  $30 \pm 5^\circ\text{C}$ .

In Table 3.2 the applied test conditions, such as mass flux, heat flux and saturation temperature, are listed for each tested fluid. The inlet liquid subcooling was set to  $5.0 \pm 1.5$  K during the entire experimental campaign. As can be noted in Table 3.2, R236fa has been tested under the largest range of conditions because it showed a good stability during flow boiling tests, and

### 3.3. Experimental procedure and uncertainty

due to its 2nd lowest pressure, higher mass flux could be tested. With R236fa, two different micro-evaporators, respectively with and without inlet restrictions, have been examined. The micro-evaporator without inlet restrictions showed significant flow instabilities, such as back flow, which led to high-amplitude temperature (0.9 – 1 K in magnitude) and pressure oscillations. Thus, the subsequent experiments with the other refrigerants have been conducted by using the micro-evaporator with inlet restrictions only.

The refrigerant R245fa was unstable over a wide range of test conditions. During the flow boiling tests, back flow and flow reversals were always present. When the mass flux was increased to stabilize the two-phase flow, nucleation stopped and the vapor phase was quickly suppressed leading to single phase flow. This behaviour, which will be described in the results, can be ascribed to its larger liquid to vapor density ratio, which triggers significant boiling instabilities.

R134a and R1234ze(E), medium to high pressure refrigerants, were stable over a wide range of test conditions. R134a is one of the most utilized working fluids in system studies as opposed to low pressure dielectric coolants (such as FC-72) or water. R1234ze(E) has a much lower Global Warming Potential than R134a, 7 compared to 1360, a slightly lower working pressure and it is considered as an immediate/future *green* replacement for R134a. For these refrigerants, the mass flux was not tested exceeding the value of  $1750 \text{ kg m}^{-2} \text{ s}^{-1}$  and the set saturation temperature of R134a was equal to  $25^\circ\text{C}$  in order to maintain a fluid pressure inside the test section lower than 8 – 9 bar. A higher fluid pressure may have caused breakage of the test section, in particular along the bounding line between silicon and Pyrex, which is the most fragile location.

Differently from the test conditions, which were varied depending on the fluid utilized, the applied experimental procedure was the same for all the fluids. An implemented in-house LabVIEW program was utilized to control the facility's instrumentation, set the desired test conditions, such as mass flux via a PI controller, and acquire the data. The data acquisition was performed using the National Instruments data acquisition system NI DAQ. In Fig. 3.10 a screenshot of the LabVIEW program interface is depicted. The scheme of the closed loop is visualized on the left side with the fundamental test parameters, whilst the control panel is on the right side. The experimental procedure, valid for both single and two-phase flow tests, is described in the following main steps:

1. Impose and maintain a constant outlet saturation temperature by adjusting the temper-

Table 3.1 – Thermophysical properties of interest of each tested refrigerant at  $T_{sat} = 30^\circ\text{C}$ .

Refrigerant	$p [\text{kPa}]$	$\rho_l [\text{kg/m}^3]$	$\rho_v [\text{kg/m}^3]$	$k_l [\text{W/(m K)}]$	$\mu_l [\mu\text{Pa s}]$	$\sigma [\text{mN/m}]$	$h_{lv} [\text{kJ/kg}]$	Pr [-]
R236fa	320.36	1342.4	21.57	71.4	267.45	8.99	142.42	4.67
R245fa	177.79	1324.9	10.16	86.5	374.63	12.99	187.33	5.77
R1234ze(E)	578.33	1146.4	30.52	72.50	187.88	8.20	163.06	3.63
R134a	770.2	1187.5	37.53	78.9	183.13	7.38	173.10	3.35

### Chapter 3. Experimental set-up and procedure

Table 3.2 – Experimental test conditions for each tested refrigerant. Dimensionless numbers are calculated at  $T_{sat} = 30^\circ\text{C}$ .

Conditions	R236fa	R245fa	R1234ze(E)	R134a
$G [\text{kg}/(\text{m}^2\text{s})]$	500 – 2500	500 – 1500	750 – 1750	750 – 1750
$q [\text{W}/\text{cm}^2]$	20 – 48	20 – 48	20 – 44	20 – 44
$T_{sat} [^\circ\text{C}]$	$30.5 \pm 0.5$	$25 - 30.5 \pm 0.5$	$25 - 30.5 - 35 \pm 0.5$	$25 \pm 0.5$
$p_{sat} [\text{bar}]$	3.2	1.8	$4.9 - 5.7 - 6.6$	6.6
$p_{red} [-]$	0.10	0.048	0.16	0.18
$Re [-]$	187 – 935	133 – 400	400 – 931	410 – 956
$Bo [-]$	$0.0013 - 0.0028$	$0.0017 - 0.0021$	$0.0015 - 0.0016$	$0.0015 - 0.0016$
$Ca [-]$	$0.011 - 0.055$	$0.010 - 0.032$	$0.015 - 0.035$	$0.0157 - 0.036$

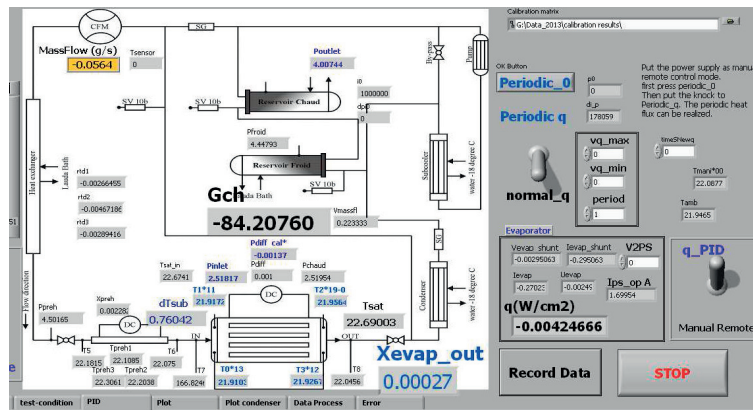


Figure 3.10 – Interface of the LabVIEW program used for the data acquisition.

ature of the thermostat;

2. Fix the inlet subcooling value by means of the pre-heater/subcooler;
3. Set the mass flux and the heat flux via the LabVIEW program and controller. The mass flux can be adjusted also by a needle valve installed upstream the test section inlet;
4. Wait for the steady-state conditions to be achieved i.e. when the standard deviations of the oscillating fluid temperatures were smaller than 0.3 K and pressure oscillations smaller than 1%. Flow visualization was useful to check the stability of the two-phase flow;
5. Acquire data for a period of 30 s with the LabVIEW program. Simultaneously, a thermal map of 110 by 110 values and a high-speed video obtained by means of the high-speed camera are registered;

The infrared (IR) camera measured the bottom surface temperature at a frequency of 60 Hz, generating 1800 frames which are averaged to obtain a time-averaged temperature map of 110x110 measurements. The high-speed camera registered videos at a frequency of 1000 Hz (or at 2000 Hz when the old camera is utilized) for a period of 2.7 s, giving 2727 frames.



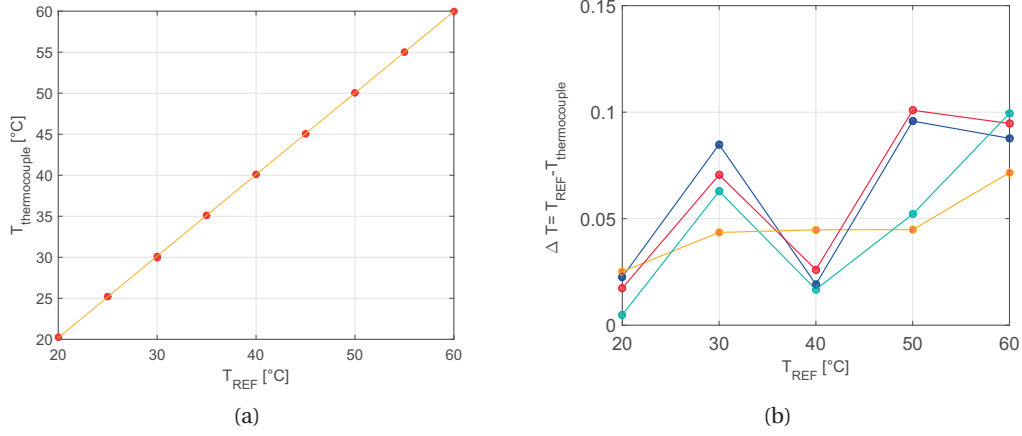


Figure 3.11 – Calibration curve of (a) one single thermocouple, and (b) temperature difference between the reference and measured temperatures by four thermocouples to be calibrated versus the reference temperature.

#### 3.3.2 Experimental uncertainties and calibration

This section illustrates the calibration procedures (for thermocouples, pressure transducers and IR camera), which are utilized to evaluate the uncertainty of the measured parameters, such as temperature and pressure.

All the K-type thermocouples are calibrated via a thermalresistance thermometer Pt-100 in a thermostatic bath LAUDA RE207 over the test range of 20 – 60 °C. The bath's temperature was increased from 20 °C to 60 °C and back to 20 °C with increments of 5 °C. No hysteresis effects were noticed. The standard temperatures (obtained with the PT100) were then linearly fitted with the raw temperatures as it is possible to observe in the calibration fit for one single thermocouple in Fig. 3.11(a). The estimated thermocouples accuracy is of  $\pm 0.1^{\circ}\text{C}$ , as shown in Fig. 3.11(b) where the difference between the reference temperature and the temperature measured by thermocouples is plotted versus the reference temperature.

The infrared camera has been calibrated with an in-house pixel by pixel calibration, in which all the pixels are calibrated individually by performing specific adiabatic single phase tests following these main steps:

1. Impose a value of mass flux of  $G = 2500 \text{ kg m}^{-2} \text{ s}^{-1}$  in order to ensure a uniform temperature distribution among the pin fin array;
2. The fluid temperature is varied by using the subcooler installed before the test section from 20 °C to 45 °C and then decreased again to 20 °C;
3. At adiabatic and steady conditions the base temperature, obtained from the IR camera, is considered to be equal to the fluid temperature measured by the inlet and outlet

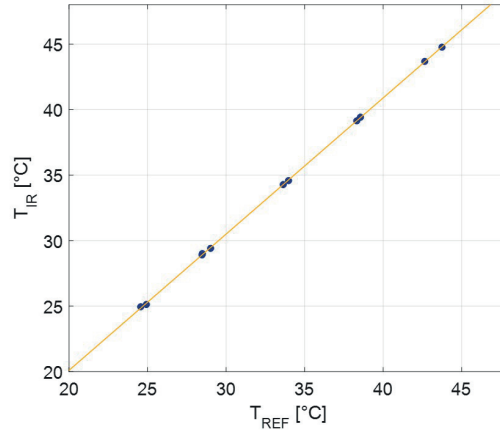


Figure 3.12 – Calibration curve for one single pixel of the infrared camera.

thermocouples;

4. The thermocouples (already calibrated) at the inlet and outlet manifold slits give the averaged fluid reference temperature;
5. A linear calibration fit for every pixel is done. An example of the linear fit for one single pixel is depicted in Fig. 3.12.

In the calibrated temperature range, the accuracy of the IR camera reading is equal to  $\pm 0.2^{\circ}C$  against the manufacture's accuracy value of  $\pm 2^{\circ}C$ . An example of a thermal map acquired with the infrared camera before and after the calibration procedure is presented in Fig. 3.13. The temperature should be uniform all over the area of interest since an adiabatic test with a value of mass flux of  $G = 2500 \text{ kg m}^{-2} \text{ s}^{-1}$  is performed. As it can be observed, before the calibration the temperature of the area extracted by the IR camera varies between  $27.9^{\circ}C$  and  $28.9^{\circ}C$  (by 1 K, see Fig. 3.13(a)), whilst after the calibration procedure it varies from  $28.85^{\circ}C$  and  $28.92^{\circ}C$  (thus only by 0.07 K), showing the improvement obtained via the pixel by pixel calibration procedure, as depicted in Fig. 3.13(b).

The absolute pressure transducers were calibrated with a standard dead weight balance manufactured by Yantrika Instruments (model REW415HAA-1), in a pressure scale range of 0 – 10 bar. Figure 3.14 shows the calibration curve for the inlet pressure sensor, with the equation applied for the correction of instrument raw signal.

Differently from the measured parameters, the uncertainty of the calculated parameters is estimated applying the error propagation method developed by Kline and McClintock [110]. This is explained in details in **Appendix B**, where the uncertainties of both the measured and calculated parameters are outlined.

Table 3.3 presents the uncertainties of the main parameters of interest, as it will serve as a reference for all the results presented during the discussion in the following chapters. As

### 3.3. Experimental procedure and uncertainty

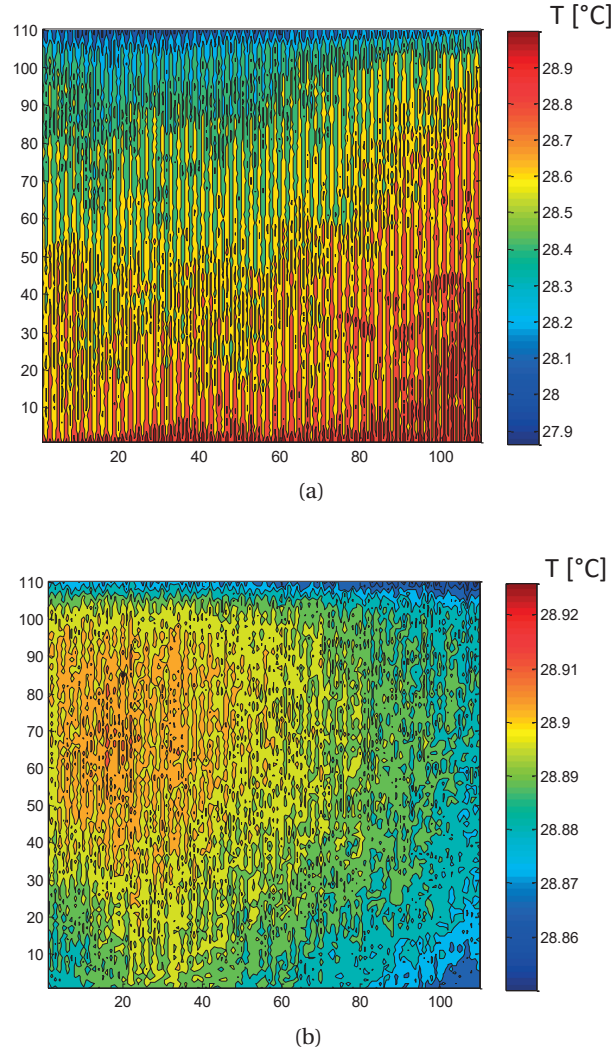


Figure 3.13 – Thermal map obtained via IR measurements (a) pre- and (b) post-calibration.

Parameter	Uncertainty	Parameter	Uncertainty
$q_{base}$ [ $\text{W}/\text{cm}^2$ ]	$\pm 5$	$G$ [ $\text{kg}/(\text{m}^2\text{s})$ ]	$\pm 7\%$
$T_{base}, T_{in,out}$ [ $^{\circ}\text{C}$ ]	$\pm 0.1 \pm 0.2$	$p_{in}, p_{out}$ [kPa]	$\pm 0.1 \text{ FS}\%$
$\Delta p_{tot}$ [kPa]	$\pm 0.023 \text{ FS}\%$	$\Delta p_{fin}$ [kPa]	$\pm 5.9\%$
$h_{ftp}$ [ $\text{W}/\text{m}^2\text{K}$ ]	$\pm 4\%$	$h_w$ [ $\text{W}/\text{m}^2\text{K}$ ]	$\pm 12\%$
$Re[-], Re_{tp}[-]$	$\pm 7\%, \pm 9\%$	$f[-]$	$\pm 15\%$
$Nu[-]$	$\pm 13.9\%$	$x[-]$	$\pm 9.2\%$

Table 3.3 – Experimental uncertainties. FS stands for full-scale.

already mentioned, the complete table with all the uncertainties is in **Appendix B**.

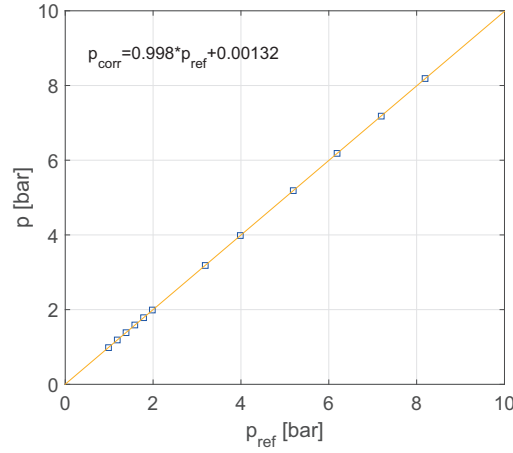


Figure 3.14 – Calibration curve for the inlet pressure sensor with the fitted correlation to correct the raw signal.

Lastly, the repeatability of the flow boiling experiments has been also tested and verified. Experiments with identical test conditions have been repeated twice on different days during the experimental campaign. Two examples of repeated tests with refrigerant R134a are depicted in Fig. 3.15. The vertical error bars in the plot indicate the uncertainty of the wall heat transfer coefficient of 12 %, as presented in Table 3.3 and in **Appendix B**. Results were shown to be repeatable as well as reproducible, with a RMS error of 6.5%, calculated as

$$\text{RMS} = \sqrt{\frac{\sum_{i=1}^n (h_{w,1} - h_{w,2})_i^2}{n}}.$$

The largest discrepancy is nearby the outlet of the test section. This could be ascribed to the heat spreading at the edges of the heated area, or probably to a slightly different development of annular flow towards the exit of the pin fin array.

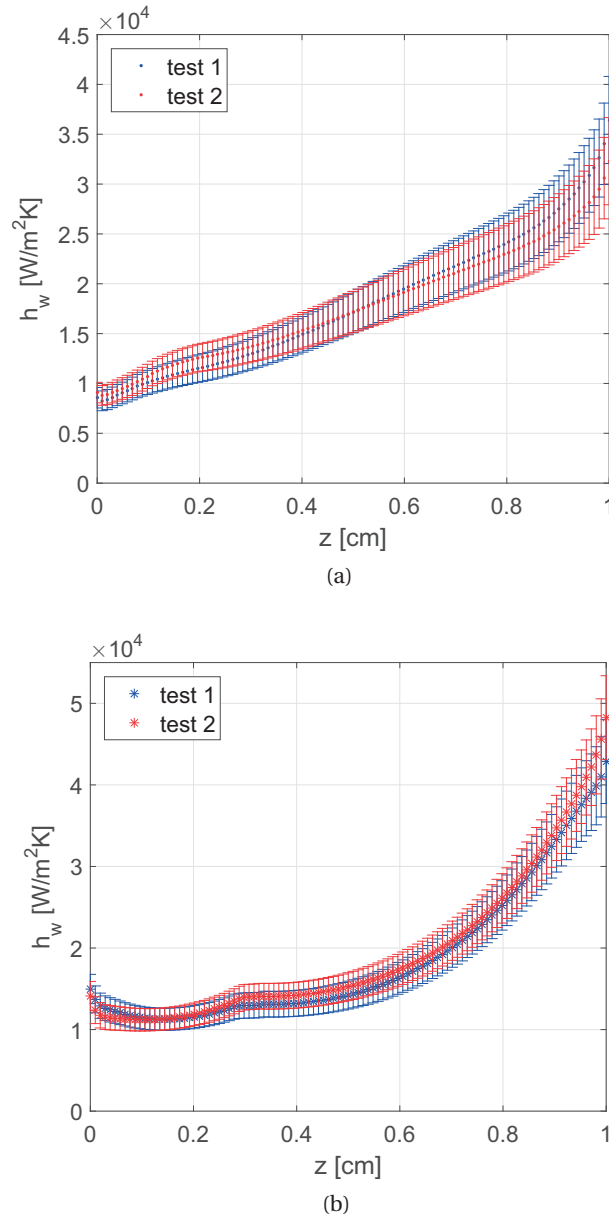


Figure 3.15 – Experimental repeatability of the obtained local heat transfer coefficient along the micro-evaporator for 2 flow boiling tests with refrigerant R134a: (a)  $G = 1000 \text{ kg m}^{-2} \text{ s}^{-1}$  and  $q = 40 \text{ W cm}^{-2}$  and (b)  $G = 1500 \text{ kg m}^{-2} \text{ s}^{-1}$  and  $q = 40 \text{ W cm}^{-2}$ . Vertical bar errors represent the uncertainty of 12%.



## 4 Single and two-phase data reduction

This chapter outlines the single and two-phase data reduction utilized in the study. The experimental procedures begin with the adiabatic and diabatic single phase tests prior to those for the boiling experiments.

The following description of the data reduction procedure will refer to three different "layers" of the microevaporator which are: the evaporator base, the evaporator footprint and the surface walls of the micro-pin fins, which are schematically depicted in Fig. 4.1. As presented in the experimental set-up description, the heat flux is applied at the base of the heat sink via two electrical film heaters. Heat propagates by heat conduction through the base layer. Part of it ( $q_{loss}$ ) leaves the evaporator through the evaporator sides, despite the thermal insulation, while the remaining part ( $q_{ftp}$ ), typically on the order of 90% of the total applied heat flux is transferred to the microevaporator footprint level. The refrigerant flows through the micro pin fin array over the footprint surface. The top of the micro-pin fins are bonded to a Pyrex transparent cover, which permits to visualize the flow by means of the high-speed camera. The infrared camera, which is installed at the bottom of the micro-evaporator, as illustrated Fig. 4.1,

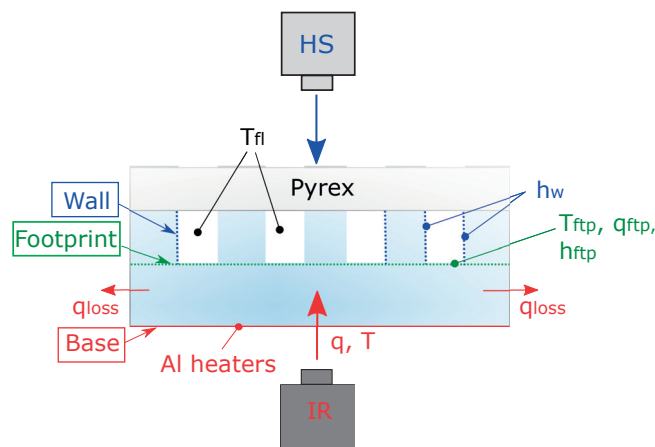


Figure 4.1 – Schematic of the micro-evaporator with the infrared camera looking at the bottom.

gives a matrix of 110x110 local pixel measurements of the base temperature, which allows to obtain two different heat transfer coefficients for the micro-pin fin heat sinks: the footprint heat transfer coefficient  $h_{ftp}$ , and the wall heat transfer coefficient  $h_w$ , calculated on the surface area of the pin fins by means of the footprint one by applying the fin efficiency method, as it will be presented below. On the top of the test section, a high-speed camera visualizes the flow dynamics development along the pin fin array.

### 4.1 Single phase data reduction

Adiabatic and diabatic single phase tests were done as preliminary tests, not only to validate the reliability of the test facility, but also to develop a correlation for the friction factor of the all liquid flow and to characterize the heat losses, which will both be used in the successive two-phase data reduction process, as explained below.

#### 4.1.1 Adiabatic single phase tests

The first parameter to calculate is the adiabatic pressure drop along the pin fin array,  $\Delta p_{fin}$ , since it is used to extract the adiabatic single phase friction factor. The pressure drop along the pin fin array is evaluated from the total pressure drop,  $\Delta p_{tot}$ , which is measured between the inlet and the outlet manifold's plenums with a differential pressure transducer, and then reduced with the inlet and outlet pressure drops,  $\Delta p_{in}$  and  $\Delta p_{out}$ , as follows:

$$\Delta p_{fin} = \Delta p_{tot} - \Delta p_{in} - \Delta p_{out} \quad (4.1)$$

$$\Delta p_{in} = \Delta p_{cont1} + \Delta p_{cont2} + \Delta p_{cont3} + \Delta p_{exp1} \quad (4.2)$$

$$\Delta p_{out} = \Delta p_{exp2} + \Delta p_{exp3} + \Delta p_{exp4} \quad (4.3)$$

The contributions to the inlet pressure drop are the pressure drop in the flow contractions between the inlet manifold's plenum and inlet slit  $\Delta p_{cont1}$ , that between the inlet slit and the test section's plenum  $\Delta p_{cont2}$  and, when present, the pressure drop across the inlet restrictions  $\Delta p_{cont3}$ . The inlet restrictions also add a pressure recovery due to the expansion into the channels, identified as  $\Delta p_{exp1}$ . The outlet pressure drop consists of 3 recoveries due to the expansions between the channels and the outlet test section plenum  $\Delta p_{exp2}$ , between the test section plenum and the outlet slit,  $\Delta p_{exp3}$ , and between the outlet slit and the outlet manifold plenum  $\Delta p_{exp4}$ . All the contraction and the expansion pressure drops are computed according to the method of Lee and Garimella [29]:

$$\Delta p_{cont} = \left[ 1 - \left( \frac{A_2}{A_1} \right)^2 + K \right] \frac{G^2}{2\rho_l} \quad (4.4)$$

$$K = 0.0088 \cdot a_r^2 - 0.1785 \cdot a_r + 1.6027 \quad (4.5)$$

$$\Delta p_{exp} = -2 \cdot 1.33 + \left( \frac{A_1}{A_2} \right) \left[ 1 - \left( \frac{A_1}{A_2} \right) \right] \frac{G^2}{2\rho_l} \quad (4.6)$$



where  $A_1$  and  $A_2$  are the two cross-sectional areas, and  $a_r$  denotes the channel aspect ratio (height to width) after the restriction in the contraction term. In the single phase tests, the  $\Delta p_{fin}$  was typically the 75 – 80% of the total measured pressure drop, while the inlet pressure drop  $\Delta p_{in}$  then represented about the 25 – 28%, and the outlet pressure recovery  $\Delta p_{out}$  was about 3 – 5% of the total measured pressure drop.

The mass flux  $G$  is evaluated from the mass flow rate  $\dot{m}$  measured by the Coriolis mass flow meter, the total number of channels between the pin fin lines  $N_{ch}$  ( $N_{ch} = 67$ ), their height  $H_{fin}$  and width  $W_{ch}$ , as showed in the equation below:

$$G = \frac{\dot{m}}{N_{ch}H_{fin}W_{ch}} \quad (4.7)$$

Once the pressure drop along the pin fin array and the mass flux have been evaluated, the single phase friction factor is obtained as follows:

$$f = \frac{\Delta p_{fin}\rho_l d_h}{2LG^2}, \quad d_h = \frac{4A_{ch}}{P} \quad (4.8)$$

where  $L$  is the length of the heated area,  $d_h$  is the hydraulic diameter of the channels,  $P = 2(H_{fin} + W_{ch})$  is the perimeter of the channel cross-section, and  $A_{ch} = H_{fin} \cdot W_{ch}$  is its area. In the literature, there are two different approaches to calculate the Reynolds number, depending on the height-to-diameter ratio  $H/D$ . For tube bundles ( $H/D > 8$ ) the length scale for calculating the Reynolds number is the fin diameter, since the pressure drop is less influenced by the endwall effects, whilst for shorter fins, as in the present study, the length scale utilized is the hydraulic diameter of the microevaporator channel. Therefore, the single phase Reynolds number is defined as:

$$Re = \frac{Gd_h}{\mu_l} \quad (4.9)$$

The single phase friction factor is necessary here to estimate the pressure drop in the two-phase data reduction procedure. In particular, it will be implemented in the separated flow model to evaluate the frictional component of the two-phase pressure drop. For this reason, a data fit of the single phase experimental results is performed. Since the friction factor trend shows a transition at a value of the Reynolds number of 300, as it will be presented in the following sections, two correlations have been developed, each depending on the Reynolds number:

$$f = 8.98Re^{-0.97}, \quad Re < 300 \quad (4.10)$$

$$f = -1.93Re^{-0.124} + 1.85Re^{-0.11}, \quad Re > 300 \quad (4.11)$$

It should be noted that Eqs. (4.10)-(4.11) do not provide general prediction correlations for the single phase friction factors, but they are only a means to improve the evaluation of the following two-phase results.

### 4.1.2 Diabatic single phase tests

In order to validate the single phase heat transfer performance versus the available correlations, liquid-phase diabatic tests were performed. As the heat transfer performance indicator, an average Nusselt number is calculated here:

$$\overline{\text{Nu}} = \frac{\overline{h_w d_h}}{k_l} \quad (4.12)$$

where  $k_l$  is the fluid thermal conductivity and  $\overline{h_w}$  is the average wall heat transfer coefficient, which is calculated by solving an inverse 3D heat conduction problem, as will be explained below.

Starting from the map of 110x110 temperatures of the micro-evaporator base obtained by means of the infrared camera, indicated as  $T_{base}$ , a polynomial surface fitting technique is utilized to filter the infrared temperature map and afterwards an inverse heat conduction problem through the heat sink volume is formulated and solved to derive the pixel-by-pixel footprint temperatures  $T_{ftp}$ , and heat fluxes  $q_{ftp}$ . The numerical solution is based on a finite-volume method to solve the steady-state 3D heat conduction problem coupled with an optimization algorithm based on the Newton-Raphson method, as implemented by Huang and Thome [111] and explained in detail in the **Appendix A**.

The 3D heat conduction equation is solved with the following boundary conditions:

- Micro-evaporator base: the total base heat flux  $q_{base}$ , calculated via the electrically applied total power  $Q_{el}$  reduced by the heat losses  $Q_{losses}$ ,  $q_{base} = (Q_{el} - Q_{losses})/A_{base}$ , where  $A_{base}$  is the heated area; the value of  $T_{base}$  is not used at this stage but it will be used in the optimization procedure.
- Micro-evaporator lateral sides: the imposed heat flux evaluated based on the Fourier law where the temperature gradient orthogonal to the micro-evaporator sides is estimated based on the 2D base temperature map; heat fluxes vary along the perimeter of the micro-evaporator base according to the IR reading, but are considered constant along the height of the micro-evaporator.
- Micro-evaporator footprint: a constant temperature boundary condition is imposed, where the temperature values are optimized according to the Newton-Raphson method.

At the first iteration, the 3D heat conduction problem is solved with a footprint temperature condition derived from the IR camera reading  $T_{ftp,0} = T_{base} - q_{base}H/k_{sil}$ , where the term  $q_{base}H/k_{sil}$  is an estimation of the temperature drop along the micro-evaporator height based on 1-D heat conduction. The thermal conductivity of silicon  $k_{sil}$  is evaluated as a parabolic function of temperature [112], as reported below:

$$k_{sil} = 7 \cdot 10^{-4} T^2 - 0.5416 T + 157.39 \quad (4.13)$$

For the successive iterations, the footprint temperature is updated according to the optimization algorithm, with the objective of decreasing the maximum deviation between the base temperature extrapolated with the IR camera and that obtained by the finite-volume method  $T_{base,FV}$ :

$$dev = \max |T_{base} - T_{base,FV}| \quad (4.14)$$

to bring this deviation below a threshold value of 0.05 K for each pixel. The heat losses, which are utilized in the boundary condition of the 3D heat conduction model to reduce the base heat flux, are calculated via the following energy balance:

$$Q_{losses} = Q_{el} - \dot{m}c_p (T_{in} - T_{out}) \quad (4.15)$$

where  $Q_{el}$  is the total electrical power input measured from the voltage and current imposed in the aluminium film heaters,  $Q_{el} = VI$ , while  $T_{in}$  and  $T_{out}$  are the fluid temperatures measured with the installed thermocouples at the inlet and outlet manifold, respectively. For the single phase tests the heat losses were estimated to be about the 15–18% of the total applied electrical power  $Q_{el}$ .

The local footprint heat flux  $q_{ftp}$ , and temperature fields  $T_{ftp}$ , obtained as the solution of the inverse heat transfer problem explained above, are then used to estimate the local footprint heat transfer coefficient  $h_{ftp}$ :

$$h_{ftp}(y, z) = \frac{q_{ftp}(y, z)}{T_{ftp}(y, z) - T_{fl}(y, z)} \quad (4.16)$$

Here, the local single phase fluid temperature  $T_{fl}$  is evaluated by means of an energy balance applied between the inlet of the heated area and a generic  $y, z$  location:

$$T_{fl}(y, z) = T_{in} + \frac{B}{\dot{m}} \int_0^z \frac{q_{ftp}(y, z)}{c_p(y, z)} dz \quad (4.17)$$

where  $T_{in}$  is the temperature measured at the manifold inlet, and  $B$  is the test section width. Finally, starting from the values of the footprint heat transfer coefficient of Eq. (4.16), the local wall heat transfer coefficient is derived applying the fin efficiency according to the following equations:

$$h_w(y, z) = \frac{h_{ftp}(y, z)A_{ftp}}{(A_b + \eta_{fin}(y, z)A_{lat})} \quad (4.18)$$

$$\eta_{fin}(y, z) = \frac{\tanh(mH_{fin})}{(mH_{fin})} \quad (4.19)$$

$$m(y, z) = 2\sqrt{\frac{h_w(y, z)}{k_{sil}D_{fin}}} \quad (4.20)$$

where  $N_{fin}$  is the total number of micro-pin fins,  $A_{ftp}$  is the footprint area (1 x 1 cm<sup>2</sup>),  $A_b$  and  $A_{lat}$  are the base and the lateral fin area, calculated as follows:

$$A_b = A_{ftp} - \frac{\pi D_{fin}^2}{4} N_{fin} \quad (4.21)$$

$$A_{lat} = \pi D_{fin} H_{fin} N_{fin} \quad (4.22)$$

The above Eqs. (4.18)–(4.20) are solved iteratively to yield the local wall heat transfer coefficients, giving a 2D map characterized by 110 × 110 values. The calculated heat transfer coefficient field is then averaged along the widthwise and streamwise directions in order to extract average parameters, such as the single phase Nusselt number in Eq. (4.12).

## 4.2 Two-phase data reduction

The main goal of the two-phase data reduction is to evaluate the local two-phase heat transfer coefficient  $h_w(y, z)$ . This is evaluated solving the Newton equation of convection illustrated in the previous section for single phase tests, Eq. (4.16). The two-phase calculation procedure differs from the single phase data reduction in the evaluation of the local fluid temperature mainly.

### 4.2.1 Heat losses calculation

The energy balance applied in the single phase data reduction to evaluate the heat losses, see Eq. (4.15), is no more applicable in the two-phase tests. Therefore, a correlation to estimate the heat losses during flow boiling tests is extracted from the single phase experimental results. An example of the calculated values of the heat losses during single phase experiments is shown in Fig. 4.2 for the fluid R236fa, where the dependency on the applied electrical heat flux, and of temperature difference between the average base temperature and the ambient is clearly visible. The equation adopted to estimate the two-phase heat losses is thus obtained by using a nonlinear least-squares fit with a maximum error of 5%, as follows:

$$q_{losses} = a(T_{base} - T_{amb}) + b \cdot 10^{-5} Q_{el} + c \quad (4.23)$$

It is worth noting that Eq. (4.23) gives the losses in term of heat flux, as  $q_{losses} = Q_{losses}/A_{base}$ . The parameter  $a$ ,  $b$  and  $c$  are listed in Table 4.1 for each tested refrigerant. The value of the

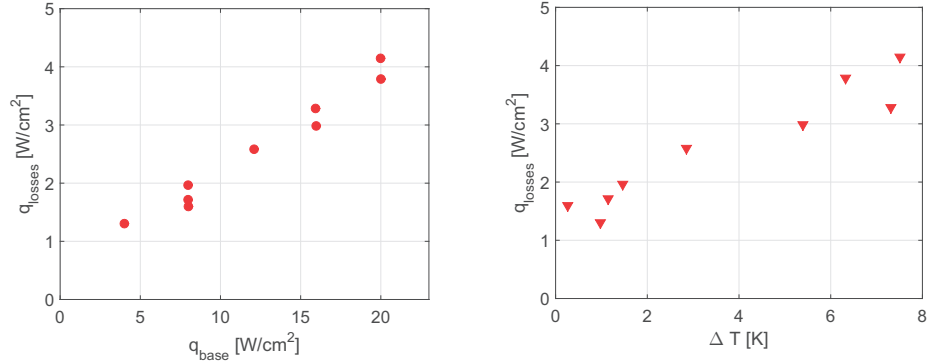


Figure 4.2 – Single phase R236fa data utilized to develop the correlation for the present two-phase data reduction. Heat losses as a function of (a) the applied heat flux, and (b) of the temperature difference between the evaporator base and the surrounding.

Table 4.1 – Heat losses correlation coefficients for each refrigerant.

Refrigerant	a	b	c
R236fa	0.09	1.65	0.66
R245fa	0.09	1.39	-0.09
R1234zE	0.168	1.73	-0.21
R134a	0.138	1.65	0.66

heat losses during flow boiling tests was about the 8 – 10% of the total applied electrical power input. Note that the heat losses associated with two-phase flow are lower than those measured for single phase at the same heat flux conditions because, due to the better heat removal capability of the two-phase flow, the evaporator base temperature used in Eq. (4.23) is lower.

#### 4.2.2 Onset of two-phase flow and fluid temperature evaluation

As already pointed out, the refrigerant enters in the micro-pin fin array in a subcooled condition and its temperature starts to increase until nucleation occurs and bubbles nucleate and coalesce forming a two-phase flow regime. In the two-phase region, the fluid temperature decreases due to the two-phase pressure drop.

In order to evaluate the local fluid temperature  $T_{fl}$  along the entire micro-evaporator length, which is utilized to calculate the local heat transfer coefficient, the pin fin area is divided into a single and a two-phase flow region, and the location of the onset of two-phase flow ( $z_{onset}$ ) and the local vapor quality ( $x$ ) are needed parameters. At the beginning of this study, the vapor quality  $x$  was calculated from the inlet of the test section, where the fluid is still in a liquid

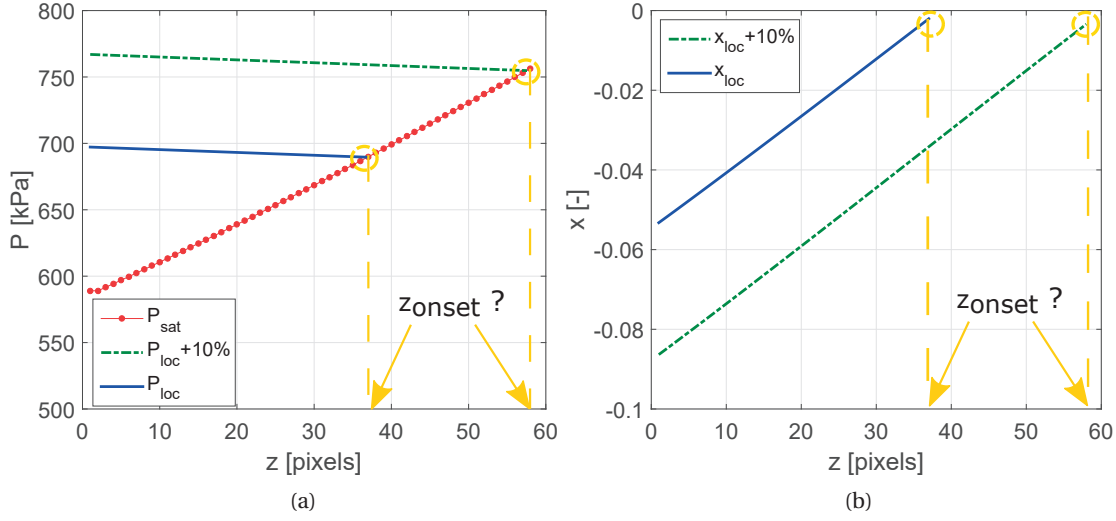


Figure 4.3 – (a) Local and saturation pressure profiles in the single phase region. (b) Local vapor quality calculated in the single phase region.

state, from its thermodynamic definition, as:

$$x(y, z) = \frac{i(y, z) - i_L[p_{loc}(y, z)]}{i_{LV}[p_{loc}(y, z)]} \quad (4.24)$$

where the local enthalpy was derived by means of an energy balance. At the location where  $x$  reached the value of  $x \sim 0$ , (since in subcooled flow it assumes negative values), and the local pressure, which is calculated as expressed below by Eq. (4.25), was equal to the saturation pressure ( $p_{loc} = p_{sat}$ ), bubble nucleation was supposed to occur and the corresponding location was then used as the onset of two-phase flow,  $z_{onset}$ .

However, this method predicted values of  $z_{onset}$  which did not correspond to the locations observed from the high-speed camera videos. In the majority of cases, the predicted  $z_{onset}$  was occurring before than what observed in reality from flow visualization. This could be explained by the fact that the local pressure at the inlet of the pin fin area, ( $p_{in,fin}$  at  $z = 0$ ), cannot be directly measured, but it is obtained by reducing the pressure measured at the inlet slit by the pressure drops due to the contractions before the pin fin area (see Eq. 4.1). The uncertainty on the inlet pressure value is then propagated to the local enthalpy from eq. 4.24, and thus to the vapor quality calculation. Figures 4.3(a)-(b) show an example of the variability of the location of  $z_{onset}$  and of the vapor quality  $x$ , when considering two values of the local pressure at the inlet. The two values of  $p_{in,fin}$  differ by 10%. As it is possible to see from Figs. 4.3(a)-(b), the vapor quality calculation strongly depends on the value of the pressure at the inlet.

In order to avoid these errors, in the present study the location of the onset of two-phase

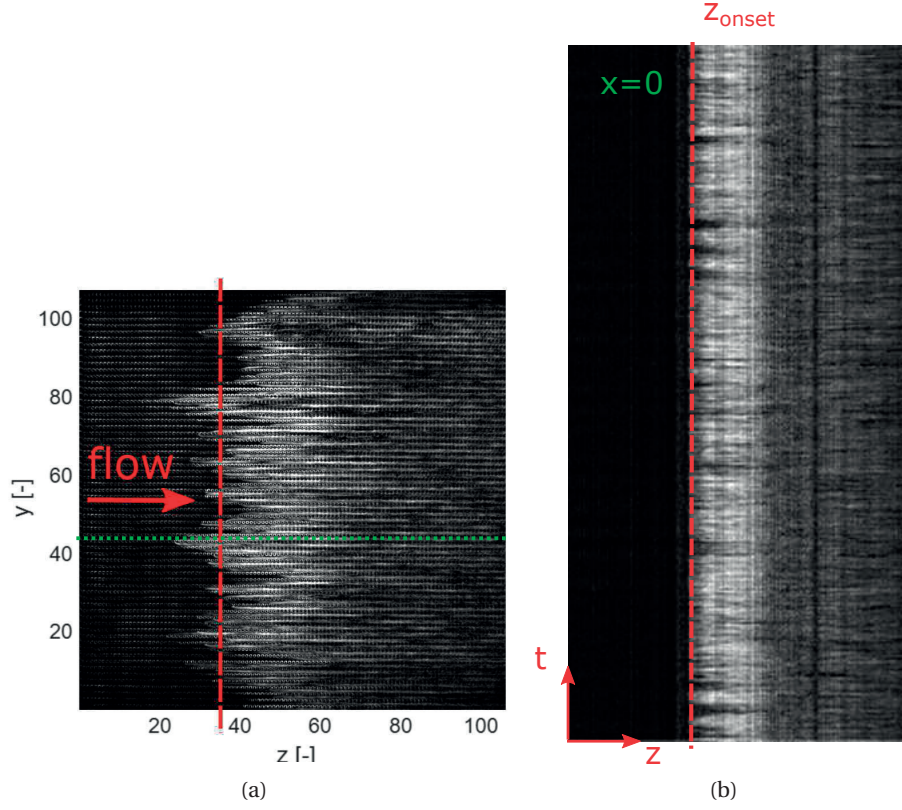


Figure 4.4 – (a) Screenshot from the high-speed camera, and (b) corresponding time-strip analysis of the centerline channel. The vertical lines indicate the onset of two-phase flow. Test conditions of  $G = 1000 \text{ kg m}^{-2} \text{ s}^{-1}$ ,  $q = 28 \text{ W cm}^{-2}$ , fluid R1234ze(E) and  $T_{sat} = 35^\circ\text{C}$ . Flow is from the left to the right.

flow is evaluated by utilizing the high-speed videos and the time-strip technique [113], obtained during each experimental test point. The time-strip technique is described in detail in **Appendix C**.

An example of a screenshot extracted from a high-speed camera video is depicted in Fig. (4.4)(a). The flow is moving from left to right, along the  $z$ -direction. For a given channel (between two pin fin lines) it is possible to extract the one-dimensional light intensity distribution along its centerline for each frame in the video sequence. Thus, a 2D space-time map (referred to as the "time-strip" technique) is obtained for each channel of the flow area. Fig. (4.4)(b) shows an example of the time-strip map referred to the channel indicated by the green horizontal line in Fig. (4.4)(a). In the figures it is possible to distinguish three different main light intensities as the different phases have different attenuation rates, and it is clearly detectable the location where two-phase flow starts (indicated by a vertical red line). In particular in Fig. (4.4)(b), the darker zone at the inlet indicates single phase liquid flow, whilst the following brighter area is associated with bubbly or/and slug flow as already explained out by a previous study based on flow visualization related techniques [113]. The time-strip analysis was performed for 8 – 10



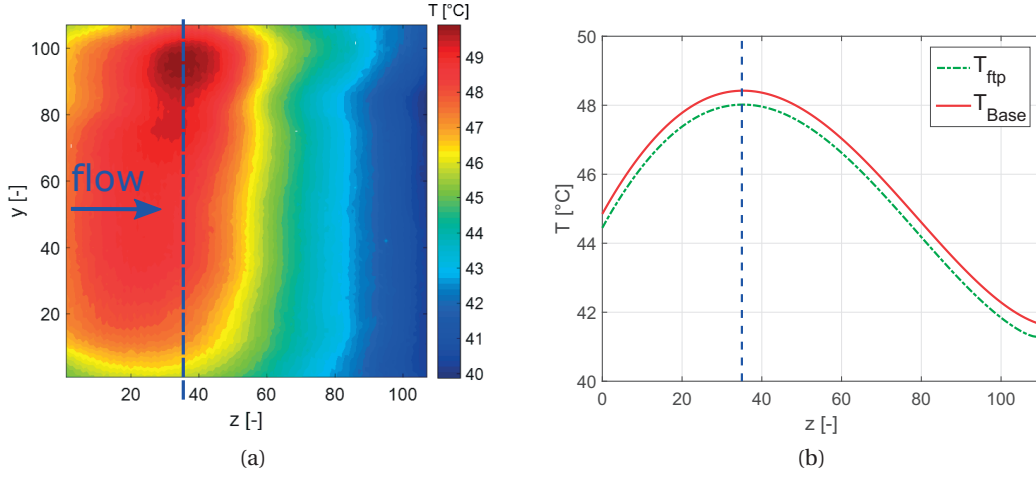


Figure 4.5 – (a) Micro-evaporator base temperature measured with the IR camera, and (b) base and footprint temperature profiles along the streamwise direction  $z$ . The vertical lines indicate the onset of two-phase flow. Test conditions of  $G = 1000 \text{ kg m}^{-2} \text{ s}^{-1}$ ,  $q = 28 \text{ W cm}^{-2}$ , fluid R1234ze(E) and  $T_{sat} = 35^\circ\text{C}$ . Flow is from the left to the right.

channels of each test and an average value of  $z_{onset}$  among the obtained 8 – 10 locations was considered. At the transition point, i.e.  $z = z_{onset}$ , the vapor quality is assumed to be  $x = 0$ .

To further confirm the results obtained from the time-strip analysis, the IR camera measurements were also considered to obtain the values of  $z_{onset}$  and check if they were corresponding to the ones obtained from the high-speed camera.

An example of 2D IR temperature map of  $110 \times 110$  values is depicted in Fig. (4.5)(a), for the same selected test case of Fig. (4.4)(a). The  $110 \times 110$  values of base temperature illustrated in the 2D map of Fig. (4.5)(a), are then averaged along the  $y$  direction in order to obtain the base temperature profile along the streamwise direction ( $z$ ),  $T_{Base}$ . The same procedure is repeated with the 2D map of footprint temperature values, obtained by solving the 3D heat conduction scheme explained above, to compute the footprint temperature profile along the  $z$  direction,  $T_{ftp}$ . The base and footprint temperature trends along the streamwise direction are plotted in Fig. (4.5)(b).

As depicted in Figs. (4.5)(a)-(b), the base and footprint temperatures increase along the streamwise direction until the transition to two-phase flow occurs, as indicated by a vertical line on the plots at about  $z \sim 36$  pixel. The locations obtained from the IR camera have been always very similar to the ones obtained from the high-speed screenshot and time-strip analysis of Fig. (4.4)(a)-(b). Therefore, the extent of single phase region begins from the inlet of the micro-pin fin area until the nucleation point,  $z_{onset}$ , where  $x = 0$ . Afterwards, two-phase flow develops along the micro-evaporator and the vapor quality is evaluated locally by using Eq.4.24.



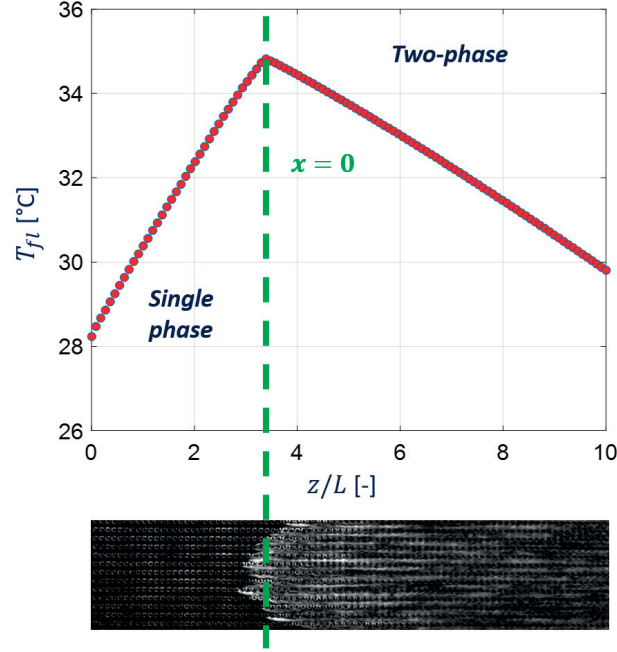


Figure 4.6 – Fluid temperature profile along the microevaporator length. The temperature increases in the single phase region and after the onset of two-phase flow starts to decrease due to the two-phase pressure drop.

Addressing now the fluid temperature calculation, in the single phase zone the fluid is sub-cooled, and the local fluid temperature is estimated by applying the energy balance starting from the temperature measured at the inlet, as indicated in Eq. (4.17). In this region, the fluid temperature increases with a non linear profile due to the non-uniform heat flux at the footprint, obtained from the 3D inverse heat conduction scheme (see Fig. 4.6). When the onset of two-phase flow occurs, the local fluid temperature starts to decrease due to the two-phase pressure drop. Indeed, in the two-phase region the fluid temperature is evaluated as the saturation temperature corresponding to the corrected local pressure  $p_{loc}$ , as:  $T_{sat}(y, z) = T_{sat}[p_{loc}(y, z)]$ . As already outlined above, rather than considering a linear pressure profile in the two-phase zone, as done in most of the experimental studies conducted so far (which is appropriate only when the pressure drops are small), here the local pressure is reconstructed by using an empirical pressure drop model with a correction to match the experimental pressure drop measured at the outlet manifold [114], as it will be explained in the following section.

#### 4.2.3 Pressure drops

The total pressure drop  $\Delta p_{tot}$ , which is a meaningful indicator of the required pumping power of the system, is readable from the differential pressure transducer directly. From the total pressure drop, the pressure drop along the pin fin array,  $\Delta p_{fin}$ , can be evaluated by subtracting

## Chapter 4. Single and two-phase data reduction

the inlet and outlet pressure drops, as indicated in the single phase data reduction by Eq. (4.1). Since the fluid at the inlet is still subcooled, Eq. (4.2) is adopted to calculate the inlet pressure drop  $\Delta p_{in}$ , as done in the single phase tests. On the contrary, the calculation of the outlet pressure drop  $\Delta p_{out}$  differs from the single phase data reduction, as it will be explained later.

As done in the previous section, in order to calculate  $\Delta p_{fin}$  locally, the pin fin area is divided into a single and two-phase regions. In the initial subcooled region, the fluid temperature increases almost linearly with the streamwise location  $z$ , and the local pressure  $p_{loc}$  is computed from the value at the inlet of the pin fin region,  $p_{in,fin} = p_{in} - \Delta p_{in}$ , (where  $p_{in}$  is the pressure measured at the inlet manifold), reduced by the frictional single phase pressure drop:

$$p_{loc}(y, z) = p_{in,fin} - \int_0^z \frac{2fG^2}{d_h \rho_l(y, z)} dz \quad (4.25)$$

where  $f$  in Eq. (4.25) is the single phase friction factor evaluated in the preliminary adiabatic single phase tests described earlier.

After the transition to two-phase flow, at  $z = z_{onset}$ , the pressure profile in the two-phase region is estimated by subtracting the momentum and frictional pressure drops according to the separated flow model, which assumes the two phases (liquid and gas) to be in thermodynamic equilibrium and to move with a different constant velocity:

$$p_{loc}(y, z) = p_{loc}(y, z_{onset}) - \int_{z_{onset}}^z dp_{fr,fin}(y, z) - \int_{z_{onset}}^z dp_{a,fin}(y, z) \quad (4.26)$$

The frictional pressure drops are evaluated for every infinitesimal element  $b$  in the domain, as:

$$dp_{fr,fin}(y, z) = 2f(y, z) [G^2(1 - x(y, z))^2] \Phi_l^2 \frac{b}{\rho_l(y, z) d_h} \quad (4.27)$$

The local vapor quality  $x$  is determined along the two-phase region with the specific enthalpy  $i$ , as expressed by Eq. 4.24.

The friction factor  $f$  is obtained from the correlation of Eqs. (4.10)-(4.11), implementing the Reynolds number referred to the liquid phase, defined as:

$$Re_l(y, z) = \frac{G(1 - x(y, z)) d_h}{\mu_l(y, z)} \quad (4.28)$$

The parameter  $\Phi_l^2$  in Eq. (4.27) denotes the liquid two-phase multiplier, introduced by Lockhart and Martinelli to calculate the frictional pressure gradient of liquid-gas two-phase flow in horizontal pipes [76]. In their study, the two-phase frictional gradient was calculated as the product of the frictional pressure gradient of the liquid phase flowing in the pipe based on the

actual liquid flow rate and the two-phase friction multiplier, as below:

$$-\left(\frac{dp}{dz}\right)_{fr} = -\left(\frac{dp}{dz}\right)_{fr,l} \Phi_l^2 \quad (4.29)$$

Chisholm [115] observed that the parameter  $\Phi_l^2$  could be expressed as a function of the Martinelli parameter  $X^2$  as:

$$\Phi_l^2 = 1 + \frac{C}{X} + \frac{1}{X^2} \quad (4.30)$$

$$X^2 = \frac{(dP/dz)_l}{(dP/dz)_v} \quad (4.31)$$

where  $C$  is an empirical constant whose value depends on the flow regimes of the two phases. For laminar liquid and laminar gas it is  $C = 5$ .

The acceleration pressure drops, which reflect the change in the momentum flux in space, are calculated as:

$$dp_{a,fin}(y, z) = G^2 \left[ \frac{x(y, z)^2}{\rho_g \epsilon(y, z)} + \frac{(1 - x(y, z))^2}{\rho_l (1 - \epsilon)} \right]_i - G^2 \left[ \frac{x(y, z)^2}{\rho_g \epsilon(y, z)} + \frac{(1 - x(y, z))^2}{\rho_l (1 - \epsilon(y, z))} \right]_{i-1} \quad (4.32)$$

where the subscripts " $i$ " and " $i - 1$ " refer to two consequent infinite elements in the domain. The void fraction  $\epsilon$ , which represents the ratio between the cross-sectional area occupied by the gas phase over the entire cross-sectional area, is here determined by implementing the kinetic energy model for annular flow proposed by Zivi [116]:

$$\epsilon = \frac{1}{1 + \frac{1-x(y,z)}{x(y,z)} \left( \frac{\rho_g(y,z)}{\rho_l(y,z)} \right)^{2/3}} \quad (4.33)$$

The pressure drop calculated for the two-phase region is then re-scaled in order for the  $\Delta p_{fin}$  (summing the single phase and two-phase zones contributions) to match the value at the outlet, reduced from the experimental data. Indeed, after the pin fin array, at the outlet section the fluid is in two-phase state, and hence Eq. (4.3) and the Garimella and Lee correlations [29] used for the expansion contributions in single phase cannot be utilized in the two-phase case to estimate the  $\Delta p_{out}$ , which is the pressure drop between the pin fin area end ( $p_{end}$  at  $z = 110$ ), and the measured value at the outlet manifold ( $p_{out}$ ),  $\Delta p_{out} = p_{end} - p_{out}$ .

The procedure chosen to estimate the outlet pressure drop,  $\Delta p_{out}$ , is based on a preliminary two-phase half-heating test, as already described by Costa-Patry et al. [117] and Szczukiewicz et al. [114]. This was performed by switching on only the first aluminium heater, which covers half of the test section nearby the inlet, thus forming an adiabatic two-phase flow toward the end of the chip. Since two-phase flow started in the first half of the micro-pin fin area close to the inlet, it is possible to assume that the fluid at the end of the flow area is at saturation conditions and at the same temperature of the micro-evaporator bottom surface, which can be evaluated from the 3D inverse heat conduction starting from the IR

measurements. Thus, the pressure at the end of the pin fin array,  $p_{end}$ , was taken equal to the saturation pressure corresponding to the local temperature of the wall, i.e. the local adiabatic saturation temperature. Once  $p_{end}$  is obtained, the outlet pressure drop could be evaluated as the difference between this local value and the measured outlet pressure,  $\Delta p_{out} = p_{end} - p_{out}$ .

In order to extend the half-heating results to the full heating case, and utilize them to correct the pressure profile along the micro-pin fin area, the obtained values of  $\Delta p_{out}$  were correlated to the outlet vapor quality  $x_{out}$  and the mass flux  $G$  as follows:

$$\Delta p_{out} = 9.828\psi^{0.2675} - 10.9 \quad (4.34)$$

$$\psi = x_{out} \left( \frac{G}{G_{min}} \right)^4 \quad (4.35)$$

where  $G_{min}$  is the minimum value among the tested mass fluxes. The pressure profile along the pin fin matrix is finally recalculated according to this correction. Please note that this method is meant only for use to reduce the present test data, not as a general method for other use.

### 4.3 Conclusions

The above presentation described the methods that will be used during the discussion in later chapters to reduce all of the experimental pressure drops and local heat transfer coefficients (footprint and wall values). The 3D inverse heat conduction method allows the local heat flux to go into the local calculation of the heat transfer coefficient (110x110 values) while likewise the local saturation pressure gives the local saturation temperature.

Table B.2 in **Appendix B** outlines the uncertainties of the parameters obtained from the described data reduction.

## 5 Operational maps, pressure drop, and heat transfer of R236fa

### 5.1 Introduction

This chapter describes the first preliminary experimental session of the present study, which focuses on the evaluation/demarcation of operationally stable and unstable flow regimes, pressure drops and heat transfer performance of two micro-pin fin evaporators (one with and one without inlet restrictions) for tests with fluid R236fa.

Channel entrances with and without inlet restrictions were tested in order to evaluate their relative effect on the stability of the flow. The inlet restriction consisted of an extra row of micro-pin fins with a larger diameter ( $100\ \mu\text{m}$  compared to the  $50\ \mu\text{m}$  diameter pin fin array) placed at the inlet of the heated area.

The scope of this first experimental investigation is mainly to define which geometry of micro-evaporator has to be adopted in all the successive studies and which set of test conditions guarantee stable flow. This is why it is presented in this manuscript in a separated chapter.

The results of this chapter were published in:

C. Falsetti, H. Jafarpoorchebab, M. Magnini, N. Borhani and J.R. Thome, *Two-phase operational maps, pressure drop, and heat transfer for flow boiling of R236fa in a micro-pin fin evaporator*, Int. J. of Heat and Mass Transfer, 107, 805 – 819, 2017.

### 5.2 Single phase validation results

Adiabatic and single phase liquid tests were done as preliminary tests, not only to validate the reliability of the test facility, but also to evaluate the single phase friction factor and to characterize the heat losses, which will be both used in the successive two-phase section.

The single phase friction factor was evaluated from the single phase liquid tests by utilizing the calculated pressure drop along the pin fin array  $\Delta P_{fin}$ , see Eqs. (4.8). The latter value is

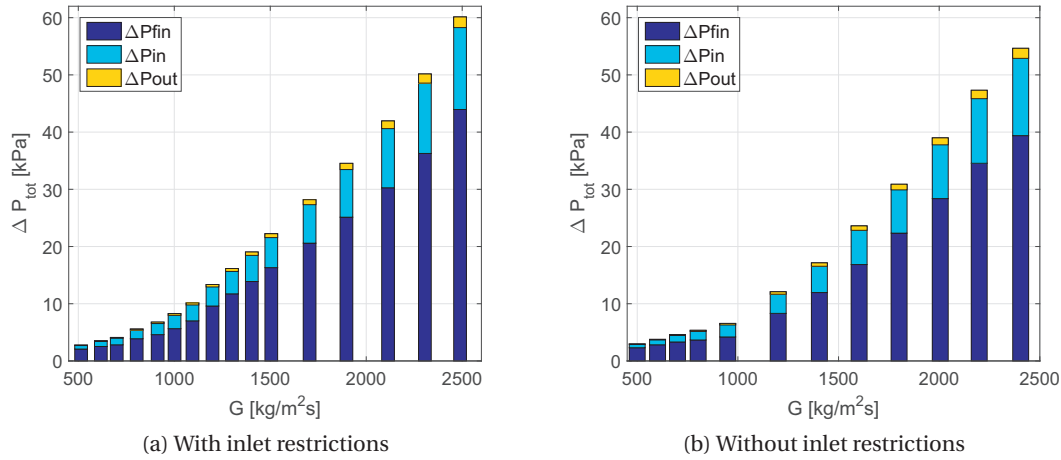


Figure 5.1 – Total single phase pressure drop as function of the mass flux for: (a) micro-evaporator with inlet restrictions, and (b) micro-evaporator without inlet restrictions. Fluid R236fa.

obtained from the total pressure drop across the micro-evaporator  $\Delta P_{tot}$  reduced by the inlet and outlet pressure drop contributions, which are depicted in Fig. 5.1 when varying mass flux. In the present adiabatic tests, the  $\Delta P_{fin}$  accounts for the 69 – 70% of the total losses, while the inlet and the outlet pressure drops account for 26–27% and 3%, respectively. The inlet pressure drops  $\Delta P_{in}$  for the micro-evaporator with inlet restrictions are slightly higher (of  $\sim 1\%$ ) than those calculated without restrictions, as the restrictions add a sudden contraction. On the contrary, the pressure drop along the pin fin array  $\Delta P_{fin}$  are similar for the two tested geometries, as illustrated in Fig. 5.2. In the  $\Delta P_{fin}$  trend versus mass flux it is possible to identify a transition at a mass flux value of about  $G = 1000 \text{ kg m}^{-2} \text{ s}^{-1}$ , which corresponds to the single phase Reynolds number  $Re=300$ . The increase of the pressure drop with mass flux is more pronounced above this threshold value.

The same transition is observed in the single phase friction factor, which is plotted in Fig. 5.3 for both the micro-evaporators as a function of the single phase Reynolds number, calculated based on the hydraulic diameter. As observed already in the pressure drop profile, there is no appreciable difference between the case with inlet restrictions and the one without. For  $Re < 300$ , the friction factor decreases with increasing the Reynolds number following a  $Re^{-1}$  law, in agreement with laminar flow theory [118]. For larger Reynolds numbers, it stabilized around a constant value of about 0.05. Indeed, when the Reynolds number increases, the boundary layer separates from the pin fin walls, and the vortices generated in the wake behind each micro-pin fin start to shed, leading to a higher pressure drop.

A transition in the friction factor trend at much lower Reynolds number values than those predicted by the laminar flow theory was already observed by Prasher et al. [44] for a staggered pin fin configuration with water flow, thus emphasizing that the pin fin are playing an

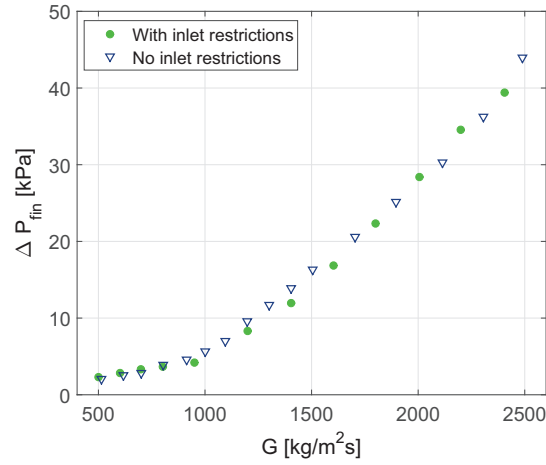


Figure 5.2 – Pressure drop along the micro-pin fins array as function of the mass flux for test sections with and without inlet restrictions.

important role on the friction factor. A similar change in the pressure drop profile was also reported by Renfer et al. [2] for  $Re=350$  and a staggered pin fin configuration. They motivated this trend with the onset of vortex shedding behind the pin fin. In particular, they noticed that at low Reynolds numbers the fluid between the obstacles recirculated without mixing with the channel-like flow, while at higher Reynolds numbers time-dependent patterns triggered mixing between the recirculating wake and the channel-like flow, thus yielding a rise of the pressure drop. The theory of flow past a cylinder indicates a transition to vortex shedding in the wake behind the obstacle at a value of  $Re$  number, defined with the cylinder diameter, of 250. This value is on the same order as the threshold value seen in the present experiments ( $Re=150$  when calculated using the pin fin diameter as the reference length), thus further confirming that vortex shedding may be the actual reason of the transition evident in Figs. 5.3 and 5.2. Actually, the transition occurs at lower  $Re$  values than those reported for flow past a cylinder, which is consistent with the more disturbed flow configuration, characterized by low aspect ratio obstacle arrays (as opposed to a single, infinitely extended cylinder) which interact with each other.

In order to validate the single phase heat transfer performance versus the available correlations, diabatic tests were performed. As the heat transfer performance indicator, the average single phase Nusselt number is calculated here based on the average heat transfer coefficient. This is plotted as a function of the Reynolds number in Fig. 5.4.

The heat transfer performance augments with rising Reynolds number, which is expected as a consequence of the enhanced fluid mixing promoted by the vortex shedding phenomenon. The transition in Nusselt number with respect to Reynolds number is not observed here as very low values of Reynolds number, i.e. mass fluxes, could not be tested during single phase diabatic tests in order to avoid bubble nucleation. In Fig. 5.4 it is possible to observe that the heat transfer is enhanced for the test section with inlet restrictions, showing higher values of Nusselt

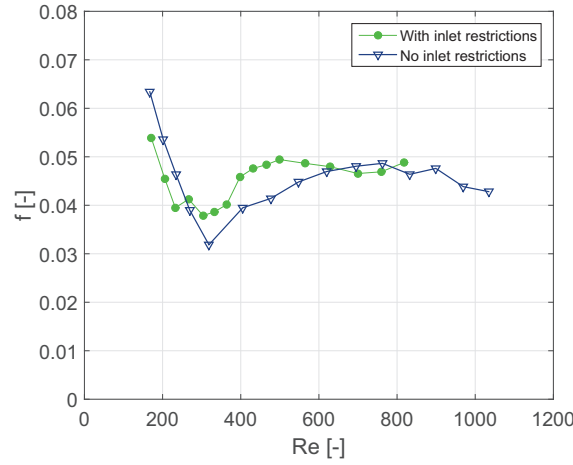


Figure 5.3 – Single phase friction factor as a function of the Reynolds number for the test sections with and without inlet restrictions.

number compared to those obtained without inlet restrictions. This could be explained by the higher velocity of the fluid induced by the restrictions at the channel entrances, which causes an increment in the convective heat transfer rate. The experimental results are also compared to two existing correlations. The data for the geometry with inlet restrictions agree very well with the Zukauskas correlation [49], which was developed for tube bundles ( $H_{fin}/D_{fin} > 8$ ), while the Kosar and Peles correlation [46], obtained by modifying the Zukauskas expression to predict their experimental data at low Reynolds number, systematically overestimates the present data.

### 5.3 Two phase results

The two-phase flow boiling results are outlined and discussed in this section. In Section 5.3.1, the test section operational maps developed thanks to the coupling of high-speed flow visualization and IR temperature measurements are presented. The pressure drop and heat transfer performance of the micro-evaporators (with and without inlet restrictions) are shown in Sections 5.3.2 and 5.3.3, respectively, together with a comparison to prior multi-microchannel evaporator results.

In the experimental two-phase flow tests, the heat fluxes ranged from  $20 \text{ W cm}^{-2}$  to  $48 \text{ W cm}^{-2}$ , while the mass fluxes varied from  $500 \text{ kg m}^{-2} \text{ s}^{-1}$  up to  $2500 \text{ kg m}^{-2} \text{ s}^{-1}$ , which corresponds to a liquid Reynolds number range, calculated based on the equivalent channel diameter, between 171 and 1035. For all the experimental studies, the outlet saturation temperature was set equal to  $30.5 \pm 0.5^\circ \text{ C}$  and the inlet liquid subcooling was set to  $5.0 \pm 1.5 \text{ K}$ . The outlet saturation temperature was kept constant by adjusting the temperature of the RK 20 KP LAUDA compact low-temperature thermostat, while the inlet subcooling value was set by means of the pre-heater/subcooler.



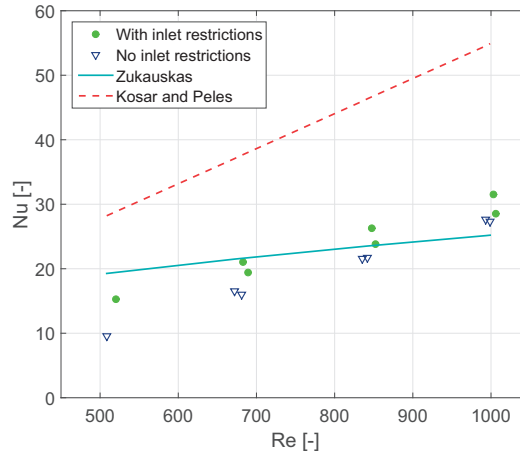


Figure 5.4 – Average Nusselt number for both the geometries and comparison with Zukauskas correlation for tube bundles [49] and Kosar and Peles for micro-pin fins [46].

### 5.3.1 Operational maps

In order to better understand the mutual effect of fluid dynamics and heat transfer in the micro-pin fins evaporator under flow boiling conditions, the videos obtained by the high-speed camera were analyzed in conjunction with the 2D thermal map given by the IR camera. The high-speed camera, which for this first experimental study was a Photron Fastcam-Ultima APX high-speed camera (this model is older than the one utilized in all the subsequent studies), has a spatial resolution of  $1024 \times 1024$  pixels and recorded at 2000 fps, while the IR camera has a resolution of  $320 \times 240$  pixels out of which an array of  $110 \times 110$  pixels covers the heated area, and measure at a frequency of 60 fps. The flow videos and IR measurements are recorded for 30 s. The high-speed video and time-dependent local values of the temperature are then processed to identify the operational regime characterizing the flow conditions set, as it is explained below for a specific case.

Figure 5.5 shows an example of the simultaneous analysis of thermal field and flow visualization for a selected set of operating conditions in the presence of inlet restrictions. In the figure, the heated section is highlighted by a square, and flow is from left to right. From the infrared temperature contours it can be seen that the evaporator temperature decreases as the end of the channel is approached. Analysis of the high-speed video reveals that flow is still single phase nearby the channel inlet (darker region in Fig. 5.5(b)) where the temperature is higher, while the development of the two-phase flow in the following zone (brighter region in Fig. 5.5(b)) yields a reduction of the micro-evaporator temperature.

A more quantitative investigation is performed by tracking the temperature behaviour versus time extracted from the IR reading for five selected pixels distributed nearby the inlet, the center, and the outlet of the heated area (see pixels location in Fig. 5.5). Figure 5.6(a) displays the time-temperature plot extracted from the IR camera reading during the 30 s acquisition

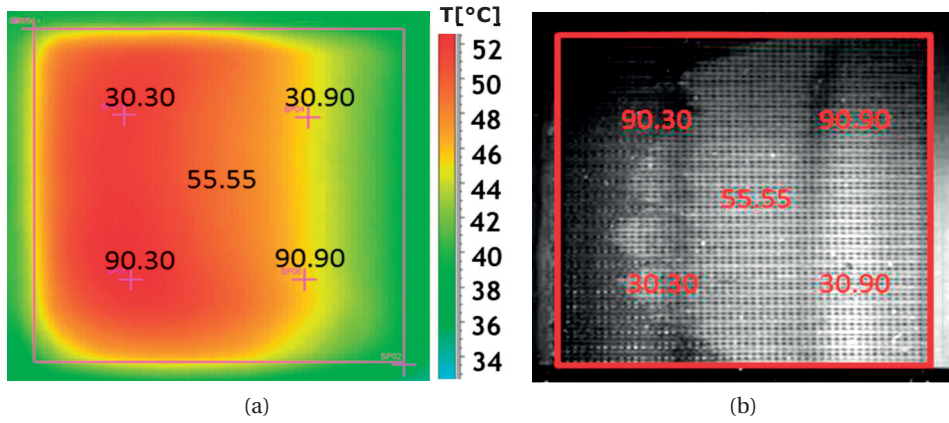


Figure 5.5 – (a) Thermal map from the IR camera and (b) screenshot from the high-speed camera taken simultaneously for test conditions of  $q = 44 \text{ W cm}^{-2}$  and  $G = 2000 \text{ kg m}^{-2} \text{ s}^{-1}$ , test section with inlet restrictions. The square drawn in the figures identifies the heated area. Flow is from left to right.

period for the case reported in Fig. 5.5, while Fig. 5.6(b) shows the same plot for a case characterized by lower mass flux and heat flux. Figure 5.6(a) confirms that the lowest values of temperature are detected towards the end of the heated area, where the flow visualization image presented in Fig. 5.5(b) revealed that the two-phase flow is present, thus emphasizing the beneficial effect the two-phase flow in cooling down the micro-evaporator. Temperature oscillations in time are small; a statistical analysis was performed and it yielded a standard deviation varying from  $0.039^\circ\text{C}$  to  $0.051^\circ\text{C}$  for the measurements taken at the five pixels. The high-speed video showed a temporally stable transition from single phase to two-phase flow, as such the operational regime corresponding to this set of operating conditions is marked as stable single phase flow followed by two-phase flow. Also in the case reported in Fig. 5.6(b) the lowest values of temperature are achieved toward the end of the heated area, although the temperature oscillations are visibly much larger, especially nearby the inlet. The high-speed video reveals strong unstable time-dependent patterns of the liquid-vapor interface in particular at the heated section inlet, thus motivating the plot in Fig. 5.6(b) where the average amplitude of the temperature oscillations is  $0.12^\circ\text{C}$  for the pixels located nearby the exit, but it rises up to  $0.48^\circ\text{C}$  nearby the entrance. These flow conditions are identified as unstable two-phase flow, although these temperature fluctuations are not that severe for cooling of electronics.

By adopting the same procedure explained above, the operational regimes for each of the experimental conditions tested were classified into different categories to generate the operational maps presented in Fig. 5.7. Every point in the operational map represents a test condition, identified by its mass flux  $G$  and heat flux  $q$ . Five different operating flow types were distinguished:

1. Single phase flow (●);

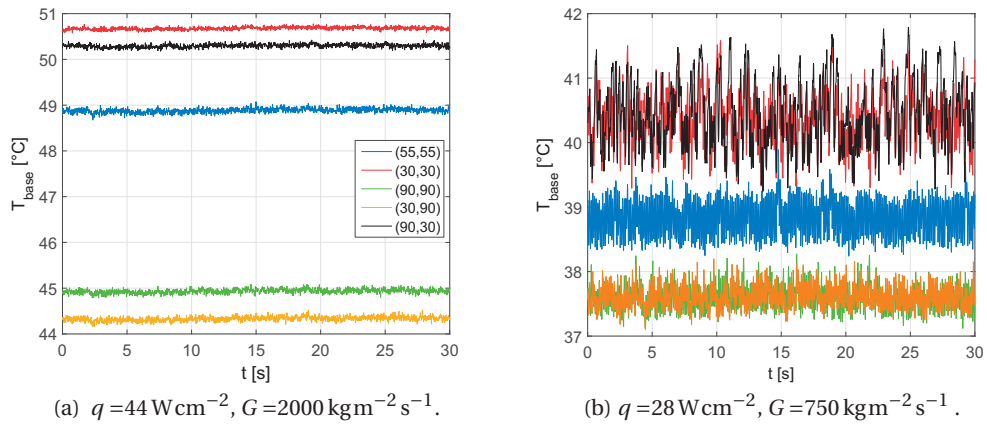


Figure 5.6 – Temperature versus time measured by the IR camera for 5 selected pixels (see Fig. 5.5(a)) within the heated area, for two different test conditions both characterized by the presence of inlet restrictions.

2. Jet-flow (●);
3. Stable single phase flow followed by two-phase flow (●);
4. Unstable two-phase flow with back flow (●);
5. Fully stable two-phase flow initiated from the beginning of the test section from flashed vapor bubbles (●);

It is worth noting that the blue and orange dots in the operational map both refer to favorable conditions, but they differ from the location where two-phase flow starts. This distinction was made during the experimental session but in the following chapters the two operating flow types will be unified. The results show that adding the inlet restrictions dropped the level of mass flux required to attain stable flow from about  $G = 1500 \text{ kg m}^{-2} \text{ s}^{-1}$  to about  $G = 1000 \text{ kg m}^{-2} \text{ s}^{-1}$ . It is possible that a larger diameter inlet flow restriction would be able to lower this threshold even further. In Fig. 5.8 snapshots of the high-speed videos related of each of the two-phase flow operational regimes are illustrated in order to further clarify the distinction among the regimes identified. Full single phase flow regime is observed only for the micro-evaporator with inlet restrictions, at the highest values of mass flux and lowest values of heat flux tested (top-left region in plot in Fig. 5.7(a)), because the thermal energy provided is not sufficient to initiate two-phase flow. For slightly larger  $q$  and lower  $G$ , two-phase flow is initiated toward the end of the test section at fixed locations. From these stable nucleation points, two-phase flow develops in the form of triangular jets that become larger downstream along the channels, as it can be observed in the snapshots taken at different time instants included in Fig. 5.8(a). This operational regime is labelled as "jet-flow" due to the jet-like interface configuration, and it is a stable flow because the interface in the

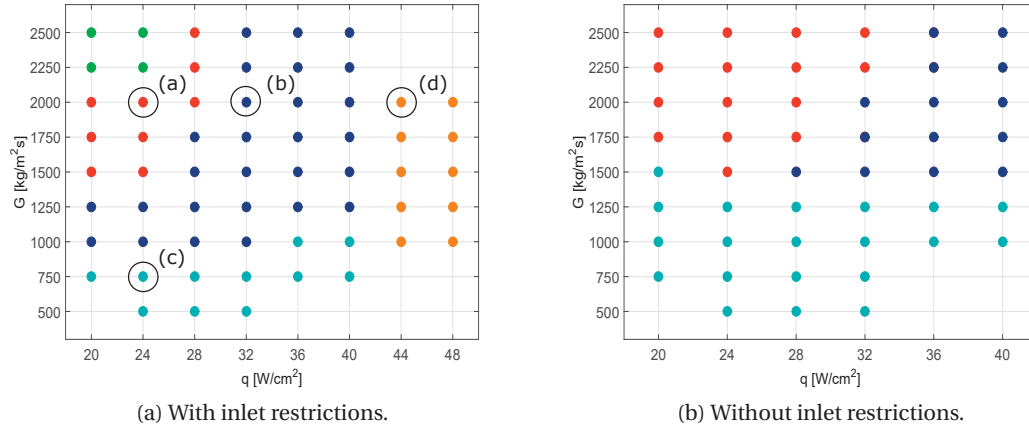


Figure 5.7 – Two-phase flow operational maps for the test section (a) with inlet restrictions and (b) without inlet restrictions. Five flow regimes are identified: ● single phase; ● jet-flow; ● stable single-phase flow followed by two-phase flow; ● unstable two-phase flow with back flow; ● fully stable two-phase flow.

high-speed video maintains a stable behaviour in time and temperature oscillations have small magnitude.

For further smaller values of  $G$  and larger  $q$  (central area in plot in Fig. 5.7), the high-speed videos show a more spatially uniform transition between single phase and two-phase flow (the jets disappear), see Fig. 5.8(b). This results in a smooth change of the temperature from the inlet to the outlet of the micro-evaporator as it is apparent from the IR camera reading given in Fig. 5.5(a). This regime is called stable single phase flow followed by two-phase flow and is a favorable flow regime because of its stability. Note from Fig. 5.8(b) that the single phase to two-phase transition occurs earlier at the center of the heated area and more downstream at the sides, possibly due to the lateral spreading of heat toward the sides of the micro-evaporator but this could also be due to the random location of favorable nucleation sites. This motivates the use of a 3D heat conduction model in the data reduction rather than employing a more simple 1D model, as the latter cannot account for such a non-uniform heat flux at the test section footprint. At the lowest values of mass fluxes, the flow configuration becomes very unstable, as it can be observed in the two successive snapshots given in Fig. 5.8(c) in which the shape and location of the single phase to two-phase transition line along the test section changes substantially. The time-temperature plot reported in Fig. 5.6(b) gives a hint of the strong time-dependent nature of the flow under such conditions. The fluid instability is reflected by larger values of the standard deviation of the temperature measurements, up to  $0.28^{\circ}\text{C}$ . Back flow toward the inlet plenum is also observed. As such, this regime is classified as unstable two-phase flow with back flow and it is an undesirable condition as it yields large spatial and temporal temperature gradients which may potentially prevent the correct functioning of the electronic device being cooled. Note that the area occupied by this unstable regime in the operational maps is wider for the test section without inlet restrictions, see Fig. 5.7(b). It

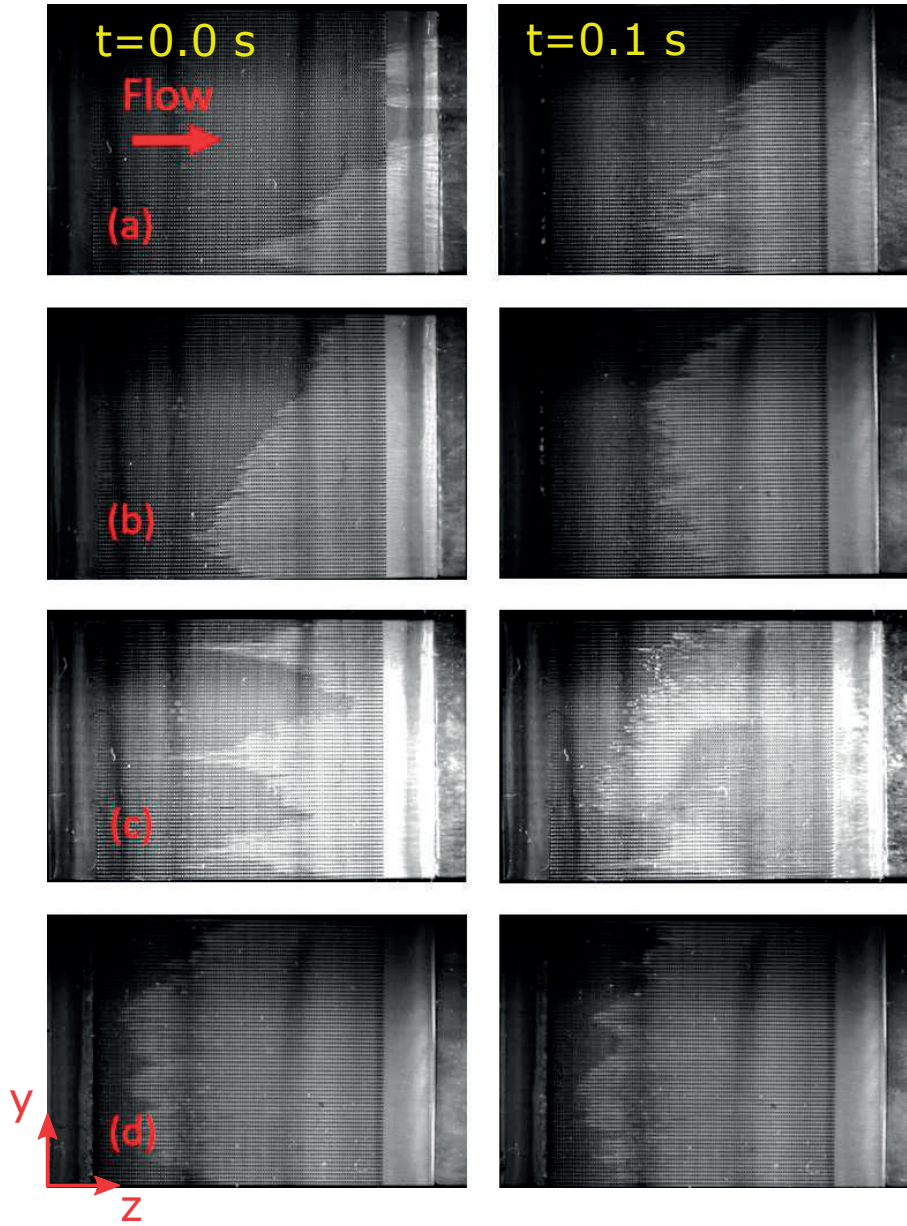


Figure 5.8 – Screenshots from the high-speed camera of the four two-phase flow regimes showed in the operational maps for the case with inlet restrictions. For every flow regime 2 different time instants are showed in order to emphasize the time-dependent nature of the flow. (a) jet-flow  $q = 24 \text{ W cm}^{-2}$  and  $G = 1750 \text{ kg m}^{-2} \text{ s}^{-1}$ , (b) single phase followed by two-phase flow  $q = 36 \text{ W cm}^{-2}$  and  $G = 1750 \text{ kg m}^{-2} \text{ s}^{-1}$ , (c) unstable two-phase flow  $q = 24 \text{ W cm}^{-2}$  and  $G = 750 \text{ kg m}^{-2} \text{ s}^{-1}$ , and (d) fully stable two-phase flow  $q = 48 \text{ W cm}^{-2}$  and  $G = 1750 \text{ kg m}^{-2} \text{ s}^{-1}$ . Flow is from left to right.

extends at mass fluxes up to  $1250 \text{ kg m}^{-2} \text{ s}^{-1}$ , while when inlet restrictions are implemented instabilities are only observed for  $G = 750 \text{ kg m}^{-2} \text{ s}^{-1}$  and below. This once more demonstrates



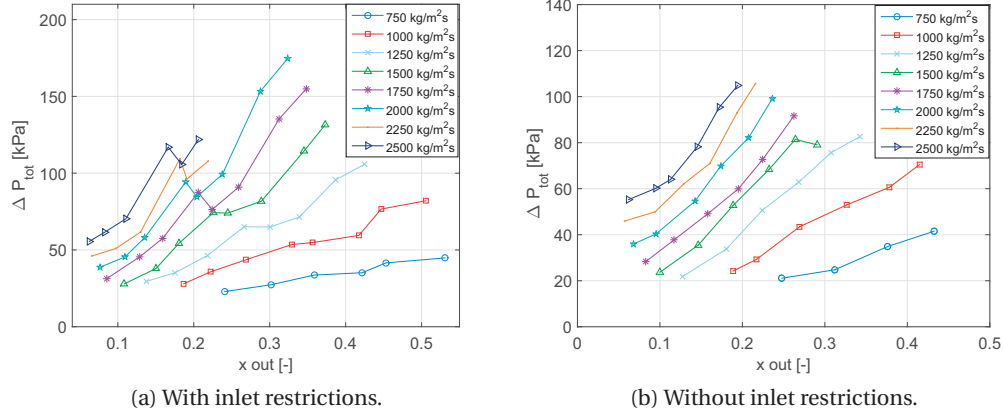


Figure 5.9 – Total measured pressure drop as function of the outlet vapor quality.

the beneficial effect of inlet restrictions on the stability of the flow.

At the highest values of  $q$  tested, a fully stable two-phase flow regime is encountered, although only for the test section with inlet restrictions. As can be seen in Fig. 5.8(d), transition to two-phase flow occurs near the inlet of the heated section and it remains stable in time. The two-phase flow covers most of heated area, and therefore this is the regime which gives the best heat transfer performance and, together with the stable single phase followed by two-phase flow operational condition, are the most stable and preferable operating regimes.

### 5.3.2 Pressure drop

The pressure drop represents a useful indicator of the necessary pumping power to push the fluid through the micro-pin fin evaporator. This information is contained in two parameters, the total pressure drop across the test section  $\Delta p_{tot}$ , and the pressure drop across the pin fin array  $\Delta p_{fin}$ . For the test conditions analyzed in this work, the  $\Delta p_{fin}$  for the two-phase flow boiling tests is about the 85 – 90% of the total pressure drop. As the  $\Delta p_{fin}$  depends on the data reduction procedure, it is here preferred to present the the total pressure drop,  $\Delta p_{tot}$ , measured via the differential pressure transducer. Furthermore, the total pressure drop is more indicative of the total power consumption needed to circulate the refrigerant, which is a more relevant thermo-hydraulic parameter to characterize the micro-evaporator. Figure 5.9 displays the total pressure drop as a function of the outlet vapor quality (representative of the imposed heat flux) at different values of the mass flux, for the test section with and without inlet restrictions. The pressure drop increases with the mass flux as expected. It also grows with the outlet vapor quality, for two main reasons: larger  $x_{out}$  means a higher heat flux and therefore a more substantial contribution of accelerational pressure drop; the higher accelerations also induce a larger drift velocity between vapor and liquid phases, thus increasing the interfacial shear stress and therefore the frictional pressure drop. The highest pressure drop measured in the presence of inlet restrictions is of about 170 kPa ( $G = 2000 \text{ kg m}^{-2} \text{ s}^{-1}$  and  $q = 48 \text{ W cm}^{-2}$ ).

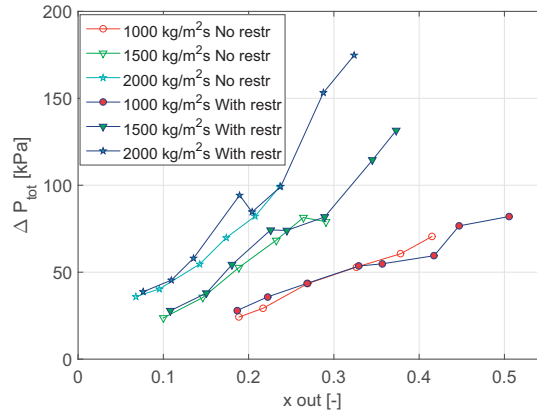


Figure 5.10 – Comparison of the total pressure drop between the geometries with and without inlet restrictions.

Note that, due to technical issues, the pressure drop test for the test section without inlet restrictions was limited to heat fluxes lower than  $40 \text{ W cm}^{-2}$  (see Fig. 5.7). Figure 5.10 presents a comparison of the pressure drops measured for the two test sections, and no appreciable differences in their magnitudes arise. These results further demonstrate the advantage of the inlet restriction, as it enhances the stability of the flow without any appreciable increase in the pumping power consumption of the system.

Szczukiewicz et al. [114] performed flow boiling experiments in a multi-microchannel evaporator using the same test facility of the present study, for a geometry of the micro-evaporator comparable to the present one (67 parallel  $100 \mu\text{m}$  square microchannels), same fluid and similar test conditions. They measured a maximum pressure drop of about 125 kPa ( $G = 2102 \text{ kg m}^{-2} \text{ s}^{-1}$  and  $q = 48.6 \text{ W cm}^{-2}$ ), thus about 25% lower than those measured here. The higher pressure drop measured for the present study can be attributed to the disturbances created by the micro-pin fin geometry.

### 5.3.3 Heat transfer coefficient

The two-phase flow heat transfer results are illustrated in this section. Figure 5.11 shows the heat transfer coefficient as a function of the local vapor quality for different values of the heat flux at a mass flux of  $1500 \text{ kg m}^{-2} \text{ s}^{-1}$ . The colors used for the plotted curves are indicative of their operational regimes as in Fig. 5.7(a). The fluid enters in the test section at subcooled conditions, which motivates the negative values of the vapor quality in Fig. 5.11. When  $x < 0$  the fluid is assumed to be at the single phase state, however the increasing trend of the heat transfer coefficient with heat flux suggests the presence of subcooled flow boiling, as a larger heat flux tends to generate more bubbles by wall nucleation. At positive values of the vapor quality, in general the heat transfer coefficient increases with the heat flux due to the effect of changes in the flow regimes, as it will be explained below. A jet-flow regime is

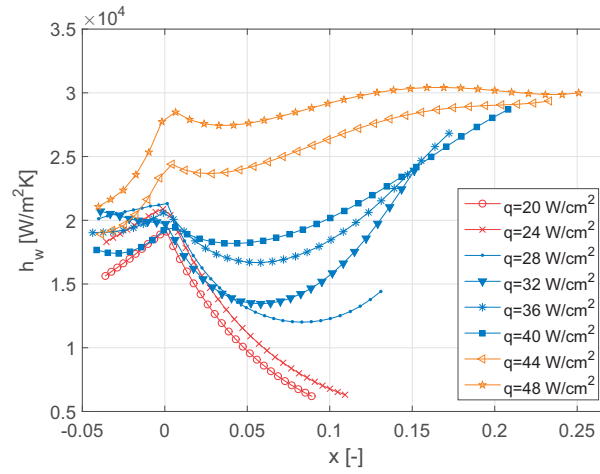


Figure 5.11 – Local heat transfer coefficient as a function of vapor quality for test section with inlet restrictions. Mass flux is  $1500 \text{ kg m}^{-2} \text{ s}^{-1}$ .

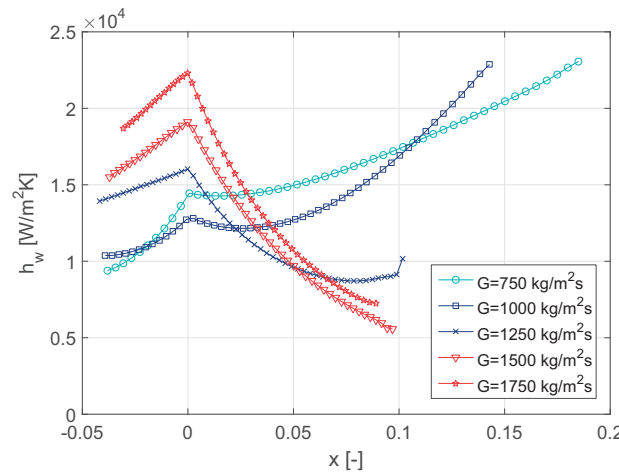


Figure 5.12 – Local heat transfer coefficient as a function of vapor quality for test section with inlet restrictions. Heat flux is  $q = 20 \text{ W cm}^{-2}$ .

observed for  $q = 20 \text{ W cm}^{-2}$  and  $q = 24 \text{ W cm}^{-2}$ , with two-phase flow only present toward the exit of the heated area. The heat transfer coefficient reduces monotonically with the vapor quality. This is consistent with the coalescing bubble flow pattern, where local dry-out nearby the tail of the very elongated bubbles causes a drop in the heat transfer coefficient. Since two-phase flow is present only at the exit, no other flow patterns develop. When the heat flux increases, the two-phase flow covers a wider area within the test section. For heat flux values between  $28 \text{ W cm}^{-2}$  and  $40 \text{ W cm}^{-2}$  (single phase followed by two-phase flow operational regime) the heat transfer curves present the typical U-shaped trend first emphasized by previous microchannel-based studies [119, 117]. This is associated with the transition from



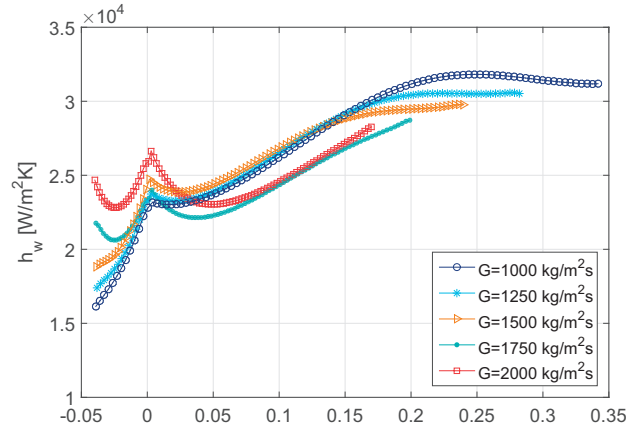


Figure 5.13 – Local heat transfer coefficient as a function of vapor quality for test section with inlet restrictions. Heat flux is  $q = 44 \text{ W cm}^{-2}$ .

the coalescing bubble to the annular flow regime (which identifies the minimum of the curve). The successive development of the annular flow enhances the heat transfer performance due to the evaporation and, therefore, thinning of the annular liquid film. At the largest heat fluxes tested, the two-phase flow covers almost entirely the heated area, thus resulting in very high heat transfer coefficients. The coalescing bubble regime is present only in a very limited initial portion of the flow area, as the local minimum of the U-shaped heat transfer coefficient curve is shifted toward very low values of the vapor quality (about 0.02), thus suggesting an earlier slug flow to annular flow transition.

In Fig. 5.12, the heat transfer coefficient versus vapor quality for different mass fluxes, at constant  $q = 20 \text{ W cm}^{-2}$  is reported for the test section with inlet restrictions. The plot colors match the related operational regimes illustrated in Fig. 5.7. In the negative vapor quality region, the heat transfer coefficient increases with the mass flux. This trend is probably attributed to the influence of the mass flux on the single phase developing flow, supplemented by addition nucleate boiling effects. In the two-phase flow region ( $x > 0$ ) an opposite trend versus mass flux is observed, and this can be ascribed to a flow pattern dependence as it will be explained below. For  $G = 750 \text{ kg m}^{-2} \text{ s}^{-1}$ , the flow is unstable as indicated by the operational map in Fig. 5.7(a), the magnitude of the heat transfer coefficient is larger than the cases with higher mass flux (higher heat transfer coefficients for unstable flows were already reported in [120] and [34]), but this operational regime is undesirable. As the mass flux is increased the flow becomes stable and the heat transfer decreases because, as the heat flux is maintained constant, the exit vapor quality drops such that the two-phase flow occupies a smaller region in the heated area and the annular flow regime cannot develop. Figure 5.13 presents the effect of mass flux on the heat transfer performance at a larger value of heat flux,  $q = 44 \text{ W cm}^{-2}$ . As can be observed in the operational map of Fig. 5.7(a), all the presented cases correspond to the fully stable two-phase flow regime. The heat transfer coefficient trends are substantially

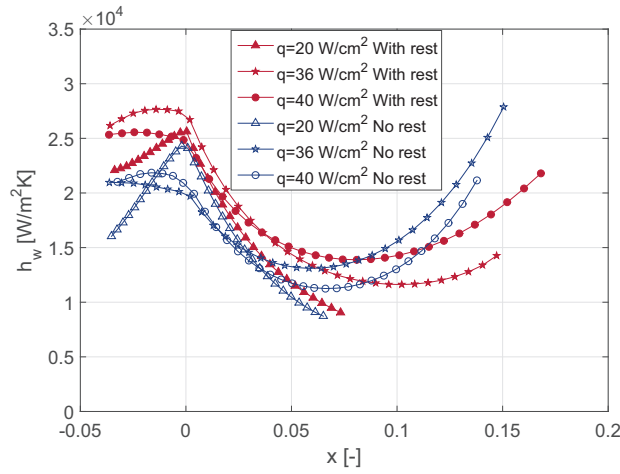


Figure 5.14 – Comparison of local heat transfer coefficient as a function of the vapor quality for the geometry with inlet restrictions and the geometry without. The test conditions shown are for a fixed mass flux equal to  $2000 \text{ kg m}^{-2} \text{ s}^{-1}$ .

different than those observed in Fig. 5.12, because the larger heat flux value promotes the transition to annular flow such that all the plotted curves show a U-shape. The heat transfer coefficient in the two-phase flow region still falls when the mass flux is increased, although to a much smaller extent than the case with  $q = 20 \text{ W cm}^{-2}$  illustrated in Fig. 5.12.

Figure 5.14 provides a comparison of the heat transfer coefficient measured in the two test sections for selected operating conditions.

In the sub-cooled flow boiling region, the geometry with inlet restrictions is characterized by larger values of the heat transfer coefficient which can be attributed to the enhanced single phase heat convection promoted by flow accelerations through the restrictions. In the saturated flow boiling region, when  $q = 20 \text{ W cm}^{-2}$  the annular flow does not develop and only a descending trend is seen, with similar heat transfer magnitude for both the test sections. At  $q = 36 \text{ W cm}^{-2}$  and  $q = 40 \text{ W cm}^{-2}$ , the two-phase flow covers a large part of the heated area, and the U-shaped trends of  $h_w$  suggest that transition to annular flow occurs. The test section without inlet restrictions presents a steeper increase of  $h_w$  at larger vapor qualities (annular flow region), however the minimum heat transfer coefficient value (coalescing bubble to annular flow transition) is shifted to smaller  $x$  compared to the case with inlet restrictions. Therefore it seems that inlet restrictions tend to delay the formation of annular flow, which in turn explains the lower heat transfer performance at a given vapor quality value in the annular flow region compared to the results obtained for the test section without inlet restrictions.

The present heat transfer results have been compared to those obtained by Szczukiewicz et al. [36, 114]. With microchannels the flow boiling curves are all U-shaped and vary in a small range ( $h_w = 15 - 25 \text{ kW m}^{-2} \text{ K}^{-1}$ ) when changing the test conditions. Indeed, mass flux was not an influential parameter and the heat flux had the only effect of shifting the

curves vertically (see Fig. 9(a) in [114]). In the micro-pin fin flow configuration, the shapes of the flow boiling curves dramatically depend on the working conditions (mass flux and heat flux) and the variation in the heat transfer magnitude is larger ( $h_w = 5 - 30 \text{ kW m}^{-2} \text{ K}^{-1}$ ). This suggests that the present geometry has a stronger impact on the heat transfer mechanisms, as the micro-pin fins are expected to disturb the flow to a larger extent than flat walls, also preventing the formation of a continuous thin liquid film which is characteristic of the annular flow regime. Therefore the present comparison does not allow one to conclude quantitatively whether flow boiling in a micro-pin fin evaporator gives a higher heat removal capability than multi-microchannels, since this depends on the local operating conditions.

## 5.4 Conclusions

In this chapter, operational maps, pressure drop, and heat transfer performance of R236fa were studied and presented for a wide range of operating conditions. The major outcomes of the current R236fa work can be drawn as follows:

1. Four different two-phase flow operational regimes are identified by using flow visualization: jet-flow, single phase followed by two-phase flow, unstable two-phase flow and fully stable two-phase flow. Two of these are found to be fully stable and favorable to achieve large values of the heat transfer coefficient.
2. The presence of inlet restrictions at the entrance of the heated area extends the map of stable operational regimes down to lower values of the mass flux,  $G = 1000 \text{ kg m}^{-2} \text{ s}^{-1}$  compared to the operational limit of  $G = 1500 \text{ kg m}^{-2} \text{ s}^{-1}$  detected without restrictions.
3. The pressure drop increases with mass flux and heat flux, and inlet restrictions do not increase the pressure drop in a noticeable way when compared to the test section without. This further demonstrates the beneficial effect of inlet restrictions, as they enhance the stability of the flow without any appreciable increase in the pumping power consumption of the system. The highest total pressure drop, measured at a mass flux of  $2000 \text{ kg m}^{-2} \text{ s}^{-1}$  and heat flux of  $48 \text{ W cm}^{-2}$ , was about 170 kPa.
4. Heat transfer coefficient trends and magnitudes show a substantial dependence on vapor quality, mass flux and heat flux, which can be mainly attributed to flow pattern effects. At higher values of the heat flux or lower values of mass flux, the U-shaped trend versus vapor quality typically observed in multi-microchannel evaporators is found, thus suggesting that transition from slug to annular flow occurs. In general, the heat transfer performance improves when increasing heat flux, and it depends on the flow regime established along the test section.
5. The influence of mass flux and heat flux on the heat transfer performance of the micro-evaporator suggests that the pin fin geometry has a much stronger impact on the two-phase flow patterns development than parallel microchannels, where such a dependence is less pronounced.



## 6 Hydrodynamic and thermal analysis of a micro-pin fin evaporator

### 6.1 Introduction

In the current chapter, the time-dependent features of the flow, operational maps, pressure drop and heat transfer performance for stable flow conditions of different refrigerants are experimentally investigated and discussed, following the same experimental work conducted for R236fa and presented in the previous chapter. In order to create a large database with wide ranges of fluid properties, the fluids tested are: R245fa, R1234ze(E) and R134a.

In addition, in order to investigate the characteristic hydrodynamic and thermal features of the two-phase flow through the micro-pin fin array, image processing and time-strip technique are applied to the high-speed camera videos, which are coupled with the time-dependent 2D temperature maps extracted from the IR camera.

The majority of the results of this chapter were published in:

C. Falsetti, M. Magnini, and J.R. Thome, *Flow Boiling Heat Transfer and Pressure Drops of R1234ze(E) in a Silicon Micro-pin Fin Evaporator*, J. of Electronic Packaging, 139, 1 – 8, 2017.

C. Falsetti, M. Magnini, and J.R. Thome, *Hydrodynamic and thermal analysis of a micro-pin fin evaporator for on-chip two-phase cooling of high density power micro-electronics*, Applied Thermal Engineering, 130, 1425–1439, 2018.

### 6.2 Single phase validation results

As already presented, the total single phase pressure drop, which is obtained from adiabatic single phase experiments and directly measured, includes three components: the pressure drop along the pin fin array  $\Delta P_{fin}$ , and the pressure drops across the inlet and outlet manifold, which are indicated as  $\Delta P_{in}$  and  $\Delta P_{out}$  respectively. The absolute values of their magnitudes are shown in Fig. 6.1 as a function of the mass flux  $G$ , for each of the tested refrigerants. Here,  $\Delta P_{fin}$  accounts for 67–70% of the total losses, while the inlet and the outlet pressure drops

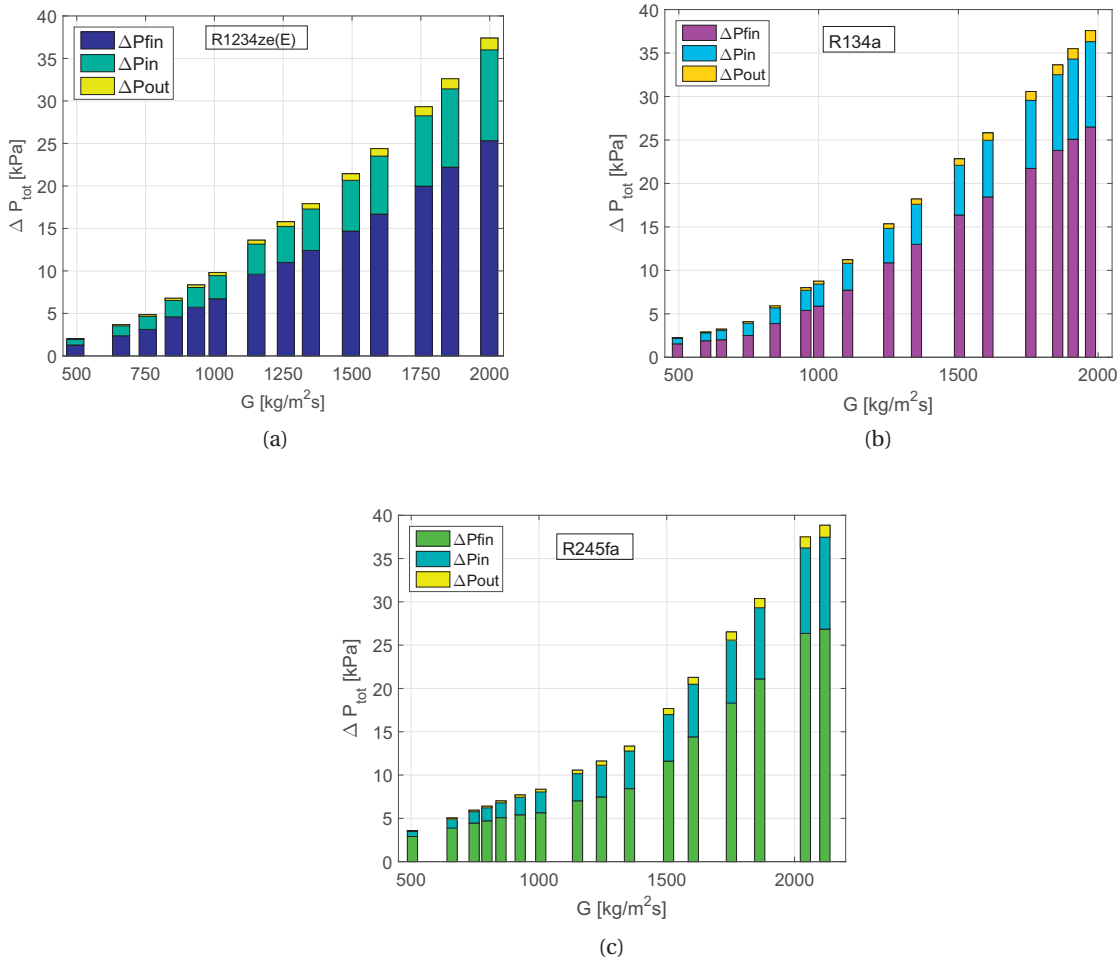


Figure 6.1 – Total single phase pressure drop as function of the mass flux for the tested refrigerants: (a) R1234ze(E), (b) R134a, and (c) R245fa. Saturation temperature of  $T_{sat} = 25^\circ\text{C}$ .

account for 26–29% and 3–4%, respectively. These ranges remain almost the same when the mass flux increases and when the refrigerant utilized changes.

From the values of the pin fin pressure drop  $\Delta P_{fin}$ , it is possible to evaluate the single phase friction factor, which is plotted as a function of the Reynolds number in Fig. 6.2 for the entire adiabatic single phase database of the current work, including also the R236fa data illustrated in the previous chapter. The friction factor shows a transition in its trend at a Reynolds number, calculated based on the hydraulic diameter, of about 300 (this value changes slightly as the fluid properties differ). The change in the friction factor slope may be explained by the fact that the presence of fins promotes mixing and vortex shedding when the fluid velocity increases, as also explained by Renfer et al. [2]. A similar trend has been reported also by Prasher et al. [44] and Nieuwstadt et al. [121] for a simple pipe flow, where the friction factor slope showed a change which was referred to as a transitional region between the laminar and the turbulent

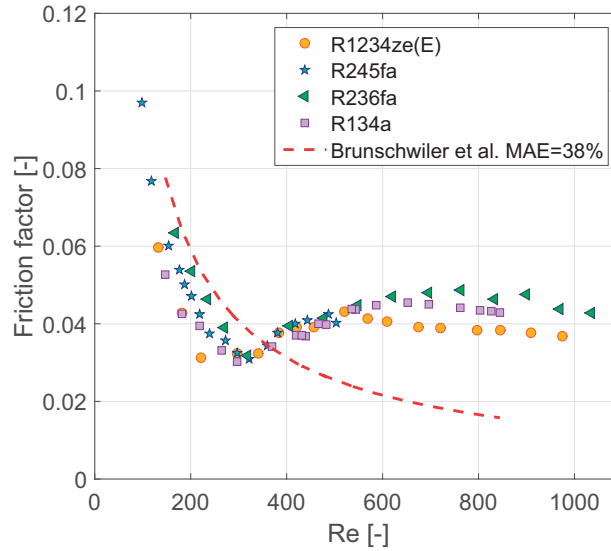


Figure 6.2 – Single phase friction factor as a function of the Reynolds number for each of the tested refrigerants.

regimes, in which the still laminar fluid flow contains the so-called “puffs,” localized turbulent states. A discussion of this result can be found also in the previous chapter.

The experimental data are compared with the correlation proposed by Brunswiler et al. [10], see Fig. 6.2. This was developed for water flowing across in-line circular pin fins with heights varying from  $100\ \mu\text{m}$  to  $200\ \mu\text{m}$  and pitches ranging from  $50\ \mu\text{m}$  to  $200\ \mu\text{m}$ , at  $Re$  smaller than a critical value of 300. Indeed, the correlation approximately captures the present data when the flow is still laminar, i.e. at values of the Reynolds number lower than 300, but it does not predict the transition.

The validation of the single phase heat transfer results is made by performing single phase diabatic tests to calculate the average Nusselt number. The single phase averaged Nusselt numbers for the fluids R245fa, R1234ze(E) and R134a are displayed in Fig. 6.3(a), Fig. 6.3(b) and Fig. 6.3(c) respectively. Figure 6.3 also includes the predictions obtained by some existing correlations for micro-pin fins and tube bundles taken from the open literature. The details of the selected correlations and their estimation errors are reported in Table 6.1. The data of the three refrigerants exhibit an approximately linear trend versus  $Re$ , in agreement with those predicted by the correlations included in Fig. 6.3. In particular, the correlation of Brunswiler et al. [10], which exhibits a milder rise of  $Nu$  with  $Re$ , estimates the R245fa trend quite well but significantly underestimates the R1234ze(E) and R134a data. The tube bank correlation of Zukauskas and Ulinskas [49], the ones given by Kosar and Peles [46] and Prasher et al. [44] overestimated R245fa data with mean absolute errors of 139.7%, 139.2%, and 175%. Addressing now R1234ze(E) and R134a, the correlations of Zukauskas et al. [49], Prasher et al. [44] and Kosar et al. [46] better predict the experimental data, although showing in general a lower

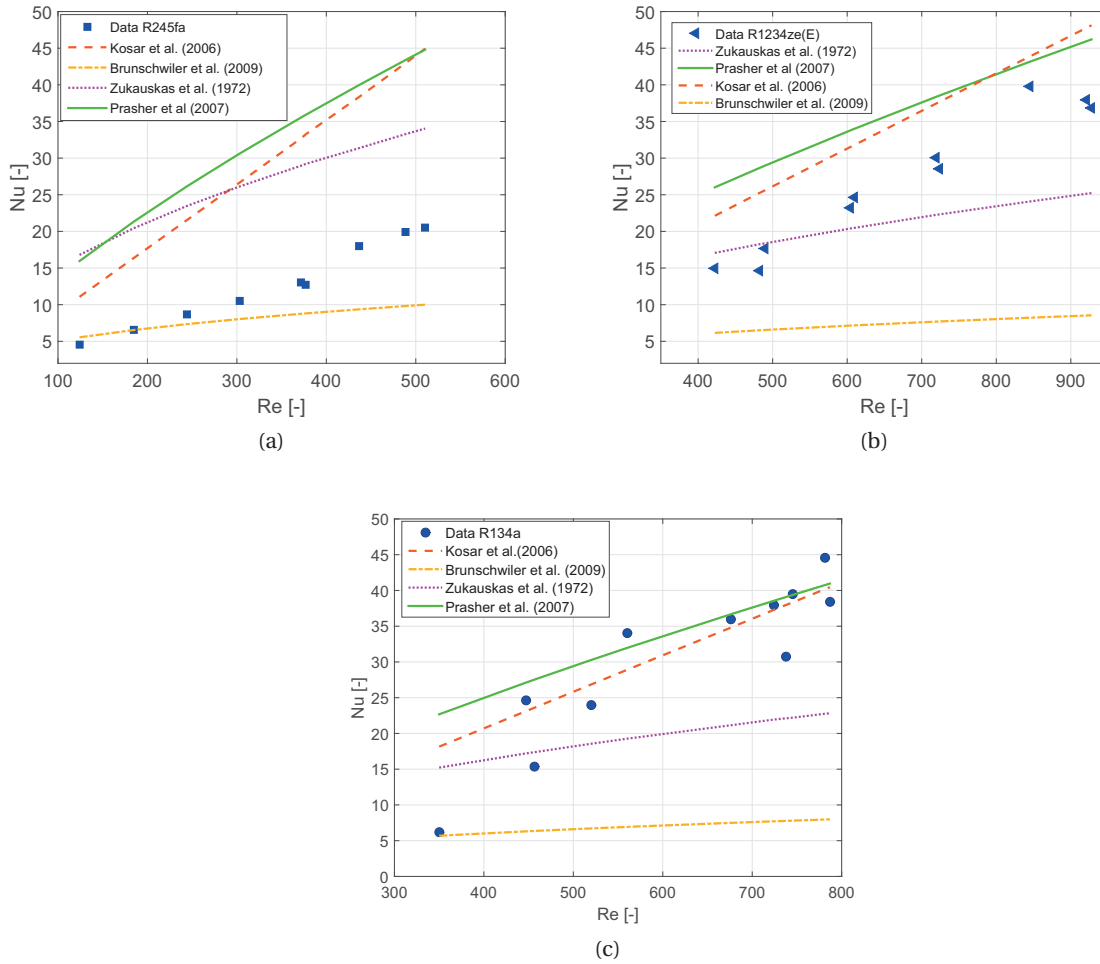


Figure 6.3 – Average Nusselt number versus Reynolds number. Fluids: (a) R245fa , (b) R1234ze(E), (c) R134a. Comparison with existing correlations. Saturation temperature of  $T_{sat} = 25^{\circ}\text{C}$ .

Study	Dimensions	Re	Fluid	MAE R245fa	R1234ze(E)	R134a
Prasher et al. [44]	$D = 50 - 150\ \mu\text{m}$ , $H/D = 1.3 - 2.8$	40 – 1000	water	175%	43.5%	39%
Kosar et al. [46]	$D = 50 - 100\ \mu\text{m}$ , $H/D = 1 - 2$	5 – 128	water	139.2%	35.3%	30%
Zukauskas et al. [49]	long tubes, $H/D > 8$	$> 100$	see [49]	139.7%	22.5%	45%
Brunswiler et al. [10]	$D = 100 - 200\ \mu\text{m}$ , $H/D = 1 - 3$	$< 1000$	water	30.5%	69%	70%

Table 6.1 – Details about the existing correlations whose predictions are included in Fig. 6.3. The Mean Absolute Error is evaluated as  $\text{MAE} = \frac{1}{n} \sum_{i=1}^n \frac{|Nu_{exp,i} - Nu_{pred,i}|}{Nu_{exp,i}}$ .

rise of Nu with Re, see Fig. 6.3(b)-(c). Note that no laminar to turbulent transition appears in Fig. 6.3(b)-(c), as that was observed to occur at  $Re = 300$  (see Fig. 6.2), while the lowest Reynolds number covered in the R1234ze(E) and R134a diabatic single-phase tests was about  $Re = 350$  in order to avoid boiling initiation. On the contrary, the trend of R245fa in Fig. 6.3(a) shows a transition at about  $Re = 350$ . In fact, R245fa could be tested at a lower Reynolds as its higher



latent heat of vaporization and surface tension delay the boiling initiation. As an example, R245fa has  $h_{lv} = 190.3 \text{ kJ kg}^{-1}$  versus  $h_{lv} = 177.7 \text{ kJ kg}^{-1}$  of R134a and  $\sigma = 13.63 \text{ mN m}^{-1}$  versus  $\sigma = 8.03 \text{ mN m}^{-1}$  of R134a at  $T_{sat} = 25^\circ\text{C}$ .

## 6.3 Two phase results

All the results presented below refer to stable flow boiling data and steady-state conditions, i.e. flows characterized by small temporal oscillations of the temperature ( $\leq 0.3 \text{ K}$ ), which represent the optimal conditions for the micro-evaporator. First, the range of stable flow conditions are identified in Section 6.3.1. Afterwards, a synchronized analysis of high-speed videos and infrared camera measurements is outlined in Section 6.3.2. Finally, in Sections 6.3.3, 6.3.4 and 6.3.5 the pressure drop and heat transfer coefficient data with a comparison between the fluids R134a and R1234ze(E) are outlined. In the experimental two-phase flow tests, the heat flux ranged from  $20 \text{ W cm}^{-2}$  to  $44 \text{ W cm}^{-2}$ , the mass flux varied from  $750 \text{ kg m}^{-2} \text{ s}^{-1}$  up to  $1750 \text{ kg m}^{-2} \text{ s}^{-1}$ , the outlet saturation temperature was set equal to  $25^\circ\text{C}$  and the inlet liquid subcooling was set to  $5.0 \pm 1.5 \text{ K}$ .

### 6.3.1 Operational maps

The operational maps include information about the two-phase flow regime identified for each test condition, and therefore they are a useful tool to identify the range of stable flow conditions. These are of great importance for industrial applications of two-phase cooling, e.g. cooling of microelectronics chips, because stable flow conditions guarantee a uniform flow distribution and absence of vapor back flow, thus minimizing spatial and temporal fluctuations of temperature of the device to be cooled.

For each test condition, i.e. a given set of parameters  $G$  and  $q$ , the IR camera temperature signal and the high speed video are analyzed. The temperature signal in time is processed as described in the previous chapter regarding R236fa to derive the amplitude of the temperature fluctuations. The location of the transition from single phase flow to two-phase flow is extracted from the high-speed video (transition between dark and very bright zones) and studied as time elapses. Different operational regimes are identified across the entire range of variation of  $G$  and  $q$  according to the flow patterns observed in the high speed images. Operational regimes are identified as stable if the temperature oscillations are on the order of  $0.1 - 0.3 \text{ K}$  and the onset of the two-phase flow is stationary in time. Larger temperature fluctuations are usually associated with significant vapor backflow observed in the high-speed videos, thus identifying unstable flow conditions.

Operational maps for the fluids R1234ze(E), R134a and R245 are presented in Figs. 6.4. Each point in the operational map represents a test condition, identified by its mass flux  $G$  and heat flux  $q$ . Four different operational regimes are distinguished:

1. Single phase flow (●);
2. Jet-flow (●);
3. Unstable two-phase flow with back flow(●);
4. Fully stable two-phase flow initiated nearby the channel entrances from flashed vapor bubbles (●);

Single phase flow is observed in the range of high  $G$  and low  $q$ , when the heat provided to the flow is not sufficient to initiate boiling. The first regime encountered for larger heat fluxes and lower mass fluxes is the "jet flow", where two-phase flow initiates at well-defined locations and departs as a jet flowing downstream to the micro-evaporator. At intermediate values of  $G$  and  $q$ , fully stable two-phase flow is observed, with several nucleation sites active and very stable jets. Under these conditions, the interface between single and two-phase flow is stable in time and is spread uniformly across the heated area width. It is worth noting that, differently from the previous chapter of R236fa, the stable single phase followed by two-phase flow is here included in this regime (therefore the "blue" dots plotted in Figs. 5.7 are here included in the "orange" ones). At larger values of  $q$  and low values of  $G$ , the extremely high evaporation rate may cause local vapor back flow to the inlet manifold, with the consequent appearance of strong dynamic patterns which trigger remarkable temperature fluctuations, i.e. the flow is unstable. The operational maps indicate that the fluids R134a and R1234ze(E) are characterized by a very stable behavior over a wide range of flow conditions. Stable two-phase flow is observed for values of the heat flux in the range  $q = 24 - 40 \text{ W cm}^{-2}$  and mass flux in the range  $G = 1000 - 1750 \text{ kg m}^{-2} \text{ s}^{-1}$  for both the fluids. It is worth noting that larger values of heat flux are possible, provided that the mass flux is sufficiently increased to avoid vapor back flow. In the present experimental study higher values of heat flux and therefore of mass flux have not been tested in order to perform experiments in a safe condition without risk of burning out of the heater, and also maintaining the fluid pressure lower than 8 bar to avoid possible breakage of the test section.

Conversely, R245fa is strongly unstable across the whole range of flow conditions. This can be ascribed to the larger liquid to vapor density ratio of this low pressure refrigerant which triggers significant boiling instabilities. The unstable behaviour of R245fa might be reduced by placing larger inlet restrictions than the ones utilized here or by testing larger mass flow rates.

An example of unstable two-phase flow with back flow is illustrated in the high-speed camera screenshots of Fig. 6.5. Flow is moving from left to right, along the  $z$  direction. The fluid is R245fa under the following test conditions:  $G = 1000 \text{ kg m}^{-2} \text{ s}^{-1}$ ,  $q = 28 \text{ W cm}^{-2}$  and outlet saturation temperature of  $T_{sat} = 30^\circ \text{C}$ . Nucleation occurs near the channel inlet and it is followed downstream by a chaotic two-phase flow, see Fig. 6.5. The interface between single and two-phase flow, i.e. where the boiling nucleation occurs, is not uniform along the test section width and it is moving back and forth, as indicated by the yellow arrows in Fig. 6.5. The observed instabilities might be induced by flow reversal as the flow resistance in the backflow

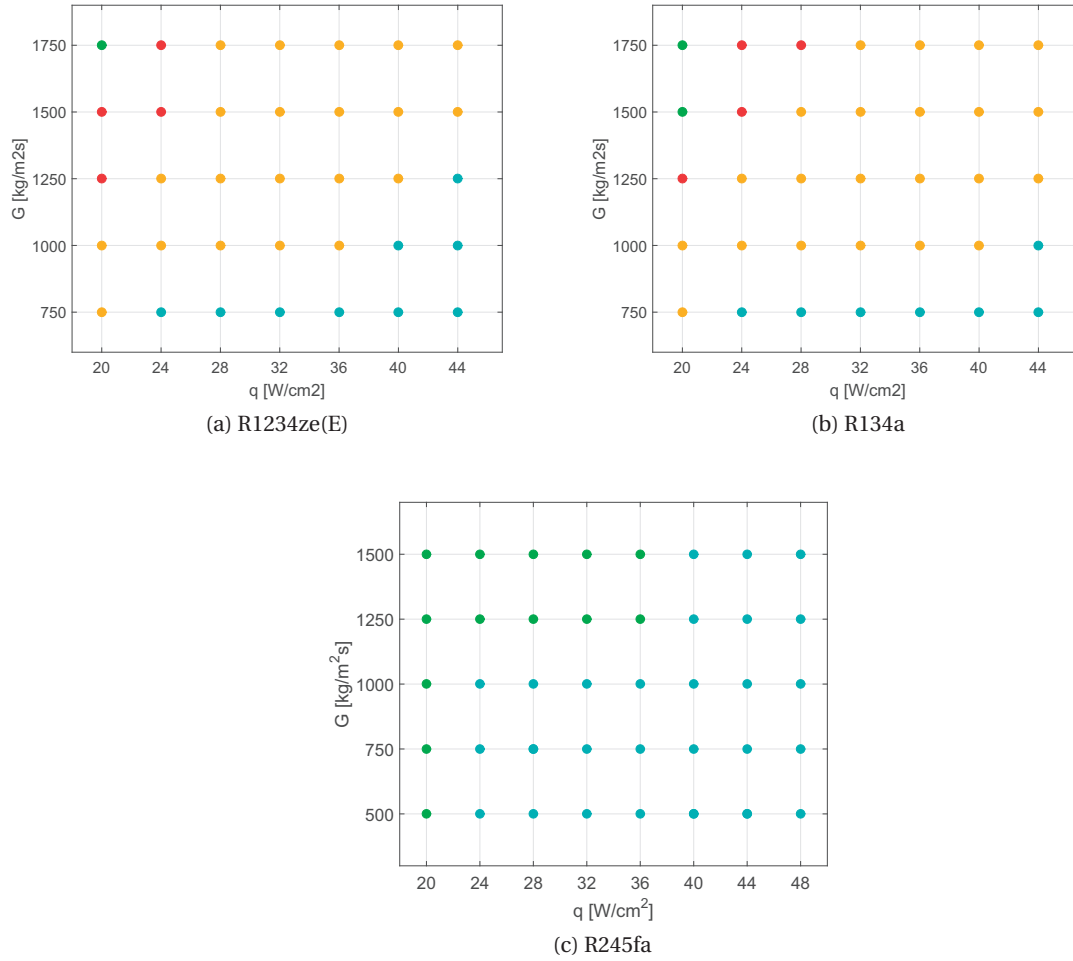


Figure 6.4 – Two-phase flow operational map, fluids (1) R1234ze(E), (2) R134a and (3) R245fa. Four flow regimes are identified: ● single phase; ● jet-flow; ● unstable two-phase flow with back flow; ● fully stable two-phase flow.

direction decreases [122], and by temporary blockage of the flow passage as the vapor bubbles nucleate and cluster. In Fig. 6.6 the micro-evaporator base temperatures obtained with the infrared camera at a central location of the heated area (pixels:  $y = 55$ ,  $z = 55$ ), for the fluids R134a and R245fa are compared under the same test conditions of  $G = 1250 \text{ kg m}^{-2} \text{ s}^{-1}$ ,  $q = 28 \text{ W cm}^{-2}$ . As it is possible to observe in the temperature profile, the unstable behaviour of R245fa, as shown in Fig. 6.5, yields a temperature of the micro-evaporator base of about  $58^\circ\text{C}$ , whilst the stable condition of R134a leads to a base temperature of about  $35^\circ\text{C}$ , demonstrating the improvement in the cooling performance. A statistical analysis of the temperature signal versus time was performed and it yielded a standard deviation of  $0.96 \text{ K}$  for the fluid R245fa with temperatures reaching  $60^\circ\text{C}$  but only  $0.05 \text{ K}$  for R134a. Indeed, once the flow becomes unstable, the pressure, temperature and mass flow rate start to oscillate with larger amplitudes, and this can have a dramatic effect on the overall system performance. Therefore, the following

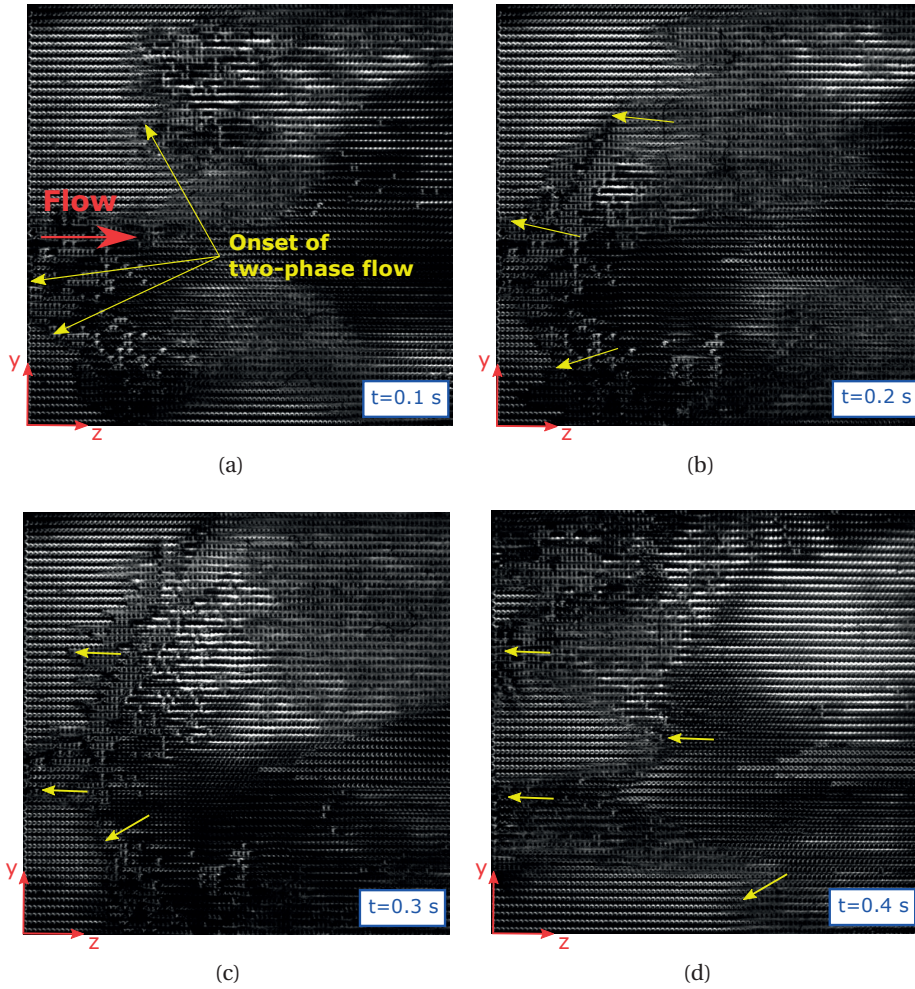


Figure 6.5 – Instabilities of R245fa in different time steps. Explosive vapor burst are created nearby the inlet of the test section and move towards the exit. Flow is moving from left to right, along the  $z$  direction. Test conditions:  $G = 1000 \text{ kg m}^{-2} \text{ s}^{-1}$ ,  $q = 28 \text{ W cm}^{-2}$  and outlet saturation temperature of  $T_{sat} = 25^\circ \text{C}$ .

results will focus on the two-phase pressure drop and heat transfer of R134a and R1234ze(E) only. The refrigerant R245fa, due to its unstable behaviour, is not considered.

### 6.3.2 Analysis of time-dependent patterns

In this section, a synchronized analysis of high-speed camera videos and time-dependent temperature profiles extracted from the IR camera is performed, with the objective of investigating characteristic hydrodynamic and thermal features of the two-phase flow. Fluid is R134a. Figure 6.7(a) shows the temperature profile versus time measured in the proximity of the onset of two-phase flow in the test section (see location indicated in Fig. 6.8(a)), for  $q = 28 \text{ W cm}^{-2}$  and  $G = 1000 \text{ kg m}^{-2} \text{ s}^{-1}$ . The temperature exhibits temporal oscillations of average amplitude

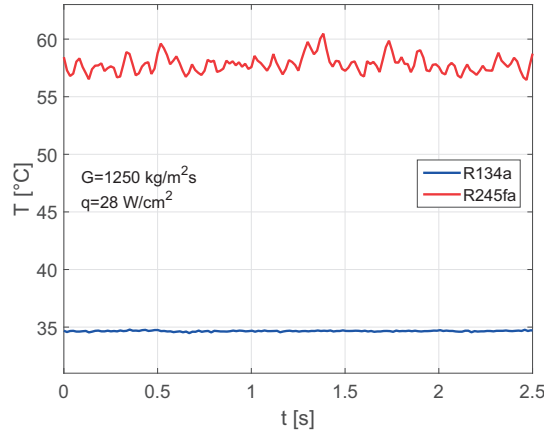


Figure 6.6 – Temperature fluctuations for the fluids R134a and R245 at the same test conditions:  $G = 1250 \text{ kg m}^{-2} \text{ s}^{-1}$ ,  $q = 28 \text{ W cm}^{-2}$  and outlet saturation temperature of  $T_{sat} = 25^\circ \text{C}$ .

of about 0.15 K. Some temperature fluctuations are always present for all the flow conditions tested. For stable flows, i.e. when the onset of two-phase flow occurs at a constant location within the micro-evaporator, their amplitude ranges from about 0.1 K (high mass flow rates) to 0.3 K (low mass flow rates and high heat fluxes). Fluctuations grow up to 1 K and above when the flow is unstable, i.e. when the onset of two-phase flow moves cyclically upstream and downstream within the heated area. Figure 6.7(b) displays the spectrum analysis of the temperature signal of Fig. 6.7(a), which reveals the presence of a single fundamental frequency of 14.8 Hz. The same frequency is uniformly measured across the entire single phase flow region of the evaporator, while no dominant frequencies emerge from the temperature signal in the two-phase flow region in the second half of the test section. The same analysis repeated for all the stable flow conditions tested in this work shows frequencies that increase with both heat and mass flux, and vary between 15 Hz and 22 Hz, see Fig. 6.7(c).

Frequencies of this magnitude cannot be attributed to vortex shedding generated by the pin fins. For Reynolds numbers of 500 – 1000 such as those characteristic of this study, the value of Strouhal number describing vortex shedding,  $St = \Omega L/U$ , is about 0.21 [123]. Adopting the pin diameter for the length scale  $L$ , and the single phase liquid velocity  $G/\rho_l$  for  $U$ , a vortex frequency on the order of  $10^3$  Hz is estimated, thus 2 orders of magnitude larger than the measured values. Other studies on flow boiling in small diameter channels reported frequencies of magnitude similar to those detected in this work [120, 124, 125, 126]. Periodic temperature and pressure fluctuations were attributed to the bubble nucleation, growth and detachment process, and to cyclic variations of the flow pattern, i.e. long vapor bubbles segmented by liquid slugs. In order to better clarify the origin of the observed temperature fluctuations, the high-speed video images are utilized. Figure 6.8(a) shows a frame extracted from the video for the case with  $q = 28 \text{ W cm}^{-2}$  and  $G = 1000 \text{ kg m}^{-2} \text{ s}^{-1}$ . Flow is from left to right. The dark zone at the upstream end of the evaporator is associated to single phase flow. The bright jets departing from this region indicate bubble nucleation, and the very bright area



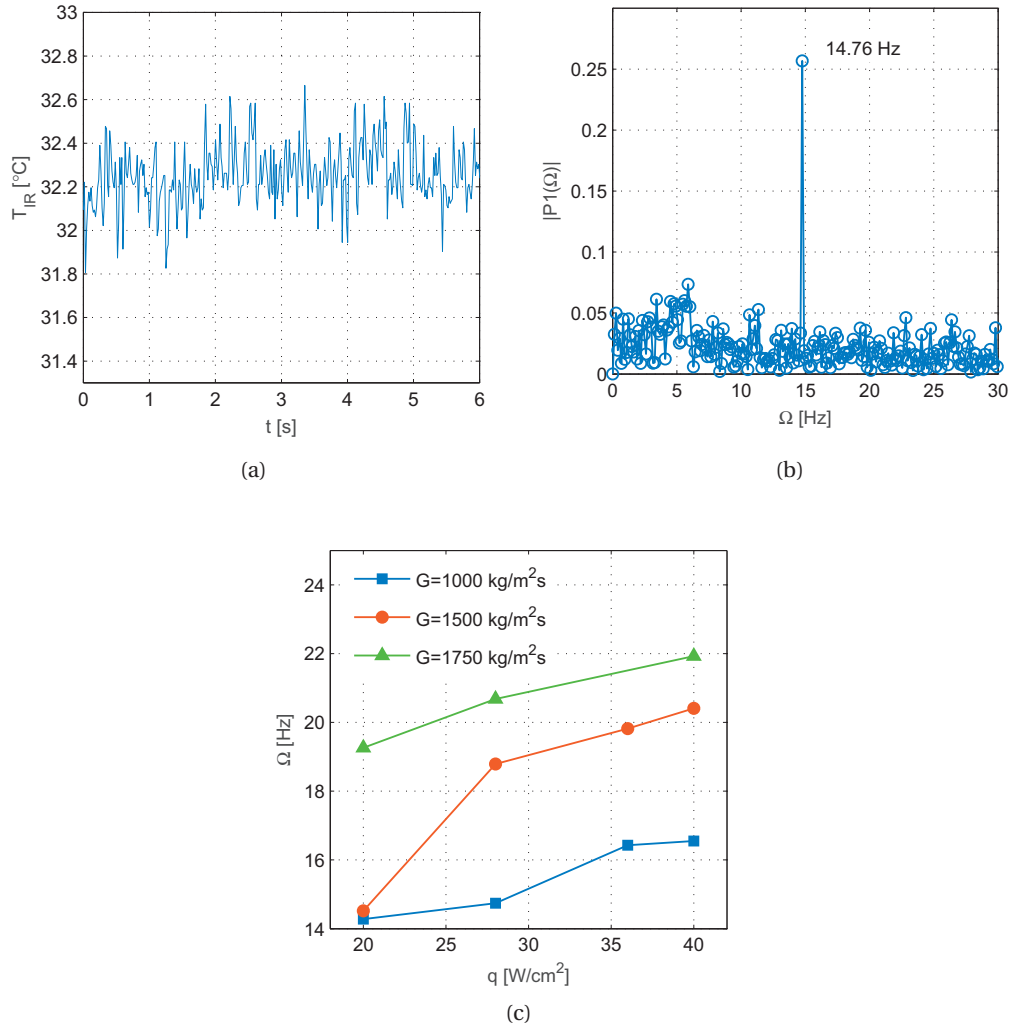


Figure 6.7 – (a) Temperature signal over time at the location indicated in Fig. 6.8(a), for  $q = 28 \text{ W cm}^{-2}$  and  $G = 1000 \text{ kg m}^{-2} \text{ s}^{-1}$  and (b) its Fourier transform. (c) Values of the fundamental frequency detected at different test conditions as a function of mass and heat flux. Fluid is R134a.

that follows is linked with the flow of short and intermediate length bubbles. The successive grey area indicates the presence of the liquid films associated with very long bubbles or annular flow. Under stable flow conditions, the transition from single to two-phase flow (dark to very bright region) and that from short to long bubbles or annular flow (very bright to grey region) change very little in time.

The high-speed video sequences are processed by means of a time-strip technique, which was first introduced in the analysis of the flow behavior in microchannels by Borhani et al. [113]. This involves extracting the one-dimensional light intensity distribution along a given channel

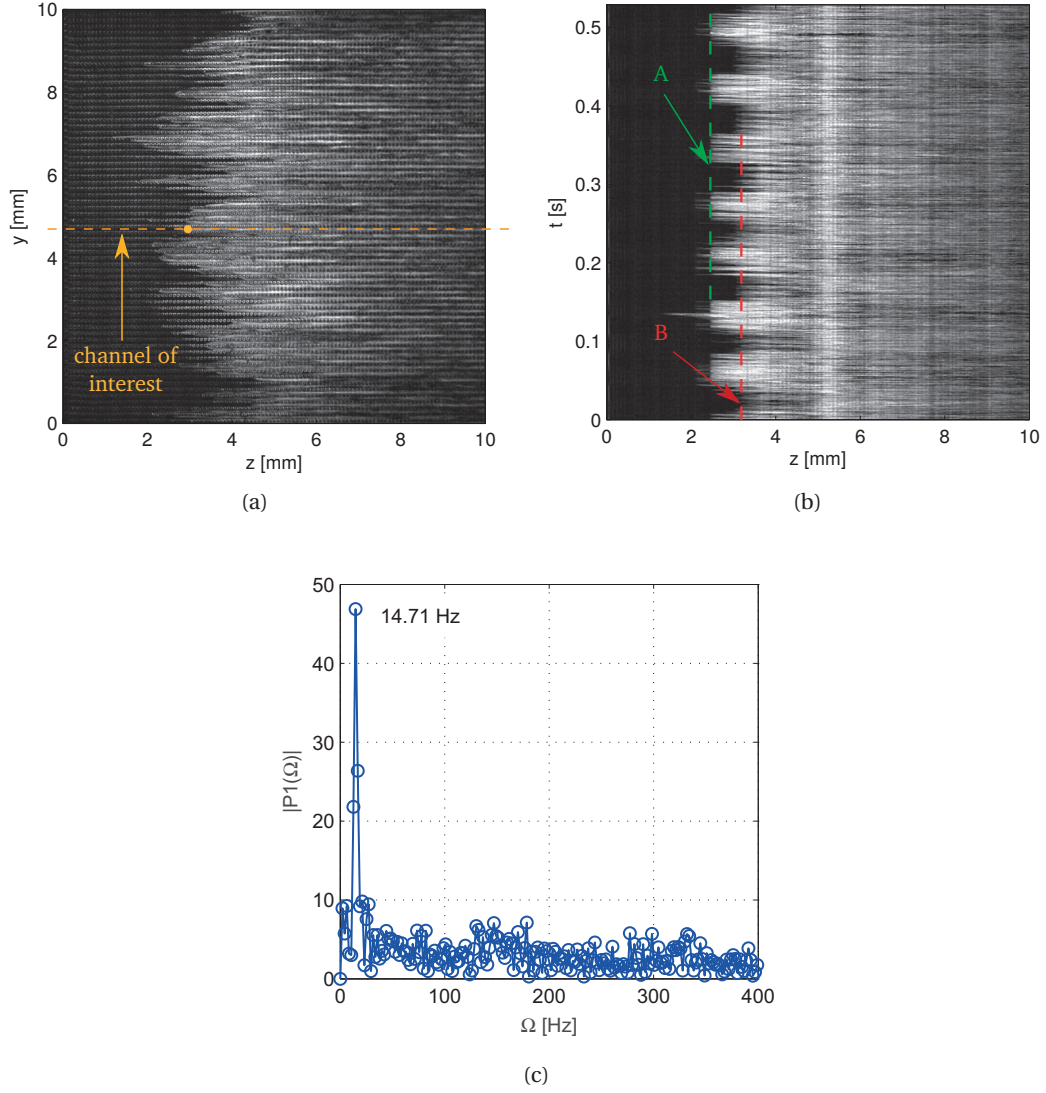


Figure 6.8 – (a) Video frame from the high-speed camera indicating the channel where the time-strip analysis is conducted. The yellow dot shows the location where the temperature signal of Fig. 6.7(a) is extracted. Flow is from left to right. (b) Time-strip analysis of the light intensity for the channel of interest. Location A indicates the most upstream nucleation site, location B identifies the successive nucleation site. (c) Fourier transform of the light intensity at the location of interest (yellow dot in (a)). Flow conditions are  $q = 28 \text{ W cm}^{-2}$  and  $G = 1000 \text{ kg m}^{-2} \text{ s}^{-1}$ . Fluid is R134a.

for each frame, and plotting it as a function of time by stacking the one-dimensional strips, i.e. along the centerline of the channel. Figure 6.8(b) shows an example of the time-strip obtained by extracting the light intensity distribution along the centerline of the channel indicated in Fig. 6.8(a). The time-strip plot suggests that there exists a single upstream nucleation site (location A) which activates and deactivates periodically, while another nucleation site

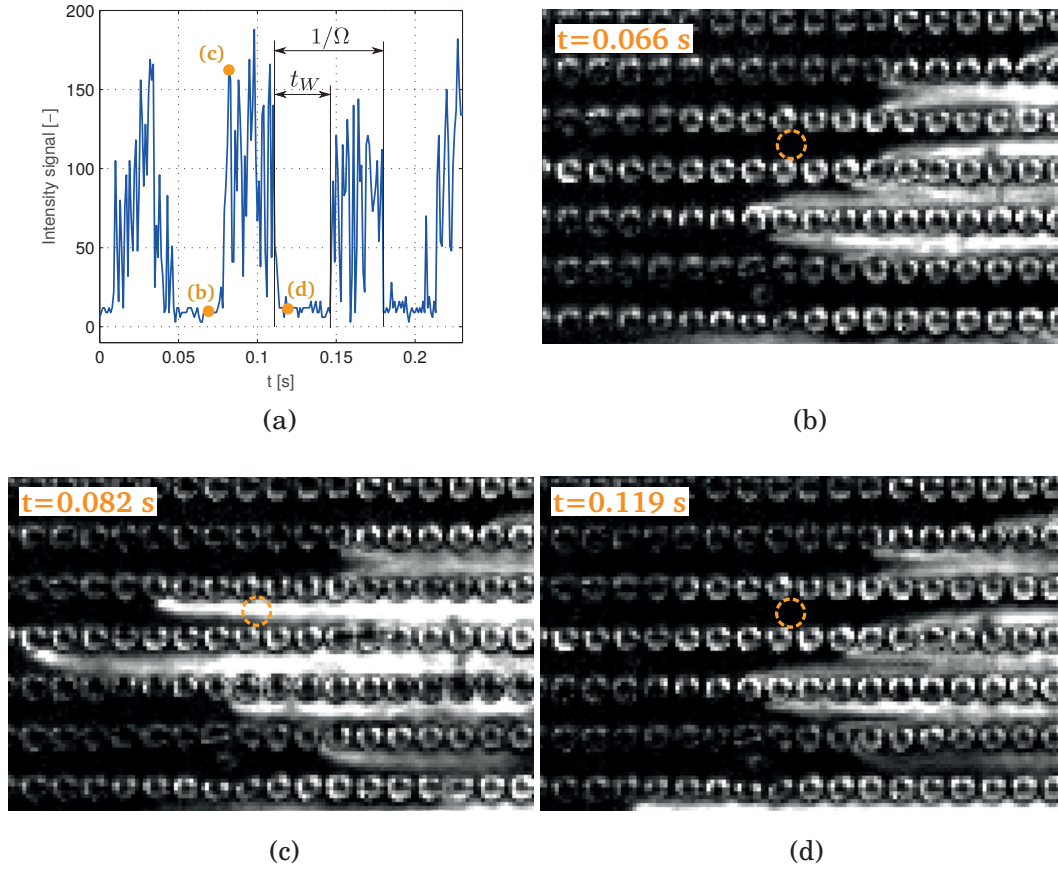


Figure 6.9 – (a) Light intensity signal over time at the location indicated with yellow dashed circles in the (b), (c) and (d) video frames at different time instants, for  $q = 28 \text{ W cm}^{-2}$  and  $G = 1000 \text{ kg m}^{-2} \text{ s}^{-1}$ .

located more downstream (location B) seems to be always active. A Fourier analysis of the light intensity signal for a pixel located between the two nucleation sites reveals the presence of a single fundamental frequency of 14.7 Hz, see Fig. 6.8(c), thus a value very close to that extracted from the temperature signal. Therefore, the temperature fluctuations observed with the IR camera can be attributed to the cyclical activity of the nucleation sites. Liquid compressibility effects induce pressure waves that are generated at the instant of bubble nucleation and that travel upstream in the channel (and also widthwise due to the gap between the pins), thus explaining the presence of temperature fluctuations with the same frequency all across the single phase region of the evaporator. A closer inspection to the bubble nucleation phenomenon is possible by Fig. 6.9, where the light intensity signal for a given pixel is plotted versus time and three video frames showing the same flow area at different time instants are presented. It can be seen that the intensity signal grows from zero to a large value as soon as bubbles begin to nucleate and cross the location under analysis. Note that the spatial and temporal resolution of the camera is not sufficient to capture the dynamics of single bubbles,



and therefore the white streams departing from the nucleation sites are actually "swarms" of bubbles. Interestingly, all the visible nucleation sites seem to be located at the corner between the foot of the pin and the footprint surface of the test section, where surface imperfections exist due to the microfabrication process.

Fig. 6.9(a) emphasizes that the period of nucleation site activity can be decomposed into a waiting time ( $t_W$ ), where no bubbles are present, and an active time. In nucleate boiling, the waiting time is traditionally interpreted as the time that it takes for the wall temperature to re-grow above the nucleation superheat [127]. During the active time, several bubbles nucleate and progressively cool down the evaporator wall to a temperature value which is below that necessary for new bubbles to be generated, and then the site deactivates. Mikic and Rohsenow [128] proposed a bubble growth model where the waiting time  $t_W$  was calculated by assuming one-dimensional transient heat conduction across the thermal boundary layer at the wall. This led to the following expression for  $t_W$ :

$$t_W = \frac{1}{4\alpha_l} r_b^2 \operatorname{erfc}^2 \left[ \frac{2\sigma T_{sat}}{(T_w - T_{sat}) h_{lv} \rho_v r_b} \right] \quad (6.1)$$

where  $\alpha_l$  is the liquid thermal diffusivity,  $\sigma$  the surface tension,  $h_{lv}$  the latent heat of vaporization and  $r_b$  the radius of the nucleating bubble. By taking a value of the bubble radius on the order of half height of the channel cross-section, Eq. (6.1) yields values of  $t_W$  which are comparable with those measured in this work ( $t_W = 15 - 30$  ms). This supports the interpretation of the period of inactivity of a nucleation site as the time necessary for the wall to reach the nucleation superheat. Furthermore, we observed that the waiting time decreases with increasing heat flux and mass flow rate, consistent with the trends of the fluctuation frequency depicted in Fig. 6.7(c). The decrease of  $t_W$  with increasing  $q$  is related to the shorter time necessary for the wall to reach the nucleation superheat, while larger mass flow rates generate thinner thermal boundary layers, thus inducing a faster thermal transient.

### 6.3.3 Pressure drop

The pressure drop represents a useful indicator of the necessary pumping power required by the present heat sink, and therefore it has significant industrial interest. The total pressure drop, measured between the inlet and outlet manifolds of the test section during flow boiling tests, is reported in Fig. 6.10 as a function of outlet vapor quality for the fluid R134a when varying test conditions  $G$  and  $q$ . The pressure drop increases with the outlet vapor quality, i.e. with the heat flux, because the larger vapor velocity and acceleration induced by the larger evaporation rate increase both the frictional and accelerational components of the pressure drop, as they generate larger shear forces between the vapor and liquid phases. Larger mass flow rates yield larger pressure drops as expected, due to the higher wall friction.

Figure 6.11 depicts the frictional and accelerational components of the two-phase pressure drop along the micro-pin fin array, which are evaluated by the separated flow model according to Eqs.(4.27) - (4.32), for two different tested mass fluxes.

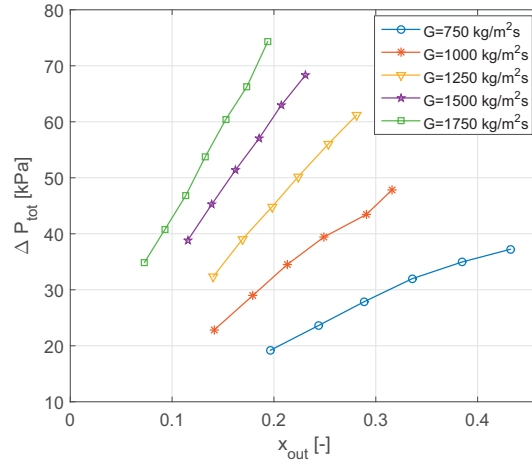


Figure 6.10 – Total measured pressure drop versus exit vapor quality for fluid R134a and all the tested conditions. The outlet saturation temperature is 25 °C

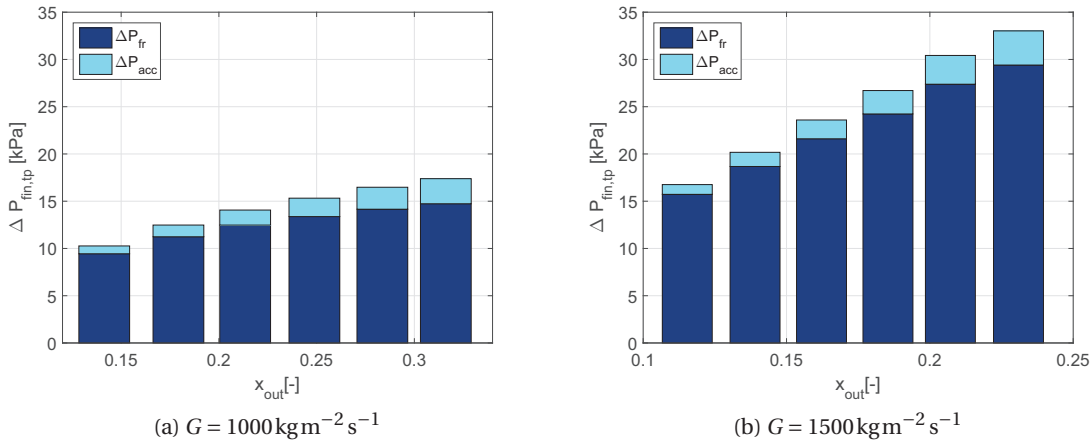


Figure 6.11 – Frictional and accelerational two-phase pressure drop components across versus exit vapor quality for fluid R134a when varying heat flux and constant mass fluxes of (a)  $G = 1000 \text{ kgm}^{-2} \text{ s}^{-1}$  and (b)  $G = 1500 \text{ kgm}^{-2} \text{ s}^{-1}$ . The outlet saturation temperature is 25 °C

For these tests, the accelerational pressure losses  $\Delta P_{acc}$  represent a fraction of about 7–18% of the total two-phase pressure drop over the pin fin array,  $\Delta P_{fin,tp}$ , while the frictional pressure losses  $\Delta P_{fr}$  are about the 82–93%. In general these percentage values vary with the test conditions  $q$  and  $G$ . When the mass flux increases the frictional pressure drop assumes the higher percentage values  $\sim 90 - 93\%$ , whilst when the mass flux is fixed and the heat flux increases as in Fig. 6.11(a)-(b), the accelerational component fraction increases slightly compared to the frictional one. As it is possible to observe in Fig. 6.11(a), when the mass flux is

fixed ( $G = 1000 \text{ kg m}^{-2} \text{ s}^{-1}$ ), the  $\Delta P_{acc}$  represents the 9 – 13% of  $\Delta P_{fin,tp}$  at lower outlet vapor qualities  $x_{out}$ , whilst it grows up to a fraction of 15 – 18% of  $\Delta P_{fin,tp}$  at higher values of  $x_{out}$ , i.e. when the heat flux increases.

#### 6.3.4 Heat transfer coefficient

The heat transfer coefficient quantifies the heat removal capability of the micro-evaporator. As already presented in the chapter of the data reduction (Chapter 2), two different heat transfer coefficients can be defined for micro-pin fin heat sinks: the footprint heat transfer coefficient  $h_{ftp}$ , calculated at the total base area of the channels cross-section and the wall heat transfer coefficient  $h_w$ , calculated on the total surface area of the pin fins in contact with the fluid. These two heat transfer coefficients are calculated locally over the micro-pin fin surface ( $110 \times 110$  values) and subsequently, they are averaged along the widthwise direction in order to obtain a vector of  $1 \times 110$  values along the streamwise direction. Figures 6.12(a)-(b) show an example of the 2D map of the heat transfer coefficient, and the heat transfer coefficient along the streamwise direction at different location of the width. In particular, Fig. 6.12(b) depicts the heat transfer coefficient averaged along the widthwise direction, which will be considered in this section, the heat transfer coefficient along the centerline of the test section and two nearby the lateral sides of the pin fin area ( $y/L = 100$  and  $y/L = 10$ ). Some edge effects due to heat spreading the non-uniform heat flux at the footprint (calculated from the 3D inverse heat conduction) are visible in Figs. 6.12(a), but they are quite limited in magnitude (see Fig. 6.12(b)), underlying a uniform flow distribution (no hot spots are visible).

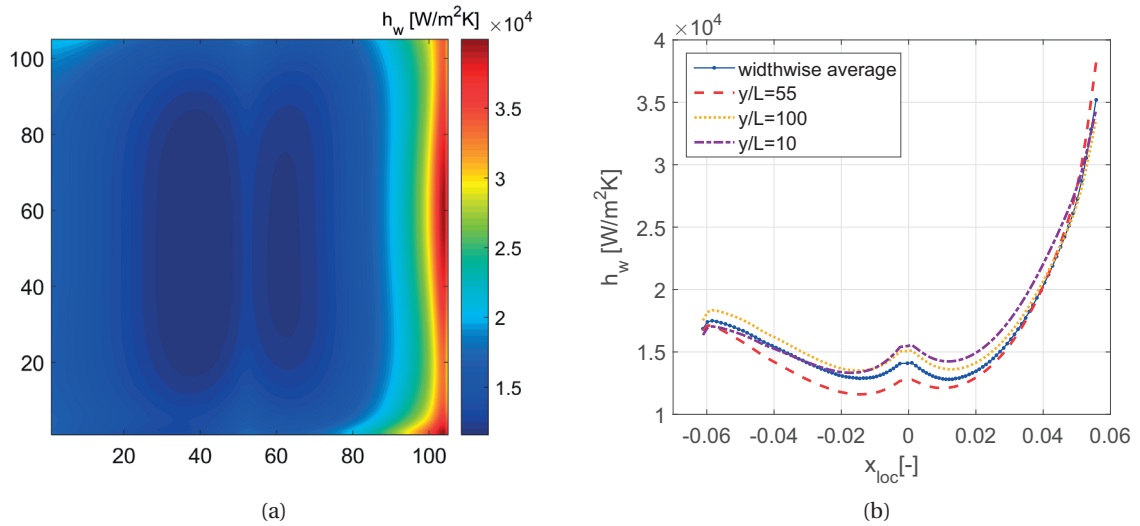


Figure 6.12 – (a) Map of local heat transfer coefficient ( $110 \times 110$  values) covering the micro-pin fin area and (b) streamwise heat transfer coefficient averaged along the widthwise direction, under the test conditions of  $G = 1500 \text{ kg m}^{-2} \text{ s}^{-1}$ ,  $q = 28 \text{ W cm}^{-2}$  and refrigerant R1234ze(E). The outlet saturation temperature is  $25^\circ \text{C}$ .

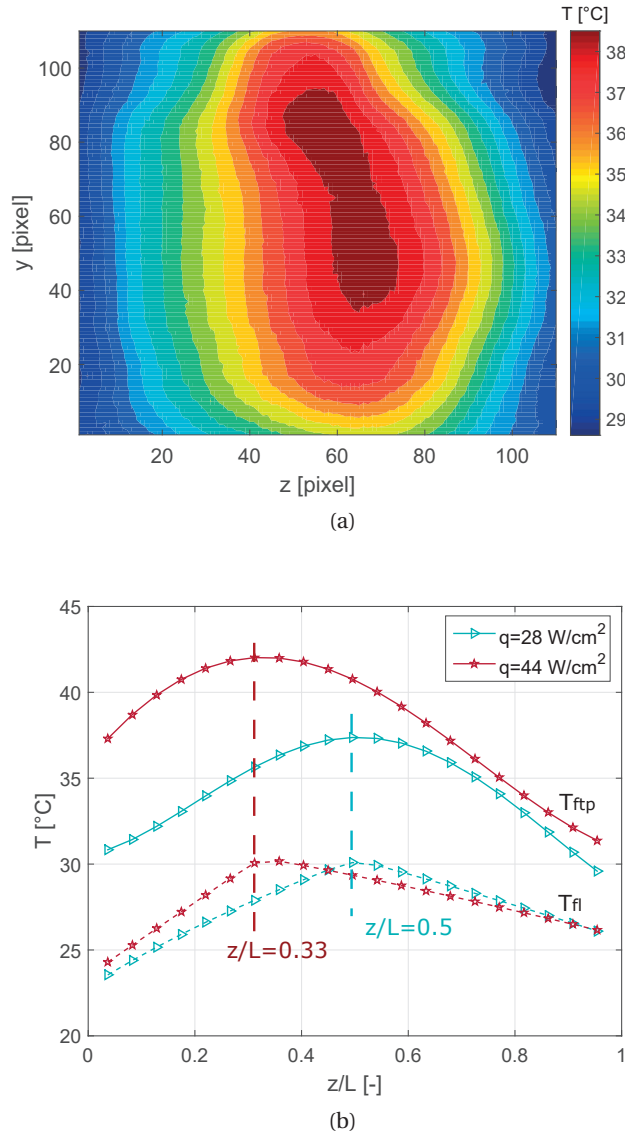


Figure 6.13 – (a) 2D temperature map obtained via the infrared camera for the test conditions  $G = 1750 \text{ kg m}^{-2} \text{ s}^{-1}$  and  $q = 28 \text{ W cm}^{-2}$ . (b) Widthwise averaged values of the footprint and fluid temperatures for  $G = 1750 \text{ kg m}^{-2} \text{ s}^{-1}$  and two selected heat flux values. Fluid is R134a. The outlet saturation temperature is  $25^\circ \text{C}$ .

Detailed heat transfer results for two selected cases with same mass flux  $G = 1750 \text{ kg m}^{-2} \text{ s}^{-1}$  and different heat flux  $q = 28 - 44 \text{ W cm}^{-2}$  are presented in Figs. 6.13 and 6.14. A 2D map of the micro-evaporator base temperature, obtained by means of the IR camera reading for  $q = 28 \text{ W cm}^{-2}$  is illustrated in Fig. 6.13(a). The widthwise averaged profiles of the footprint and fluid temperatures, footprint heat flux, and wall heat transfer coefficient are plotted as a function of the axial coordinate in Fig. 6.13(b), and Fig. 6.14(a)-(b), respectively. The insets in Fig. 6.14(b), representing snapshots of the high speed videos, allow to locate the onset of two-phase flow within the evaporator. Figure 6.13(a)-(b) indicate that, respectively, the base and

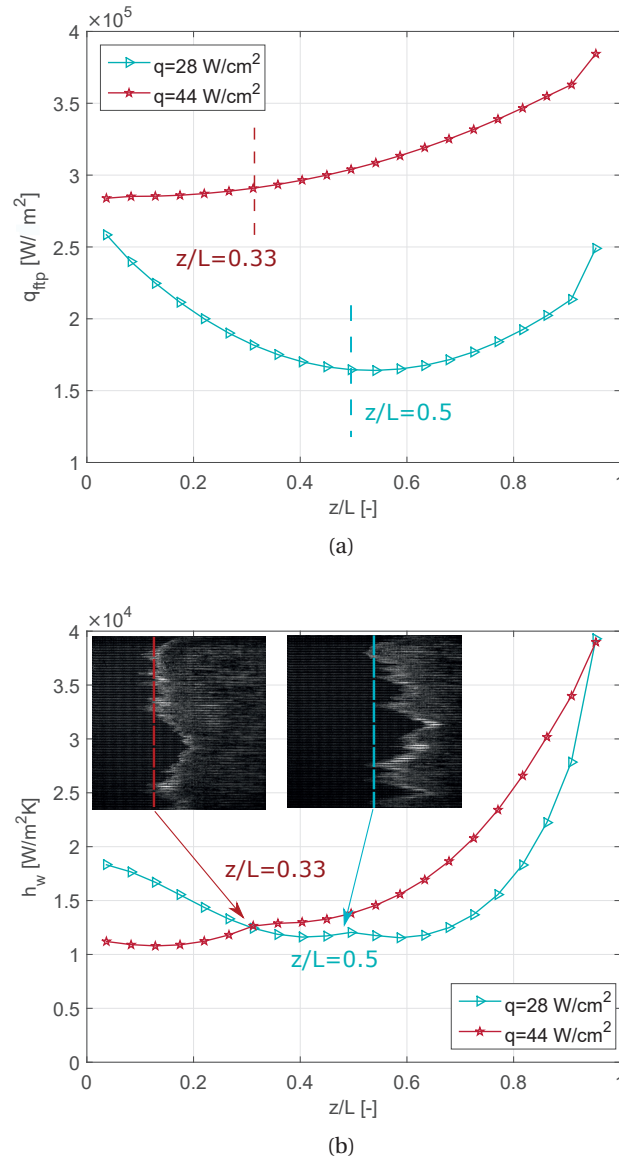


Figure 6.14 – Widthwise averaged values of the (a) footprint heat flux, and (b) heat transfer coefficient along the test section for  $G = 1750 \text{ kg m}^{-2} \text{ s}^{-1}$  and two selected heat flux values. Fluid is R134a. The outlet saturation temperature is  $25^\circ \text{C}$ . The insets in (b) show two image frames from the high-speed videos.

the footprint temperatures grow in the single phase region due to the applied heat, and reach a maximum where the images in the insets in Fig. 6.14(b) reveal the onset of two-phase flow. This happens earlier for  $q = 44 \text{ W cm}^{-2}$ ,  $z/L = 0.33$  compared to  $z/L = 0.5$  for  $q = 28 \text{ W cm}^{-2}$ , due to the higher heat flux and similar inlet liquid temperature. Note that the peak of  $T_{ftp}$  is smooth as a result of lateral heat spreading in the evaporator base and because the two-phase flow does not initiate uniformly along the widthwise direction.

In the two-phase flow region, the footprint temperature drops considerably as the exit of the

test section is approached, due to the higher heat removal capacity of the flow. The fluid temperature follows closely the trend of  $T_{ftp}$ , although its peak at the two-phase transition is sharper due to the data reduction procedure. At the evaporator exit,  $T_{fl}$  reaches a value close to 25°C, which is the temperature set with the LAUDA thermostat, independently of the applied heat flux.

The curves of the footprint heat flux  $q_{ftp}$  displayed in Fig. 6.14(a) indicate that the heat actually transferred to the footprint surface of the evaporator does not distribute uniformly across the heated area. As already showed by Huang and Thome [129], the heat applied at the test section base is directed towards the regions where the fluid temperature is lower, according to the Fourier law. Conversely, less heat is transferred to the region where the highest fluid temperatures are observed, i.e. at the boiling inception location. When the heat applied is low (or the mass flux is high), so that boiling initiates at about  $z/L = 0.5$ , the footprint heat flux  $q_{ftp}$  exhibits maximum values at the inlet and outlet ends of the flow area, where the fluid is cooler. This motivates the convex shape of  $q_{ftp}$  for  $q = 28 \text{ W cm}^{-2}$  in Fig. 6.14(a). When the heat load is high (or the mass flux is low), so that the boiling point moves closer to  $z = 0$ ,  $q_{ftp}$  has its lowest value nearby the inlet, as observed in Fig. 6.14(a) for  $q = 44 \text{ W cm}^{-2}$ . Afterwards, the footprint heat flux increases monotonically as the fluid temperature reduces along the streamwise direction.

The heat transfer coefficient trends presented in Fig. 6.14(b) reflect the behavior of the footprint to fluid temperature difference,  $T_{ftp} - T_{fl}$ , and of the footprint heat flux, according to Eq. (4.16) (the fin efficiency is approximately constant across the test section with values in the range from 91 – 93 %). In the single phase region,  $h_w$  is larger for  $q = 28 \text{ W cm}^{-2}$  due to the convex shape of  $q_{ftp}$  which yields relatively high values of the heat flux at the beginning of the flow area. The descending trend of  $h_w$  versus  $z$  for  $q = 28 \text{ W cm}^{-2}$  can be ascribed to the decreasing values of  $q_{ftp}$  as the fluid temperature is growing. The slightly descending trend of  $h_w$  detected right after the onset of two-phase flow for  $q = 28 \text{ W cm}^{-2}$  may be attributed to the steep reduction of  $T_{fl}$  as opposed to the milder reduction of  $T_{ftp}$ , as observed in Fig. 6.13(b), so that the local temperature difference  $T_{ftp} - T_{fl}$  slightly increases. This descending trend of  $h_w$  at  $x \gtrsim 0$  disappears as  $q$  is raised or  $G$  is lowered (see Fig. 6.14(b)) because the reduction of  $T_{ftp}$  becomes steeper. Such an effect can be related to a quick transition from slug to annular flow pattern (as  $dx/dz \sim q/G$ ), which greatly enhances heat transfer and therefore the evaporator cooling performance. As the two-phase flow develops towards the end of the test section, the heat transfer coefficients displayed in Fig. 6.14(b) grow rapidly to magnitudes which are two to four times larger than those measured in the single phase region. This can be attributed to the presence of very elongated bubbles or annular flow, which trap a thin film of liquid against the channel wall which thins along  $z$  as an effect of evaporation, thus promoting higher heat transfer [90, 93]. The heat transfer coefficient averaged across the entire footprint area is  $\overline{h_w} = 16.2 \text{ kW m}^{-2} \text{ K}^{-1}$  and  $\overline{h_w} = 17.7 \text{ kW m}^{-2} \text{ K}^{-1}$  for, respectively,  $q = 28 \text{ W cm}^{-2}$  and  $q = 44 \text{ W cm}^{-2}$ , with an enhancement of about 10% when the heat flux is increased. This is due to: (i) larger area covered by the two-phase flow, and (ii) larger vapor qualities achieved which promote thinning of the liquid film. The heat transfer coefficient versus vapor quality

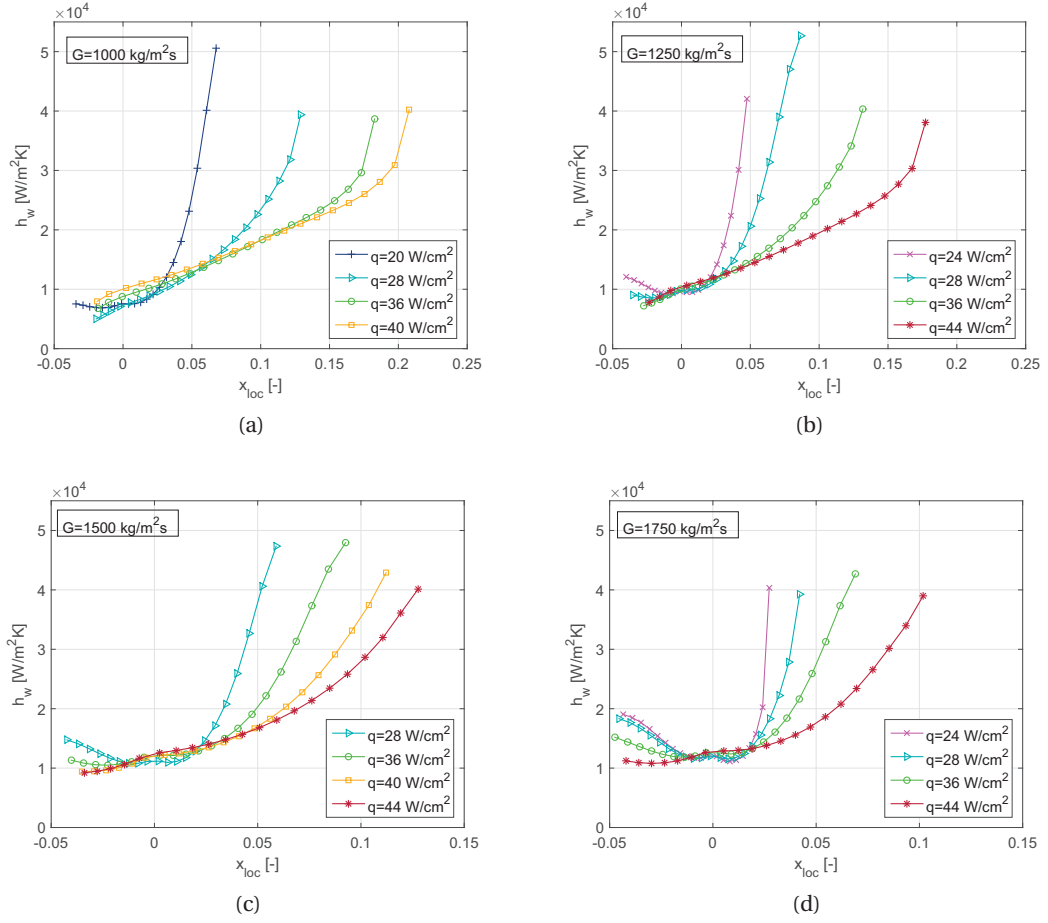


Figure 6.15 – Two-phase heat transfer coefficient versus local vapor quality for fluid R134a at different values of mass flux and heat flux. The outlet saturation temperature is 25°C.

for different values of the heat flux are displayed in Fig. 6.15, where each subfigure refers to a specific mass flux value. In the single phase zone, the heat transfer coefficient ranges from about  $h_w = 5 \text{ kW m}^{-2} \text{ K}^{-1}$  to  $20 \text{ kW m}^{-2} \text{ K}^{-1}$  when increasing the mass flux. This happens because: (i) the boiling location in the evaporator moves farther from  $z = 0$ , so that  $q_{ftp}$  increases at the evaporator entrance as observed in Fig. 6.13(b), thus yielding larger  $h_w$ ; (ii) the single phase flow is developing hydrodynamically, so that  $Nu \sim Re^{1/2}$  [130].

The two-phase heat transfer coefficient exhibits trends which grow rapidly with  $x$ , up to magnitudes of  $h_w = 40 - 50 \text{ kW m}^{-2} \text{ K}^{-1}$ . The rise of  $h_w$  with  $x$  is less steep as the heat load is raised because larger vapor qualities are achieved. This is an effect of the  $x - h_w$  representation. When plotted as a function of  $z$  (figures not included in order to preserve compactness), the heat transfer coefficient trends for different  $q$  are similar to those presented in Fig. 6.13(c), with larger  $h_w$  for higher  $q$  in the two-phase region due to the flow patterns development. The spatial average of  $h_w$  across the entire heated area ranges from values of about  $\overline{h_w} =$

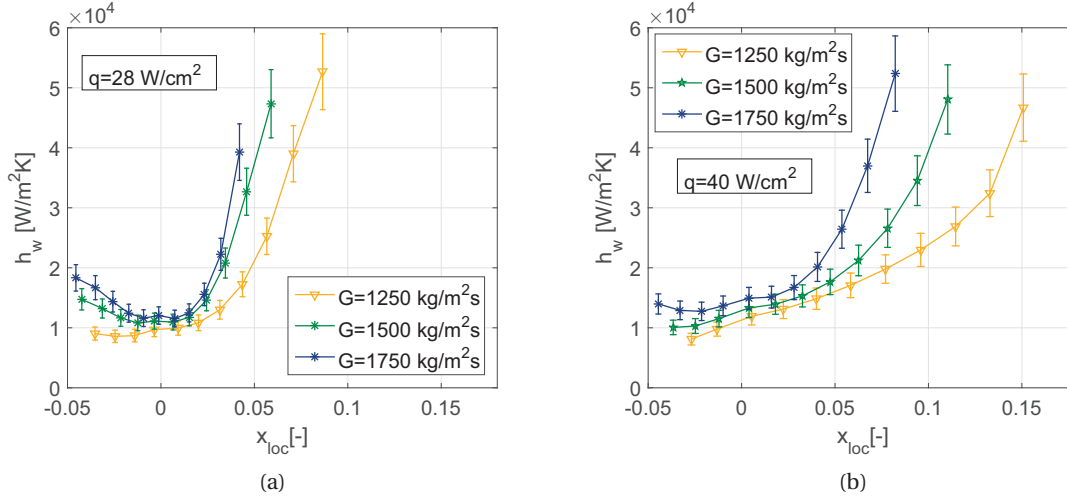


Figure 6.16 – Two-phase heat transfer coefficient versus local vapor quality when varying the mass flux with error bars of 12 %. Fluid is R134a. The outlet saturation temperature is 25 °C.

$14 \text{ kW m}^{-2} \text{ K}^{-1}$ , measured at  $q = 20 - 24 \text{ W cm}^{-2}$ , to  $\overline{h_w} = 19 \text{ kW m}^{-2} \text{ K}^{-1}$  at  $q = 40 - 44 \text{ W cm}^{-2}$ . No clear dependency on the mass flux is observed, thus suggesting that this does not have a significant impact on the heat transfer performance.

Plots of the heat transfer coefficient  $h_w$  as a function of the vapor quality, for different values of the mass flux, are presented in Fig. 6.16 with the error bars of 12 % (equal to the calculated accuracy). The heat transfer trends in the single phase region are in line with the previous observations. Larger values of  $G$  increase the heat transfer performance of the single phase developing flow and retard the formation of two-phase flow thus yielding larger values of  $q_{f,tp}$  towards the entrance in the heated section. In the two-phase flow zone,  $h_w$  grows more steeply with  $x$  for larger  $G$  as lower values of the vapor quality are achieved. When plotted versus the axial coordinate (so that the curves for higher  $G$  stretch horizontally towards those for lower  $G$ ), the  $h_w$  curves show very similar trends and magnitudes. The average heat transfer coefficient varies in the range  $\overline{h_w} = 16 - 18 \text{ kW m}^{-2} \text{ K}^{-1}$  at  $q = 20 \text{ W cm}^{-2}$ , Fig. 6.16(a), and  $\overline{h_w} = 20 - 21 \text{ kW m}^{-2} \text{ K}^{-1}$  at  $q = 40 \text{ W cm}^{-2}$ , Fig. 6.16(b), with a little tendency to increase as  $G$  is reduced as the test section area occupied by the two-phase flow becomes wider. This confirms the weak dependency of the heat transfer performance on the mass flux that emerged already from the data illustrated in Fig. 6.15.

### 6.3.5 Comparison between R134a and R1234ze(E)

In this section, a comparison of pressure drop and heat transfer coefficient between the refrigerants R134a and R1234ze(E) is presented. R134a is a high pressure refrigerant with an ODP of 0 and a GWP of 1360. R134a is one of the most used fluids in the household and automotive refrigeration, and a potential candidate for microelectronics cooling. The fluid



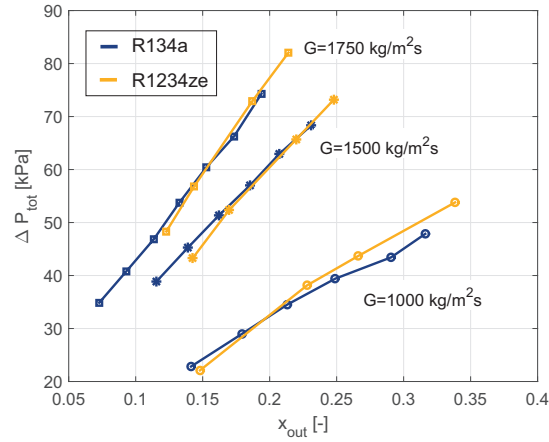


Figure 6.17 – Two-phase pressure drop versus outlet vapor quality. Comparison of refrigerants R134a and R1234ze(E). The outlet saturation temperature is 25 °C.

R1234ze(E) is an isomer of tetrafluoropropene, it has a ODP (Ozone Depletion Potential) of 0 and a GWP (Global Warming Potential) of 7, and is therefore characterized by a much lower environmental impact than R134a. R1234ze(E) was developed as a potential replacement of R134a, in particular for applications where a medium pressure refrigerant can be efficiently employed and where a low GWP fluid is needed or desired. Within this context, it is of industrial and environmental interest to compare the thermal and hydraulic performances of the micro-evaporator when the two fluids are utilized. The two refrigerants showed a very large range of stable operating conditions when varying the mass flux and heat flux, as discussed in Section 6.3.1. This is a very positive feature for the practical application of these fluids. The total pressure drop measured for the two fluids is presented in Fig. 6.17 as a function of the exit vapor quality, for different values of the mass flux. The fluids show very similar values of the pressure drop, with the R1234ze(E) exhibiting slightly larger values at low  $G$  and high exit vapor quality (i.e. high  $q$ ). Therefore, it can be concluded that the pumping power necessary to circulate the fluid in the micro-evaporator is approximately the same for both R134a and R1234ze(E). The heat transfer performance of the fluids are compared in Fig. 6.18 for selected values of  $q$  and  $G$ . The fluids exhibit the same  $h_w$  magnitude in the negative vapor quality region (single phase zone). This is expected as the fluids properties yield similar values of the liquid Prandtl and Reynolds numbers, thus leading to similar heat transfer performance in the single phase developing region, where  $Nu \sim Re^{1/2} Pr^{1/3}$ . In the saturated flow region ( $x > 0$ ), R134a gives slightly larger values of the heat transfer coefficient, in particular in the high vapor quality range,  $x > 0.05 - 0.1$ , i.e. when the flow is in the annular flow regime. In annular flow, the governing heat transfer mechanism in small channels is heat conduction across the thin evaporating liquid film at the wall, and the heat transfer coefficient has been observed to scale as  $h_w \sim k_l \delta^{-0.1} Pr^{0.5}$  [93], where  $k_l$  is the thermal conductivity of the liquid and  $\delta$  is the liquid film thickness. The fluids have about the same value of the Prandtl number, while simulations run with the boiling heat transfer model of

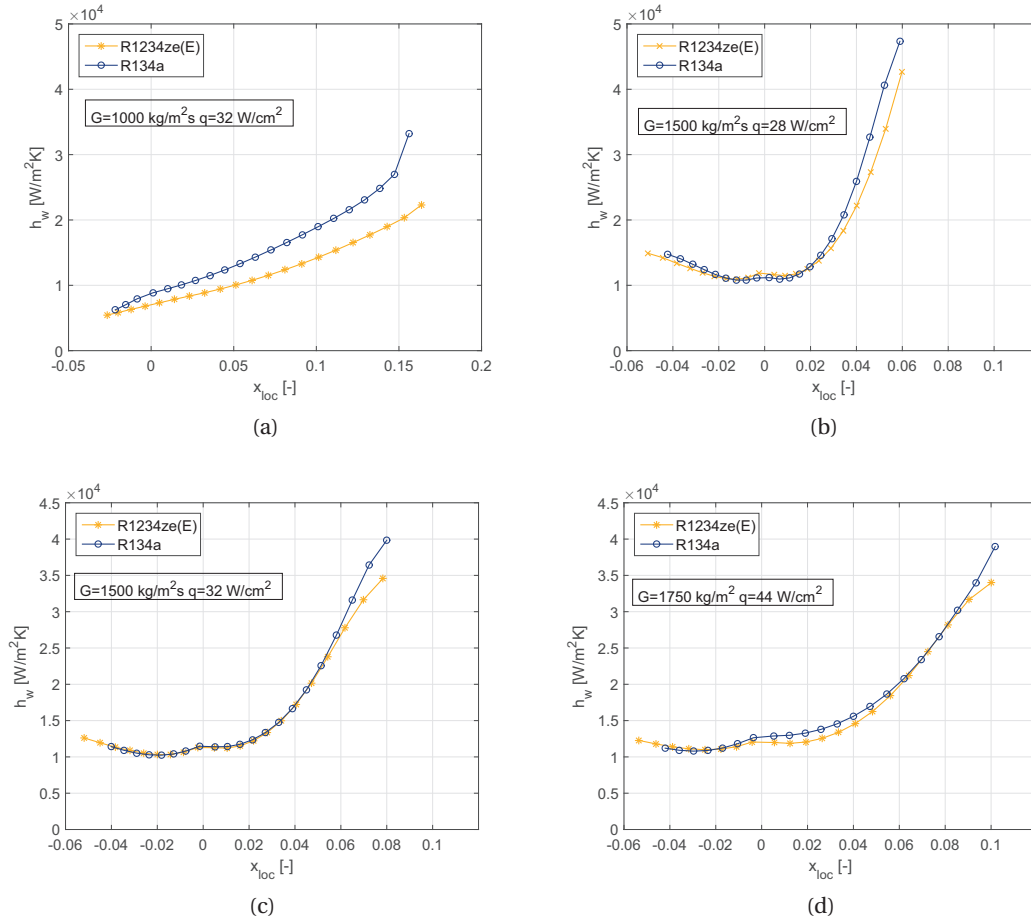


Figure 6.18 – Two-phase heat transfer coefficient versus local vapor quality. The outlet saturation temperature is  $25^\circ\text{C}$ . Comparison of refrigerants R134a and R1234ze(E).

[93] yield similar liquid film thickness values for R134a and R1234ze(E) in the present flow conditions. However, R134a has a higher liquid thermal conductivity,  $k_l = 0.081 \text{ W m}^{-1} \text{ K}^{-1}$  versus  $k_l = 0.074 \text{ W m}^{-1} \text{ K}^{-1}$  of R1234ze(E),  $T_{sat} = 25^\circ\text{C}$ . This enhances heat conduction across the liquid film, thus motivating the better performance of R134a observed in Fig. 6.18. The average reduction of the heat transfer coefficient when using R1234ze(E) in place of R134a, calculated for the plots of Fig. 6.18, is 11.3%.

## 6.4 Conclusions

This chapter presented an experimental investigation of single and two-phase flow with the fluids R245fa, R134a and R1234ze(E). A fine resolution infrared temperature measurement technique was coupled with high-speed flow visualization in order to analyze the interrelation between time-dependent fluid mechanics and heat transfer. Operational maps, pressure drop, and heat transfer performances were studied under a wide range of operating conditions.

Time-dependent features of the flow were analyzed by processing the high-speed videos and temperature signals. The major outcomes of this chapter can be drawn as follows:

1. R134a exhibits a very stable flow boiling behavior under a wide range of flow conditions,  $q = 24 - 40 \text{ W cm}^{-2}$  and  $G = 1000 - 1750 \text{ kg m}^{-2} \text{ s}^{-1}$ . Larger values of the heat flux are possible, provided that the mass flux is sufficiently high to prevent vapor back flow. In these conditions, temperature oscillations of the micro-evaporator surface in time are minimal, on the order of  $0.1 - 0.3 \text{ K}$ . This makes R134a an optimal fluid for on-chip cooling, since high amplitude temperature oscillations may limit the life of the electronic components.
2. A Fourier analysis of the temperature signal emphasized the presence of oscillation frequencies of magnitude  $14 - 22 \text{ Hz}$ , increasing with both heat and mass flux. A time-strip analysis of the high-speed video revealed that this behavior was related to the cyclical activation and deactivation of nucleation sites, from which "swarms" of bubbles are periodically generated. The duration of the site inactivity period is comparable to the waiting time for the channel wall to reach nucleation superheat conditions.
3. The high-speed video images highlight the presence of single phase flow at the entrance of the heated area, followed by a very dynamic zone where small and intermediate size bubbles are present, while a steady elongated bubble and annular flow region develops towards the end of the heated area.
4. The micro-evaporator pressure drop increases with both heat and mass flux. The maximum total pressure drop, including the drop across the inlet and outlet manifolds, is about  $75 \text{ kPa}$  at  $G = 1750 \text{ kg m}^{-2} \text{ s}^{-1}$  and  $q = 44 \text{ W cm}^{-2}$ .
5. An insight on the local trends and magnitudes of the heat transfer coefficient is provided by the analysis of the local footprint heat flux and temperature extracted from the 3D heat conduction model. In the two-phase region, a strong influence of the vapor quality, and hence of the flow patterns, is detected. Very high values of  $h_w$  are achieved as the flow transitions to annular flow, with  $h_w$  as high as  $50 \text{ kW m}^{-2} \text{ K}^{-1}$  in the proximity of the flow area exit. The average heat transfer performance  $\overline{h_w}$  calculated across the entire heated area enhances significantly with the heat flux, as the two-phase flow occupies a larger area, while the impact of the mass flux is weak. This signifies that a relatively low fluid pumping power can already dissipate a substantial amount of heat.
6. The refrigerant R1234ze(E), which represents an immediate/future *green* replacement for R134a, shows a wide range of stable flow conditions and pressure drop values similar to those measured for R134a. The heat transfer performance is only slightly inferior (about 10%), thus suggesting that R1234ze(E) is a promising fluid for on-chip two-phase cooling. Conversely, R245fa presented a very unstable behaviour during flow boiling tests and therefore it would not be an ideal replacement for R134a.



## 7 Flow pattern-based boiling heat transfer model

### 7.1 Introduction

The present chapter describes the last step of this study, which is the development of a new flow pattern-based prediction method for flow boiling heat transfer in a micro-pin fin evaporator. The heat transfer mechanisms associated with slug flow and annular flow regimes are inferred by updating the widely used three-zone slug flow model of Thome et al. [90, 91] and the algebraic turbulence annular flow model of Cioncolini and Thome [93], respectively. In order to predict the trends in the heat transfer coefficient versus the vapor quality, these two models are linearly combined by utilizing a smoothing function acting on a buffer zone centered in the slug-to-annular flow transition region, whose location is here obtained by means of a new method based on flow visualization analysis and time-strip technique of the available experimental high speed videos. The model is compared to a wide experimental database (7219 points), which covers three refrigerants, R134a, R236fa and R1234ze(E), three outlet saturation temperatures (25, 30, and 35 °C), mass fluxes varying from 500 to 2000 kg m<sup>-2</sup> s<sup>-1</sup> and heat fluxes from 20 to 44 W cm<sup>-2</sup>. The database is also compared to competing prediction methods available in the literature.

The results of this chapter were published in:

C. Falsetti, M. Magnini, and J.R. Thome, *A new flow pattern-based boiling heat transfer model for micro-pin fin evaporators*, Int. J. of Heat and Mass Transfer, under review, 2018.

### 7.2 Presentation of the model

The goal of the present study is to develop a prediction method for the local heat transfer coefficient in the saturated flow boiling regime ( $x > 0$ ). The structure of the new flow pattern-based model is illustrated in Fig. 7.1(a) while the development of flow regimes along a channel between two parallel lines of micro-pin fins is schematically depicted in Fig. 7.1(b). The flow is moving from left to the right. After the onset of two-phase flow (at  $x = 0$ ), the nucleating

(or flashing) bubbles quickly coalesce due to their expansion in the micro-scale channels, creating an elongated bubble/slug flow regime, indicated as "SF" in Fig. 7.1(b). In this region, a modified version of the original three zone model [90, 91], originally developed for flow in circular microchannels, is implemented to account for the peculiar features of the micro-pin fin configuration and to predict the experimental heat transfer coefficient associated with the slug flow regime, which is plotted versus vapor quality and indicated as  $h_{SF}$  in Fig. 7.1(a). Since the bubbly flow regime is very short, it is ignored here and it is incorporated into the slug flow model. When the vapor quality is above the flow transition value, here identified as  $x = x_{SF-AF}$ , the elongated bubbles are supposed to be very long such that an annular flow regime is formed. The annular flow is composed of a vapor core, flowing along the center of the channels, surrounded by a liquid film in contact with the top and bottom walls and with the lateral pin fin surfaces, see Fig. 7.1(b). The liquid films on the pin fin walls tend to merge at the back side of the pin fins and it is assumed that the liquid creates a liquid-bridge between two consequent pin fins, as observed in a flow visualization based study of Krishnamurthy and Peles [131], thus forming an "annular" flow on the pin fin array. The liquid film on the base area between the fins also flows as a film of this annular flow. Therefore, in this region, i.e. when  $x \geq x_{SF-AF}$  and indicated as "AF", the experimental heat transfer coefficients are predicted by a modified version of the annular flow model developed by Cioncolini and Thome [93] for circular channels, depicted as  $h_{AF}$  in Fig. 7.1(a). As it is possible to observe in Fig. 7.1(a), the two modified models,  $h_{SF}$  and  $h_{AF}$ , which are plotted over the entire vapor quality range for visualization purpose only, yield predictions that do not necessarily match up in value at the transition point from slug-to-annular flow. Hence, they need to be merged by a smoothing function acting in a buffer zone, which is centered at  $x = x_{SF-AF}$  and has an extension of  $2\Delta x$ , indicated by the yellow region in Fig. 7.1(a). The values of  $x_{SF-AF}$  and  $\Delta x$ , which define the central location and the half width of the buffer zone respectively, will be determined and then predicted by means of a flow visualization analysis, which will be presented in the following section. A smoothing function  $\Sigma(x)$  is utilized to combine the model predictions in the buffer zone as follows:

$$\Sigma(x) = \begin{cases} 0, & x \leq x_{SF-AF} - \Delta x \\ 1, & x \geq x_{SF-AF} + \Delta x \\ 0 < \Sigma(x) < 1, & x_{SF-AF} - \Delta x < x < x_{SF-AF} + \Delta x \end{cases}$$

Two different expressions of the smoothing function  $\Sigma(x)$ , linear and hyperbolic, have been implemented in the present study, as it will be described in Section 7.2.4, to see which is most realistic based on a comparison to the heat transfer data trends. The final structure of the predicted local heat transfer coefficient, indicated as  $h_{pred}$  in Fig. 7.1(a) is summarized by the expression below:

$$h_{pred}(x) = h_{SF}(x) \cdot (1 - \Sigma(x)) + h_{AF}(x) \cdot \Sigma(x) \quad (7.1)$$

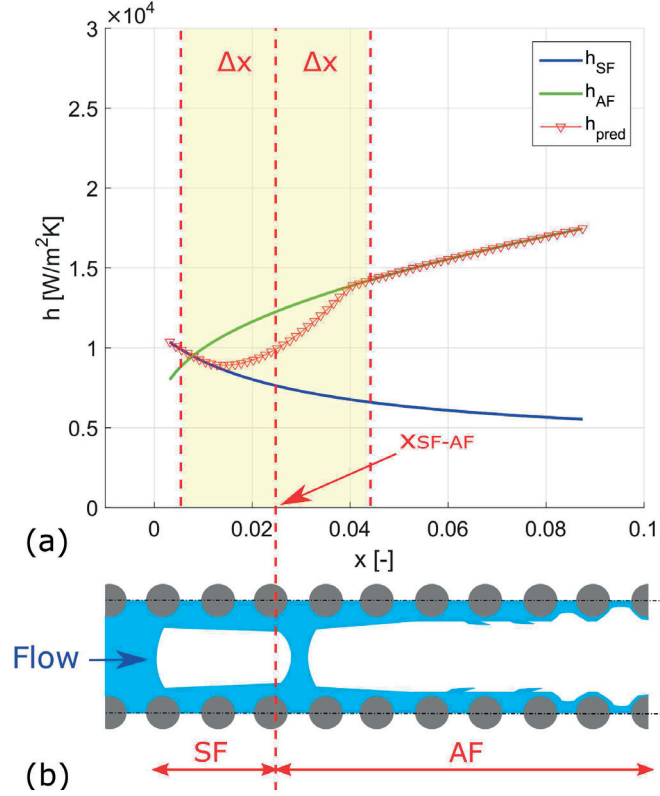


Figure 7.1 – (a) Working principle of the new flow pattern-based boiling heat transfer prediction model. A heat transfer prediction for slug flow ( $h_{SF}$ ) is used when  $0 < x < x_{SF-AF} - \Delta x$ , and another one for annular flow ( $h_{AF}$ ) is used when  $x \geq x_{SF-AF} + \Delta x$ . In the flow transition region, a smoothing function is used to ensure a smooth transition between  $h_{SF}$  and  $h_{AF}$ . (b) Top view schematic of flow regimes development along a channel between two parallel lines of micro-pin fins.

Below, the flow visualization analysis utilized to obtain the values of  $x_{SF-AF}$  and  $\Delta x$  will be presented in Section 7.2.1 whilst the slug and annular flow models, and the smoothing function will be described respectively in Sections 7.2.2, 7.2.3, 7.2.4.

### 7.2.1 Slug-to-annular flow transition

The slug-to-annular flow transition value  $x_{SF-AF}$  is obtained here by means of flow visualization and time-strip techniques, starting from the high-speed camera videos of in-house experimental data [40, 132, 41]. Figure 7.2(a) shows a high-speed camera screenshot of the micro-pin fin array during a R1234ze(E) flow boiling test and Fig. 7.2(b) depicts the plot of the 2D intensity gray signal under the same operating conditions. The flow is moving from left to the right, along the  $z$ -direction, for stable conditions, i.e. the interface maintains a stable behaviour in time and the temperature fluctuation amplitude is smaller than 0.1 K. As already described in the previous chapter, the dark zone on the left side nearby the inlet



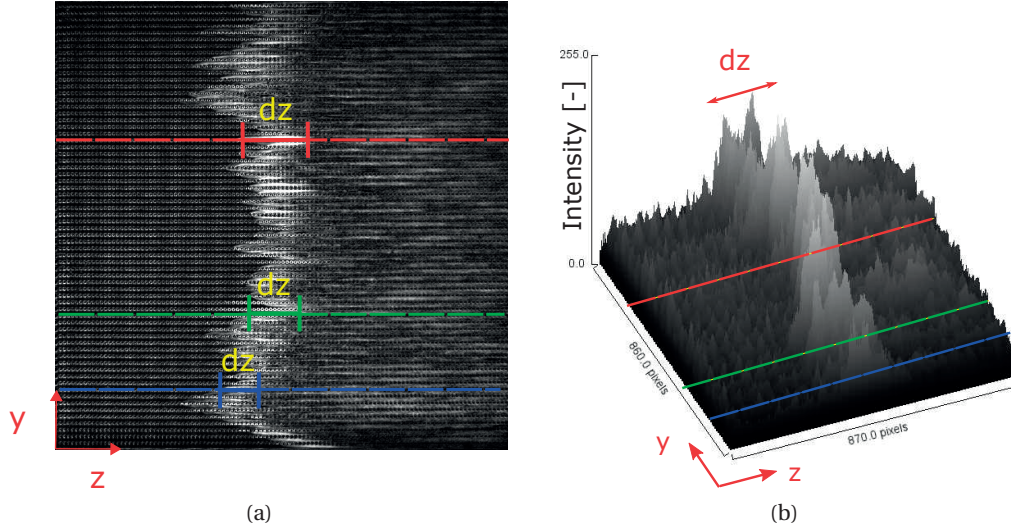


Figure 7.2 – (a) High-speed camera screenshot and (b) reconstructed 2D gray intensity plot for a boiling test with conditions:  $q = 36 \text{ W cm}^{-2}$ ,  $G = 1500 \text{ kg m}^{-2} \text{ s}^{-1}$ , R1234ze(E) and  $T_{sat} = 35^\circ \text{C}$ . Flow is from left to right. The length of the slug flow region  $dz$ , is measured from the onset of two-phase flow to the slug-to-annular flow transition.

of the test section indicates single phase flow. The following bright jets and the white area, identified with  $dz$  in Fig. 7.2(a), are associated with short and intermediate length bubbles (slug flow regime), and the gray area afterwards is the liquid films surrounding the vapor core of the very long bubbles and annular flow. The width of the bubbly/slug flow region, identified as  $dz$ , is utilized here to evaluate where the transition to annular flow occurs,  $z_{SF-AF}$ . Despite the stable behaviour of the flow, the onset of two-phase flow and the extent of the slug flow region,  $dz$ , change slightly from one channel to another, as it is indicated by the three horizontal coloured lines in Fig. 7.2(a). This is also observable in Fig. 7.2(b), where the peaks of the light intensity signal are not uniform along the widthwise direction  $y$ , showing different heights and widths. In order to better visualize and extrapolate the length of the bubbly/slug flow zone  $dz$ , and thus identify the location of the slug-to-annular flow transition  $z_{SF-AF}$ , the high-speed videos were processed using the time-strip technique [113, 41]. The one-dimensional light intensity along a given channel is extracted and plotted as a function of time to obtain the development in time of the slug flow regime for every channel, as shown in Fig. 7.3(a). Starting from the time-strip result of Fig. 7.3(a), the light intensity signal is plotted for every time instant, see Fig. 7.3(b). The intensity signal has very low values in the single phase zone, from  $z/L = 0$  to  $z/L \approx 0.43$ , where  $L = 1 \text{ cm}$  is the total length of the pin fin area. It suddenly increases in intensity where the two-phase flow starts ( $z = z_{onset}$ ), assuming high values in the plateau zone  $dz$  until the location  $z = z_{SF-AF}$ , at which the elongated bubbles start to coalesce and the signal abruptly decreases. From the high-speed video images,  $dz$  is



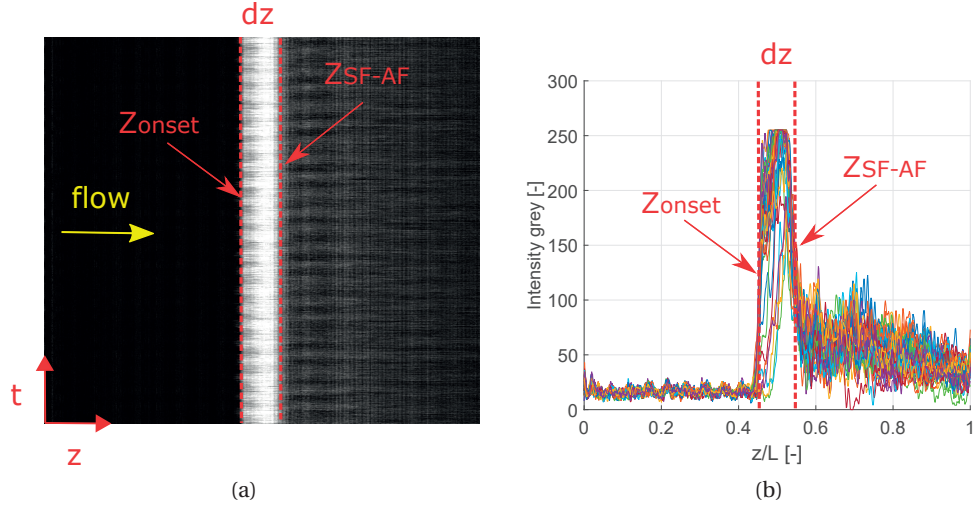


Figure 7.3 – (a) Time strip analysis of the light intensity along one single channel at the center of the test section. The slug flow region length is  $dz$ . (b) Grey intensity signal along the length of the test section of the time-strip image for the same channel, at different time instants. The peak in the intensity signal evidences the extent of the bubbly region, which starts from the onset of two-phase flow  $z_{onset}$  until the slug-to-annular flow transition  $z_{SF-AF}$ . Test conditions are:  $q = 36 \text{ W cm}^{-2}$ ,  $G = 1500 \text{ kg m}^{-2} \text{ s}^{-1}$ , R1234ze(E) and  $T_{sat} = 35^\circ \text{C}$ .

evaluated as:

$$dz = z_{SF-AF} - z_{onset} \quad (7.2)$$

and it represents an average value across the entire width of the test section. Once the location  $z_{SF-AF}$  is known, the corresponding vapor quality change is obtained with an energy balance over the evaporator width:

$$dx = \frac{q dz}{G h_{lv} H} \quad (7.3)$$

The slug-to-annular flow transition vapor quality,  $x_{SF-AF}$ , is obtained from Eq. (7.3) assuming that the value of  $x_{onset}$  is equal to zero at  $z = z_{onset}$ :

$$dx = x_{SF-AF} - x_{onset}, \quad x_{onset} = 0 \quad (7.4)$$

The results of this procedure are shown in Fig. 7.4 for several test conditions for changing heat flux, mass flux and refrigerant. The values of  $x_{SF-AF}$  do not show a strong dependency, neither on the refrigerant or on test conditions. Therefore, an average and fixed value equal to  $x_{SF-AF} = 0.025$  (red horizontal line in Fig. 7.4) is extracted and used in the current model as the slug-to-annular flow transition. It is worth noting that some assumptions are made in the procedure to obtain the value of  $x_{SF-AF}$ : (i) uniform heat flux  $q$  over the entire pin fin array is considered, (ii) the vapor quality at the onset of two-phase flow is assumed to be  $x_{onset} = 0$ ,

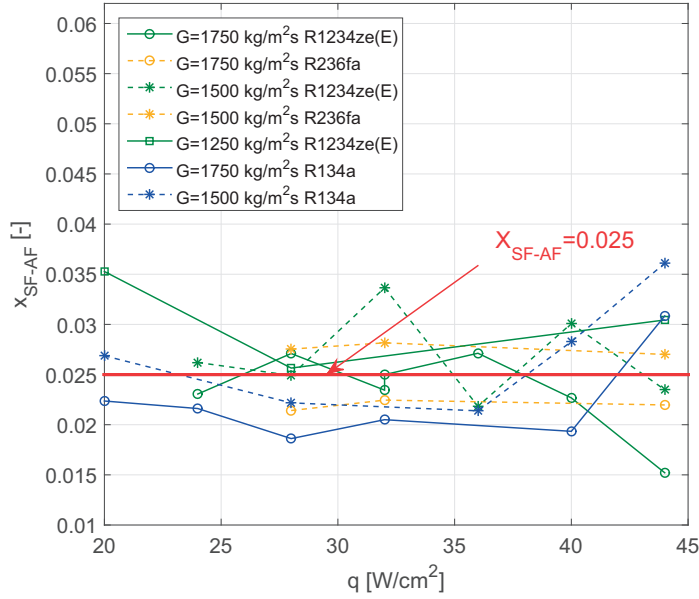


Figure 7.4 – Slug-to-annular flow transition vapor quality value  $x_{SF-AF}$  under different test conditions. The horizontal red line indicates the mean value obtained from averaging the points in the plot,  $x_{SF-AF} = 0.025$ .

and (iii) only data for  $G \geq 1250 \text{ kg m}^{-2} \text{ s}^{-1}$  are utilized, as the intensity signal for the tests with  $G \leq 1000 \text{ kg m}^{-2} \text{ s}^{-1}$  did not show a clear transition from the slug to the annular flow regimes. In order to account for the variability of the  $x_{SF-AF}$  results related to the assumptions outlined above, and for the standard deviation of the values of  $dz$  calculated in different channels, an extension of the buffer zone of  $\Delta x = 0.02$  is considered.

Previous experimental works on microchannel flow boiling proposed different methods to predict the slug-to-annular flow vapor quality transition value  $x_{SF-AF}$ . These are utilized here for comparison purposes. Costa-Patry and Thome [97] identified the diabatic slug-to-annular flow transition as the vapor quality corresponding to the local minimum in the heat transfer coefficient curves versus  $x$ . The obtained local minimum was then correlated as a function of the liquid to vapor density ratio, Boiling number, and Confinement number. The resulting transition value obtained with their method for much larger sized microchannels, averaged for the present conditions, is  $x_{SF-AF} = 0.105$ . Huang and Thome [99] modified the coefficients to fit the correlation of Costa-Patry and Thome [97] to their experimental data, giving  $x_{SF-AF} = 0.08$  when applied to the current data. Ong and Thome [102] detected the transition by optical means and flow visualization techniques and developed a correlation as a function of the fluid properties, vapor Reynolds number, liquid Weber number, and Confinement number, which gives the result of  $x_{SF-AF} = 0.021$  when applied to the current database. This value is close to the one obtained by the present analysis, underlying that flow visualization may be a more reliable tool to detect flow pattern transitions, than indirect

methods based on heat transfer data reduction.

### 7.2.2 Slug flow model

In the region between the onset of two-phase flow and the slug-to-annular flow transition,  $0 < x < x_{SF-AF}$ , a modified version of the three-zone model of Thome et al. [90, 91] is applied to predict the heat transfer coefficient associated with the slug flow regime,  $h_{SF}$ .

The original three-zone model was developed to predict the heat transfer coefficient associated to the slug flow regime in circular horizontal microchannels. It was developed and compared to a databank covering seven refrigerants (R-11, R-12, R-113, R-123, R134a, R141 and CO<sub>2</sub>), and channel diameters in the range of 0.77 – 3.1 mm. Within the model the flow is schematized as a cyclic passage of three zones: (i) a saturated liquid slug, (ii) an elongated vapor bubble surrounded by a liquid film in contact with the wall, and (iii) a dry vapor zone which might occur before the arrival of the following liquid slug. Since the dry vapor zone gives a negligible contribution to heat transfer, the heat transfer coefficient in this zone is set to zero here. The overall heat transfer coefficient is evaluated as the average over the bubble generation period,  $\tau = 1/\Omega$ , with  $\Omega$  being the bubble generation frequency, as follows:

$$h_{SF}(z) = \frac{1}{\tau} (t_l h_l(z) + t_f h_f(z)) \quad (7.5)$$

where  $h_l$ ,  $h_f$ , are the heat transfer coefficient of the liquid slug and the evaporating film respectively, and  $t_l$ ,  $t_f$ , are their residence periods. The bubble generation period is given by the sum of the three periods,  $\tau = t_l + t_f + t_{dry}$ , where the film and dry out periods compose the residence time of the vapor,  $t_v = t_f + t_{dry}$ . These residence time periods ( $t_l$ ,  $t_v$ ) and the zone lengths ( $L_l$ ,  $L_v$ ) are calculated assuming that the vapor and liquid travel at the same velocity (homogeneous flow model). The three-zone model heat transfer predictions depend on three key parameters: (i) the dryout film thickness  $\delta_{min}$ , (ii) the liquid film thickness at the bubble nose  $\delta_0$ , and (iii) the bubble frequency  $\Omega$ .

The dryout film thickness is set here for the pin fin array to the value of the micro-evaporator surface roughness,  $\delta_{min} = 40$  nm, measured with optical and mechanical profilers, since previous studies underlined that the three-zone model works best with this choice [119, 133]. The film thickness at the bubble nose  $\delta_0$  is calculated by implementing the method of Magnini and Thome [96]. In their work, the film thickness for circular channel,  $\delta_{0,circ}$ , was set as the minimum among three values:

1. the film thickness for long bubbles traveling at a constant speed,  $\delta_{0,STD}$ ;
2. the film thickness for accelerating bubbles  $\delta_{0,ACC}$ ;
3. the thickness of the viscous boundary layer developing at the wall in the liquid slug between two bubbles  $\delta_{0,VBL}$ .

## Chapter 7. Flow pattern-based boiling heat transfer model

The lowest value is chosen to consider that the liquid film thickness is affected by several factors, as the viscous boundary layer development and the surface tension. Indeed, when the acceleration effect are larger, the viscous boundary layer becomes thinner, yielding to liquid film thickness restriction. The values of  $\delta_{0,STD}$ ,  $\delta_{0,ACC}$  and  $\delta_{0,VBL}$  are obtained by implementing the following correlations:

$$\frac{\delta_{0,STD}}{d_h} = \frac{0.67Ca^{2/3}}{1 + 3.13Ca^{2/3} + 0.504Ca^{0.672}Re^{0.589} - 0.352(CaRe)^{0.629}} \quad (7.6)$$

$$\frac{\delta_{0,ACC}}{d_h} = \frac{0.968Ca^{2/3}Bo_a^{-0.414}}{1 + 4.838Ca^{2/3}Bo_a^{-0.414}} \quad (7.7)$$

$$\frac{\delta_{0,VBL}}{d_h} = \left( \frac{L_l}{d_h Re} \right)^{0.5} \quad (7.8)$$

where Eq. (7.6) and Eq. (7.7) derive from two studies of Han and Shikazono [134, 135] while Eq. (7.8) is from Aussillous and Qu  r   [136]. The capillary number,  $Ca = \mu_l U / \sigma$ , and the Reynolds number,  $Re = \rho_l U d_h / \mu_l$  have been calculated at the bubble nose velocity  $U$ , calculated as the pair velocity assuming homogeneous flow conditions. The acceleration Bond number of Eq. (7.7) is evaluated with the bubble nose acceleration  $A_v$ , as  $Bo_a = \rho_l A_v d_h^2 / \sigma$ . The hydraulic diameter in Eqs. (7.6)-(7.8) is  $d_h = 4A/P$ , where  $A$  is the cross-sectional area and  $P$  the wetted perimeter, referring to the rectangular cross-sectional area of the flow passage. However, as illustrated in Fig. 7.5(a), the cross-sectional area changes along the streamwise direction  $z$ , as its width  $W_{ch}$  varies from a minimum value of  $100 \mu m$  (location indicated by point A) to a maximum value of  $150 \mu m$  (point B). Therefore, to consider the sudden contractions and expansions induced by two consequent pin fins along the flow direction, A and P are based on an average width  $\overline{W}_{ch}$  ( $A = \overline{W}_{ch} H$ ) and  $P = 2(\overline{W}_{ch} + H)$ , which is calculated over the yellow region highlighted in Fig. 7.5(a):

$$\overline{W}_{ch} = \frac{S_z S_y - \pi D^2 / 4}{H} \quad (7.9)$$

For the present geometry Eq. (7.9) yields the value of  $\overline{W}_{ch} = 128.5 \mu m$  (note: this width definition makes the model respond to the size and density of the pin fins in an array). Figure 7.5(b) depicts the average rectangular cross-sectional area considered for the channels: the vapor phase of the elongated bubble occupies the center of the channel, and the surrounding liquid film is considered to be uniformly distributed around the perimeter with a constant thickness  $\delta_0$ . Since Eqs. (7.6)-(7.8) give a radial liquid film thickness  $\delta_{0,circ}$  for a circular channel, this needs to be redistributed to the perimeter of the rectangular flow passage by keeping the same liquid cross-sectional area. Therefore, the liquid film thickness  $\delta_0$  adapted for the rectangular cross-section is calculated by dividing the cross-sectional area occupied by the circular liquid

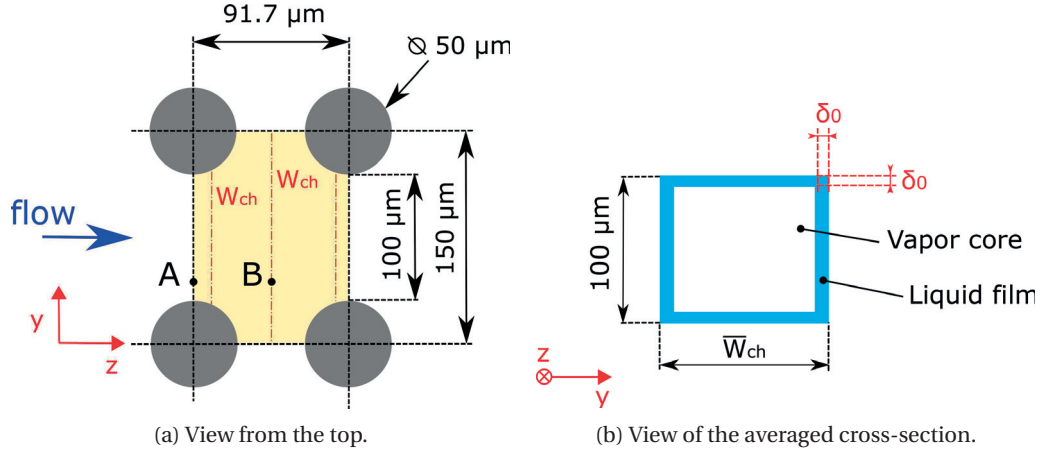


Figure 7.5 – (a) Micro-pin fins configuration. The yellow region is the area considered to calculate an averaged value for the channel width  $\overline{W}_{ch}$ . (b) Averaged cross-section area of the flow passage with a uniform distribution of the liquid-phase around the perimeter with a constant thickness  $\delta$ .

film by the rectangular channel perimeter, resulting in the following expression:

$$\delta_0 = \frac{\pi d_h \delta_{0,circ}}{2(\overline{W}_{ch} + H)} \quad (7.10)$$

From the knowledge of  $\delta_0$ , the heat transfer coefficient averaged within the film zone is estimated by assuming a 1D steady-state heat conduction across the liquid film:

$$h_f(z) = \frac{k_l}{\delta_0 - \delta_{end}} \ln \left( \frac{\delta_0}{\delta_{end}} \right) \quad (7.11)$$

where the liquid film is considered to vary linearly between the value at the bubble nose  $\delta_0$  and the terminal value  $\delta_{end}$  [90].

Addressing now the bubble frequency  $\Omega$ , in the original model it is expressed as a power-law function of the heat flux ( $\propto q^{1.74}$ ) and the reduced pressure ( $\propto P_{red}^{0.87}$ ). Since in the current study direct measurements of the bubble frequency were not feasible, a search of an optimum value of  $\Omega$  was performed following the method proposed by Magnini and Thome [96]: for each experimental measurement belonging to the slug flow regime, an optimum value of the frequency was obtained minimizing the deviation between the experimental ( $h_{exp}$ ) and the predicted ( $h_{pred}$ ) heat transfer coefficients, as:

$$E(\Omega) = \frac{|h_{exp} - h_{pred}(\Omega)|}{h_{exp}} < 10^{-3} \quad (7.12)$$

The initial guess value of the bubble frequency  $\Omega$  is taken from the empirical correlation utilized in the original model [91]. A statistical analysis of the identified values of  $\Omega$  revealed

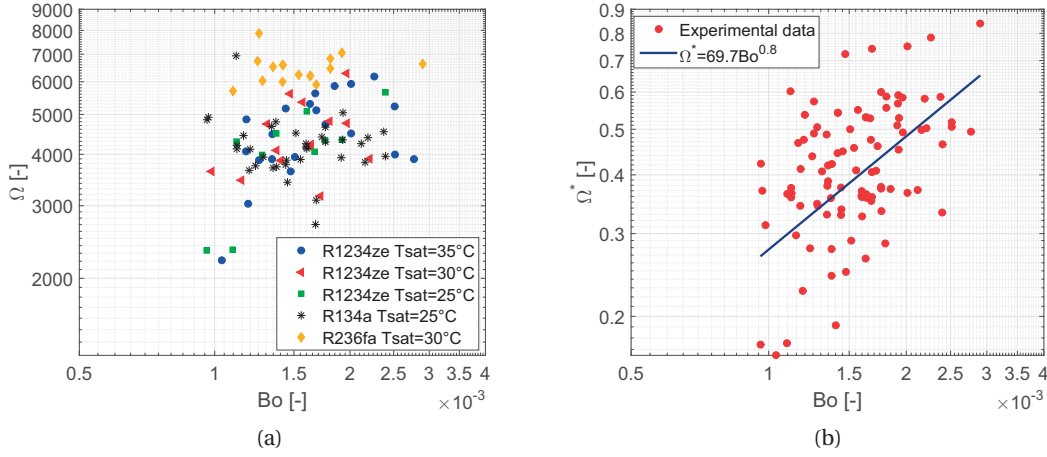


Figure 7.6 – (a) Bubble generation frequency  $\Omega$  for the slug flow model versus the Boiling number. (b) Dimensionless frequency  $\Omega^*$  correlation and data-points versus Boiling number.

that the Boiling number,  $Bo = \frac{q}{Gh_{lv}}$ , was the only parameter that showed a feasible trend in influencing the bubble departure frequency in the present tests.

Figure 7.6(a) shows the frequency results versus the  $Bo$  number of the tested fluids considering the data in the slug flow region, i.e. when  $x < x_{SF-AF}$ . Values on the order of  $\Omega \sim (10^3 - 10^4)$  1/s are comparable to those measured during HFE-7000 flow boiling tests in a row of pin fins performed by Krishnamurthy and Peles [73]. Note that  $\Omega$  increases with the  $Bo$  number, as higher values of heat flux promote an increment of active nucleation sites and a reduction of the bubble waiting time. Differently from the original model [91], the influence of  $P_{red}$  is not evident, noting that the values of  $P_{red}$  covered by this study have a narrow range of variation, i.e. between 0.137 for R236fa to 0.183 for R1234ze(E), and therefore a statistical evaluation of the influence of  $P_{red}$  was not possible. Hence, the identified values of the bubble frequency are utilized to develop a correlation for the non dimensional frequency,  $\Omega^* = \Omega \cdot \rho_l \cdot d_h / G$ , as a function of the Boiling number only:

$$\Omega^* = 69.7Bo^{0.8} \quad (7.13)$$

The values of  $\Omega^*$  and the fit are depicted in Fig. 7.6(b). The correlated frequency increases with the heat flux as  $\Omega \propto q^{0.8}$ , similarly to the dependency inferred by previous studies of flow boiling in mini/microchannels [138, 96], and micro-pin fins [78].

The last modification implemented in the original three-zone model concerns the average single phase Nusselt number  $\overline{Nu}_{sp}$ , which is utilized to evaluate the heat transfer coefficient associated to the liquid slug,  $h_l$ , as follows:

$$h_l(z) = \frac{\overline{Nu}_{sp} k_l}{d_h} \quad (7.14)$$

The correlation for  $\overline{Nu}_{sp}$  is obtained by fitting in-house experimental single phase results taken here. Adiabatic measurements of the single phase pressure drop revealed a laminar to turbulent flow transition at  $Re_{sp} = \frac{d_h G}{\mu_l} \approx 300$  [41], which corresponds to a mass flow rate of about  $G = 600 \text{ kg m}^{-2} \text{ s}^{-1}$  for the fluids used here. Since most of the present data are for  $G > 600 \text{ kg m}^{-2} \text{ s}^{-1}$ , a correlation for the  $\overline{Nu}_{sp}$  number of the kind  $Nu \sim C Re^n Pr^m$ , typical for turbulent flows, is expected to work well. This correlation is commonly adopted in studies of cross flow over circular tubes for both long tubes [49] and micro-pin fins [46]. Despite knowing that the boundary layer development will affect the convective heat transfer, the range of  $Pr$  values covered in the present study was too narrow to be statistically relevant; thus the single phase heat transfer data were correlated with the single phase Reynolds number only:

$$\overline{Nu}_{sp} = 0.0013 Re_{sp}^{1.37} \quad (7.15)$$

Previous studies correlated the average Nusselt number also considering the influence of the channel aspect ratio, the longitudinal and transversal pitches and the pin diameter [10, 44], but in the current work only one sample of micro-pin fin inline geometry was tested, therefore no geometrical parameters were included in the fit.

### 7.2.3 Annular flow model

In order to predict the local heat transfer coefficient associated with the annular flow regime, i.e. when  $x \geq x_{SF-AF}$ , the unified annular flow model of Cioncolini and Thome [93] is modified here. This was originally developed with a database covering 9 fluids (water, 2 hydrocarbons and 6 refrigerants) for both vertical and horizontal tubes of 1.03 – 14.4 mm diameter. It considers the annular flow regime as a high velocity gas core with entrained liquid droplets, which drags and atomizes the surrounding annular liquid film, and the liquid-gas core aerodynamic interaction is assumed to control the liquid atomization process [93]. In the original model, the heat transfer coefficient is predicted by the following correlation:

$$h_{AF}(z) = (77.6 \cdot 10^{-3} \delta^{+(-0.1)} Pr_l^{0.52}) \frac{k_l}{y^*} \quad (7.16)$$

where the parameters  $\delta^+$  and  $y^*$  are, respectively, the dimensionless liquid film thickness (averaged cross-sectional value) and the length scale utilized to define the dimensionless distance from the wall ( $y^+ = y/y^*$ ). The parameter  $\delta^+$  is linked to the dimensional liquid film thickness  $\delta$ :

$$\delta^+ = \frac{\delta}{y^*} \quad (7.17)$$

where  $y^*$  is calculated as:

$$y^* = \frac{\mu_l}{\sqrt{\rho_l \tau_w}} \quad (7.18)$$



## Chapter 7. Flow pattern-based boiling heat transfer model

The wall shear stress,  $\tau_w$ , is related to the two-phase Fanning friction factor  $f_{tp}$  as:

$$\tau_w = \frac{1}{2} f_{tp} J_g^2 \rho_g \quad (7.19)$$

where the gas core density  $\rho_g$  and superficial velocity  $J_g = Gx/\rho_g$  are used as characteristic scales. In order to use Eq. (7.16), Cioncolini and Thome [93] developed specific methods to calculate these three crucial parameters: (i) the entrained liquid fraction  $e$  [139], (ii) the void fraction  $\epsilon$  [140] that enters in the mass balance of the liquid flow and thus determines the liquid film thickness  $\delta$ , and (iii) the two-phase friction factor  $f_{tp}$  [141].

In the present study, due to the micro-scale pin fin geometry, the liquid film atomization process is assumed to be suppressed due to the small Weber number. Moreover, the micro-pin fin configuration, differently from parallel multi-microchannels, induces a swirling effect on the flow downstream, which tends to drift the liquid toward the pin fin walls and the vapor phase into the center of the channels. This effect would lead to a reduction of the entrainment, as the droplets in the vapor core, displaced by the swirls, merge into the surrounding liquid film, as also observed by Carey [142]. Therefore, the first modification implemented in the model of Cioncolini and Thome [93] is to consider no entrainment in the vapor core, i.e.  $e = 0$ .

As described in the previous section and illustrated in Fig. 7.5(b), the liquid film is considered to be uniformly distributed around the perimeter of the cross-sectional area, with a constant thickness  $\delta$ . Eqs. (7.6)-(7.8) cannot be applied to annular flow as they were developed for long bubbles; therefore the value of  $\delta$  is extracted knowing the portion of the cross-sectional area occupied by the vapor phase,  $A_v$ , which is calculated via the void fraction  $\epsilon$ :

$$A = \overline{W}_{ch} H, \quad A_v = \epsilon A \quad (7.20)$$

$$\delta = \frac{A - A_v}{2(H + \overline{W}_{ch})} \quad (7.21)$$

The void fraction is determined with the formulation proposed by Cioncolini and Thome [140].

A new calculation of the two-phase friction factor,  $f_{tp}$ , is implemented in the current model in order to capture the pressure drop for flow through an array of pin fins. This will be utilized to estimate  $\tau_w$  by means of Eq. (7.19). From the horizontal experimental pressure drop data, removing the accelerational pressure drop, the friction factor is evaluated from the local frictional pressure drop  $dp_{fr}/dz$ :

$$f_{tp} = \frac{2\tau_w}{\rho_g J_g^2} = \frac{1}{2} \frac{dp_{fr}}{dz} \frac{d_h}{\rho_g J_g^2} \quad (7.22)$$

where only annular flow data ( $x \geq x_{SF-AF}$ ) are utilized. A multiple regression analysis is then utilized to infer the influence of several dimensionless groups on  $f_{tp}$  [141]. The statistical analysis revealed that the vapor Weber number, defined as  $We_g = \frac{\rho_g J_g^2 d_h}{\sigma}$ , is the only parameter



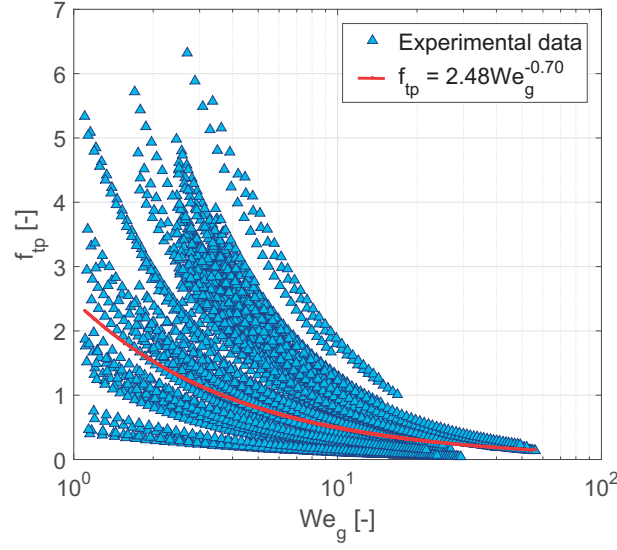


Figure 7.7 – Two-phase friction factor versus Weber core number for annular flow data. Experimental data and correlation.

pertinent to the two-phase friction factor. As such, the wall friction in the annular flow regime is mainly attributed to the interfacial interaction between the vapor core and the surrounding liquid film. Figure 7.7 reports the calculated values of  $f_{tp}$  versus  $We_g$ , and the best fit to the experimental data is reported below:

$$f_{tp} = 2.48We_g^{-0.70} \quad (7.23)$$

The new correlation predicts higher friction factor values than that of the original model [93] that has the same format, as the micro-pin fin geometry induces a larger pressure drop due to the mixing of the fluid than a single, straight channel. It should be noted that Eq. (7.23) does not provide a general prediction correlation for the two-phase friction factor for micro-pin fins evaporators, but it is only a means here to improve the evaluation of the two-phase heat transfer coefficient. The scatter showed in Fig. 7.7 at low  $We_g$ , i.e. low vapor qualities, can be explained by the fact that some data may still be in a slug or slug/churn regime, where parameters other than  $We_g$  might be influential.

Once the modifications described above have been implemented in the model, the coefficients of Eq. (7.16) have been recalibrated to best fit the current database for annular flow data only, yielding the following expression:

$$h_{AF}(z) = \left(0.138 \cdot \delta^{+(-0.347)} Pr_l^{0.52}\right) \frac{k_l}{y^*} \quad (7.24)$$

Note that the dependency of the Prandtl number,  $Pr^{0.52}$ , has been assumed to be the same as in the original formulation of Eq. (7.16), as the range of  $Pr$  numbers covered by the present

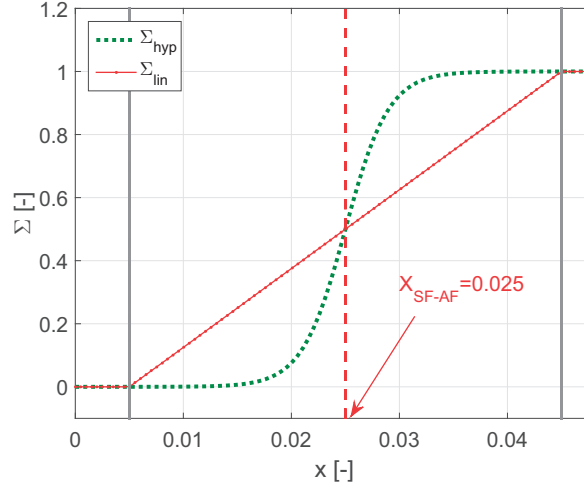


Figure 7.8 – Hyperbolic and linear expressions of the smoothing function  $\Sigma(x)$  in the transitional range of vapor qualities, defined as:  $x_{SF-AF} \pm \Delta x$ . The grey solid lines identify the buffer zone limits.

database is not large enough (see Table 1) to infer a proper dependency.

#### 7.2.4 Smoothing function

The slug and annular flow model predictions,  $h_{SF}$  and  $h_{AF}$ , do not necessarily match in the location of the slug-to-annular flow transition; therefore a buffer zone is created to link these two models together in a smooth transition without a non-physical jump in the value. This is centered at the slug-to-annular flow transition value,  $x_{SF-AF} = 0.025$ , and has a half-width equal to  $\Delta x = 0.02$ , where a smoothing function,  $\Sigma(x)$ , combines the  $h_{SF}$  and  $h_{AF}$  values. In order to merge the two models in the buffer zone, both linear and hyperbolic expressions of the smooth function have been considered:

$$\Sigma_{lin}(x) = \frac{x - (x_{SF-AF} - \Delta x)}{2\Delta x} \quad (7.25)$$

$$\Sigma_{hyp}(x) = \frac{1}{1 + e^{-(x - x_{SF-AF})/w}} \quad (7.26)$$

Figure 7.8 depicts the two different smoothing functions, and the vertical grey lines identify the beginning and ending ranges of the buffer zone. For both the expressions,  $\Sigma(x)$  is equal to 0 in the slug flow regime and is set to 1 in the annular flow region. In Fig. 7.9, the experimental and the predicted heat transfer coefficients as a function of the local vapor quality are depicted when changing the buffer zone width  $\Delta x$  (Fig. 7.9(a)), and the smooth function  $\Sigma(x)$  expression (Fig. 7.9(b)). In Fig. 7.9(a), a buffer zone width of  $\Delta x = 0$  is utilized, showing that the values of the slug flow model and the annular flow do not match at the transition value  $x_{SF-AF}$ . When

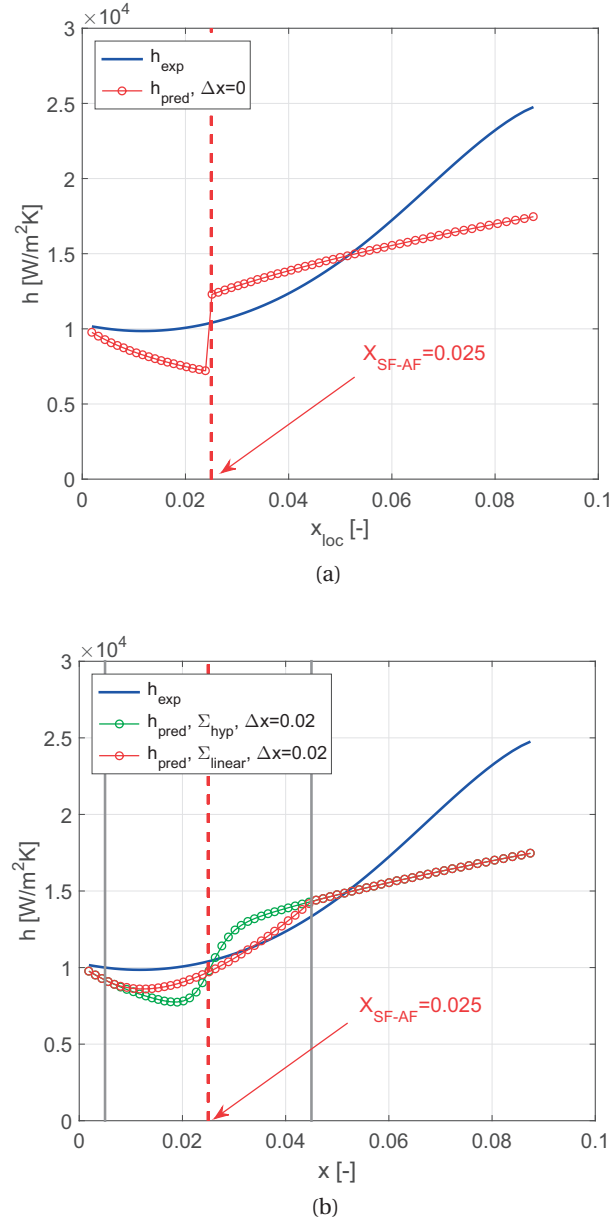


Figure 7.9 – Experimental and predicted heat transfer coefficients with hyperbolic and linear smoothing functions in two different buffer zones centered at  $x_{\text{SF-AF}} = 0.025$ : (a) when  $\Delta x = 0$ , and (b)  $\Delta x = 0.02$ . Test conditions are:  $q = 28 \text{ Wcm}^{-2}$ ,  $G = 1500 \text{ kgm}^{-2} \text{ s}^{-1}$ , R1234ze(E) and  $T_{\text{sat}} = 30^\circ \text{C}$ .

the buffer zone width is defined by using  $\Delta x = 0.02$ , the linear and hyperbolic smoothing approaches yield different trends, as indicated in Fig. 7.9(b). The linear expression has been chosen here, as it only depends on the buffer zone width  $\Delta x$ , whilst the hyperbolic one depends also on the parameter  $w$ , which defines the width of the smoothing, and thus would introduce an additional parameter to be calibrated (which we wish to avoid).

### 7.3 Results

In this section, the predicted and experimental trends of the local heat transfer coefficients versus the vapor quality are briefly described, then comparisons with previous micro-pin fin and microchannel heat transfer predictive models are performed, and finally the results of the new model are presented.

#### 7.3.1 Heat transfer coefficient trend versus vapor quality

The current flow pattern-based model predicts the local variation of the heat transfer coefficient from the beginning of the two-phase region nearby the inlet to the outlet of the pin fin array. In Fig. 7.9(b), the experimental and predicted local heat transfer coefficients versus the vapor quality are depicted. In the slug flow region, the experimental heat transfer coefficient  $h_{exp}$  shows a decreasing trend with the vapor quality. This is well captured by the model, because, as described by Eq. (7.6), the bubble velocity increment leads to a thicker liquid film, and thus to a lower heat transfer rate. After the slug-to-annular flow transition,  $h_{exp}$  increases with vapor quality, thanks to the evaporating liquid film surrounding the vapor core. The model correctly catches the change in the experimental heat transfer coefficient, thus following the development of the annular flow regime. The underprediction at large vapor qualities was also observed in the original annular flow model's comparison to microchannel data, perhaps due to the assumption of not liquid entrainment in the annular flow (which would reduce the liquid film thickness and thus increase the heat transfer coefficient).

#### 7.3.2 Evaluation of existing boiling heat transfer prediction models

The assessment of previous micro-pin fin heat transfer prediction methods, and the two original microchannel models considered in the present study [90, 91, 93], is carried out below. In addition, the current databank is also compared to the recent microchannel heat transfer prediction method of Huang and Thome [99]. The latter has been chosen for these main reasons: (1) the experimental test facility is the same as the one of the present study; (2) the data reduction method, accounting for 3D heat spreading and local values of the heat transfer coefficient, is similar to the one applied here, and thus any errors due to a different data processing should be reduced.

Macroscale correlations, which are mostly developed for tube bundles in cross-flow boiling, will not be considered in the present comparison, as it has been largely demonstrated that they are unable to predict micro-scale flow boiling heat transfer data, as a reduction in length scale effects the two-phase flow characteristics and the nucleate boiling [5, 143, 144, 28, 131]. The results of the comparison are shown in Figs. 7.10-7.11 and in Table 7.1 with the calculated mean absolute error, defined as  $MAE = \frac{1}{n} \sum_{i=1}^n \frac{|h_{exp,i} - h_{pred,i}|}{h_{exp,i}}$ . In general, the best predictions are given by the two micro-pin fin correlations proposed by Krishnamurty and Peles [6], with MAE's of 37 % and 35 %. Their two correlations are both based on a Chen-type equation developed

Table 7.1 – Statistical comparison between the experimental data and existing correlations.

Authors	MAE [%]	(1)	(2)	(3)
Kosar and Peles (2007)	123.4 %	3.8 %	8.3 %	14.4 %
Qu and Siu-Ho (2009)	239 %	0.8 %	2 %	4 %
Krishnamurthy and Peles (2008), 1 <sup>a</sup>	37 %	22.3 %	51 %	78 %
Krishnamurthy and Peles (2008), 2 <sup>a</sup>	35 %	23.4 %	54 %	80 %
Huang and Thome (2016)	44 %	26.4 %	47 %	67 %
Thome et al. <sup>b</sup> (2004)	91.4 %	0 %	0 %	0 %
Cioncolini and Thome <sup>c</sup> (2011)	37.6 %	10.6 %	31 %	76 %
Present model	23.4 %	40.4 %	72 %	90.5 %

(1),(2),(3) Data within  $\pm 15\%$ ,  $\pm 30\%$ ,  $\pm 50\%$ .

(a) correlation 1 and 2 as reported in Table 1.

(b) Data at  $x < x_{SF-AF}$ .

(c) Data at  $x \geq x_{SF-AF}$ .

for in-tube forced convective boiling [87], neglecting the nucleate boiling contribute. They differ in the formulation of the correction factor and of the frictional multiplier, see Table 2.1 in Chapter 2.

Kosar and Peles [5] proposed two predictive correlations, based on a developed map which segregates the main boiling mechanisms according to the Boiling and Reynolds numbers. The first correlation applies at low  $G$  and is based on a Chen-type formula [87]. It evaluates the heat transfer coefficient based on the Boiling number, considering nucleate boiling as the governing mechanism. The second correlation applies at high  $G$ , and the heat transfer coefficient depends mainly on the mass flux (via the liquid Reynolds number  $Re_l$ ), as convective boiling is assumed to be the fundamental heat transfer mechanism. Their method predicts the experimental data with a MAE=123.4 %, see Fig. 7.10(a) and Table 7.1. This large discrepancy comes from a decreasing trend of the heat transfer coefficient with the outlet vapor quality predicted by their correlation for high  $G$  (see Table 7.1), which was never been observed in the current experimental results.

The model of Qu et al. [74] was developed based on water flow boiling data. It predicts a constant heat transfer coefficient at high vapor qualities, contrary to what is observed in the present experimental heat transfer coefficient, which sharply increases as the annular flow develops. The prediction method of Huang and Thome [99] predicts 47 % of the experimental data within the  $\pm 30\%$ , with a MAE of 44 %, see Fig. 7.11(a). Such a deviation can be mainly attributed to the calculation of the slug-to-annular flow transition value, which was based on the local minimum in the heat transfer coefficient trends and resulted in a different (higher) transition value compared to that obtained here by means of flow visualization analysis.

The original slug flow [90, 91], and annular flow [93] models are compared to the present data over their specific range of vapor quality, see Fig. 7.11(b)-(c). The original three-zone

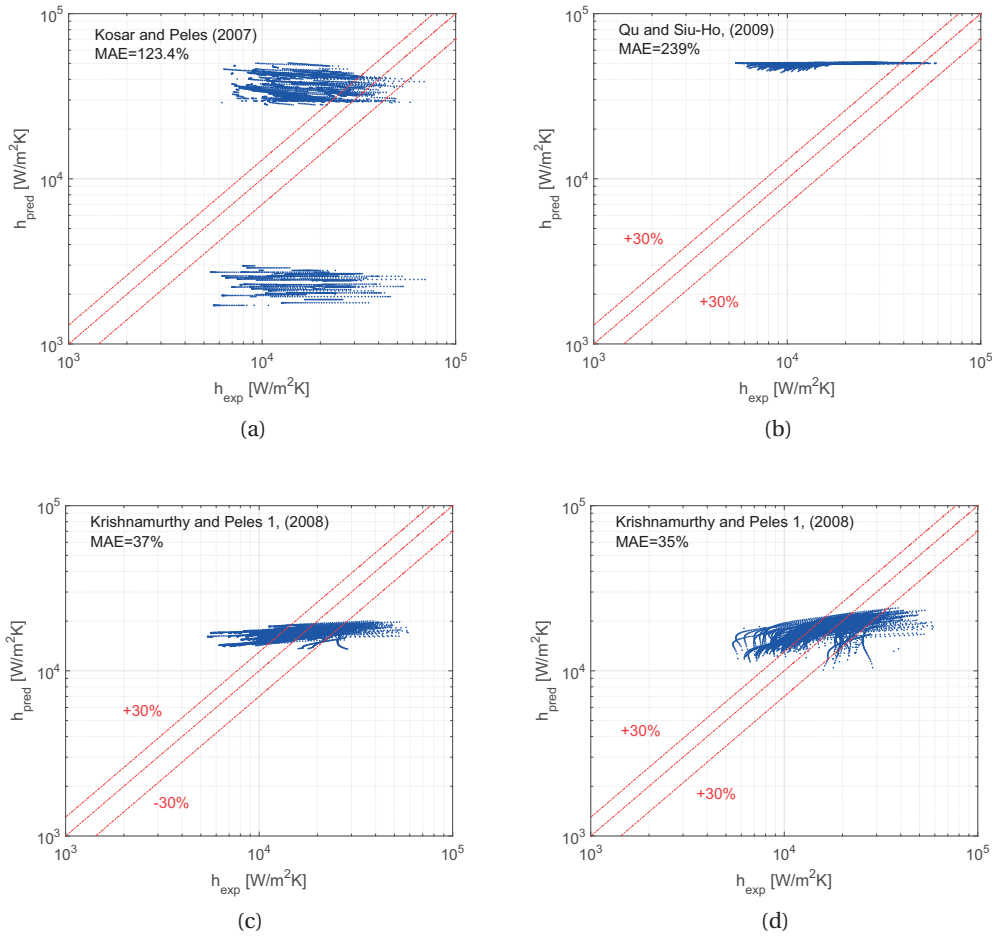


Figure 7.10 – Comparison of existing micro-pin fin predictive models with the experimental database. (a) Kosar and Peles [5], (b) Qu et al. [74], (c)-(d) Krishnamurthy and Peles [6].

model [90, 91] underestimates the heat transfer coefficient by about one order of magnitude, as it predicts a value of the film thickness which is about 10 times smaller than the one obtained with Eqs. (7.6)-(7.8). Indeed, the Moriyama and Inoue [145] correlation used in the original three-zone model was developed for bubbles growing radially between two parallel plates that was available at that time. Due to the smaller film thickness predicted by Moriyama and Inoue correlation [145], the original three-zone model predicts a very large dry vapor zone for the present geometry, thus severely underestimating the micro-pin fin heat transfer database.

The annular flow model of Cioncolini and Thome [93] presents a quite satisfactory correlating capability, suggesting that heat transfer induced by annular flow across the current micro-pin fin array is well emulated by modelling the evaporation of the thin liquid film on the channel wall.

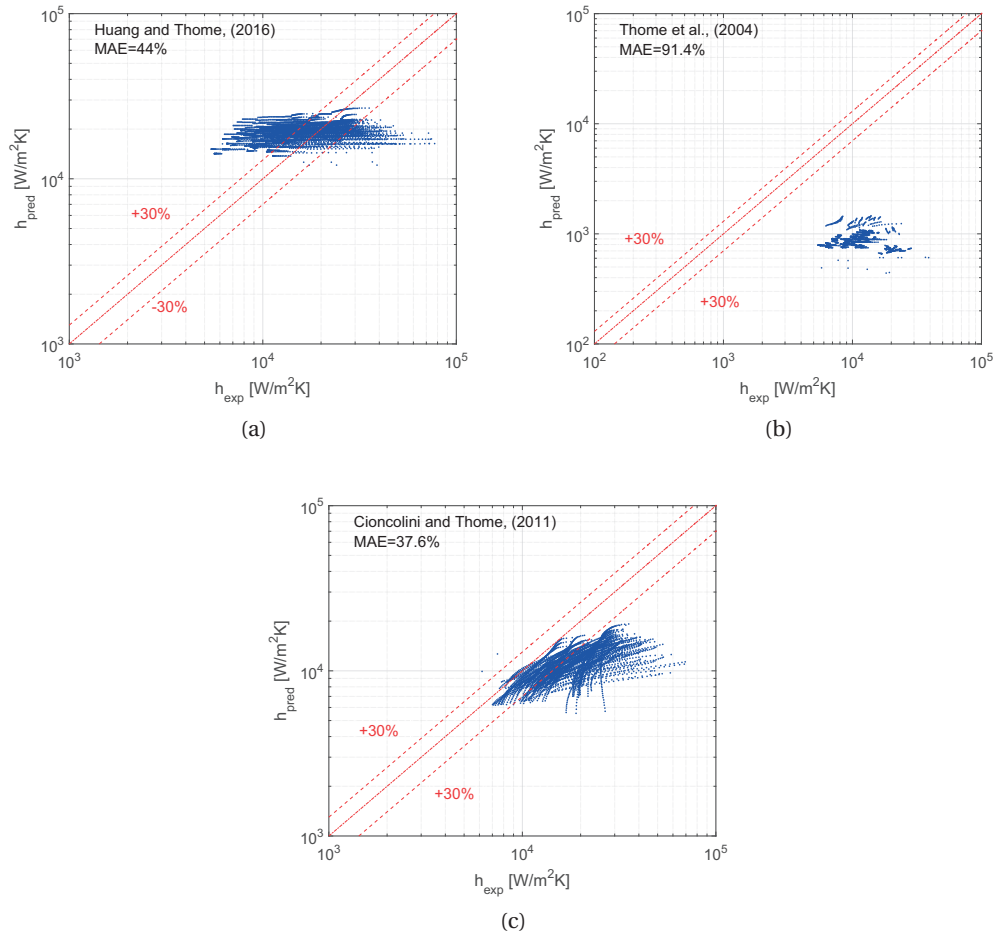


Figure 7.11 – Comparison of existing predictive models with the experimental database: (a) Huang et al. [99], (b) Thome et al. [90] for  $x < x_{SF-AF}$ , and (c) Cioncolini and Thome [93] for  $x \geq x_{SF-AF}$ .

### 7.3.3 New model results

The new flow pattern-based method estimates the entire experimental database with a MAE of 23.4%, and predicts 72% of the databank within  $\pm 30\%$ , as presented in Table 7.1. The detailed prediction results for each tested refrigerant are listed in Table 7.2 and illustrated in Fig. 7.12. The prediction of the slug flow data ( $x \leq 0.025$ ) exhibits slightly larger deviations than those of the annular flow data, with an MAE=27.9% versus MAE=22.1% for the latter. The largest deviations are observed near the onset of boiling at  $x \gtrsim 0$ . Rather than attribute such deviations to the model, this may be actually ascribed to the difficulty of assigning the location where  $x = 0$  in the experimental data reduction.

As a matter of fact, when  $x \approx 0$  the flow may still be in a single phase state with superheated liquid, or it could be composed of very short bubbles such that a liquid film has not yet formed

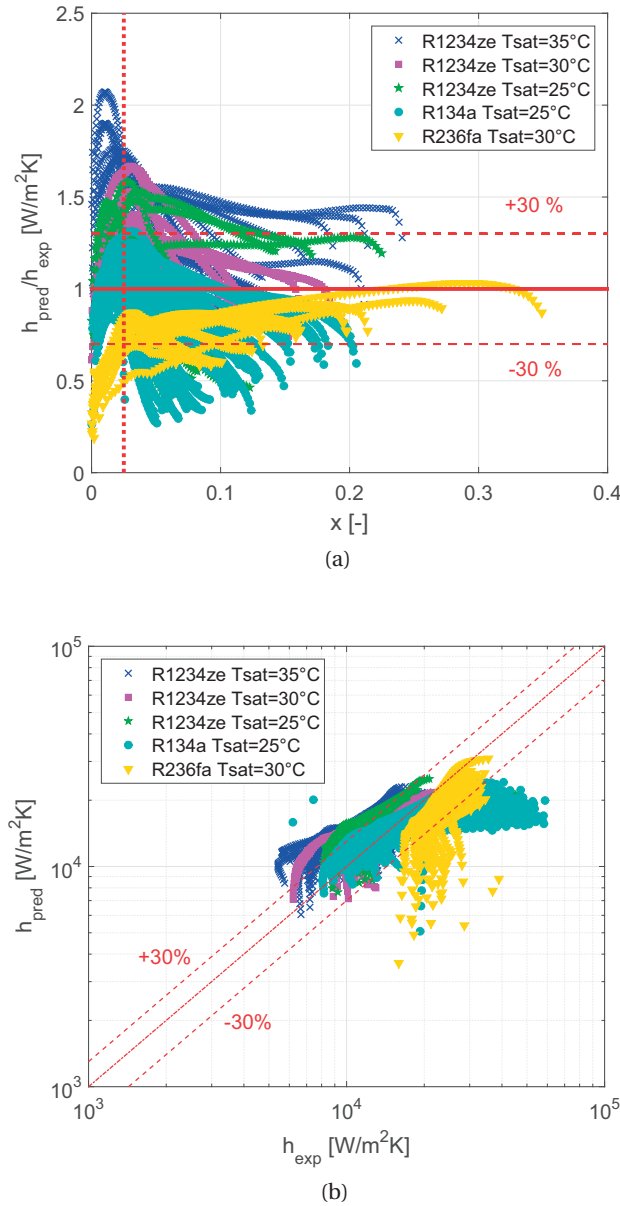


Figure 7.12 – Results of the current model on predicting the entire experimental database for every refrigerant and saturation temperature tested.

or it may reflect the effect of the onset of boiling front having some width-wise variation as can be seen in Fig. 7.2(a). Under such circumstances, the slug flow model overestimates the heat transfer performances. On the other hand, flashing may generate vapor bubbles after the inlet restrictions, such that the actual vapor quality is larger than that evaluated by the energy balance when reducing experimental measurements. In this case, bubbles are larger than predicted by the model, and underestimation of the heat transfer coefficient occurs.



Table 7.2 – Heat transfer prediction results of the experimental database for each tested refrigerant.

Results	R1234ze(E) <sup>a</sup>	R1234ze(E) <sup>b</sup>	R1234ze(E) <sup>c</sup>	R134a	R236fa
MAE	29.8 %	20.2 %	27.3 %	18.2 %	23.6 %
Data within $\pm 15\%$	33.4 %	44 %	22.7 %	57.1 %	26.9 %
Data within $\pm 30\%$	57.4 %	78 %	58.4 %	78.8 %	75.2 %
Data within $\pm 50\%$	81.6 %	94.2 %	95.6 %	93.2 %	94.9 %

(a)  $T_{sat} = 35^\circ\text{C}$

(b)  $T_{sat} = 30^\circ\text{C}$

(c)  $T_{sat} = 25^\circ\text{C}$

## 7.4 Conclusions

The current chapter presented a new flow pattern-based mechanistic model for predict boiling heat transfer in a micro-pin fin evaporator. The model considers the successive development of slug and annular flow regimes, and heat transfer is assumed to be governed by a convective boiling mechanism. In the slug flow region, the heat transfer prediction is obtained by an updated version of the three-zone model of Thome et al. [90, 91], which includes revised formulations to estimate the film thickness around long bubbles, and the single phase heat transfer in the liquid slug for a micro-pin fin geometry.

A modified version of the boiling heat transfer model of Cioncolini and Thome [93] is adopted to predict the heat transfer coefficient in annular flow. This incorporates new submodels for determining the thickness of the annular liquid film and the two-phase friction factor for flow through a micro-pin fin array.

The model is calibrated and benchmarked over an experimental heat transfer database that covers three fluids and 7219 local measurements. The predictions given by the slug and annular flow models are merged together at the slug to annular flow transition location using a linear smoothing function, whose location is extracted by processing high-speed camera videos. The new flow pattern-based model predicts the 72 % of the experimental databank within the  $\pm 30\%$  with a mean absolute error equal to 23.4 %.



## 8 Conclusions and recommendations

### 8.1 Summary and highlights

The present study aims to contribute to the research on new solutions for the thermal management of high power density micro-electronics, which is becoming nowadays a critical issue due to the rapid advances in performance and miniaturization, as outlined in **Chapter 1** and **Chapter 2**. In fact, this work represents one of the final steps of a long chain of studies (experimental, theoretical and numerical ones) performed during the last two decades in the Laboratory of Heat and Mass Transfer (LTCM), which focused on the predictive capability and physical understanding of two-phase flow in the micro-scale, with the final goal of assessing the feasibility of evaporating flow-based cooling systems.

The design of these novel cooling systems and the ability to predict their performance depend on both the availability of high-accuracy experimental data and appropriate models that can be used to describe the physical processes associated to two-phase flows.

However, a broad understanding of the thermo-fluid dynamics of two-phase flow involves significant difficulties and challenges, generated by different aspects and parameters such as fluid properties, system configuration and size scale, moving gas-liquid interfaces, and so forth.

Therefore, the main goal of the present study is to create a large high-accuracy experimental database (by using the test facility illustrated in **Chapter 3**) to characterise the thermal and hydraulic performances of a new two-phase flow micro-pin fin evaporator for future use of on-chip interlayer cooling of high power micro-electronics. The thermal and hydraulic characteristics of the micro-evaporator can be qualitatively estimated by evaluating two main parameters: (i) the local **heat transfer coefficient**, and its dependency on flow regime's development and on test conditions, such as mass flux and heat flux, and (ii) the total **pressure drop** across the heat sink, which is directly measured. The results were discussed in **Chapter 5** and **Chapter 6**. In order to calculate the local heat transfer coefficient, the procedure to extract a 2D map of the channel wall temperature is based on a 3D inverse heat conduction

## Chapter 8. Conclusions and recommendations

---

model, whilst the local fluid temperature is obtained from the local fluid pressure profile along the test section, which is reconstructed by means of a separated flow model, as described in **Chapter 4**.

In this work, fine resolution temperature measurements and high-speed flow visualization are coupled and synchronized in order to analyse the interrelation between time-dependent fluid dynamics and heat transfer associated with flow boiling in the micro-evaporator. Moreover, image processing and the time-strip technique were applied to the high-speed camera videos, yielding a deeper insight on the two-phase flow configuration along the micro-pin fin array.

The last step of the study, presented in **Chapter 7**, was to develop a new flow pattern-based mechanistic model for predict local boiling heat transfer in the micro-pin fin evaporator, which is to date missing in the open literature. Noting that the bubbly flow regime was short-lived, the slug flow was assumed to begin at vapor qualities of  $x > 0$ . Therefore, heat transfer mechanisms associated with slug flow and annular flow regimes were inferred by updating the widely used three-zone slug flow model of Thome et al. [90, 91] and the algebraic turbulence annular flow model of Cioncolini and Thome [93], respectively. These two models were linearly combined by utilizing a smoothing function acting on a buffer zone centered in the slug-to-annular flow transition region, whose location was obtained by means of a new method based on flow visualization analysis and the time-strip technique of the available experimental high-speed videos.

Based on the current experimental results, the following observations and conclusions can be highlighted:

- Micro-pin fin evaporators represent a potential alternative to the widely studied multi-microchannel geometries as pin fins act as a natural housing for the TSV between the chip dies (similar to the fins between parallel microchannels), and enhance the fluid mixing. In fact, the single phase friction factor and Nusselt number underlined a laminar to turbulent flow transition at a critical value of the Reynolds number;
- The high-speed flow visualization highlighted four different two-phase flow configurations and it was utilized to generate the operational maps in order to define the range of favorable operating conditions. The fully stable and most favorable condition to achieve larger heat transfer coefficient values is characterised by the presence of single phase flow at the entrance of the heated area, followed by a very dynamic zone where small and intermediate size bubbles are present, while steady elongated bubble and annular flow regions develop towards the end of the heated area;
- The beneficial effect of inlet restrictions was experimentally proved, as they extended the map of stable operating conditions to lower flow rates by reducing or eliminating back flow effect. This finding, together with the developed operational maps, should be considered in the optimization of a micro-heat sink design.
- The dielectric refrigerants R236fa, R245fa, R1234ze(E) and R134a were experimentally

tested over a large range of conditions. Except for R245fa, the other fluids exhibited a very stable flow boiling behavior and limited temperature oscillations of the micro-evaporator surface in time. This makes R236fa, R1234ze(E) and R134a optimal fluids for on-chip cooling technologies. The choice among these three dielectric refrigerants should depend on the application requirements, such as operating pressure or saturation temperature. Conversely, R245fa had a very unstable and unpredictable behaviour during flow boiling tests;

- Total two-phase pressure drops were measured (comprising the single and two-phase parts) and their dependency on test conditions, such as heat flux and mass flux, were inferred. The pressure drops induced by inlet restrictions and outlet expansions were also considered in the study;
- Insights on the local trends and magnitudes of the heat transfer coefficient were provided by the analysis of the local footprint heat flux and temperature extracted from the 3D inverse heat conduction model. In the two-phase region, a strong influence of the vapor quality and heat flux was detected, which can be mainly attributed to flow pattern effects. A significant improvement of the thermal performances was achieved as the flow transitions to annular flow. These results underlined that a fundamental understanding of flow patterns is necessary to develop reliable design tools;
- The developed synchronized thermal measurements and high speed visualization analysis permitted new insights on the nucleation process, bubble dynamics and slug-to-annular flow transition location. Additionally, a Fourier analysis of the evaporator base temperature signal in time was coupled with the frequency spectra computed on the intensity grey signal obtained by means of the time-strip technique applied at the same locations along the evaporator. This allowed us to gain a deeper understanding of the mutual influence between the thermal performance of the system and the flow pattern development during operation. In particular, the captured frequency related to the cyclical activation and deactivation of nucleation sites, corresponded to the oscillation of the micro-evaporator surface temperature at the same locations;
- A flow boiling heat transfer predictive model that incorporates the complex flow geometry and flow pattern effects was missing in the literature of micro-pin fins. In fact, the newly developed flow pattern-based model here attempts to capture the two-phase characteristics and transport processes associated to slug and annular flow regimes, which are the most commonly observed regimes in micro-pin fin arrays. The new physics-based mechanistic model predicted the 72 % of the experimental databank (7219 local measurements) within the  $\pm 30\%$  with a mean absolute error equal to 23.4%.

### 8.2 Future recommendations

Within the scope of the present study, many objectives were fulfilled and the accomplishments were presented above. However, there remain challenges associated with a fundamental understanding of two-phase flow dynamics in micro-pin fin array and open questions that require additional research to be done. Thus, further research is suggested to focus on the following aspects:

1. Test different micro-pin fin sizes and distributions. Indeed, the channel aspect ratio, the longitudinal and transversal pitches and the pin diameter influence the boundary layer development and the hydrodynamics inside the pin fin array. As shown in the single phase results, a critical value of the Reynolds number triggers the onset of vortex shedding, which yields higher heat transfer. Therefore, testing different geometries would help to find the best configuration combining the integrated system design and the hydrothermal performance (also considering any hotspot locations);
2. Improve the resolution and magnification of the high-speed camera in order to gain a deeper insight of the local two-phase flow in between the micro-pin fins. This would permit investigation of the bubble interaction during the nucleation and coalescence processes. Secondly, it would be nice to directly measure the liquid film thickness, which is a crucial parameter in the heat transfer mechanism during the annular flow development;
3. The flow pattern-based model could be further improved by considering the subcooled flow as well as the bubbly flow region, starting from the onset of two-phase flow until the slug flow development. This cannot be attempted without a higher resolution camera, since the detection of the bubble size and a fundamental understanding of the nucleation process are mandatory for this stage;
4. Starting from the unstable two-phase flow tests, it would be interesting to investigate dynamic instabilities in the current micro-evaporator, which could be analysed by testing transient dynamics of the system. Although this has been studied in microchannels and large scale systems [146, 147], a study focused on the onset of flow instabilities in micro-pin fin geometry could lead to a way to predict this threshold.

Finally, further improvements in the experimental set-up, in particular possible modifications during the fabrication of the test section are listed below:

1. It would be nice to include pressure ports directly in the test vehicle to measure the inlet and outlet pressures at the beginning and at the end of the micro-pin fin array. This would provide a more accurate local fluid temperatures and thus local values of the heat transfer coefficient;

2. Choose a material with lower conductivity than copper for the manifold housing of the test section. This would reduce the heat spreading from the film heaters at the bottom of the test section;
3. The transparent layer on the top is made by a Pyrex cover, which is anodically bonded to the silicon micro-pin fins. This makes the test section very fragile along the bounding perimeter. Thus, a different transparent material should be considered, still suitable for the micro-fabrication process, and this would improve the ability of the test section to withstand higher pressures without failure.





## A 3D heat conduction scheme

In this Appendix, the methodology implemented to determine the temperature and heat flux at the footprint level (  $T_{ftp}$  and  $q_{ftp}$  ) is presented. Indeed, an inverse heat conduction method is used to determine the local heat fluxes and local temperatures on an inaccessible surface (footprint) by measuring the local temperatures on the accessible boundary (micro-evaporator base).

The methodology utilized to calculate  $T_{ftp}$  and  $q_{ftp}$  is based on these main steps:

1. Guess the 2D temperature map at the footprint level  $T_{ftp}$  as top boundary condition to solve the 3D heat conduction problem by implementing a TridiagonalMatrix (TDMA) algorithm. At the base the temperature and heat flux are known, and on the lateral sides uniform heat fluxes are imposed;
2. Update the  $T_{ftp}$  value using a local Newton-Raphson iteration method based on the error between the calculated base temperature (by utilizing the 3D conduction scheme) and the experimentally measured base temperature (by using the IR camera).

It is worth noting that the noise present in any measurement of temperature can cause instabilities in the predicted heat fluxes. In order to reduce oscillations in the final solution, a polynomial surface fitting is implemented to filter the IR temperature map. This method seems to be efficient in reducing the noise in the present large number of measurements points (110 x 110 pixels ), as observed by Bozzoli et al.[148]. The present method is a geometric variation of that proposed and used by Huang et al. [111].

## A.1 Discretization and Tri-Diagonal Matrix Algorithm

The present experimental case is governed by the following heat conduction problem in three dimensions:

$$\frac{\partial}{\partial x} \left( k \frac{\partial T}{\partial x} \right) + \frac{\partial}{\partial y} \left( k \frac{\partial T}{\partial y} \right) + \frac{\partial}{\partial z} \left( k \frac{\partial T}{\partial z} \right) = \rho c_p \left( \frac{\partial T}{\partial t} \right) \quad (\text{A.1})$$

which at steady state conditions reduces to:

$$\frac{\partial}{\partial x} \left( k \frac{\partial T}{\partial x} \right) + \frac{\partial}{\partial y} \left( k \frac{\partial T}{\partial y} \right) + \frac{\partial}{\partial z} \left( k \frac{\partial T}{\partial z} \right) = 0 \quad (\text{A.2})$$

$x, y, z$  are the coordinates in the thickness, in the widthwise and lengthwise directions respectively. At the bottom side of the evaporator ( $x = 0$ ), Dirichlet and Neumann boundary conditions are applied, which are obtained from the infrared camera measurements and the electrical power input, as follows:

$$T(0, y, z) = T_{Base, IR}(0, y, z) \quad q(0, y, z) = q_{Base}(0, y, z) \quad (\text{A.3})$$

Differently from what was observed in the majority of existing studies, where adiabatic conditions were assumed at the lateral sides, in the present study constant Neumann boundary conditions are imposed in order to take into account the heat spreading to the housing manifold. Starting from the measured temperature map at the base, it is possible to calculate the heat fluxes on the external perimeter as lateral losses,  $q = -k \frac{dT}{dz}$  and  $q = -k \frac{dT}{dy}$ . The terms  $dT$  on the four sides are computed as the difference between the temperature in the control volume at the edge and the temperature in the second to last control volume. These computed heat fluxes are then utilized as boundary conditions on the sides:

$$q(x, 0, z) = q_s \quad q(x, y_{end}, z) = q_n \quad q(x, y, 0) = q_w \quad q(x, y, z_{end}) = q_e \quad (\text{A.4})$$

Then, equation (A.2) is discretized to solve the 3D heat conduction problem, by integrating it over each control volume, following the method proposed by Patankar [149].

The three-dimensional vertex-centered grid is chosen and it is depicted in Fig. A.1. In the  $z$ - and  $y$ - directions the grid is composed of 110 control volumes, whilst in the  $x$ - direction (along the height of the evaporator) the mesh comprises 10 control volumes, giving a total of  $110 \times 110 \times 10$  grid points (121000). For the control volume centered in the grid point P (see the zoom in the right side of Fig. A.1), points E and W are its  $z$ - direction neighbors, while N and S and T and B are the  $y$ - and  $x$ -directions neighbors respectively. The multidimensional discretization equations (obtained starting from (A.2)) are expressed as:

$$\begin{aligned} a_P T_P &= \sum a_{nb} T_{nb} + b \\ b &= S_c \Delta x \Delta y \Delta z \\ a_P &= \sum a_{nb} - S_p \Delta x \Delta y \Delta z \end{aligned} \quad (\text{A.5})$$

### A.1. Discretization and Tri-DiagonalMatrix Algorithm

where the constant term  $b$  represents the rate of heat generation (source term  $S_c$ ), and the neighbor coefficients  $a_{nb}$  are the conductance between the point P and the corresponding neighbor. As example, the coefficient for the top boundary is written as:

$$a_T = \frac{k_t \Delta y \Delta z}{\delta x} \quad (\text{A.6})$$

Further details of the discretization method can be found in [149].

In order to write the nodal equations and calculate the coefficient for the TDMA of Eqs. A.5, the equivalent thermal conductivities are calculated as harmonic average between two neighboring nodes [149], as reported below for the  $y$ - direction:

$$k_{eq,i} = \left( \frac{1 - f_{e,i}}{k_i} + \frac{f_{e,i}}{k_i + 1} \right) \quad f_{e,i} = \frac{\Delta y_{i+1}}{\Delta y_i + \Delta y_{i+1}} \quad (\text{A.7})$$

The new set of discretized equations (A.5) are solved by utilizing the TridiagonalMatrix (TDMA) algorithm, which proceeds from south to north, then from west to east and lastly from bottom to top. After each loop of the TDMA algorithm, the thermal conductivities are updated with the obtained temperatures of each node, and the initial footprint temperature  $T_{ftp}$  is updated by using the Newton-Raphson method, until the convergence is reached. A flowchart diagram summarizing the loop of convergence of the 3D heat conduction solver is presented in Fig.A.2. The main steps to solve the 3D heat conduction and obtain the temperature in each nodes of the volume,  $T_{3D}$ , are summarized below:

1. Filter the temperature map measured by the infrared camera to obtain  $T_{Base,IR}$ ;
2. Guess an initial temperature at the footprint  $T_{ftp}^0$  by solving a 1D conduction along the micro-evaporator height and calculate the lateral heat fluxes ( $q_w$ ,  $q_e$ ,  $q_s$ ,  $q_n$ ) from the  $T_{Base,IR}$ ;

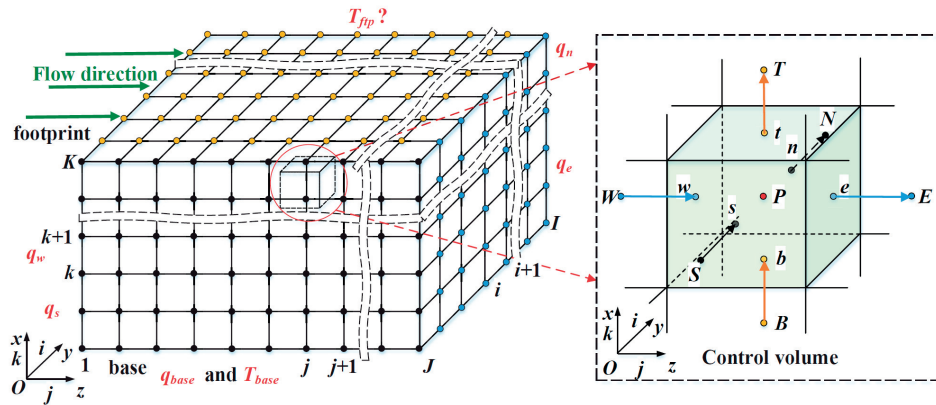


Figure A.1 – Scheme of the geometry and boundary conditions applied to solve the 3D heat conduction. The image is taken from the study of Huang et al. [111].

## Appendix A. 3D heat conduction scheme

3. Run the TDMA algorithm with the initially guessed  $T_{ftp}^0$  value until convergence is reached, i.e. when the maximum absolute temperature difference between two consecutive calculations (between the previous and the new calculated temperature) is smaller than  $10^{-4}$ ;
4. If  $\delta T \leq 10^{-4}$  the TDMA re-starts with the new initial value  $T_{ftp}^{k+1}$ , updated by using the Newton-Raphson method.

The Newton-Raphson method is utilized here to optimize the temperature map at the footprint level, by utilizing the difference between the calculated base temperature  $T_{base,3D}$  and the measured one  $T_{base,IR}$  as the convergence criterion:

$$\max(\max(|T_{base,3D} - T_{base,IR}|)) < 0.05 \quad (A.8)$$

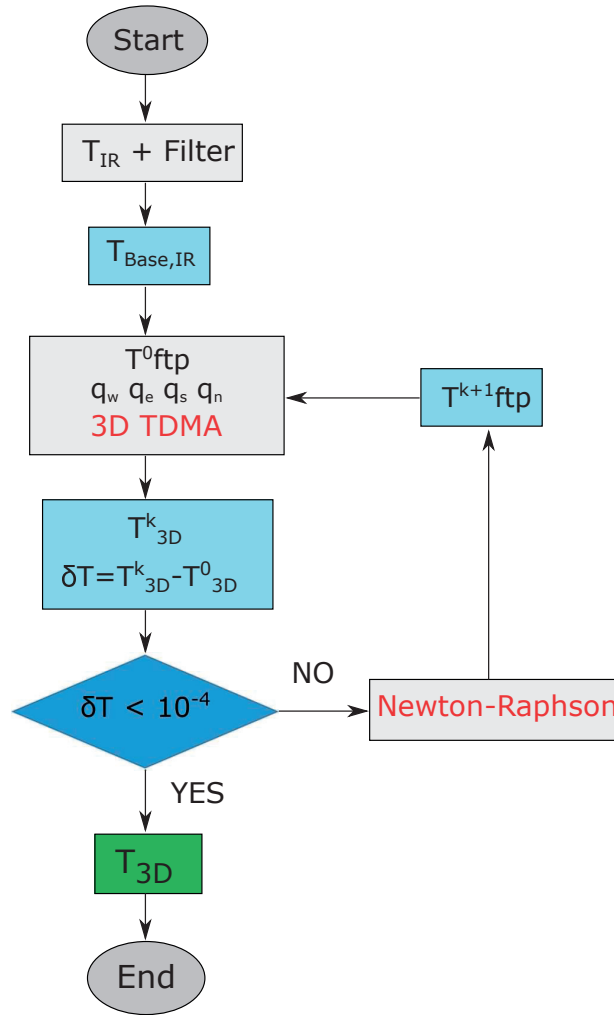


Figure A.2 – 3D TDMA and Newton-Raphson algorithm flowchart.

$$\delta T_{base} = T_{base,3D} - T_{base,IR} \quad (A.9)$$

$$\delta T_{base,pert} = T_{base,3D,pert} - T_{base,IR} \quad (A.10)$$

$$T'_{base,pert} = \frac{\delta T_{base,pert} - \delta T_{base}}{pert} \quad (A.11)$$

$$T_{ftp}^{k+1} = T_{ftp}^k - \frac{\delta T_{base}}{T'_{base,pert}} \quad (A.12)$$

where the perturbation, indicated as "*pert*" was set to be 0.0001.



## B Uncertainty analysis

This appendix deals with the uncertainty calculations of both the measured and calculated parameters.

The uncertainty of a measurement from a sensor can be defined as a sum of random  $R$  and systematic (or bias)  $S$  errors, and it is evaluated as the Euclidian norm of the two components, as:

$$\delta X = \sqrt{R^2 + S^2} \quad (\text{B.1})$$

In general, the random errors  $R$  can be treated statistically and they can be evaluated by repeating the measurement several times and obtaining the sample standard deviation or the standard error [150]. In the current study, the random uncertainty is very small due to the accuracy of the acquisition system. The systematic errors  $S$  are determined by calibration of instruments and mathematical regression. The results were presented in **Chapter 3** for the thermocouples, pressure transducers and infrared camera, and are listed here in Table B.1. The reference uncertainty for the Coriolis flow meter has been obtained from the manufacturer's data sheet.

Differently from the procedure explained above for the measured values, the calculated parameter uncertainty is evaluated following the Kline and McClintock [110] error propagation method.

Let's consider that a suite of independent variables  $x_1, \dots, x_n$  with uncertainties  $\delta x_1, \dots, \delta x_n$  is used to compute a function  $q = q(x_1, \dots, x_n)$ . If the uncertainties in  $x_1, \dots, x_n$  are independent and random, then the uncertainty of  $q(x_1, \dots, x_n)$  is:

$$\delta q = \sqrt{\left(\frac{\delta q}{\delta x_1} \delta x_1\right)^2 + \dots + \left(\frac{\delta q}{\delta x_n} \delta x_n\right)^2} \quad (\text{B.2})$$

The uncertainty propagation in the result  $\delta q$  depends on the squares of the uncertainties in the independent variables  $x_1, \dots, x_n$ . Because of the square propagation expressed in Eq. (B.2), if the uncertainty of one variable is significantly larger than the uncertainties in the other

## Appendix B. Uncertainty analysis

Measured Parameter	Uncertainty
$L, B, H$ [ $\mu\text{m}$ ]	$\pm 5$
$W_{ch}, D_{fin}, H_{fin}$ [ $\mu\text{m}$ ]	$\pm 5$
$W_{restr}$ [ $\mu\text{m}$ ]	$\pm 5$
$I$ [A]	$\pm 0.61\%$
$V$ [V]	$\pm 0.53\%$
$\dot{m}$ [kg/s]	$\pm 0.1\%$
$T_{base}$ [ $^{\circ}\text{C}$ ]	$\pm 0.2$
$p_{in}, p_{out}$ [kPa]	$\pm 0.1FS\%$
$\Delta p_{tot}$ [kPa]	$\pm 0.023FS\%$

Table B.1 – Experimental uncertainties of the measured parameters. FS stands for full-scale.

Calculated Parameter	Uncertainty
$G$ [kg/m <sup>2</sup> s]	$\pm 4.6\%$
$\Delta p_{fin}$ [kPa]	$\pm 5.9\%$
$q_{base}$ [W/cm <sup>2</sup> ]	$\pm 1.3\%$
$q_{losses}$ [W/cm <sup>2</sup> ]	$\pm 3\%$
$Re$ [–]	$\pm 7\%$
$Re_{tp}$ [–]	$\pm 9\%$
$f$ [–]	$\pm 15\%$
$Nu$ [–]	$\pm 13.9\%$
$x$ [–]	$\pm 9.2\%$
$T_{sat}$ [ $^{\circ}\text{C}$ ]	$\pm 0.5$
$h_{ftp}$ [W/m <sup>2</sup> K]	$\pm 4\%$
$h_w$ [W/m <sup>2</sup> K]	$\pm 12\%$

Table B.2 – Uncertainty propagation results of the calculated parameters.

variables, it predominates and the others may be neglected. This result is crucial for the design of an experiment, as any improvement in the experimental result can be achieved by improving the instrumentation or calculation relative to the largest uncertainty. Table B.2 illustrates the uncertainties of the calculated values.

The uncertainty propagation of three parameters of interest is illustrated below. It is worth noting that the procedure is the same for each calculated variable outlined in Table B.2.



## B.1 Examples of uncertainty propagation

### B.1.1 Base heat flux uncertainty

Let's consider the total power applied by means of the electrical heaters. It is calculated as:

$$Q = VI \quad (\text{B.3})$$

Its uncertainty is evaluated from the method of Kline and McClintock [110] as:

$$\delta Q = \sqrt{\left(\frac{\delta Q}{\delta V} \delta V\right)^2 + \left(\frac{\delta Q}{\delta I} \delta I\right)^2} = \sqrt{(I \delta V)^2 + (V \delta I)^2} \quad (\text{B.4})$$

Once the electrical power uncertainty  $\delta Q$  is obtained, the uncertainty of the base heat flux  $q_{base}$  can be estimated as:

$$\delta q_{base} = \sqrt{\left(\frac{1}{A} \delta Q\right)^2 + \left(-\frac{Q}{A^2} \delta A\right)^2} \quad (\text{B.5})$$

### B.1.2 Mass flux uncertainty

The mass flux  $G$  is evaluated from the mass flow rate  $\dot{m}$  measured by the Coriolis mass flow meter, the total number of channels between the pin fin lines  $N_{ch}$  ( $N_{ch} = 67$ ), and their height  $H_{fin}$  and width  $W_{ch}$ , as presented in the data reduction of **Chapter 4** and below:

$$G = \frac{\dot{m}}{N_{ch} H_{fin} W_{ch}} \quad (\text{B.6})$$

Its uncertainty is thus:

$$\delta G = \sqrt{\left(\frac{1}{N_{ch} H_{fin} W_{ch}}\right)^2 (\delta \dot{m})^2 + \left(\frac{-\dot{m}}{N_{ch} H_{fin}^2 W_{ch}}\right)^2 (\delta H)^2 + \left(\frac{-\dot{m}}{N_{ch} H_{fin} W_{ch}^2}\right)^2 (\delta W)^2} \quad (\text{B.7})$$

As it is possible to observe in the results depicted in Tables B.1 and B.2, the uncertainty  $\delta G$  is 4.6% against the value of  $\delta \dot{m} = 0.1\%$  due to the uncertainties attributed to the sizes of the test section ( $H_{fin}$  and  $W_{ch}$ ).

### B.1.3 Heat transfer coefficient uncertainty

The heat transfer coefficient at the footprint level is calculated from the convection equation, as:

$$h_{ftp} = \frac{q_{ftp}}{T_{ftp} - T_{fl}} \quad (\text{B.8})$$

## Appendix B. Uncertainty analysis

---

The uncertainty of the fluid temperature in the two-phase flow tests is evaluated considering the fluid temperature equal to the saturation temperature. Therefore the uncertainty  $\delta T_{sat}$  is calculated via the saturation tables:

$$\delta T_{sat} = \sqrt{(\delta P)^2 \left( \frac{\delta T}{\delta P} \right)^2} \quad (\text{B.9})$$

To compute the uncertainty in the footprint temperature  $\delta T_{ftp}$ , the uncertainties in the infrared camera measurement and in the TDMA and Newton-Raphson method are propagated. The uncertainty of the heat transfer coefficient is thus:

$$\delta h_{ftp} = \sqrt{(\delta q_{ftp})^2 \left( \frac{1}{\Delta T} \right)^2 + (\delta \Delta T)^2 \left( -\frac{q_{ftp}}{(\Delta T)^2} \right)^2} \quad (\text{B.10})$$

where the uncertainty in the temperature difference  $\delta \Delta T$  is:

$$\delta \Delta T = \sqrt{(\delta T_{ftp})^2 + (\delta T_{sat})^2} \quad (\text{B.11})$$

The wall heat transfer coefficient,  $h_w$ , is obtained starting from the footprint heat transfer coefficient by applying the fin efficiency equations, as outlined in the data reduction in **Chapter 4**. Therefore, in order to evaluate the  $h_w$  uncertainty, the area's uncertainties need to be considered ( footprint area, base and lateral pin fin surface), while the uncertainty of the efficiency  $\eta$  is here neglected as its contribute is very small compared to the others. The propagation is:

$$\delta h_w = \sqrt{\left( \frac{\delta h_w}{\delta h_{ftp}} \delta h_{ftp} \right)^2 + \left( \frac{\delta h_w}{\delta A_{ftp}} \delta A_{ftp} \right)^2 + \left( \frac{\delta h_w}{\delta A_b} \delta A_b \right)^2 + \left( \frac{\delta h_w}{\delta A_{lat}} \delta A_{lat} \right)^2} \quad (\text{B.12})$$

## C Image processing techniques

This Appendix aims to illustrate the methodology adopted to process the images and perform the time-strip technique, starting from the high-speed digital camera videos.

Indeed, high-speed flow visualization has been largely utilized in the present study, as it showed good potential to investigate the flow dynamics occurring along the micro-evaporator, such as the development of flow regimes and their associated heat transfer mechanisms. In fact, it has been adopted in several previous studies to better investigate flow boiling characteristics in microchannels [151, 101, 152, 113, 153, 154, 155].

Besides, the high-speed camera is a useful instrument during the two-phase flow tests, as it helps to keep under control the nucleation process along the evaporator (and in case, adjust the test conditions to have a stable two-phase flow).

The images and screenshots reported here are some examples, and they refer to the stable flow boiling test with heat flux of  $36 \text{ W cm}^{-2}$ , mass flux of  $1500 \text{ kg m}^{-2} \text{ s}^{-1}$ , fluid R134a and saturation temperature of  $25 \pm 0.5^\circ$ . In the present study the high-speed camera resolution was  $1024 \times 1024$  pixels with a resulting scale factor of approximately 1 pixel per  $11 \mu\text{m}$ . The heated area of  $11 \text{ cm}^2$  covered a size of  $856 \times 856$  pixels. The videos were acquired with a frequency of 1000 fps for a period of 2.7 seconds, giving 2727 frames. The frames were then reconstructed by the camera software to a frequency of 30 Hz in order to produce a low speed video for each test.

A screenshot obtained by the high-speed camera during a two-phase flow test is depicted in its original format (before processing the image) in Fig. C.1. In Fig. C.1 the inlet restrictions before the pin fin area, and the inlet and outlet manifold slits are also visible.

Starting from the original screenshot of Fig. C.1, it is firstly cut along the perimeter of the flow area. Additionally, a minimum intensity filter and a contrast enhancement are applied to better distinguish the two phases (liquid and liquid-vapor mixture) and the interface between single and two-phase flow, i.e. the interface at the onset of two-phase flow along the test section. This process has been developed by using the software *ImageJ*, a Java-based image processing program developed at the National Institutes of Health. The improvements obtained by

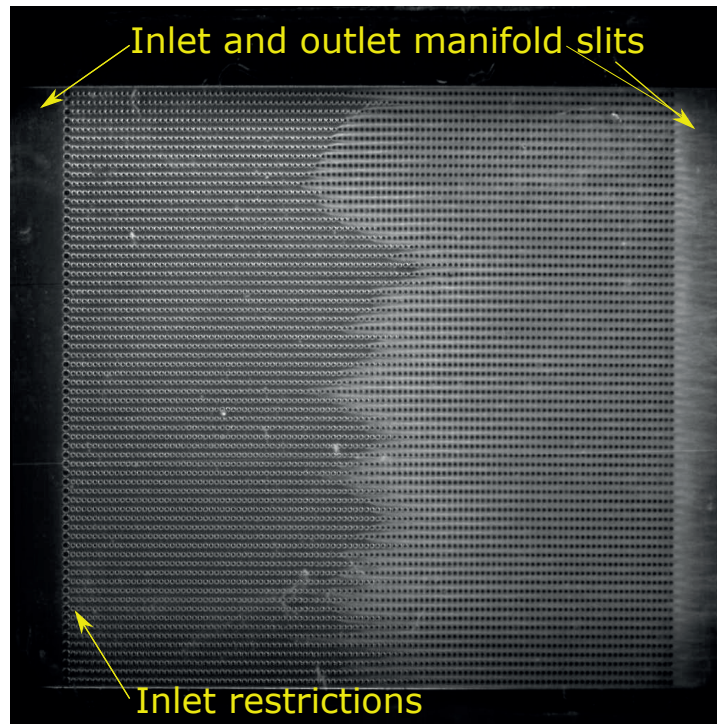


Figure C.1 – Original screenshot extracted from a high-speed camera video during a flow boiling test. Flow is moving from left to right.

processing the original images are visible in the screenshot depicted in Fig. C.2.

Afterwards, the processed screenshots have been analysed using a time-strip technique, which has been introduced firstly by Borhani et al. [113] to study bubble dynamics in microchannels, and subsequently it has been adopted to investigate pulsating heat pipes by Spinato et al. [156]. These previous studies underlined how this novel technique can be a helpful instrument to improve the understanding in two-phase flow behaviour. For a given channel (between two pin fin lines) it is possible to extract the one-dimensional light intensity distribution along its centerline for each frame in the video sequence. Thus, a 2D space-time map (referred to as the "time-strip" technique) is obtained for each channel of the flow area. In a video sequence, the different phases have different attenuation rates of grey intensity (light), and the effects of reflection and refraction play a role to catch the different flow regimes.

Figure C.3(a)-(b) illustrates two examples of a time-strip map obtained by extracting the light intensity signal of two selected channels, indicated in the screenshot of Fig. C.2 as A and B. In Fig. C.3 on the horizontal axis the length along the channel ( $z$ - direction), while on the vertical axis the time lapse of the video  $t$  are plotted, i.e. each successive horizontal line image stacked above the previous one of the selected channel. From the image it is possible to distinguish three different main light intensities: the darker region at the inlet of the heated area indicates single phase liquid flow, the grey zones on the right side represent the fully developed two-phase flow moving downstream up to the outlet of the test section,

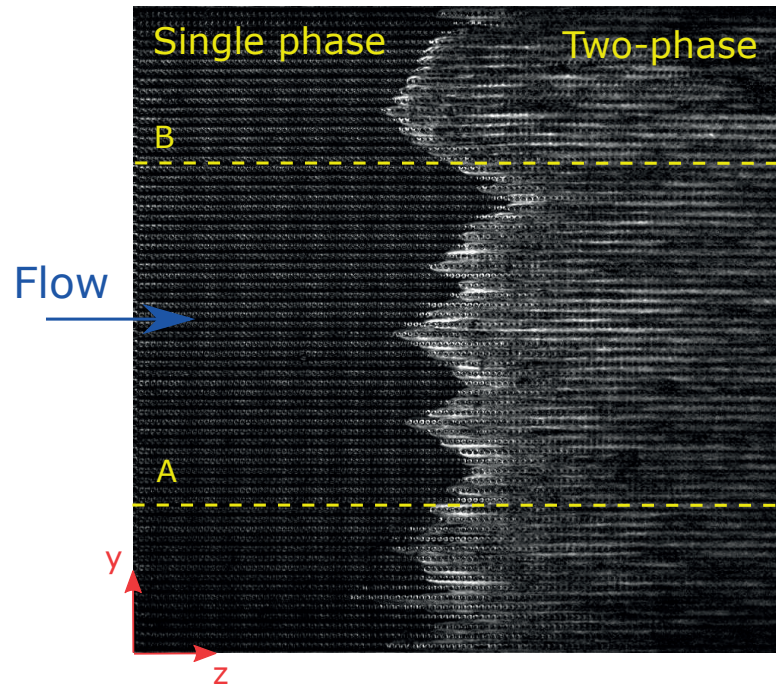


Figure C.2 – Processed screenshot by using the software *ImageJ*.

whilst the brighter area in between the dark and grey regions corresponds to the transition region in which the nucleation starts and bubbly or/and slug flow is present. Due to a limited magnification when viewing the entire test section area, it is should be noted that no bubble size or film thickness measurements could be made.

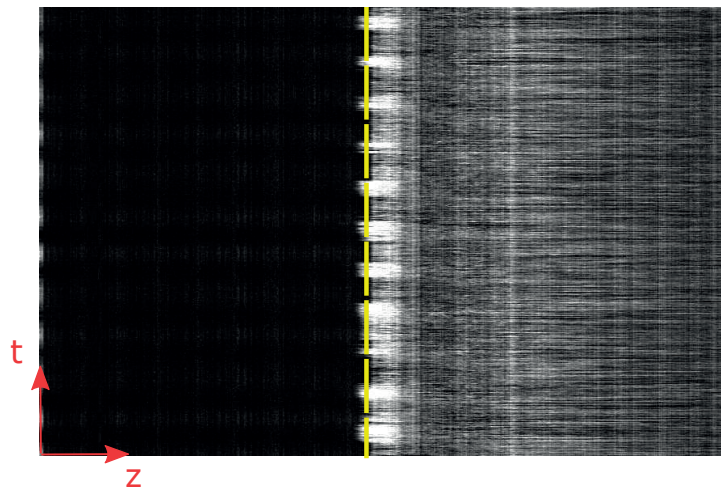
The present study focused in particular on the development of the bright area, as already presented in the results, as it gives information on the location of the nucleation process as well as on the bubble dynamics. In the two examples was observed that the dynamics of the interface changed slightly from one channel to another. Thus, 10-15 channels were then selected and processed by the time-strip technique in order to derive average parameters for each selected test case.

Starting from the time-strip map, two separated analysis have been performed to extract different parameters, as outlined in **Chapter 6** and **Chapter 7**, respectively.

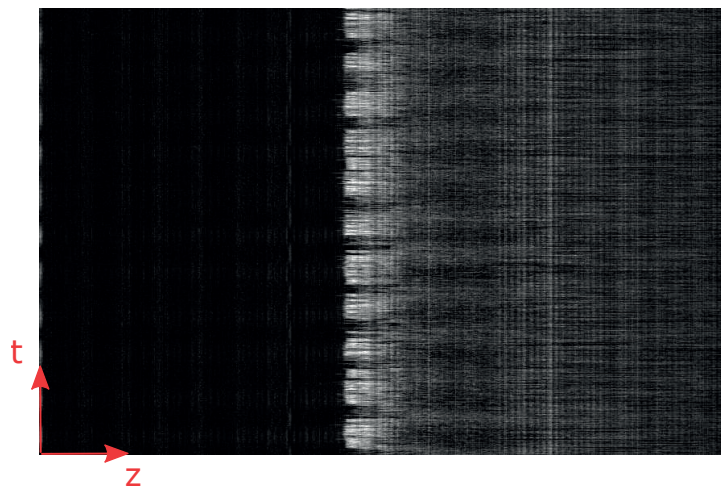
The two types of processing are here summarized below:

1. A vertical line at the beginning of the bright zone (see the yellow line in Fig. C.3(a)) was selected by using *ImageJ*, and then plotted as it is illustrated in Fig. C.4. This signal, which is the intensity of the shade of grey versus time, is then processed by means of the Fast Fourier Transform (FFT) algorithm. The vertical line is placed where the onset of two-phase flow occurs in order to catch the dynamics of the nucleation process during the acquisition period and study the frequency and amplitudes of bubble nucleation. Note that the Nyquist condition, for which the frame rate has to be twice the maximum





(a) Channel A



(b) Channel B

Figure C.3 – Time-strip technique applied to two selected channels extracted from the screenshot depicted in Fig. C.2.

component frequency of the signal being sampled, is satisfied.

2. The second way to process the time-strip maps of Figs. C.3, is to plot the intensity signal along the length of the evaporator for each successive time step, as depicted in Fig. C.5. As it is possible to observe in Fig. C.5, where each curve represents a time step, it is easy to distinguish when the flow regime transitions occur (single, bubbly/slug flow and developed two-phase flow), and it is possible to measure the bubbly/slug flow extent.

These two approaches have been applied to the high-speed videos as illustrated in **Chapter 6** and **Chapter 7**, in order to better investigate the two-phase flow dynamics along the micro-pin fin array.

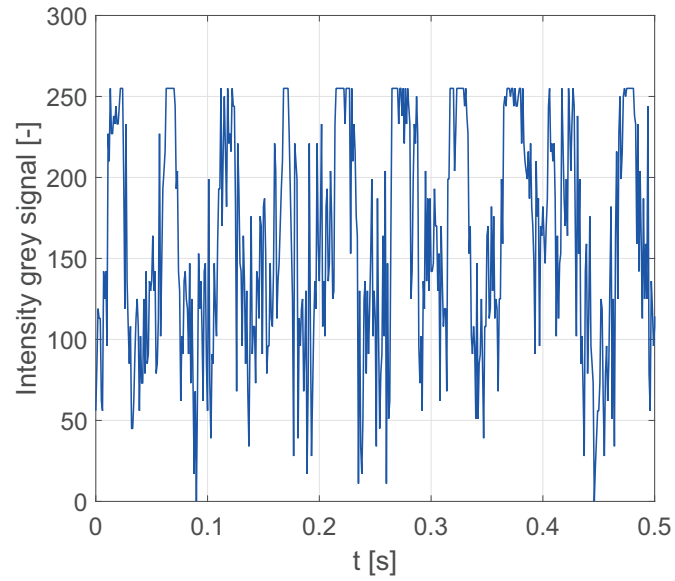


Figure C.4 – Intensity grey oscillation versus time along the interface between single and two-phase flow. Analysis type 1.

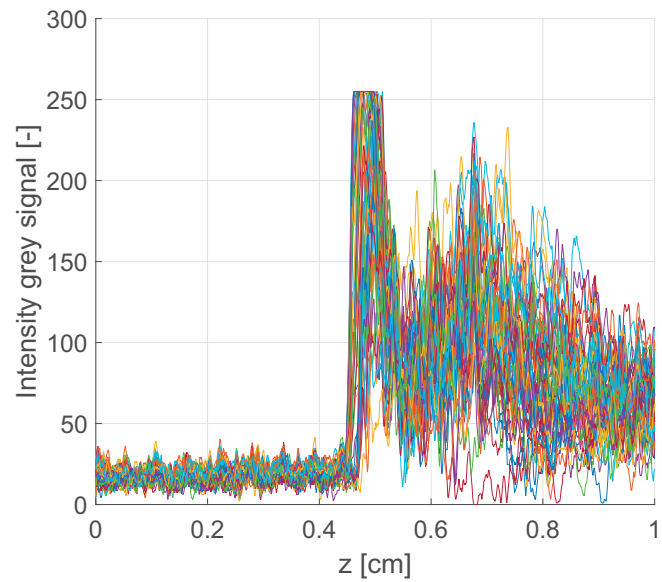


Figure C.5 – Intensity grey oscillation versus space for each time step. Analysis type 2.





## Bibliography

- [1] H. Oh, J. Gu, S. Hong, G. May, and M. Bakir, "High-aspect ratio through-silicon vias for the integration of microfluidic cooling with 3D microsystems," *Microelectronic Engineering*, vol. 142, pp. 30–35, 2015.
- [2] A. Renfer, M. Tiwari, B. Michel, D. B. Murray, D. Poulikakos, and T. Brunschwiler, "Experimental investigation into vortex structure and pressure drop across microcavities in 3D integrated electronics," *Exp. Fluids*, vol. 51, pp. 731–741, 2011.
- [3] A. Renfer, M. K. Tiwari, R. Tiwari, F. Alfieri, B. Michel, and D. Poulikakos, "Vortex shedding from confined micropin arrays," *Microfluid Nanofluid*, vol. 15, pp. 231–242, 2013.
- [4] A. Renfer, M. K. Tiwari, R. Tiwari, F. Alfieri, B. Michel, and D. Poulikakos, "Microvortex-enhanced heat transfer in 3D-integrated liquid cooling of electronic chip stacks," *Int. J. of Heat and Mass Transfer*, vol. 65, pp. 33–43, 2013.
- [5] A. Kosar and Y. Peles, "Boiling heat transfer in a hydrofoil-based micro pin fin heat sink," *Int. J. of Heat and Mass Transfer*, vol. 50, pp. 1018–1034, 2007.
- [6] S. Krishnamurthy and Y. Peles, "Flow boiling of water in a circular staggered micro-pin fin heat sink," *Int. J. of Heat and Mass Transfer*, vol. 51, pp. 1349–1364, 2008.
- [7] S. Isaacs, Y. Kim, A. J. McNamara, Y. Joshi, Y. Zhang, and M. S. Bakir, "Two-phase flow and heat transfer in pin-fin enhanced micro-gaps," *Thermal and Thermomechanical Phenomena in Electronic Systems (ITherm)*, 13th IEEE Intersociety Conference, 2012.
- [8] M. M. Waldrop, "More than Moore," *Nature*, vol. 530, pp. 144–147, 2016.
- [9] Y. Madhour, T. Brunschwiler, M. E. Kazzi, J. R. Thome, and B. Michel, "Patterned die-to-die thin film bonding for 3D chip stacks with integrated microfluidic cooling," *Int. Conference on electronic packaging technology & high density packaging, part of the CMOSAIK project*, 2012.
- [10] T. Brunschwiler, B. Michel, H. Rothuizen, U. Kloter, B. Wunderle, H. Oppermann, and H. Reichl, "Interlayer cooling potential in vertically integrated packages," *Microsystem Technologies*, vol. 15, pp. 57–74, 2009.

## Bibliography

---

- [11] T. Brunschwiler, A. Sridhar, C. Ong, and G. Schlottig, "Benchmarking study on the thermal management landscape for three-dimensional integrated circuits: From back-side to volumetric heat removal," *J. of Electronic Packaging*, vol. 138, pp. 010911: 1–10, 2016.
- [12] C. R. J. King, D. C. Sekar, M. S. Bakir, B. Dang, J. Pikarski, and J. D. Meindl, "3D stacking of chips with electrical and microfluidic I/O interconnects," in *Proceedings of the Electronic Components and Technology Conference, Lake Buena Vista, FL, 2008*, 2008.
- [13] B. Dang, M. S. Bakir, D. C. Sekar, C. R. J. King, and J. D. Meindl, "Integrated microfluidic cooling and interconnects for 2D and 3D chips," *IEEE Trans. Adv. Pack.*, vol. 33, pp. 79–87, 2010.
- [14] B. Guenin, "When Moore is less: Exploring the 3rd dimension in IC packaging," *Electronics Cooling*, vol. 15, pp. 24–27, 2009.
- [15] S. Kandlikar, "Review and projections of integrated cooling systems for three-dimensional integrated circuits," *J. of Electronic Packaging*, vol. 136, p. 024001, 2014.
- [16] C. Petti, S. Herner, and A. Walker, *Monolithic 3D Integrated Circuits, Wafer-Level 3D ICs Process Technology*. New York: Springer, Chap. 2, 2008.
- [17] F. Alfieri, M. Tiwari, I. Zinovik, D. Poulikakos, T. Brunschwiler, and B. Michel, "3D integrated water cooling of a composite multilayer stack of chips," *J. of Heat Transfer*, vol. 132, pp. 121402:1–9, 2010.
- [18] P. Ball, "Feeling the heat," *Nature*, vol. 492, pp. 174–176, 2012.
- [19] T. Brunschwiler, S. Paredes, U. Drechsler, B. Michel, W. Cesar, Y. Leblebici, B. Wunderle, and H. Reichl, "Heat-removal performance scaling of interlayer cooled chip stacks," *IEEE Intersociety Conference on Thermal and Thermomechanical Phenomena in Electronic Systems (Itherm)*, Las Vegas, 2010.
- [20] T. G. Karayiannis and M. M. Mahmoud, "Flow boiling in microchannels: Fundamentals and applications," *Applied Thermal Engineering*, vol. 115, pp. 1372–1397, 2017.
- [21] J. G. Koomey, *Estimating total power consumption by servers in the U.S. and the world*. Oakland, CA: Analytics Press, 2007.
- [22] L. Berkeley and R. Mahdavi, "Air cooling evaluation in the Maui high performance computing centre," *Federal Energy Management Program, FEMP*, 2014.
- [23] EPA, "Report to congress on server and data center efficiency public law," *U.S. Environmental Protection Agency*, pp. 109–431, 2007.
- [24] M. Saini and R. L. Webb, "Heat rejection limits of air cooled plane fin heat sinks for computer cooling," *IEEE Transactions on Components and Packaging Technologies*, vol. 26, pp. 71–79, 2003.

- 
- [25] J. F. Tullius, R. Vajtai, and Y. Bayazitoglu, "A review of cooling in microchannels," *Heat Transfer Engineering*, vol. 32, pp. 527–541, 2011.
- [26] M. M. Sabry, A. Sridhar, D. Atienza, Y. Temiz, Y. Leblebici, S. Szczukiewicz, N. Borhani, J. R. Thome, T. Brunschweiler, and B. Michel, "Towards thermally-aware design of 3D MPSoCs with inter-tier cooling," *Design, Automation and Test in Europe Conference & Exhibition*, 2011.
- [27] D. B. Tuckerman and R. F. W. Pease, "High-performance heat sinking for VLSI," *Electron Device Letters, IEEE*, vol. 2(5), pp. 126–129, 1981.
- [28] J. R. Thome, "Boiling in microchannels: a review of experiments and theory," *Int. J. of Heat and Fluid Flow*, vol. 25, pp. 128–139, 2004.
- [29] P. Lee and V. Garimella, "Saturated flow boiling heat transfer and pressure drop in silicon microchannel arrays," *Int. J. of Heat and Mass Transfer*, vol. 51, pp. 789–806, 2008.
- [30] S. G. Kandlikar, "Fundamental issues related to flow boiling in minichannels and microchannels," *Experimental Thermal and Fluid Science*, vol. 26, pp. 389–407, 2002.
- [31] G. D. Wang, P. Cheng, and H. Wu, "Unstable and stable flow boiling in parallel microchannels and in a single microchannel," *Int. J. of Heat and Mass Transfer*, vol. 50, pp. 4297–4310, 2007.
- [32] G. Hetsroni, D. Klein, A. Mosyak, Z. Segal, and E. Pogrebnyak, "Convective boiling in parallel microchannels," *Microscale Thermophysical Engineering*, vol. 8, pp. 403–421, 2004.
- [33] W. Qu and I. Mudawar, "Flow boiling heat transfer in two-phase micro-channel heat sinks - I. Experimental investigation and assessment of correlation methods," *Int. J. of Heat and Mass Transfer*, vol. 46, pp. 2755–2771, 2003.
- [34] S. Szczukiewicz, M. Magnini, and J. R. Thome, "Proposed models, ongoing experiments, and latest numerical simulations of microchannel two-phase flow boiling," *Int. J. of Multiphase Flow*, vol. 59, pp. 84–101, 2014.
- [35] T. Harirchian and S. V. Garimella, "Microchannel size effects on local flow boiling heat transfer to a dielectric fluid," *Int. J. of Heat and Mass Transfer*, vol. 51, pp. 3724–3735, 2008.
- [36] S. Szczukiewicz, N. Borhani, and J. R. Thome, "Two-phase heat transfer and high-speed visualization of refrigerant flows in  $100 \times 100 \mu\text{m}$  silicon multi-microchannels," *Int. J. of Refrigeration*, vol. 36, pp. 402–413, 2013.
- [37] H. Huang, N. Borhani, and J. R. Thome, "Experimental investigation on flow boiling pressure drop and heat transfer of R1233zd(E) in a multi-microchannel evaporator," *Int. J. of Heat and Mass Transfer*, vol. 98, pp. 596–610, 2016.

## Bibliography

---

- [38] S. G. Kandlikar, "Mechanistic considerations for enhancing flow boiling heat transfer in microchannels," *J. of Heat Transfer*, vol. 138, pp. 1–16, 2016.
- [39] Y. Zhang, A. Dembla, and M. Bakir, "Silicon micropin-fin heat sink with integrated tsvs for 3-D ICs: Tradeoff analysis and experimental testing," *IEEE Transactions on Components, packaging and manufacturing technology*, vol. 3, pp. 1842–1850, 2013.
- [40] C. Falsetti, H. Jafarpoorchekab, M. Magnini, N., and J. R. Thome, "Two-phase operational maps, pressure drop, and heat transfer for flow boiling of R236fa in a micro-pin fin evaporator," *Int. J. of Heat and Mass Transfer*, vol. 107, pp. 805–819, 2017.
- [41] C. Falsetti, M. Magnini, and J. R. Thome, "Hydrodynamic and thermal analysis of a micro-pin fin evaporator for on-chip two-phase cooling of high density power micro-electronics," *Applied Thermal Engineering*, vol. 130, pp. 1425–1439, 2018.
- [42] C. L. Ong, S. Paredes, A. Sridhar, B. Michel, and T. Brunschwiler, "Radial hierarchical microfluidic evaporative cooling for 3D integrated microprocessors," *Exp. Thermal and Fluid Science*, vol. 35, pp. 37–47, 2011.
- [43] B. Jasperson, Y. Jeon, K. Turner, F. Pfefferkorn, and W. Qu, "Comparison of micro-pin-fin and microchannel heat sinks considering thermal-hydraulic performance and manufacturability," *IEEE Transaction on components and packaging technology*, vol. 33, pp. 148–160, 2010.
- [44] R. Prasher, J.-Y. Chang, A. Myers, D. Chau, and D. He, "Nusselt number and friction factor of staggered arrays of low aspect ratio micropin-fins under cross flow for water as fluid," *ASME J. Heat Transfer*, vol. 129, pp. 141–153, 2007.
- [45] A. Kosar, C. Mishra, and Y. Peles, "Laminar flow across a bank of low aspect ratio micro pin fins," *J. of Fluids Engineering*, vol. 127, pp. 419–430, 2005.
- [46] A. Kosar and Y. Peles, "Convective flow of refrigerant (R-123) across a bank of micro pin fins," *Int. J. of Heat and Mass Transfer*, vol. 49, pp. 3142–3155, 2006.
- [47] W. Qu and A. Siu-Ho, "Liquid single phase flow in an array of micro-pin-fins part I: Heat transfer characteristics," *ASME J. Heat Transfer*, vol. 130, pp. 122402–1–11, 2008.
- [48] J. Mita and W. Qu, "Pressure drop of water flow across a micro-pin-fin array part 1: Isothermal liquid single-phase flow," *ASME J. Heat Transfer*, vol. 89, pp. 1073–1082, 2015.
- [49] A. Zukauskas and R. Ulinskas, "Heat transfer from tubes in cross flow," *Advances in Heat Transfer, Academic, New York*, vol. 8, 1972.
- [50] X. Yu, C. Woodcock, J. Plawsky, and Y. Peles, "An investigation of convective heat transfer in microchannel with pirahna pin fin," *Int. J. of Heat and Mass Transfer*, vol. 103, pp. 1125–1132, 2016.

- 
- [51] Z. Wan and Y. Joshi, "Pressure drop and heat transfer characteristics of pin fin enhanced microgaps in single phase microfluidic cooling," *Int. J. of Heat and Mass Transfer*, vol. 115, pp. 115–126, 2017.
- [52] C. Rubio-Jimenez, S. Kandlikar, and A. Hernandez-Guerrero, "Performance of online and offset micro pin-fin heat sinks with variable fin density," *IEEE Transaction on components, packaging and manufacturing technology*, vol. 3, pp. 86–93, 2013.
- [53] C. Liang, G. Papadakis, and X. Luo, "Effect of tube spacing on the vortex shedding characteristics of laminar flow past a inline tube array: A numerical study," *Computers & Fluids*, vol. 38, pp. 950–964, 2009.
- [54] J. B. Marcinichen, J. A. Olivier, and J. R. Thome, "Reasons to use two-phase refrigerant cooling," *Electr. Cool*, vol. 17, pp. 22–27, 2011.
- [55] Y. Madhour, B. P. d'Entremont, J. B. Marcinichen, B. Michel, and J. R. Thome, "Integration of intra chip stack fluidic cooling using thin-layer solder bonding," *J. of Electronic Packaging*, vol. 136, p. 021006, 2014.
- [56] J.-M. Koo, S. Im, L. Jiang, and K. Goodson, "Integrated microchannel cooling for three-dimensional electronic circuit architectures," *J. of Heat Transfer*, vol. 127, pp. 49–59, 2005.
- [57] J. B. Marcinichen, J. A. Olivier, and J. R. Thome, "Reasons to use two-phase refrigerant cooling," *Electronics Cooling*, vol. 17, pp. 22–27, 2011.
- [58] S.-M. Kim and I. Mudawar, "Review of databases and predictive methods for heat transfer in condensing and boiling mini/micro-channel flows," *Int. J. of Heat and Mass Transfer*, vol. 77, pp. 627–652, 2014.
- [59] S. Garimella, L.-T. Yeh, and T. Persoons, "Thermal management challenges in telecommunication systems and data centers," *IEEE Trans. on Components, packaging and manufacturing technology*, vol. 2, pp. 1307–1317, 2012.
- [60] B. Agostini, M. Fabbri, J. Park, L. Wojtan, J. R. Thome, and B. Michel, "State of the art of high heat flux cooling technologies," *Heat Transfer Engineering*, vol. 28, pp. 258–281, 2007.
- [61] R. Hannemann, J. Marsala, and M. Pitasi, "Pumped liquid multiphase cooling," in *IMECE - International Mechanical Engineering Congress and Exposition, Anaheim, CA, 2004*, 2004.
- [62] R. Mongia and et al., "Small scale refrigeration system for electronics cooling within a notebook computer," in *ITHERM, San Diego, CA, 2006*, 2006.
- [63] S. Trutassanawin, E. A. Groll, S. Garimella, and L. Cremaschi, "Experimental investigation of a miniature scale refrigeration system for electronics cooling," *IEEE Transaction on Components and Packaging Technologies*, vol. 29, pp. 678–687, 2006.

- [64] J. B. Marcinichen, J. A. Olivier, V. de Oliveira, and J. R. Thome, "A review of on-chip micro-evaporation: Experimental evaluation of liquid pumping and vapor compression driven cooling systems and control," *Applied Energy*, vol. 92, pp. 147–161, 2012.
- [65] J. B. Marcinichen, D. Wu, S. Paredes, J. R. Thome, and B. Michel, "Dynamic flow control and performance comparison of different concepts of two-phase on-chip cooling cycles," *Applied Energy*, vol. 114, pp. 179–191, 2014.
- [66] D. J. Chamund, L. Coulbeck, D. R. Newcombe, and P. R. Waind, "High power density IGBT module for high reliability applications," in *IEEE 6th Int. Power Electronics and Motion Control Conference, 17-20 May 2009, Wuhan, China, 2009*.
- [67] M. Bohr, "Interconnect scaling- the real limiter to high performance ULSI," *IEEE Int. Electronic Device Meeting, IEDM*, pp. 241–244, 1995.
- [68] J. B. Marcinichen, J. A. Olivier, and J. R. Thome, "On-chip two-phase cooling of datacenters: Cooling system and energy recovery evaluation," *Applied Thermal Engineering*, vol. 41, pp. 36–51, 2012.
- [69] J. B. Marcinichen, J. A. Olivier, N. Lamaison, and J. R. Thome, "Advances in electronics cooling," *Heat Transfer Engineering*, vol. 34, pp. 434–436, 2013.
- [70] N. Lamaison, C. L. Ong, J. B. Marcinichen, and J. R. Thome, "Two-phase mini-thermosyphon electronics cooling: Dynamic modeling, experimental validation and application to 2U servers," *Applied Thermal Engineering*, vol. 110, pp. 481–494, 2017.
- [71] F. Cataldo and J. R. Thome, "Experimental evaluation of the thermal performances of a thermosyphon cooling system rejecting heat by natural and forced convection," *Applied Thermal Engineering*, vol. 127, pp. 1404–1415, 2017.
- [72] D. Chisholm and A. D. K. Laird, "Two-phase flow in rough tubes," *Trans. ASME*, vol. 80, p. 276, 1958.
- [73] S. Krishnamurthy and Y. Peles, "Flow boiling heat transfer on micro pin fins entrenched in a microchannel," *J. of Heat Transfer*, vol. 132, pp. 1–7, 2010.
- [74] W. Qu and A. Siu-Ho, "Experimental study of saturated flow boiling heat transfer in an array of staggered micro-pin-fins," *Int. J. of Heat and Mass Transfer*, vol. 52, pp. 1853–1863, 2009.
- [75] J. Mita and W. Qu, "Pressure drop of water flow across a micro-pin-fin array part 2: Adiabatic liquid–vapor two-phase flow," *ASME J. Heat Transfer*, vol. 89, pp. 1007–1015, 2015.
- [76] R. Lockhart and R. Martinelli, "Proposed correlation of data for isothermal two-phase, two-component flow in pipes," *Chemical Eng. Progress*, vol. 45, pp. 39–48, 1949.



- 
- [77] A. Reeser, A. Bar-Cohen, and G. Hetsroni, "High quality flow boiling heat transfer and pressure drop in microgap pin fin arrays," *Int. J. of Heat and Mass Transfer*, vol. 78, pp. 974–985, 2014.
- [78] Y. Lie, J. Ke, W. Chang, T. Cheng, and T. Lin, "Saturated flow boiling heat transfer and associated bubble characteristics of FC-72 on a heated micro-pin-finned silicon chip," *Int. J. of Heat and Mass Transfer*, vol. 50, pp. 3862–3876, 2007.
- [79] A. Ma, J. Wei, M. Yuan, and J. Fang, "Enhanced flow boiling heat transfer of fc-72 on micro-pin-finned surfaces," *Int. J. of Heat and Mass Transfer*, vol. 52, pp. 2925–2931, 2009.
- [80] W. Chang, C. Chen, J. Ke, and T. Lin, "Subcooled flow boiling heat transfer and associated bubble characteristics of FC-72 on a heated micro-pin-finned silicon chip," *Int. J. of Heat and Mass Transfer*, vol. 53, pp. 5605–5621, 2010.
- [81] M. Law and P.-S. Lee, "A comparative study of experimental flow boiling heat transfer and pressure characteristics in straight- and oblique-finned microchannels," *Int. J. of Heat and Mass Transfer*, vol. 85, pp. 797–810, 2015.
- [82] D. Deng, W. Wan, Y. Qin, J. Zhang, and X. Chu, "Flow boiling enhancement of structured microchannels with micro pin fins," *Int. J. of Heat and Mass Transfer*, vol. 105, pp. 338–349, 2017.
- [83] T. David, D. Mendler, A. Mosyak, A. Bar-Cohen, and G. Hetsroni, "Thermal management of time-varying high heat flux electronic devices," *Trans. ASME. J. Electronic Packaging*, vol. 136, pp. 1–10, 2014.
- [84] C. Woodcock, X. Yu, J. Plawsky, and Y. Peles, "Piranha pin fin (ppf) - advanced flow boiling microstructures with low surface tension dielectric fluids," *Int. J. of Heat and Mass Transfer*, vol. 90, pp. 591–604, 2015.
- [85] D. A. McNeil, A. Raeisi, P. Kew, and P. Bobbili, "A comparison of flow boiling heat-transfer in in-line mini pin fin and plane channel flows," *Applied Thermal Engineering*, vol. 30, pp. 2412–2425, 2010.
- [86] M. Nasr, C. Green, P. Kottke, X. Zhang, T. Sarvey, Y. Joshi, M. Bakir, and A. Fedorov, "Flow regimes and convective heat transfer of refrigerant flow boiling in ultra-small clearance microgaps," *Int. J. of Heat and Mass Transfer*, vol. 108, pp. 1702–1713, 2017.
- [87] J. Chen, "Correlation for boiling heat transfer to saturated fluids in convective flow," *I and EC Process Design Develop*, vol. 5, p. 322, 1966.
- [88] A. Kawahara, P. Chung, and M. Kawaji, "Investigation of two-phase flow pattern, void fraction and pressure drop in a microchannel," *Int. J. of Multiphase Flow*, vol. 28, p. 1411, 2002.

## Bibliography

---

- [89] B. Short, P. Raad, and D. Price, "Performance of pin fin cast aluminium, coldwalls, part 2: Colburn j-factor correlations," *J. of Thermophysics and Heat Transfer*, vol. 16, pp. 397–403, 2002.
- [90] J. R. Thome, V. Dupont, and A. Jacobi, "Heat transfer model for evaporation in microchannels. Part I: Presentation of the model," *Int. J. of Heat and Mass Transfer*, vol. 47, pp. 3375–3385, 2004.
- [91] V. Dupont, J. R. Thome, and A. Jacobi, "Heat transfer model for evaporation in microchannels. Part II: Comparison with the database," *Int. J. of Heat and Mass Transfer*, vol. 47, pp. 3387–3401, 2004.
- [92] W. Qu and I. Mudawar, "Flow boiling heat transfer in two-phase micro-channel heat sinks- II. Annular two-phase flow model," *Int. J. of Heat and Mass Transfer*, vol. 46, pp. 2773–2784, 2003.
- [93] A. Cioncolini and J. R. Thome, "Algebraic turbulence modeling in adiabatic and evaporating annular two-phase flow," *Int. J. of Heat and Fluid Flow*, vol. 32, pp. 805–817, 2011.
- [94] M. Magnini, B. Pulvirenti, and J. R. Thome, "Numerical investigation of hydrodynamics and heat transfer of elongated bubbles during flow boiling in microchannel," *Int. J. of Heat and Mass Transfer*, vol. 59, pp. 451–471, 2013.
- [95] M. Magnini, B. Pulvirenti, and J. R. Thome, "Numerical investigation of the influence of leading and sequential bubbles on slug flow boiling within microchannel," *Int. J. of Thermal Sciences*, vol. 71, pp. 36–52, 2013.
- [96] M. Magnini and J. R. Thome, "An updated three-zone heat transfer model for slug flow boiling in microchannels," *Int. J. of Heat and Mass Transfer*, vol. 91, pp. 296–314, 2017.
- [97] E. Costa-Patry and J. R. Thome, "Flow pattern-based flow boiling heat transfer model for microchannels," *Int. J. of Refrigeration*, vol. 36, pp. 414–420, 2013.
- [98] T. Harirchian and S. V. Garimella, "Flow regime-based modeling of heat transfer and pressure drop in microchannel flow boiling," *Int. J. of Heat and Mass Transfer*, vol. 55, pp. 1246–1260, 2012.
- [99] H. Huang and J. R. Thome, "Local measurements and a new flow pattern based model for subcooled and saturated flow boiling heat transfer in multi-microchannel evaporators," *Int. J. of Heat and Mass Transfer*, vol. 103, pp. 701–714, 2016.
- [100] R. Revellin and J. R. Thome, "A new type of diabatic flow pattern map for boiling heat transfer in microchannels," *J. of Micromechanics and Microengineering*, vol. 17, pp. 788–796, 2007.



- 
- [101] R. Revellin and J. R. Thome, "Experimental investigation of R134a and R245fa two-phase flow in microchannels for different flow conditions," *Int. J. of Heat and Fluid Flow*, vol. 28, pp. 63–71, 2007.
- [102] C. L. Ong and J. R. Thome, "Macro-to-microchannel transition in two-phase flow: Part 1 - two-phase flow patterns and film thickness measurements," *Experimental Thermal and Fluid Science*, vol. 35, pp. 37–47, 2011.
- [103] R. Revellin, *Experimental two-phase fluid flow in microchannels*. PhD thesis, EPFL-STI-LTCM, Lausanne, 2005.
- [104] L. Consolini, *Convective boiling heat transfer in a single micro-channel*. PhD thesis, EPFL-STI-LTCM, Lausanne, 2008.
- [105] C. L. Ong, *Macro-to-microchannel transition in two-phase flow and evaporation*. PhD thesis, EPFL-STI-LTCM, Lausanne, 2010.
- [106] S. Szczukiewicz, *Thermal and visual operational characteristics of multi-microchannel evaporators using refrigerants*. PhD thesis, EPFL-STI-LTCM, Lausanne, 2012.
- [107] H. Huang, *Flow boiling pressure drop and heat transfer of refrigerants in multi-microchannel evaporators under steady and transient states*. PhD thesis, EPFL-STI-LTCM, Lausanne, 2016.
- [108] H. Wu and P. Cheng, "Visualization and measurement of periodic boiling in silicon microchannels," *Int J. Heat Mass Transfer*, vol. 46, pp. 2603–2614, 2003.
- [109] J. E. Park, J. R. Thome, and B. Michael, "Effect of inlet orifices on saturated CHF and flow visualization in multi-microchannel heat sinks," *In: 25th IEEE SEMI-THERM Symposium*, 2009.
- [110] S. J. Kline and F. A. McClintock, "Describing uncertainties in single-sample experiments," *Mech. Eng.*, vol. 75, pp. 3–8, 1953.
- [111] H. Huang, N. Borhani, N. Lamaison, and J. R. Thome, "A new method for reducing local heat transfer data in multimicrochannel evaporators," *Int. J. of Thermal Sciences*, vol. 115, pp. 112–124, 2017.
- [112] H. R. Shanks, P. H. Sidles, P. D. Maycock, and G. C. Danielson, "Thermal conductivity of silicon from 300 to 1400 K," *Phys. Rev.*, vol. 130(5), pp. 1743–1748, 1963.
- [113] N. Borhani, B. Agostini, and J. R. Thome, "A novel time strip flow visualisation technique for investigation of intermittent dewetting and dryout in elongated bubble flow in a microchannel evaporator," *Int. J. of Heat and Mass Transfer*, vol. 53, pp. 4809–4818, 2010.
- [114] S. Szczukiewicz, N. Borhani, and J. R. Thome, "Fine-resolution two-phase heat transfer coefficient measurements of refrigerants in multi-microchannel evaporators," *Int. J. of Heat and Mass Transfer*, vol. 67, pp. 913–929, 2013.

## Bibliography

---

- [115] D. Chisholm, "A theoretical basis for the Lockhart-Martinelli correlation for two-phase flow," *Int. J. of Heat and Mass Transfer*, vol. 10, pp. 1767–1778, 1967.
- [116] S. Zivi, "Estimation of steady-state steam void-fraction by means of principle of minimum entropy production," *J. of Heat Transfer*, vol. 86, pp. 247–252, 1964.
- [117] E. Costa-Patry, E. Olivier, B. Nichita, B. A. Michael, and J. R. Thome, "Two-phase flow of refrigerants in 85  $\mu\text{m}$ -wide multi-microchannels: Part I-Pressure drop," *Int. J. of Heat and Fluid Flow*, vol. 32, pp. 451–463, 2011.
- [118] T. Bergman, A. Lavine, F. Incropera, and D. Dewitt, *Fundamentals of Heat and Mass Transfer*. 111 River Street, Hoboken,: John Wiley and Sons, 2011.
- [119] C. L. Ong and J. R. Thome, "Macro-to-microchannel transition in two-phase flow: Part 2 – flow boiling heat transfer and critical heat flux," *Exp. Th. Fluid Science*, vol. 35, pp. 873–886, 2011.
- [120] L. Consolini and J. R. Thome, "Micro-channel flow boiling heat transfer of R-134a, R-236fa, and R-245fa," *Microfluid Nanofluid*, vol. 6, pp. 731–746, 2009.
- [121] F. T. M. Nieuwstadt, B. J. Boersma, and J. Westerweel, *Turbulence. Introduction to theory and applications of turbulent flows*. Springer, 2015.
- [122] S. G. Kandlikar, "Nucleation characteristics and stability considerations during flow boiling in microchannels," *Experimental Thermal and Fluid Science*, vol. 30, pp. 441–447, 2006.
- [123] F. White, *Fluid Mechanics*. New York: Mc Graw Hill, 2002.
- [124] D. Brutin, F. Topin, and L. Tadrist, "Experimental study of unsteady convective boiling in heated minichannels," *Int. J. of Heat and Mass Transfer*, vol. 46, pp. 2957–2965, 2003.
- [125] D. B. R. Kenning and Y. Yan, "Saturated flow boiling of water in a narrow channel: experimental investigation of local phenomena," *Chemical Engineering Research and Design*, vol. 79, pp. 425–436, 2001.
- [126] M. Jagirdar and P. S. Lee, "A diagnostic tool for detection of flow-regimes in a microchannel using transient wall temperature signal," *Applied Energy*, vol. 185, pp. 2232–2244, 2017.
- [127] V. P. Carey, *Liquid-vapor phase change phenomena*. New York: Taylor and Francis, 1992.
- [128] B. B. Mikic and W. M. Rohsenow, "Bubble growth rates in non-uniform temperature field," *Prog. Heat and Mass Transfer*, vol. 2, pp. 283–292, 1969.
- [129] H. Huang, N. Borhani, and J. R. Thome, "Experimental investigation on flow boiling pressure drop and heat transfer of R1233zd(E) in a multi-microchannel evaporator," *Int. J. of Heat and Mass Transfer*, vol. 98, pp. 596–610, 2016.

- 
- [130] VDI-Wärmeatlas. Heidelberg: Springer-Verlag, Berlin, 1997.
- [131] S. Krishnamurthy and Y. Peles, "Gas-liquid two-phase flow across a bank of micropillars," *Physics of Fluids*, vol. 19, p. 043302, 2007.
- [132] C. Falsetti, M. Magnini, and J. R. Thome, "Flow boiling heat transfer and pressure drops of R1234ze(E) in a silicon micro-pin fin evaporator," *J. of Electronic Packaging*, vol. 139, p. 031008, 2017.
- [133] B. Agostini, R. Revellin, J. R. Thome, M. Fabbri, B. Michel, D. Calmi, and U. Kloter, "High heat flux flow boiling in silicon multi-microchannels - part III: Saturated critical heat flux of R236fa and two-phase pressure drops," *Int. J. of Heat and Mass Transfer*, vol. 51, pp. 5426–5442, 2008.
- [134] Y. Han and N. Shikazono, "Measurement of the liquid film thickness in microtube slug flow," *Int. J. of Heat and Fluid Flow*, vol. 30, pp. 842–853, 2009.
- [135] Y. Han and N. Shikazono, "The effect of bubble acceleration on the liquid film thickness in micro tubes," *Int. J. of Heat and Fluid Flow*, vol. 31, pp. 630–639, 2010.
- [136] P. Aussillous and D. Quéré, "Quick deposition of a fluid on the wall of a tube," *Physics of Fluids*, vol. 12, pp. 2367–2371, 2000.
- [137] L. Consolini and J. R. Thome, "A heat transfer model for evaporation of coalescing bubbles in micro-channel flow," *Int. J. of Heat and Fluid Flow*, vol. 31, pp. 115–125, 2010.
- [138] R. Situ, M. Ishii, T. Hibiki, J. Tu, G. Yeoh, and M. Mori, "Bubble departure frequency in forced convective subcooled boiling flow," *Int. J. of Heat and Mass Transfer*, vol. 51, pp. 6268–6282, 2008.
- [139] A. Cioncolini and J. R. Thome, "Entrained liquid fraction prediction in adiabatic and evaporating annular two-phase flow," *Nuclear Engineering and Design*, vol. 243, pp. 200–213, 2012.
- [140] A. Cioncolini and J. R. Thome, "Void fraction prediction in annular two-phase flow," *Int. J. of Multiphase Flow*, vol. 43, pp. 72–84, 2012.
- [141] A. Cioncolini, J. R. Thome, and C. Lombardi, "Unified macro-to-microscale method to predict two-phase frictional pressure drops of annular flows," *Int. J. of Multiphase Flow*, vol. 35, pp. 1138–1148, 2009.
- [142] V. Carey, "Two-phase flow in small-scale ribbed and finned passages for compact evaporators and condensers," *Nuclear Engineering and Design*, vol. 141, pp. 249–268, 1993.
- [143] P. Lee, F. Tseng, and C. Pan, "Bubble dynamics in micro channels. Part I: Single microchannel," *Int. J. of Heat and Mass Transfer*, vol. 47, pp. 5575–5589, 2004.

## Bibliography

---

- [144] C. J. Kuo, A. Kosar, Y. Peles, S. Virost, C. Mishra, and M. Jensen, "Bubble dynamics during boiling in enhanced surface microchannels," *J. of Microelectromechanical Systems*, vol. 15(6), pp. 1514–1527, 2006.
- [145] K. Moriyama and A. Inoue, "Thickness of the liquid film formed by a growing bubble in a narrow gap between two horizontal plates," *J. Heat Transfer*, vol. 118, pp. 132–139, 1996.
- [146] J. A. Boure, A. Bergles, and L. Tong, "Review of two-phase flow instability," *Nuclear engineering and design*, vol. 25, pp. 165–192, 1973.
- [147] S. Kakac and B. Bon, "Review of two-phase flow dynamic instabilities in tube boiling systems," *Int. J. of Heat and Mass Transfer*, vol. 51, pp. 399–433, 2008.
- [148] F. Bozzoli, G. Pagliarini, and S. Rainieri, "Experimental validation of the filtering technique approach applied to the restoration of the heat source field," *Exp. Thermal and Fluid Science*, vol. 44, pp. 858–867, 2013.
- [149] S. Patankar, *Numerical heat transfer and fluid flow*. New York: Mc Graw Hill, 1980.
- [150] J. Taylor, *An introduction to error analysis. The study of uncertainties in physical measurements*. Sausalito, California: University Science Books, 2002.
- [151] T. Chen and S. V. Garimella, "Measurements and high-speed visualizations of flow boiling of a dielectric fluid in a silicon microchannel heat sink," *Int. J. of Multiphase Flow*, vol. 32, pp. 957–971, 2006.
- [152] T. Harirchian and S. V. Garimella, "Effects of channel dimension, heat flux, and mass flux on flow boiling regimes in microchannels," *Int. J. of Multiphase Flow*, vol. 35, pp. 349–362, 2009.
- [153] R. A. B. Palm, C. Martin-Callizo, and M. Maqbool, "Study of flow boiling characteristics of a microchannel using high speed visualization," *J. of Heat Transfer*, vol. 135, pp. 1–8, 2013.
- [154] S. Khodaparast, N. Borhani, and J. R. Thome, "Application of micro particle shadow velocimetry IPSV to two-phase flows in microchannels," *Int. J. of Multiphase Flow*, vol. 62, pp. 123–133, 2014.
- [155] N. Borhani and J. R. Thome, "Intermittent dewetting and dryout of annular flows," *Int. J. of Multiphase Flow*, vol. 67, pp. 144–152, 2014.
- [156] G. Spinato, N. Borhani, and J. R. Thome, "Understanding the self-sustained oscillating two-phase flow motion in a closed loop pulsating heat pipe," *Energy*, vol. 90, pp. 889–899, 2015.

# Chiara Falsetti

## Education

- 2015–Present **École Polytechnique Fédérale de Lausanne (EPFL)**, *Laboratory of Heat and Mass Transfer*, PhD candidate.
- 2012–2014 **Università degli Studi di Brescia**, *Mechanical Engineering Masters of Science*, 110/110 - Specialization in Energy.
- Feb–July 2014 **Delft University of Technology**, *Master Thesis*, Laboratory of Aero and Hydro Dynamics in collaboration with J.M. Burgerscentrum (JMBC), Delft (NL).
- Sep–Feb 2013 **Université Pierre et Marie Curie (UPMC)**, Paris (FR), Erasmus exchange program.
- 2009–2012 **Università degli Studi di Brescia**, *Mechanical Engineering Bachelor*, 106/110.

## Professional Experience

- 2015–Present **Phd candidate**, École Polytechnique Fédérale de Lausanne, Laboratory of Heat and Mass Transfer, Switzerland.

**Project description:** An extensive experimental analysis of flow boiling across a micro-evaporator for cooling of high power and density micro-electronics was performed to define the thermal and hydraulic performance of the device. Several geometries and refrigerants were tested to define the potential design and the optimal operation ranges of the micro-evaporator. Heat transfer mechanisms and fluid mechanics were deeply investigated by utilizing advanced techniques, such as infrared camera measurements and high-speed flow visualization. Delivered four class lectures on temperature measurement techniques, heat and mass transfer, and two-phase flows and heat transfer.

### Achievements and developed skills:

- Solid multidisciplinary and multilingual background;
- Responsible for designing and assembling the experimental set-up and Lab instrumentation;
- Directed and supervised students for bachelor and master courses;
- Learned how to manage a group activity and collaborate with project partners.

- Feb–July 2014 **Visiting fellow**, Delft University of Technology, Netherlands.  
Laboratory of Aero and Hydro Dynamics in collaboration with J.M. Burgerscentrum (JMBC)

**Master Thesis project:** Computational fluid dynamics simulations on water-oil systems in the field of transport in gas and oil pipelines. Thesis title: Numerical analysis of laminar liquid-liquid core-annular flow.

## Scientific publications:

- **C. Falsetti**, H. Jafarpoorchebab, M. Magnini, J.R. Thome, Two-phase operational maps, pressure drop, and heat transfer for flow boiling of R236fa in a micro-pin fin evaporator, *Int. Journal of Heat and Mass Transfer*, 107, 2017 805-819;
- **C. Falsetti**, M. Magnini, J.R. Thome, Flow boiling heat transfer and pressure drops of R1234ze(E) in a silicon micro-pin fin evaporator, *Journal of Electronic Packaging*, 139, (2017), 1-10;
- **C. Falsetti**, M. Magnini, J.R. Thome, Hydrodynamic and thermal analysis of a micro-pin fin evaporator for on-chip two-phase cooling of high density power micro-electronics, *Applied Thermal Engineering*, 130, (2018), 1425-1439.
- **C. Falsetti**, M. Magnini, J.R. Thome, A new flow pattern-based boiling heat transfer model for micro-pin fin evaporators, *Int. Journal of Heat and Mass Transfer*, under review (2017).

## Technical Skills

### IT

OS Linux, MS Windows  
Programming C, C++  
Software OpenFOAM, LabView, ImageJ, Matlab, Python, Fortran, Aspen, SolidWorks, AutoCAD

### Languages

Italian **Native language**  
English **Advanced** C1  
French **Advanced** C1  
Spanish **Basic** A2

### Additional training and courses

Feb. 2015 Eurotech winter school, Integrated Approaches to Energy Systems. Energy conversion, storage devices and integrated urban energy systems design. *EPFL, Lausanne*.  
March 2015 LabVIEW course, CORE I, *EPFL, Lausanne*.  
June 2015 Dynamics of Bubbly Flows, *CISM, Udine*. Poster presentation.  
June 2016-17 The intersociety Conference on Thermal and Thermomechanical Phenomena in Electronic Systems (ITHERM), *Orlando, United States*. Conference paper and invited presentation.  
May 2017 Ecocloud: sustainable cloud computing technologies, *Lausanne*. Invited presentation.

## Interests

- Long distance running competitions, half-marathon  
- Alpine Skiing

## Personal Information

Date of Birth **08.11.1990**  
Place of Birth **Brescia, Italy**  
Nationality **Italian**  
Adress **Avenue de Lavaux 10, 1009, Pully, Switzerland**  
Mobile **+41 78 934 13 65**  
E-mail **chiara.falsetti@gmail.com**

